University of Nevada, Reno

Repetitive Control for Hysteretic Systems: Theory and Application in Piezo-Based Nanopositioners

A dissertation submitted in partial fulfillment of the requirements for the degree of

Doctor of Philosophy

in

Mechanical Engineering

by

Yingfeng Shan

Dr. Kam K. Leang/Dissertation Advisor

December, 2011

UNIVERSITY OF NEVADA, RENO

THE GRADUATE SCHOOL

We recommend that the dissertation
prepared under our supervision by

YINGFENG SHAN

entitled

**Repetitive Control for Hysteretic Systems:
Theory and Application in Piezo-Based Nanopositioners**

be accepted in partial fulfillment of the
requirements for the degree of

DOCTOR OF PHILOSOPHY

Kam K. Leang, Ph.D., Advisor

Kwang J. Kim, Ph.D., Committee Member

Eric L. Wang, Ph.D., Committee Member

M. Sami Fadali, Ph.D., Committee Member

Yantao Shen, Ph.D., Committee Member

Mark Pinsky, Ph.D., Committee Member

M. Sami Fadali, Ph.D., Graduate School Representative

Marsha H. Read, Ph.D., Associate Dean, Graduate School

December, 2011

University of Nevada, Reno
Statewide • Worldwide

THE GRADUATE SCHOOL

We recommend that the thesis
prepared under our supervision by

YINGFENG SHAN

entitled

Repetitive Control for Hysteretic Systems:
Theory and Application in Piezo-Based Nanopositioners

be accepted in partial fulfillment of the
requirements for the degree of

DOCTOR OF PHILOSOPHY

Kam K. Leang, Ph.D., Advisor

Kwang J. Kim, Ph.D., Committee Member

Eric L. Wang, Ph.D., Committee Member

Yantao Shen, Ph.D., Committee Member

Mark Pinsky, Ph.D., Committee Member

M. Sami Fadali, Ph.D., Graduate School Representative

Marsha H. Read, Ph.D., Associate Dean, Graduate School

December, 2011

Nomenclature

SPM Scanning probe microscope;

AFM Atomic force microscope;

L Length;

d_{31} Piezoelectric strain coefficient (deflection normal to polarization direction);

D_i Inside diameter;

n Number of ceramic layers in piezoelectric stack actuators or the number of play operators for the Prandtl-Ishlinskii hysteresis model;

d_{33} Piezoelectric strain coefficient (along the axial direction);

d_{15} Piezoelectric shear-strain coefficient;

T_p Period;

$R(z)$ Reference trajectory;

$Y(z)$ System output;

$G(z)$ Discrete-time linear dynamics model;

N Number of points per period of a reference trajectory;

T_s Sampling period;

k_{rc} Repetitive control gain;

$Q(z)$ Low-pass filter;

$P_{1,2}(z)$ Positive phase-lead compensators;

$\theta_{1,2}(\omega)$ Phase lead contributed by positive phase-lead compensators $P_{1,2}(z)$;

$m_{1,2}$ Non-negative integers for phase-lead compensators;

$G_c(z)$ Feedback controller;

$E(z)$ Tracking error;

$S(z)$ Sensitivity function of the feedback system without a repetitive controller;

$S_{rc}(z)$ Sensitivity function of a repetitive control system;

$T(z)$ Complimentary sensitive function of the closed-loop feedback system without a repetitive controller;

$\theta_T(\omega)$ Phase of $T(z)$;

$\widetilde{S}_{rc}(z)$ Sensitivity function of the closed-loop dual-stage repetitive control system;

$\overline{S}_{rc}(z)$ Sensitivity function of the closed-loop odd-harmonic repetitive control system;

$\mathbb{C}$ Set of all complex numbers;

$\mathbb{N}$ Set of all natural numbers;

$\mathbb{R}$ Set of all real numbers;

$\mathcal{P}_r[\,\cdot\,](t)$ Play operator of the Prandtl-Ishlinskii hysteresis model;

u Input signal;

$f(t)$ Linear function;

g_0, g_1 Constants for the Prandtl-Ishlinskii hysteresis model;

γ Threshold of the play operator;

ρ Constant for the Prandtl-Ishlinskii hysteresis model;

j Operator index number;

$d(\gamma)$ Prandtl-Ishlinskii hysteresis model density function;

$v(t)$ Output signal;

$\mathcal{H}[\,\cdot\,](t)$ Prandtl-Ishlinskii hysteresis function;

$\mathcal{H}[\,\cdot\,](k)$ Discrete-time version of the Prandtl-Ishlinskii hysteresis function;

$\overline{P}_{r'}[\,\cdot\,](t)$ Operator for the inverse Prandtl-Ishlinskii hysteresis model;

$h(t)$ Linear function;

g_0', g_1' Constants for the inverse Prandtl-Ishlinskii hysteresis model;

γ' Threshold of the inverse Prandtl-Ishlinskii hysteresis model operator;

$d_{inv}(\gamma')$ Inverse Prandtl-Ishlinskii hysteresis model density function;

$\mathcal{H}^{-1}[\,\cdot\,](t)$ Inverse Prandtl-Ishlinskii hysteresis function;

$\mathcal{H}^{-1}[\,\cdot\,](k)$ Discrete-time version of the inverse Prandtl-Ishlinskii hysteresis function;

$\mathbf{x}$ State vector of the state-space representation of the linear dynamic $G(z)$;

$\mathbf{A}$, $\mathbf{B}$, $\mathbf{C}$, D Matrices for the state space model;

$G_{rp}(z)$ Transfer function for the repetitive controller and the controller $G_c(z)$ in Fig. 6.1(a);

$\mathbf{z}$ State vector of the state-space representation of $G_{rp}(z)$;

$\mathbf{A}_{rp}$, $\mathbf{B}_{rp}$, $\mathbf{C}_{rp}$, D_{rp} Matrices for the state-space model of $G_{rp}(z)$;

H_p Perturbed system;

H_u Unperturbed system;

$\mathbf{A}_L$, $\mathbf{B}_1$, $\mathbf{B}_2$, $\mathbf{C}_L$, D_1, D_2 Matrices for the state-space model of the unperturbed system H_u;

$G_L(z)$ Transfer relation between the reference $R(z)$ and the controller output $U(z)$ of the RC closed-loop linear system in Fig. 3.1(a);

M_{G_L} Gain margin of the RC system in Fig. 3.1(a);

P Force applied to the AFM tip during nanofabrication using force-lithography;

σ_{max} Maximum bending of the AFM cantilever due to force P;

k Spring constant;

l Length of the AFM cantilever;

E Young's modulus; and

I Moment of inertia.

University of Nevada, Reno

Abstract

Repetitive Control for Hysteretic Systems:
Theory and Application in Piezo-Based Nanopositioners

by Yingfeng Shan

Chair of Supervisory Committee:

Associate Professor Kam K. Leang
Mechanical Engineering

This dissertation studies the design and analysis of repetitive controllers for hysteretic systems. An example hysteretic system is a piezoelectric actuator (piezoactuator), the workhorse of actuators used for positioning and manipulating objects and tools at the micro and nano scale. For example, in scanning probe microscopes (SPMs) a piezoactuator is used to raster (back and forth in a repetitive fashion) a probe tool with sub-nanometer precision relative to a sample surface for imaging, manipulating, and fabricating organic or inorganic nano-scale features. Likewise, piezoactuators are used to position optics in space telescopes and tools in micro-machining systems. Despite their importance, piezoactuators exhibit hysteresis effect, a nonlinear behavior between the applied input voltage and the resulting output displacement of the piezoactuator. If left uncompensated for, hysteresis (and dynamic effects) cause positioning error that significantly limits the performance of piezo-based positioning systems. Repetitive control, a feedback-based approach which exploits the process of repetition, is commonly applied to track periodic reference trajectories and/or to reject periodic disturbances. The major challenges in the design of RC are closed-loop

stability, robustness, and minimizing the steady-state tracking error. For hysteretic systems such as piezo-based nanopositioners, the nonlinearity can drastically limit the performance of RC designed around a linear dynamics model. In this work, the effect of hysteresis on the closed-loop stability of RC is analyzed and the allowable size of the hysteresis nonlinearity for a stable RC is quantified. In the stability analysis, the bounded-input bounded-output (BIBO) stability of the repetitive controlled hysteretic system in the $\mathcal{L}_2$-norm sense is shown. Combining this result with the Small-Gain Theorem, an acceptable size of the hysteresis nonlinearity is determined that guarantees closed-loop stability. Therefore, one main contribution of this study is to provide a theoretical framework for analyzing the performance of RC for hysteretic systems. When the hysteresis effect exceeds the maximum bound, a new inverse-hysteresis feedforward controller based on the Prandtl-Ishlinskii hysteresis model is proposed. The control approach is applied to a custom-designed piezoactuator driven nanopositioning stage, and experimental tracking and nanofabrication results are presented to validate the RC and inverse model design. The tracking results at 1 kHz show that by adding hysteresis compensation the stability margin and rate of convergence of RC are improved by 14%. Likewise, the maximum tracking error is reduced from 13.7% (using industry-standard integral control) to 3.9% (using RC and hysteresis compensation), a 71% reduction. The RC approach is also applied to nanofabrication, where it is shown that by using RC with hysteresis compensation the error during fabrication is substantially reduced.

Contents

List of Figures

List of Tables

Acknowledgment

I would like to express my sincere appreciation to my advisor, Kam, for his guidance, energy, inspiration, encouragement, and support. This project would not have seen the light of day without his guidance and insight. I also thank Drs. Kim, Wang, Fadali, Shen, and Pinsky for their expertise and for serving on my dissertation committee.

I gratefully acknowledge support from the National Science Foundation grants CMMI-0910570 and DUE-0633098. I am also grateful for the teaching experiences I gained from the University of Nevada, Reno.

I thank Brian Kenton for developing the piezo-based nanopositioners used in the experiments. Many thanks goes to Lai Wei at Pennsylvania State University for helping me with the PMMA spin-coating process and his help with preparing the samples. I also thank my lab mates Maxwell Fleming, Joel Hubbard and Chris Dudley for the laughs and insightful discussions.

I thank my friends and family for their continued support. Also, a big thanks goes to Yingjia Chen for her support.

DEDICATION

To my parents, Zhanjun Shan and Xinrong Zhang.

Chapter 1

Introduction

Hysteretic systems, such as piezoelectric actuators (piezoactuators) [1,2], shape memory alloy actuators [3,4], magnetostrictive actuators [5], and other types of active (or smart) material actuators used for motion control, are critical in emerging nanotechnologies. For example, piezoelectric actuators are used to fabricate, manipulate, and investigate patterns, structures, and objects at nano or atomic scale [6]. However, these mechanical systems commonly exhibit hysteresis as well as dynamic effects, which can cause significant positioning error and consequently limit the performance. In piezo-based nanopositioners, the hysteresis is range-dependent and the effect alone can lead to approximately 20% positioning error. Dynamics, on the other hand, increase with input frequency and can contribute another 10% or more in positioning error. During raster-style scanning, the positioning error caused by the hysteresis and dynamics can repeat from one operating cycle to the next [7]. The positioning errors can cause, for example, distortion in AFM imaging and damage to the tip or the substrate in a number of nano-scale applications. Currently, feedback and model-based feedforward control have be studied to address the positioning error caused by hysteresis and dynamics in piezo-based nanopositioners [1]. However, these methods provide limited performance in terms of reducing the repeating tracking error for tracking periodic trajectories [8]. Herein, the design and analysis of a repetitive

controller for a system that exhibits hysteresis behavior between the applied input and the output response is studied. Such a study has received limited attention in the past, and one major outcome of this research is a theoretical framework for analyzing the stability and performance of repetitive controllers for hysteretic systems.

Repetitive control (RC) is a feedback-based approach that is suited for tracking periodic reference trajectories and/or for rejecting periodic disturbances. The control structure essentially exploits the process of repetition to reduce the tracking error [9, 10]. Although RC has been used in a number of applications, the design of RC for hysteretic systems has not been rigorously studied. One of the main challenges is the complex nonlinear behavior of hysteresis. The complexity causes undesirable effects on the performance of a closed-loop system, especially when the controller is designed around a linear dynamics model and subsequently applied to control the nonlinear system. In this study, the hysteresis behavior is treated as a static input nonlinearity with an output that drives the linear dynamics as shown in Fig. 1.1. This cascade-model structure is commonly used to model hysteretic systems such as piezo-based nanopositioners [11, 12]. By exploiting this model structure, the acceptable size of the hysteresis nonlinearity that ensures the stability of the closed-loop RC system is determined. If, on the other hand, the hysteresis behavior is unacceptably large, a feedforward controller is proposed to compensate for the hysteresis behavior to ensure a stable RC. In the following chapters, the hysteresis effect is modeled using the Prandtl-Ishlinskii approach, and an inverse hysteresis compensator is developed based on the structure of the Prandtl-Ishlinskii model. The control approach is applied to a custom-designed piezo-based nanopositioner to validate the inverse model and RC design. Finally, the RC approach is applied to nanofabrication example to demonstrate the feasibility of the control scheme to realize high-speed precision nanofabrication.

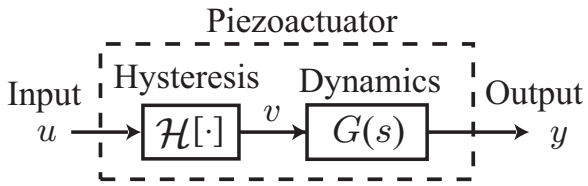

Figure 1.1: A nonlinear input-output model for a system, such as a piezoelectric actuator, that exhibits hysteresis and dynamic effects.

1.1 Thesis Goal and Objectives

The main goal of this dissertation is to precisely track periodic motion trajectories in hysteretic systems for nano-scale applications. Specifically, this work focuses on designing a repetitive controller to minimize the repeating tracking error, for scanning-type applications, caused by hysteresis and dynamic effects in a piezo-based nanopositioner. The research goal is achieved by completing the following two main objectives:

1. **Analyze and design a repetitive controller for tracking periodic trajectories for a hysteretic**

   First, an enhanced repetitive controller is designed based on the linear dynamics of the system. This first result serves as a starting point for analyzing and designing an RC for hysteretic systems. This step includes designing an RC that considers robustness, stability, and tracking performances. The hysteresis is modeled using the Prandtl-Ishlinskii approach for analysis. Then the stability of the RC system containing hysteresis is analyzed. Finally, an inverse hysteresis compensator is designed to compensate for the hysteresis nonlinearity to ensure good stability and tracking performance.

2. **Validate the theory on an experimental nanopositioning system**

   Second, both the theoretical results and controller designs are applied to track periodic scanning trajectories in a nanopositioner and experimental AFM. Also,

patterns of nano-sized holes are created using the AFM which employs the new control technique. Such holes can be used for ZnO nanowire array growth.

1.2 Contributions

This research has three main contributions. First, this work provides a theoretical framework for analyzing closed-loop stability for hysteretic systems, which is one of the first works that offers a tool for quantifying the effect of hysteresis on RC closed-loop system stability. Second, a new inverse hysteresis compensator is developed to account for the hysteresis when the size of the hysteresis exceeds a tolerable size. The advantage of this hysteresis compensator is that it has fewer parameters than other popular models, making it more computationally tractable for online feedforward hysteresis compensation. Finally, the proposed control approach is applied to explore the potential application in AFM-based nanofabrication, where repetitive operation is required.

1.3 Dissertation Overview

This dissertation is organized as follows. Chapter 2 presents a background of hysteretic systems, specifically, the piezo-based nanopositioning systems. The information includes the principle and characteristics of piezoelectric materials. The applications of piezoelectric positioner-based scanning probe microscopy are also discussed, which focuses on nanofabrication using the AFM. The main challenges associated with using piezoelectric actuators are also discussed.

In Chapter 3, the repetitive control method for linear dynamics is introduced. This introduction offers the foundations to study and design repetitive controllers for hysteretic systems. Topics include robustness issues, stability analysis, and consider-

ations for good tracking performance.

Chapter 4 presents a dual-stage RC designed for improving the tracking performance of the proposed enhanced RC. Also, the challenges with RC for hysteretic systems are discussed, namely, the effect of the hysteresis on closed-loop system robustness, stability, and tracking performances.

Chapter 5 provides the key elements for designing RC for hysteretic systems. The Prandtl-Ishlinskii hysteresis model is introduced and used in the analysis. Chapter 6 dives into the details of quantifying the effect of hysteresis on the performance of RC.

The control approach is applied to an experimental piezo-based nanopositioing system and the results are discussed in Chapter 7. The chapter also discusses the system modeling, controller design and implementation, and the stability theorem verification.

Chapter 8 discusses the AFM-based fabrication of patterns of nano-holes for potential growth of ZnO nanowires. The experimental tracking results compare the performances of the RC, with and without hysteresis compensation, to the performances of a standard PID controller, with and without hysteresis compensator.

Conclusions are presented in Chapter 9, followed by appendices.

Chapter 2

Background: Hysteretic Systems and Scanning Probe Microsopy

This chapter provides a background on hysteresis and hysteretic systems, particularly piezoelectric actuators used in scanning probe microscopes (SPMs). The piezoelectric actuator serves as an example hysteretic system studied in this work. An overview of the applications for piezo-based atomic force microscopy is presented. In particular, AFM-based nanofabrication will be the central focus. Finally, a detailed discussion of the main challenges with piezoelectric positioners are described. It is noted that addressing the hysteresis effect is the focus of this dissertation.

2.1 Hysteresis

Hysteretic systems include piezoelectric actuators (piezoactuators) [1], shape memory alloy actuators [4], magnetostrictive actuators [5], and other types of active (or smart) material actuators employed for motion control (see Fig. 2.1). These devices can be activated electrically, that is, an applied electric signal causes the material to change shape, and as a result these devices can be used as solid-state actuators for a wide variety of positioning applications. However, one of the main challenges is that the materials exhibit hysteresis between the applied input signal and output displacement. Hysteresis significantly limits the performance in terms of actuation,

and this research specifically focuses on precision motion control of hysteretic systems such as piezoelectric actuators.

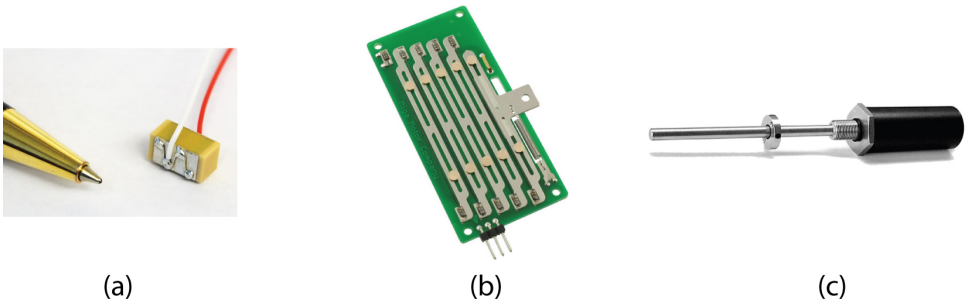

Figure 2.1: Examples of active (smart) material-based actuators for motion control: (a) piezoelectric actuator [www.noliac.com], (b) shape memory alloy actuator (Miga Motor Co.) [www.migamotors.com], and magnetostrictive actuator (Nordisk Transducer Teknik) [www.ntt.dk]. These solid-state actuators exhibit hysteresis.

The word hysteresis comes from the Greek word "to be late" or "come behind". An interesting writing on the history of hysteresis can be gleaned from reference [14], which describes other systems which exhibit this behavior. The mechanism responsible for hysteresis, for example in piezoactuators, is "internal forces" (such as frictional forces) between domains of electric dipoles within the material. Similarly, in magnetic materials tiny elementary magnetic dipoles align to an applied field, and the boundaries that separate regions of similarly-oriented dipoles grow or shrink depending on the nature of the applied field. The non-recoverable interactions between the different domains is believed to be the main cause of hysteresis in this case [15–17]. Figure 2.2 shows an example input-output response for a hysteretic system. The input-output behavior is not only nonlinear, but hysteresis "remembers" the effect of the past and it exhibits non-local memory [18].

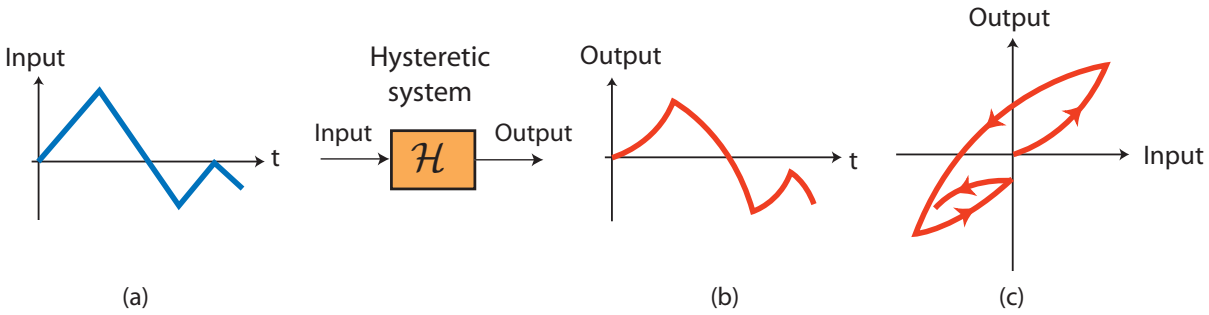

Figure 2.2: Input-output response for a hysteretic system: (a) input vs. time, (b) output vs. time, and (c) hysteresis curve (plot of output vs. input).

2.2 Piezoelectric Materials and Piezoelectric Actuators

In 1880, Pierre and Jacques Curie discovered that certain crystals (such as quartz, sodium chlorate, boracite, calamine, topaz, cane sugar, and Roschelle salt) when subjected to mechanical stress produce electric charge. One year later, the French physicist Lippmann predicted, on the basis of thermodynamic analysis, the converse effect: strain as a result of applied voltage. That same year, the Curie brothers verified Lippmann's prediction [19]. The discovery was named the *piezoelectric* effect from the greek word *piezein*, meaning to press or squeeze. For the interested reader, a more detailed discussion of the history of piezolectricity can be read in references [20, 21]. Also, according to these references, the piezoelectric effect was known prior to the Curie brothers's time. Charles Coulomb, in 1815, conjectured that electricity might be produced by pressure; however, the discovery was undoubtedly made by the Curie brothers in 1880. The piezoelectric effect is based on the unique characteristic of certain crystalline lattices to deform under pressure, thereby separating the center of gravity of the positive and negative charges creating a dipole moment (product of charge value and their separation). The resulting dipole moment induces an electric charge which can be measured across the surface of the material. Conversely, an ap-

plied voltage induces a mechanical strain, and this behavior is exploited for actuation in positioning systems.

For piezoelectric materials, mechanical stress or applied voltage produce electric dipoles. Materials which exhibit a spontaneous polarization in the absence of an applied stress or electric field are referred to as ferroelectric. Some ferroelectrics exhibit the piezoelectric effect. For example, the microscopic crystallites of lead zirconate titanate ($Pb(Ti,Zr)O_3$) (PZT) exhibit a spontaneous polarization due to the arrangement of atoms within the unit cell. However, when manufactured, the random orientations of the crystallites in this ferrorelectric material produce no net effect when mechanically stressed or when voltage is applied. However, through a process called *poling*, the material can be made to exhibit a considerable piezoelectric effect. Basically, the poling processes forces the dipoles in the material to align in a favorable direction as illustrated in Fig. 2.3. The poling process involves heating the material near its Curie temperature, typically between 100° and 300° C, then applying a strong electric field while cooling the material. The heating process allows movement of the individual crystallites, and application of a strong electric field causes the dipoles to align with the field, in favor of a net effect [22, 23]. As the field is maintained during the cooling process, the majority of the dipoles maintain their alignment. The dimensions of the material after poling permanently changes as illustrated in Fig. 2.3. In the figure, the poling axis is the dimension between the poling electrodes. During poling, the material increases its dimensions parallel to the poling axis and the dimensions along the electrodes decrease. After poling, the ferroelectric PZT material exhibits considerable piezoelectric effect. Lead zirconate titanate is one of the most widely used piezoelectric materials and it is manufactured into a wide variety of shapes and sizes, from tube-shaped actuators to stacks. In the 1950s, barium titanate ($BaTiO_3$) was the first ferroelectric material used for

piezo-based applications, however, lead zirconate titanate has since then replaced barium titanate because it has nearly twice the piezoelectric effect. For the interested reader, reference [21] provides an detailed coverage of the theory of piezoelectricity and constitutive equations.

Piezoelectric materials are available in many shapes and forms. In addition to their traditional application in microphones, accelerometers, ultrasonic transducers and spark generators, piezoelectric transducers are now used in applications such as structural vibration control, precision positioning, aerospace systems and nanotechnology. Figure 2.4 shows the basic modes of deformation for a piezoelectric element that can be exploited for nanopositioning. Based on these deformation modes, unimorph, bimorph, stack, and tube piezoelectric actuators have been developed.

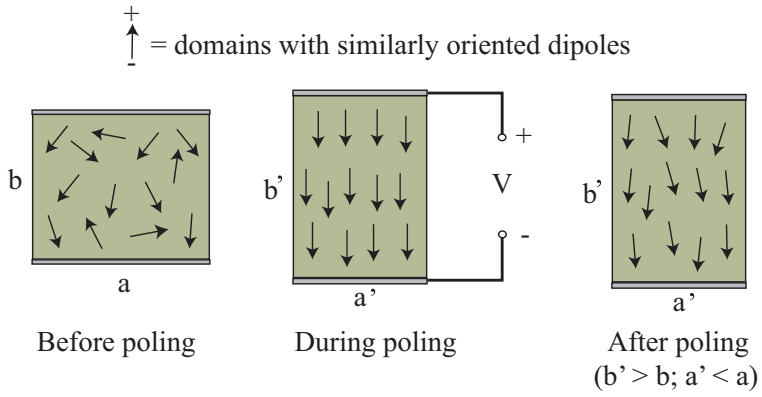

Figure 2.3: The poling process.

Unimorphs and bimorphs are bender style actuators with large range of motion, but low force. Sawyer in 1931 developed the first bender actuator using Rochelle salt bars [24]. Bimorph actuators consist of two ceramic elements bonded together, and can be configured serially or in parallel. The parallel configuration in Fig. 2.5 shows an electrode sandwiched between two piezo plates. For this configuration, the static

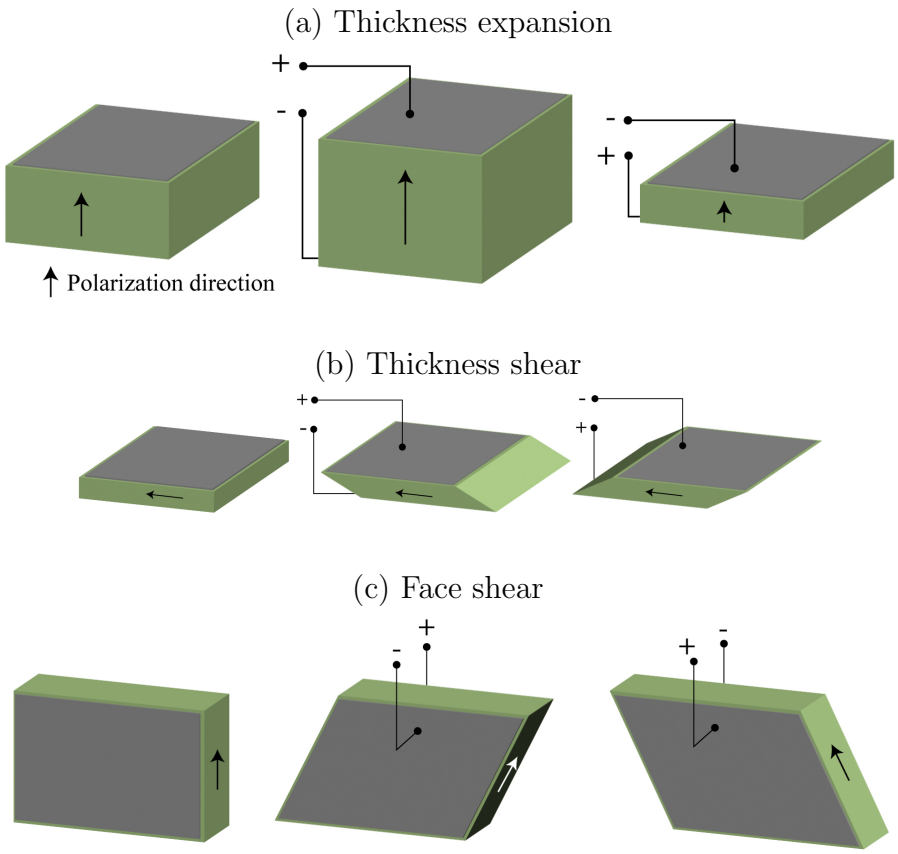

Figure 2.4: Basic modes of piezoelectric element deformation.

deflection at the end can be estimated by [25]

$$\Delta x = \frac{3 d_{31} L^2 V}{t^2}, \tag{2.1}$$

where L and t are the bender's length and thickness, respectively, and d_{31} is the strain coefficient (displacement normal to the polarization direction). On the contrary, unimorph actuators employ only one piezoceramic element that is bonded to an elastic shim, such as aluminum, brass, or steel. Bending motion for both unimorph and bimorph actuators is due to the difference in expansion and/or contraction between the opposing plates.

Quarter-sectored tube-shaped piezoelectric actuators were developed for 2- and

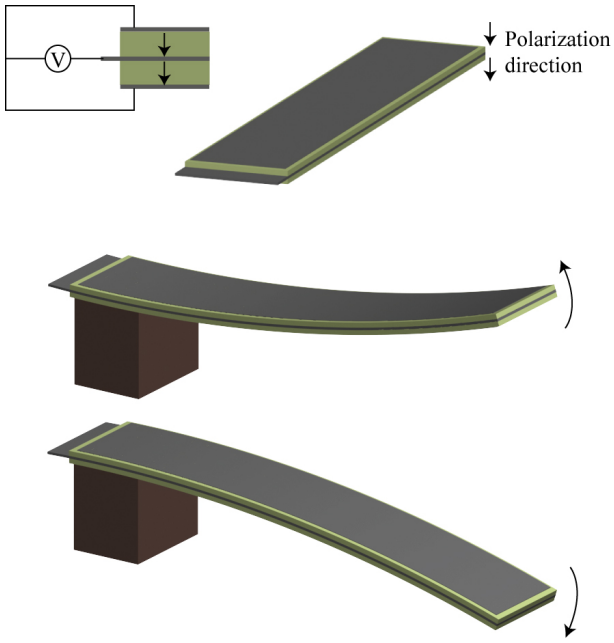

Figure 2.5: Piezoelectric bimorph actuator.

3-D positioning and they are used extensively in scanning probe microscopes [12]. The tube-shaped PZT ceramic is poled radially and the electrodes are deposited on the inner and outer circumferential surfaces of the tube as shown in Fig. 2.6. If the inner electrode is held at ground and the two opposing electrodes are driven by ±V, then the resulting static deflection of the tube's distal end can be estimated by [26],

$$\Delta x \approx \frac{2\sqrt{2}d_{31}L^2V}{\pi D_i t}, \tag{2.2}$$

where L, t, and D_i are the tube's length, thickness, and inside diameter, respectively. Compared to the bender style actuators discussed above, tube-shaped actuators are stiffer because of their cylindrical geometry.

Piezoelectric stack actuators emerged after the development of poled ceramic transducers of PZT [27]. A stack actuator is made by bonding thin layers of piezoelectric materials between electrodes such that the polarization direction is aligned with

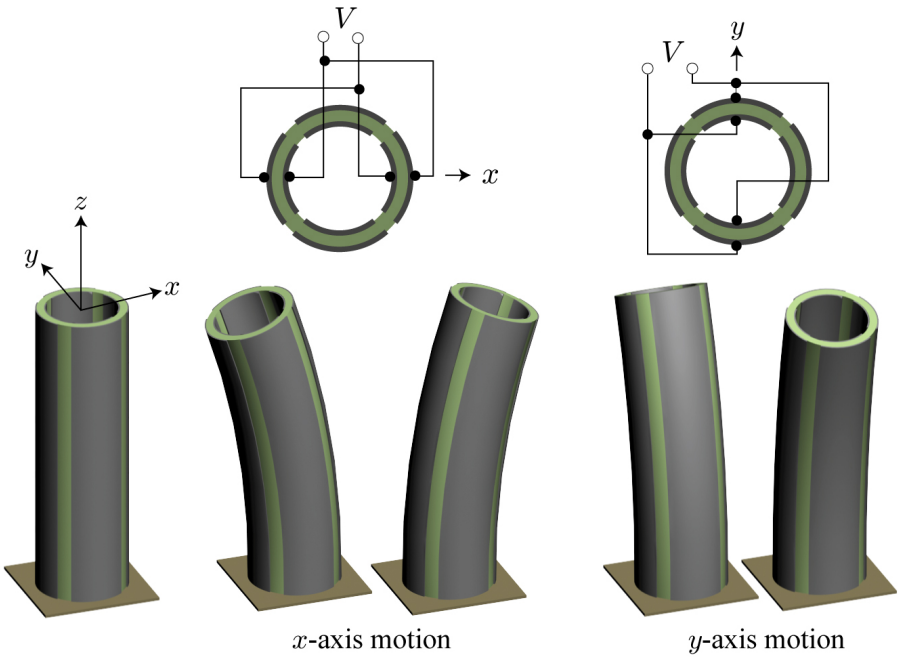

Figure 2.6: Quarter-sectored piezoelectric tube actuator.

the direction of stroke and blocking force. All the elements are connected in parallel as depicted in Fig. 2.7(a). The thin ceramic layers (100 μm thick) wired in parallel enables the stack to be operated at 100 V or less, with an achievable stroke of 0.2% of the stack height [25]. Due to their high stiffness and force output, stack actuators are used extensively in high-speed nanopositioning designs [28–30]. Because the ceramic layers are connected in parallel, the overall capacitance of stacks is high compared to tubes and bender actuators, and thus power requirements must be carefully considered, in particular for dynamic applications. The static axial elongation of a stack actuator is given by

$$\Delta x = n d_{33} V, \tag{2.3}$$

where n is the number of ceramic layers and d_{33} is the strain coefficient along the axial direction of the stack.

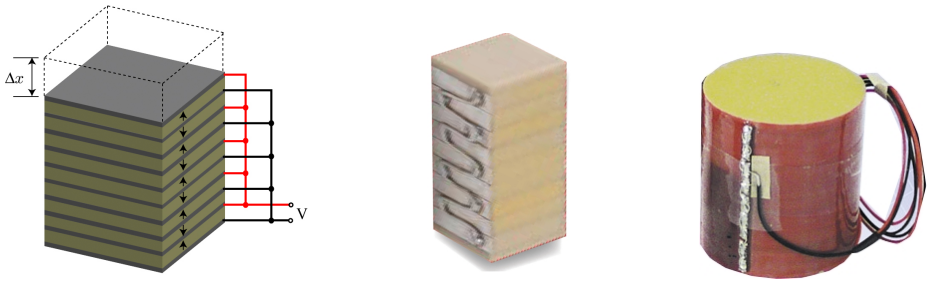

(a) (b) (c)

Figure 2.7: Piezoelectric stack actuators. (a) Electrode configuration; (b) Monolithic stack actuator; and (c) Multilayer stack actuator.

Shear actuators make use of the shear-strain coefficient d_{15}, whereby an electric field is applied perpendicular to the polarization direction to induce shape change (see Fig. 2.4). The strain due to shear can be has much as twice the deformation of a comparable size material based on d_{33}. Some advantages include high force output and bipolar operation. When thin shear actuators are used for high-speed nanopositioning applications, the range is relatively small [31].

In the past few decades, piezo-based sensors and actuators have been developed for a wide variety of applications [32]. For example, piezo-based actuators are used in bioengineering systems [33], disk drives [34], micropumps [35], and scanning probe microscopy-based imaging and manipulation of nanoscale surface processes [6, 36].

2.3 Scanning Probe Microscopy

A popular application of piezo-based nanopositioning stages is scanning probe microscopy (SPM). In an SPM, a piezo-positioning stage is used to position a small SPM probe relative to a specimen for nano-scale imaging, surface modification and interrogation [37]. Unlike a traditional optical microscope which uses light for imaging, in SPM an image is formed by rastering a small (typically micron-size) probe over a sample surface and then plotting the probe's interaction as a function of its

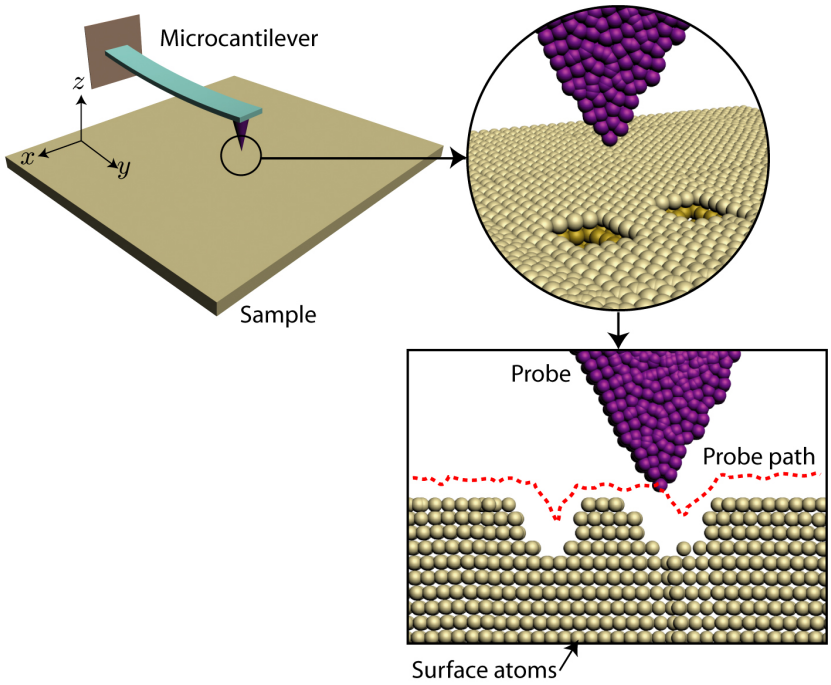

Figure 2.8: An example SPM, the atomic force microscope.

position [6]. For example, consider the AFM shown in Fig. 2.8, a type of SPM. This instrument is one of the most versatile SPMs because of its ability to work with conducting and nonconducting samples, as well as operate in a vacuum, air, or in water. The AFM was invented in the mid-1980s [38]. In AFM, a micro-machined cantilever with sharp probe tip protruding from its bottom is positioned relative to a sample surface as shown in Fig. 2.8. When the probe tip is rastered over a sample's surface, tip-to-sample interaction causes the cantilever to deflect vertically with respect to the sample topology. The deflection is then measured and used to construct an image of the sample surface. In this case, the AFM essentially 'feels' the surface with a tiny, finger-like cantilever. In a vacuum an AFM's resolution is on the order of 0.01 nm. With such high resolution, an AFM can generate topographical images of atoms, as well as to control, manipulate, and alter the properties of matter at the nano-scale [37].

The positioning of the SPM probe tip relative to the sample is achieved with two

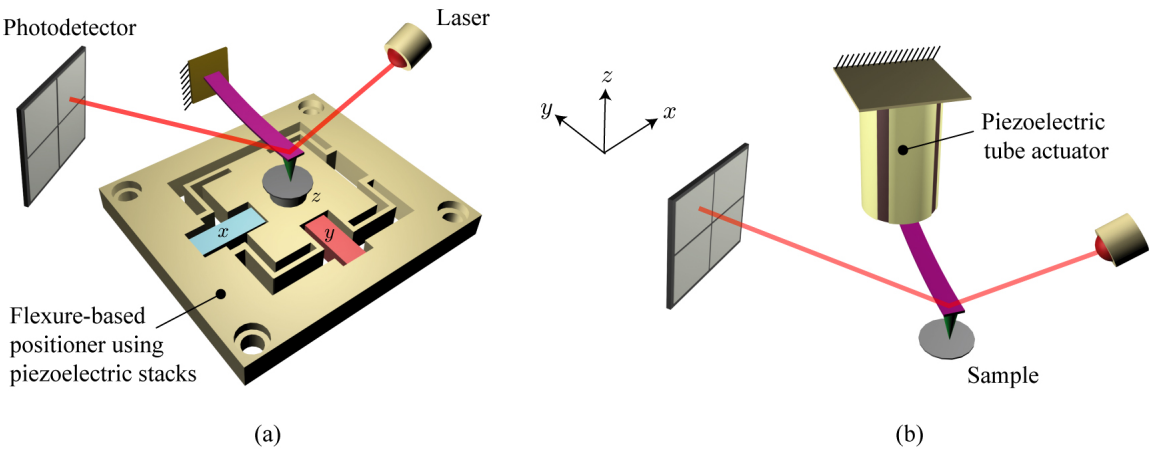

Figure 2.9: Two positioning schemes for SPMs: (a) scan-by-sample and (b) scan-by-probe.

basic configurations: (a) scan-by-sample or (b) scan-by-probe as shown in Fig. 2.9. In the scan-by-sample configuration, the nanopositioner, such as the flexure-based design shown equipped with three piezo stacks, moves the sample relative to a fixed SPM probe. The x and y axis piezos position the sample along the lateral direction (parallel to the sample surface); a z axis stack moves the sample vertically. The deflection of the cantilever is measured optically, by reflecting a laser beam off the end of the cantilever onto a nearby photodetector. In the scan-by-probe arrangement [Fig. 2.9(b)], a nanopositioner, such as the sectored tube-shaped piezoactuator, is used to move the probe relative to a fixed sample laterally and vertically. Typically, in scan-by-probe system the laser and photodector are required to move with the cantilever; however, this can be avoided by incorporating sensing elements into the cantilever itself, such as using piezoresistive, piezoelectric, and capacitive elements. In general, the mechanical resonances of scan-by-sample systems are lower compared to the scan-by-probe systems due to the fact that more mass is being displaced in the former configuration.

There are three basic operating modes of AFM: contact, noncontact, and tapping mode. Contact mode is the most common and the AFM probe interacts with the

sample surface at a very close range where the dominate force on the tip is repulsive. In this mode, the deflection of the AFM cantilever is sensed and a feedback controller is used to maintain a desired deflection. The spring constant of a contact mode AFM cantilever varies between 0.001 to hundreds of N/m. Although contact-mode AFM is the simplest, electrostatic charge on surfaces of certain samples can present additional challenges by heavily influencing the total force acting on the tip.

For samples in which contact mode AFM can affect or alter the surface of a specimen, noncontact mode avoids this problem by exploiting attractive Van der Waals forces. In this mode, the AFM tip is hovered above the surface (at approximately 50 to 150 Angstroms) such that the attractive forces act to deflect the cantilever. Because the attractive forces are significantly weaker than the repulsive forces in contact mode, the tip is given a small oscillation and the small forces are detected by monitoring the change in amplitude, phase, or frequency of the oscillating cantilever. In general, noncontact mode AFM provides low resolution and the cantilever's oscillation can be affected by surface contaminants.

For high-resolution imaging of soft samples, tapping mode AFM is preferred. In this mode, the AFM cantilever is oscillated with large amplitude near its resonance (at 50,000 to 500,000 cycles per second) using a piezoelectric crystal. The AFM tip is not in contact with the surface as it's being oscillated, but then slowly brought close to the surface until the tip lightly touches or taps the surface. When the cantilever intermittently contacts the surface, the oscillating behavior is altered by the energy loss during the tip-to-sample interaction. The change in energy is monitored and used, for example, to construct an image of the surface.

2.4 Nanofabrication using the AFM

The atomic force microscope is an important and versatile tool to study insulators and semiconductors, as well as conductors [39]. As mentioned before, the AFM has been used to visualize the sample surface (imaging). Also, the AFM can provide details of the surface properties for research in physics, chemistry, biology, biochemistry, engineering, and other disciplines [40]. The AFM can also be used to physically or chemically modify surfaces to create nanometer scale structures/features and to perform manipulation at the level of molecules or atoms [41].

Recently, the AFM has become a promising tool for nanofabrication. Other approaches include photolithography using short wavelength light [42], self-assembly [43], and nanoimprint [44]. Compared to these other approaches, the AFM allows both fabrication and visualization of the nanostructure using the same tool. Compared to a scanning tunneling microscope (STM) and near-field scanning optical microscope, the AFM is more flexible and can be applied to metal, semiconductor, polymer, bio/organic materials, and inorganic samples [45]. AFM-based nanofabrication technologies mainly include nanomanipulation [46], forcelithography [47], nanografting [48], nanooxidation [49], and dip-pen nanolithography [50].

2.4.1 AFM Tip Manipulation

An AFM tip can be used to position or manipulate nanoclusters or nanoparticles that are deposited on substrate surface [46]. The capability of the AFM for nanomanipulation was discovered during the early days of the instrument when using the tool to visualize surfaces in contact mode. It was found that the nanoparticles that were weakly adsorbed on the sample surface could be displaced to a new position using the tip [51, 52]. The AFM was normally treated as the main tool for imaging; however, some researchers realized that they could construct nano-scale features on surfaces

by carefully manipulating the AFM probe tip.

In nanomanipulation, the displacement of the desired nanocluster or nanoparticle is achieved by pushing with an AFM tip. In this process, the AFM tip can be used in contact mode or non-contact mode. In contact mode, the nanoclusters or nanoparticles are moved by applying higher loads to the AFM cantilever than for imaging. In non-contact mode, there are two approaches to relocate nanoclusters or nanoparticles. The first approach is to turn off the z-axis feedback controller on the AFM cantilever when the tip approaches a desired object or feature. This results in a contact of the tip and the object, and the force caused by the contact between the tip and particle forces the particle to move with the tip to a desired location. The other approach is to adjust the setpoint of the static load applied on the cantilever for manipulation.

A significant amount of research has been done on AFM-based nanomanipulation. For example, nanocrystals and nanoclusters such as C_{60}, Ag, Au, Pd, GaAs, and Cu were manipulated [53–58]. Baur's group used an AFM tip to manipulate 15 nm Au nanocrystals, which were randomly deposited on the silicon surface, to form a 'USC' pattern after a series of pushing operations of the Au nanoparticles [55]. The comparison between the random pattern of Au particles with the manipulated Au pattern is shown in Fig. 2.10 [55]. More complex 2-dimensional and 3-dimensional structures were also fabricated by properly controlling the manipulation process [59, 60].

2.4.2 Polarizing Materials and Electrostatic Nanolithography with AFM

Apart from visualizing the ferroelectric material topological information, AFM can also polarize ferroelectric materials [61–67]. Compared with conventional polarizing methods, which can only polarize a large area of the sample, AFM based polarization

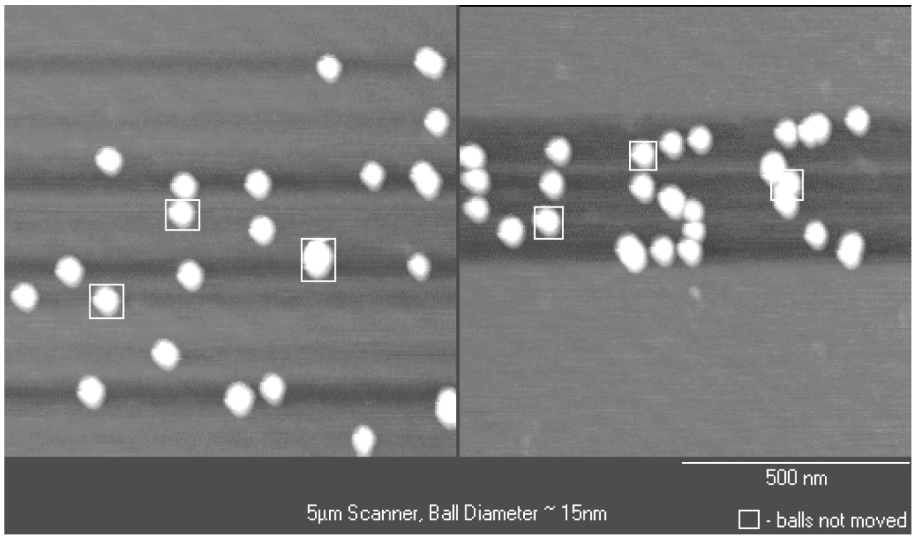

Figure 2.10: An nanomanipulation example for Au nano particles from reference [Baur et al. (1997)]. (a) The random Au pattern before nanomanipulation. (b) The Au pattern in structure of 'USC' after AFM-based nanomanipulation.

allows the polarization of ferroelectric materials locally to create a ferroelectric domain on the sample at the nanometer or micrometer scale. Moreover, the AFM can also detect and visualize the ferroelectric domain after polarizing for analysis. A schematic diagram in Fig. 2.11 shows the AFM system for polarization and detection of the ferroelectric domain. From the diagram, it can be seen the polarization and detection require the ferroelectric material to be located on an electrode base, and the AFM tip to be conductive. During polarization, the conductive AFM tip approaches the ferroelectric material in contact mode, and a certain DC voltage is applied between the tip and the electrode base to form an electric field. The ferroelectric domain is generated on ferroelectric material by scanning the AFM tip relative to the material. For detecting, a small AC voltage is applied between the tip and the electrode base to simulate the ferroelectric variation, which is reflected by the vibration of the AFM cantilever. Then the vibration information of the cantilever is input to a lock in amplifier, which outputs ferroelectric information of the surface. In the past decade,

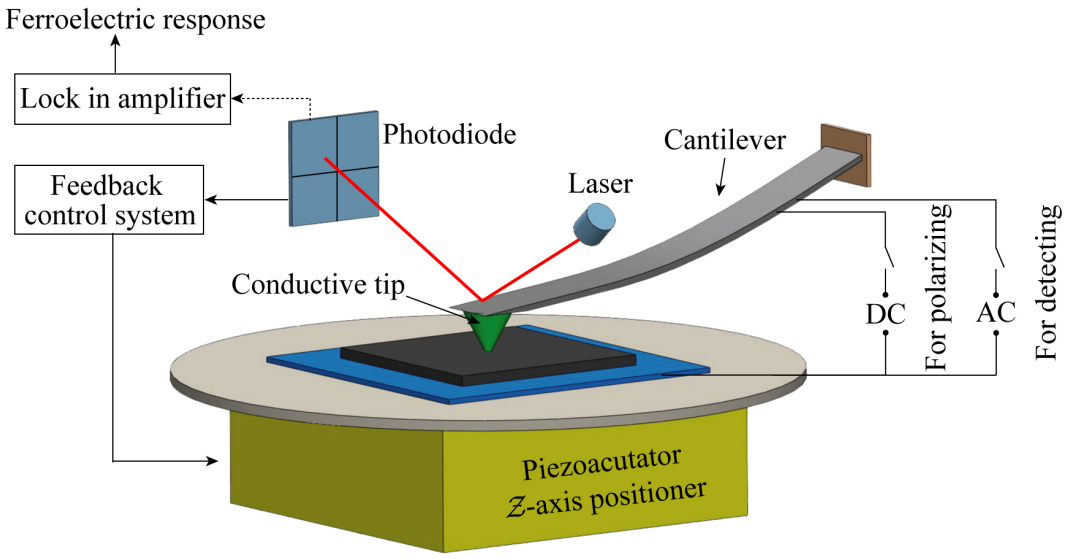

Figure 2.11: A schematic diagram for AFM based polarizing and detecting ferroelectric domain on a sample.

studies have been undertaken on the polarization and detection of micro- to nano-scale ferroelectric domains using AFM [61–64]. An example result from Paruch et al., is shown in Fig. 2.12. The figure shows a close-view of nano-sized ferroelectric domain fabricated by AFM polarization with 10 V pulses applied for 3 ms.

Furthermore, the AFM system in Fig. 2.11 can also be used to do electrostatic nanolithography on polymer samples by replacing the ferroelectric material sample with a polymer sample [68]. In this process, a polymer sample with thickness of $20 \sim 100$ nm is rested on the electron base, and a voltage is applied between the tip and the electron base similar to polarization process. Then nanopatterns can be fabricated on the polymer by positioning the AFM tip. The configuration of the nanopatterns are affected by the applied bias voltage, which is determined by the writing conditions, polymer compositions, and film thickness. An example result of AFM-based electrostatic nanolithography is from [68], and is shown in Fig. 2.13 [68]. A pattern is created in spun-cast, vacuum-annealed 100 k PS films. The capability of AFM on electrostatic nanolithography gives it a potential application for developing

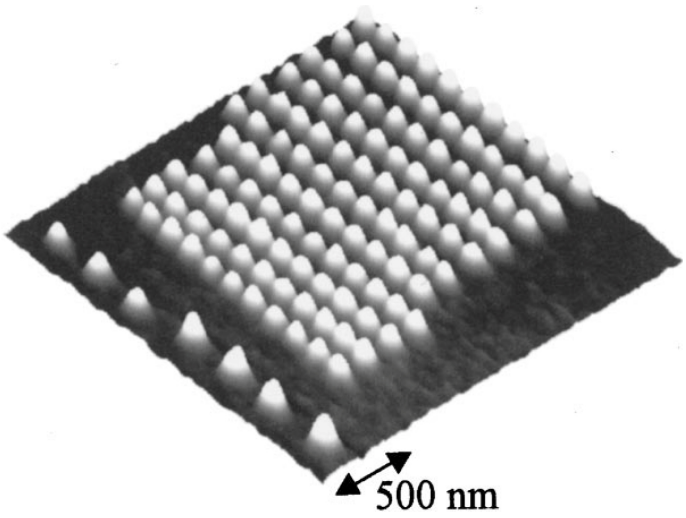

Figure 2.12: Piezoelectric image of an 11×11 array, written at 4 $Gbit/cm^2$ information density with 10 V pulses applied for 3 ms [Paruch et al. (2001)].

data storage devices with polymers.

2.4.3 Force Lithography or Mechanical Scratching

Another convenient nanofabrication method to physically modify a sample surface using AFM is called force lithography or mechanical scratching. In force lithography, a rigid AFM tip is used to mechanically modify the surface of a soft sample by applying a certain load on the cantilever. The load depends on the condition of the substrate, such as the hardness. Force lithography can be conducted in contact mode or semi-contact mode. The disadvantages of contact mode are that the contact force not only causes difficulties in the tip moving direction, but can also create undesired features on the sample surface, especially for soft materials, as well as causes damages to the AFM tip. Therefore, in implementation, semi-contact mode is a better option for operating force lithography. A schematic illustration of force lithography is presented in Fig. 2.14(a). Nano-hole arrays are fabricated on a photoresist PMMA thin film by an AFM tip through force lithography. The thickness of the PMMA thin film is about 28 nm. The fabrication is operated in semi-contact mode by loading a static force

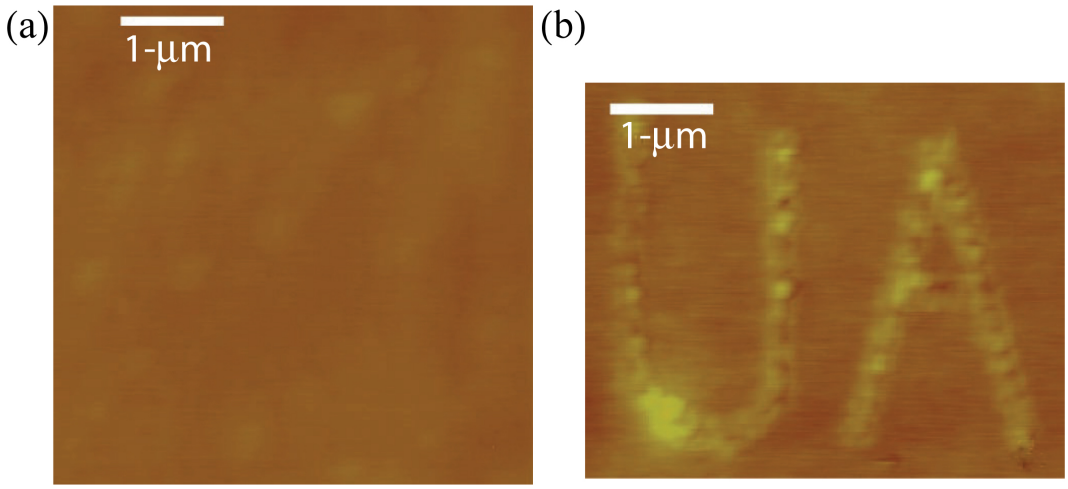

Figure 2.13: An example of electrostatic nanolithography-patterned structures on a spun-casted polymer films (100 k PS) with AFM. (a) The surface of sutstrate before fabrication. (b) Electrostatic nanolithography-patterned letters with width of 450 nm and height of 1.2 nm with average current of 13 nA (20 V at 0.1 μs^{-1}) [Lyuksyutov et al. (2003)].

on the AFM tip and driving the z-axis positioner with a periodic motion to expend and contract in the z direction. The fabrication results are shown in Fig. 2.14(b) to (d). The 2-D and 3-D images in plots (b) and (c) show the configuration of fabricated holes. Plot (d) is the depth of the depth profile of the holes in the 3^{rd} row, which shows the holes have nearly the same depth as the thickness of the polymer, demonstrating that the substrate is exposed. It is noted that the applied load, lithography speed, and lithography cycles affect the pattern height and surface roughness.

Research on fabricating nano-scale patterns on different materials using the AFM-based force lithography has been conducted by several groups [69–76]. Generally, nanopatterns on soft materials were fabricated directly with force lithography. Yan et al. [69] applied the AFM-based force lithography directly to copper film to study the application of AFM as a micro/nano-CNC machining system. Brandow et al. [57] fabricated patterns on Au and Pd nanocluster films. For direct fabrication of patterns on polymer, silicon, and titanium film readers are referred to [73, 76, 77]. Fabrication

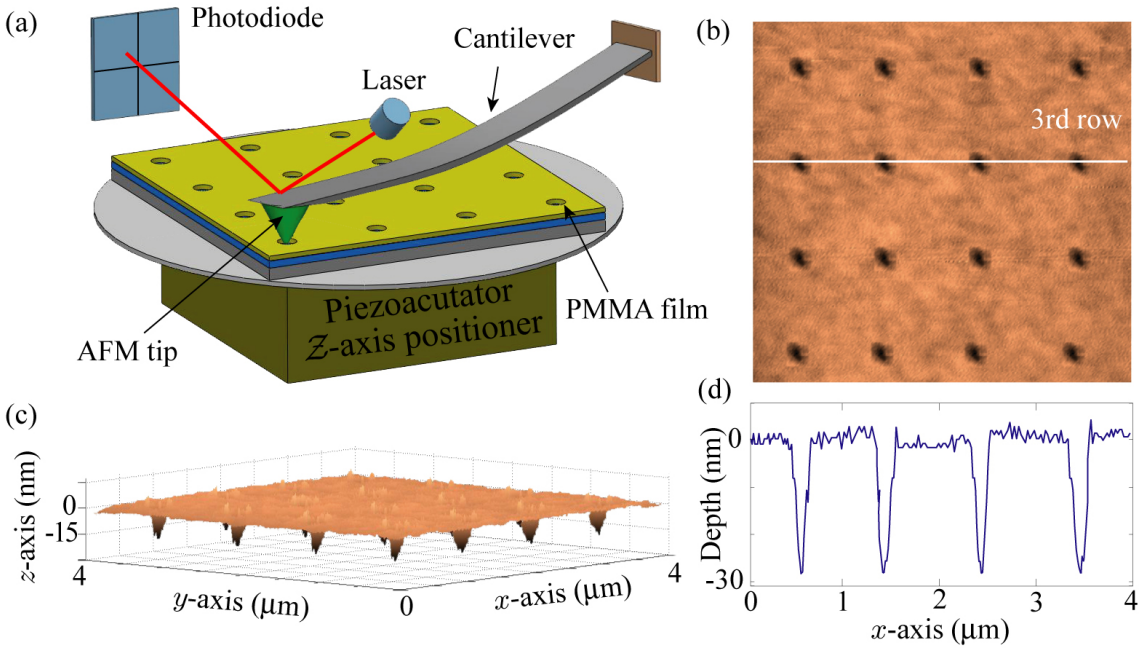

Figure 2.14: (a) A schematic diagram for AFM based Force lithography on 15kg/mol PMMA thin film with thickness of 28 nm to create nano-hole arrays. (b) 2-D AFM image of the fabricated nano-hole arrays. (c) 3-D AFM image of (b). (d) The depth of the holes at 3rd row.

of nanopatterns on hard materials is generally produced indirectly with force lithography, since the direct fabrication method makes the silicon AFM tip degrade rapidly, and often results in defects around the patterned structure. Therefore, fabrication of patterns on hard materials with the combination of a sacrificial layer and various selective etching techniques is often done [71, 72, 78]. The sacrificial layer is normally one or two thin films of soft materials coated on the target substrate with a thickness of several nanometers. The soft sacrificial material could be a polymer, III-V semiconductors (10 nm thick), or a soft metal (Al, Ti) [47, 71, 73–75]. In the fabrication of hard materials, patterns are first fabricated on the soft sacrificial layer. Then the desired nanostructures on the substrate can finally be obtained through selective etching and removing of the sacrificial layer [71, 72, 74, 78]. Other than using selective etching, nanopatterns are first fabricated on the sacrificial layer via force lithography, and gold is then deposited on exposed portions of the substrate (Ge) through electroless deposition. Subsequently, the desired metallic features are obtained through removing the resist layer [70].

Force lithography is very useful for fabricating nanodevices, especially on nonconducting substrate that cannot be oxidized with AFM tip-directed nanooxidation. For example, semiconductor quantum point contacts [79], nanoscale transistor [80], and single electron transistor (SET) [81] were fabricated with the combination of force lithography and selective etching. In this study, force lithography is used to fabricate nano-hole array pattern for potential ZnO nanowire arrays growth via selective etching.

2.4.4 Nanografting using AFM

Nanografting has evolved from force lithography, and was developed by Liu et al. in 1997 [82]. Basically, the process replaces the need for self-assembled monolayers (SAMs) on a substrate by another material using force lithography to chemically mod-

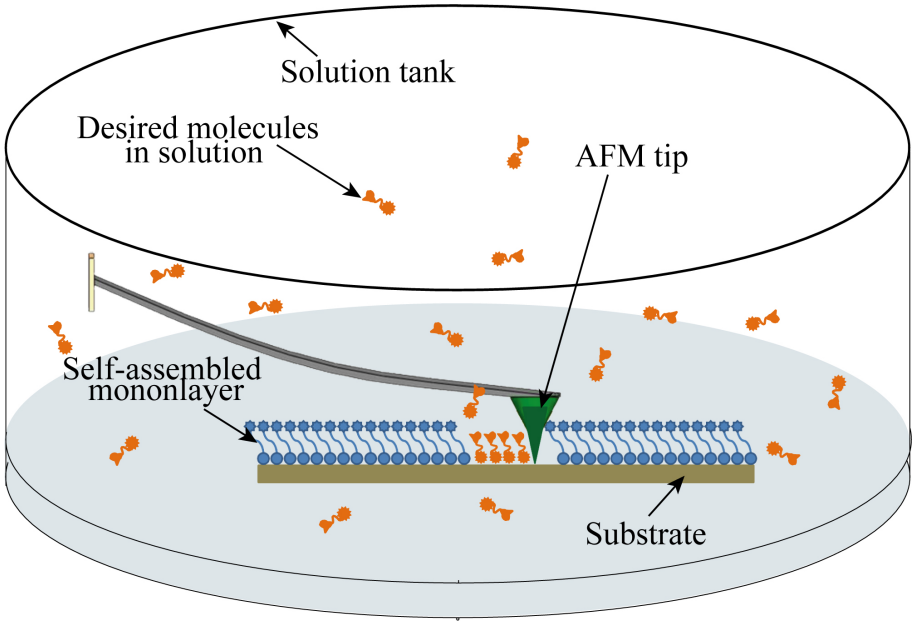

Figure 2.15: Schematic diagram of nanografting using AFM.

ify the substrate to form desired nanopatterns. A schematic diagram of AFM-based nanografting is shown in Fig. 2.15. From the figure, it can be seen that nanografting is conducted in a solution. The solution contains the desired molecules used to replace the component of the SAMs. The sample for nanografting is a substrate of interest with a self-assembled monolayer. The sample is usually a thiol-gold system [83]. An AFM tip is used to scratch the SAMs at the desired location, and then substrate is exposed to the desired molecules for absorption.

From nanografting, another fabrication method called nanopen reader and writer was developed by Liu's group [84]. Unlike nanografting, where the desired molecules are in the solution, in the nanopen reader and writer approach, the desired molecules are coated on the AFM tip. In the nanofabrication process, the AFM tip coated with desired molecules acts like a pen. The process removes the SAMs from the desired location of the substrate and leaves the desired molecules behind to form nanostructures. The nanopen reader and writer method has been conducted in air

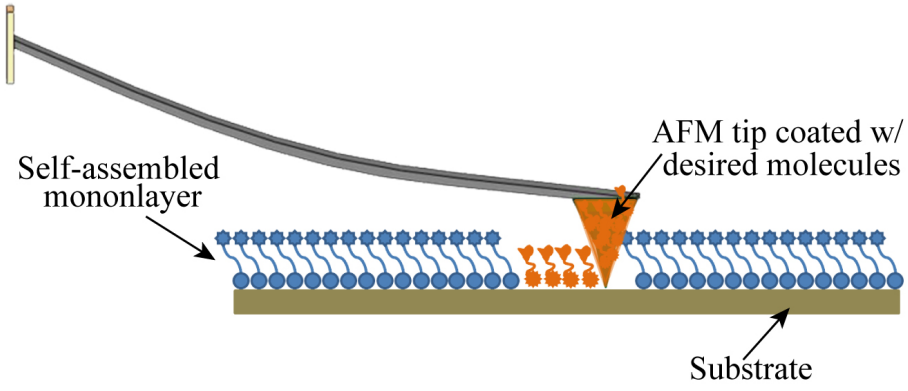

Figure 2.16: Schematic diagram of nanopen reader and writer with AFM.

with improved resolution [84]. A schematic diagram of it is shown in Fig. 2.16. The 2D and 3D nanostructures of thiols with different chain length or/and different terminal groups have been constructed [85–87]. An example result of nanografting is shown in Fig. 2.17 [87]. A cell size of octadecanethiol 20×20 nm surrounded by decanethiol is fabricated by nanografting.

2.4.5 Nanooxidation with AFM

Nanooxidation is another AFM-based nanofabrication technique. In this approach, the surface of a semiconductor or metal sample is modified through oxidization by applying a bias voltage between the conductive AFM tip and the substrate. By making the voltage level on the tip lower than the substrate, a protruded oxide feature can be formed on the sample surface. The reaction in the nanooxidation is called an anodic oxidation. A schematic diagram of AFM tip directed nanooxidation is shown in Fig. 2.18. The nanooxidation process can be conducted in contact mode, semi-contact mode, or non-contact mode. In these three operating modes, the semi-contact mode and non-contact mode cause less wear to the conductive layer of the AFM tip compared to contact mode. This happens because only the contact mode requires a constant physical contact between the tip and the sample. However, the

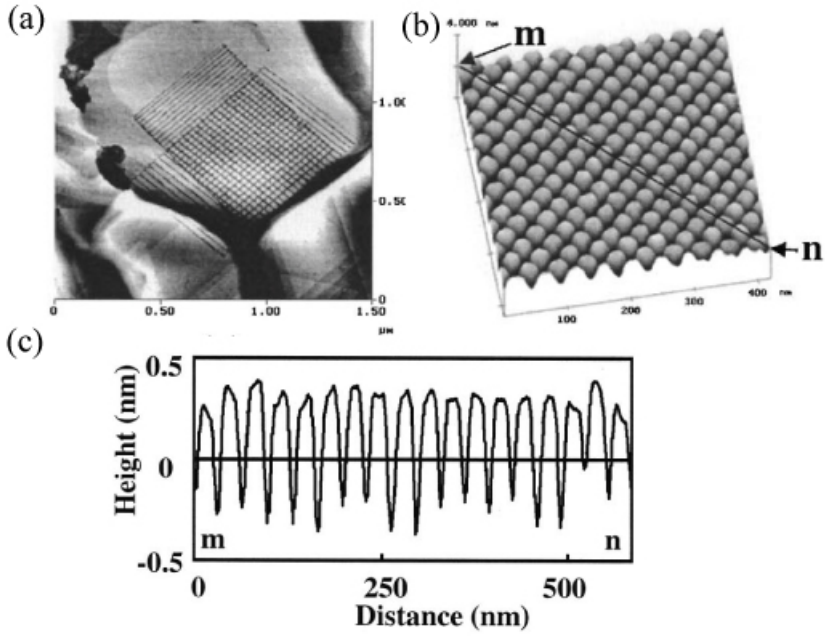

Figure 2.17: Alternating nanostructures of octadecanethiol and decanethiol: (a) Cell size of octadecanethiol 20×20 nm. (b) Closed-view of (a). (c) Cross-sectional analysis of (b) [Liu et al. (1994)].

non-contact mode requires a threshold voltage for oxidizing a sample due to a larger gap between the tip and sample than that in contact mode and semi-contact mode. Also semi-contact mode has higher resolution than non-contact mode.

The experimental implementation of nanooxidation is complex, because the oxidation results can be affected significantly by a lot of parameters, such as the bias voltage, substrate, separation between tip and sample surface, duration, and ambient humidity [41]. Several research groups have studied the mechanism of the oxidation and the effect of these parameters on the oxidation results [88–92]. These results illustrate the effect of, for example, electric field, humidity and oxygen of the environment on the dimension of oxide feature.

AFM tip-directed anodic nanooxidation approach has applications in electric nanodevices of metals or semiconductors. Oxide nanostructures as small as several nanometers to tens of nanometers were fabricated directly on poly(methylmethacrylate)

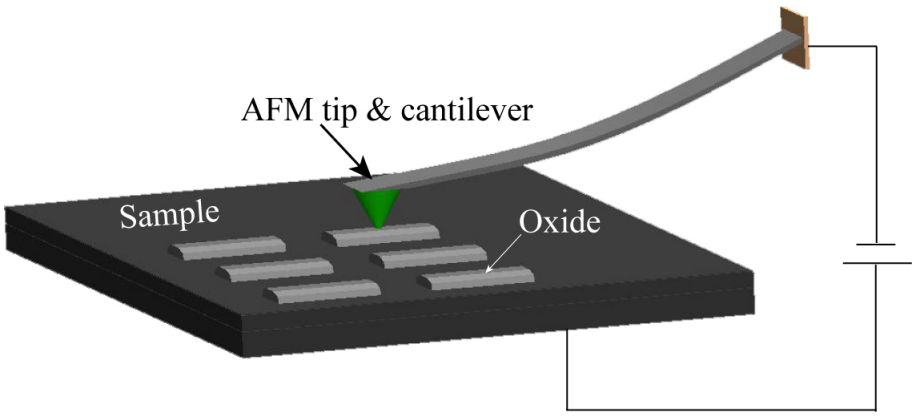

Figure 2.18: Schematic diagram of nanooxidation with AFM.

(PMMA) [93], Si [94], Ti, Si_3N_4 [95, 96], and etc. 2-dimensional and 3-dimensional nanostructures were constructed with the combination of anodic oxidation and selectively chemical etching [97, 98].

2.4.6 Dip-Pen Nanolithography using AFM

Dip-Pen nanolithography (DPN) is a nanofabrication method to create features on the surface of a substrate by depositing chemical molecules to the substrate surface using an AFM tip. This method was developed by Mirkin et al. in 1999 [99]. In dip-pen nanolithography, the AFM tip is coated with a thin film of chemical of interest, which could be organic materials, bio-molecules or inorganic salt. During the scanning of the AFM tip relative to the substrate surface, the chemical molecules transfer from the tip to the substrate surface and deposit on the surface to form chemical nanostructures. A schematic diagram of DPN is described in Fig. 2.19. From the figure, it can been easily seen that the DPN process is similar to a writing process with a fountain pen, where the coated tip works as a pen, the chemical is as ink, and the substrate is as the paper to write on. Therefore, it is named as dip-pen nanolithography. Usually, a soft AFM tip with a small spring constant, such as 1 N/m, is selected as the pen [100], and thiols are frequently used as DPN inks to be coated on the AFM tip [101, 102].

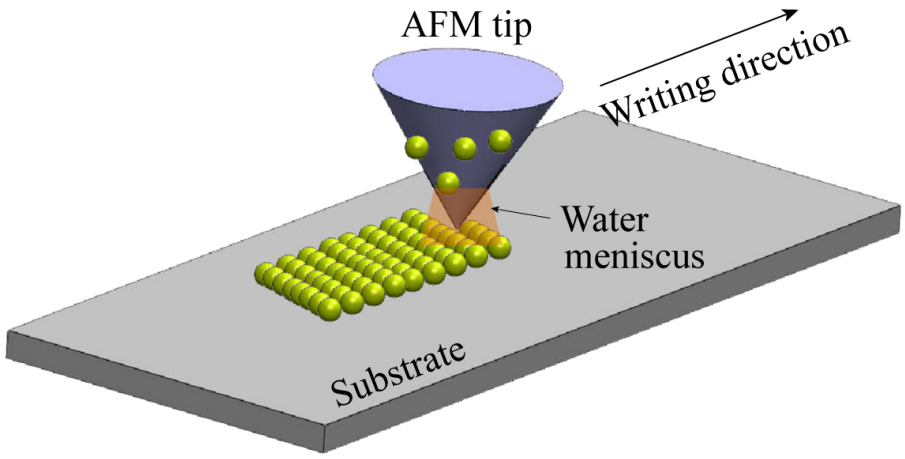

Figure 2.19: Schematic diagram of Dip-Pen nanolithography using AFM.

In the lithography process, the AFM tip is conducted in a contact mode or a tapping mode [100].

Nanostructures of various materials were fabricated via DPN [101,103–105]. Combined with wet chemical etching, DPN had fabricated 3-dimensional multilayered nanostructures, which implies potential applications of DPN in electronic nanodevices [106]. For example, a small nano gap of 12 nm is fabricated by DPN and subsequent chemical etching [106], as shown in Fig. 2.20. Apart from electronic nanodevices fabrication, the DPN can be applied to biomolecules, organic, magnetic, and inorganic material nanostructures fabrication. Nanostructures containing biomolecules, such as protein or DNA, were fabricated directly or indirectly via DPN [105, 107–109]. In direct methods, biomolecules containing sulfur or thiolated biomolecules were coated to an Si or Si_3N_4 AFM tip as DPN ink to directly create biomolecule patterns on protein or DNA to modify the property [107, 108]. In indirect methods, a selective template containing nanopatterns is created via DPN, and biomolecules are selectively adsorbed on the template, resulting in nanopatterns of biomolecules [105, 109]. Nanostructures of organic materials [103, 110, 111], and polymers [104, 112, 113] with special properties were fabricated via DPN. This method

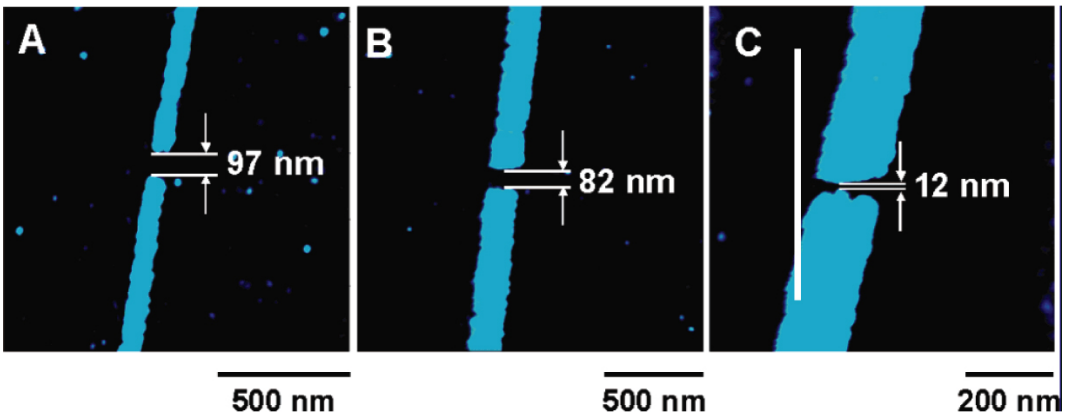

Figure 2.20: TMAFM topographic images of etched MHA/Au/Ti/SiO_x/Si nanogaps fabricated by DPN and subsequent chemical etching [Zhang et al. (2003)].

can be used to study chemical reaction. The nanostructures composed of organic materials such as dye and conductive polymer have potential applications in electrical, optical and sensing devices. Nanostructures of magnetic materials have potential technological applications in molecular electronics, high-density recording and biosensors. Magnetic nanopatterns were constructed via DPN using sol-based magnetic inks [114]. Furthermore, nanopatterns of inorganic materials can be created by an AFM tip coated with DPN ink, such as metal nanoclusters [115] and inorganic salt [100, 110, 116–118].

In these applications of AFM, precision positioning is needed. In particular, precise position control in both the lateral and vertical directions is needed to hold the probe at a desired location or to track a desired motion trajectory. For instance, when the AFM is used to indent nanofeatures on a semiconductor surface to create quantum dots (2-80 nm in size), accurate position control of the indenter tip is needed because the probe position error directly affects the size, spacing, and distribution of the nanofeatures. Even 2-4 nanometers variation in size and spacing of the nanofeatures can drastically alter their properties [119]. Additionally, high-speed control of the probe's movement is needed for high throughput fabrication, imag-

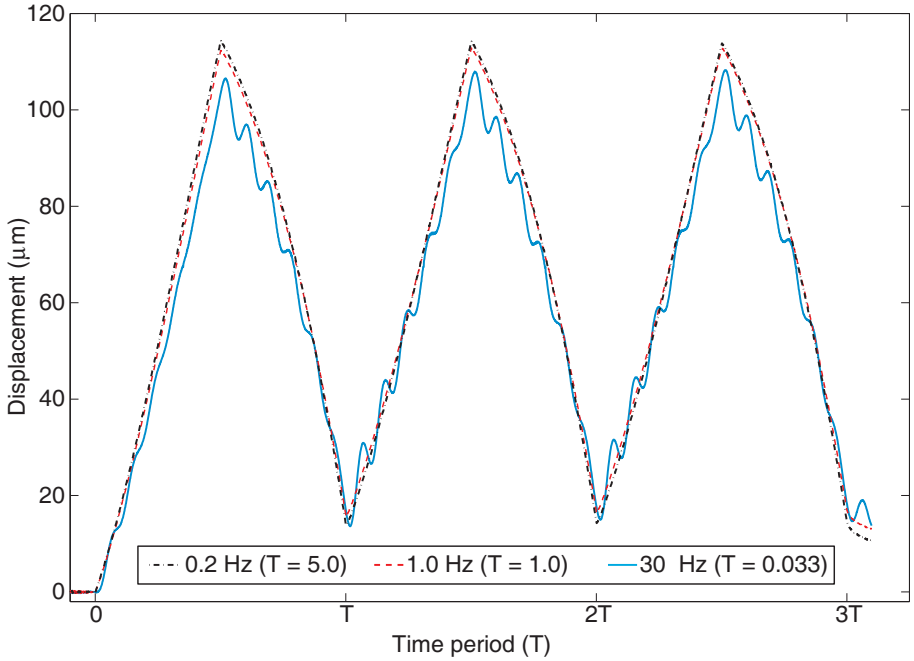

Figure 2.21: Experimentally measured response of a piezoactuator showing hysteresis, creep, and vibration effects.

ing, and metrology. Without accurate motion control along a specific trajectory at high speed, oscillations can cause the tip to collide with nearby features, which leads to excessive tip-to-sample forces. The large forces can damage the tool tip or soft specimens such as cells.

2.5 Challenges with Piezoelectric Positioners

It is usually assumed that piezoelectric actuators expand and contract proportionally to applied voltage. Unfortunately this assumption is not accurate and is particularly erroneous when considering moderate or high electric fields, and when the frequency of operation becomes high. There are three significant sources of error that degrade and complicate the response of piezoelectric positioners: hysteresis, creep, and vibration, as illustrated in the measured response shown in Fig. 2.21.

Hysteresis, which is a nonlinear behavior between the applied electric field and

the mechanical displacement of a piezoelectric actuator, is believed to be caused by irreversible losses that occur when similarly oriented electric dipoles interact upon application of an electric field [15]. The effect of hysteresis on the displacement of a piezoelectric actuator is more pronounced over large-range motion [120, 121]. In Fig. 2.21, the curve depicts the nonlinearity that arises due to hysteresis. In addition to poor positioning accuracy, hysteresis causes poor repeatability and the mixing of harmonic content into the displacement response. Hysteresis can be avoided by operating in the linear range, *i.e.*, over short range displacements; however, this limits the achievable positioning range. Controlling the charge delivered to the piezoelectric transducer, rather than the voltage, helps to minimize hysteresis [122].

When a piezoelectric transducer is commanded by a step change in voltage, the response consists of high-frequency transients followed by low frequency drift known as creep. The time constant for creep is typically a few minutes. Creep severely degrades the low-frequency and static positioning ability of piezoelectric actuators [123–125]. In mechanics, creep is a rate-dependent deformation of the material when subjected to a constant load or stress [126]. Similarly, creep in piezoelectric materials is a rate-dependent deformation due to a constant electric field. Creep manifests itself as the remnant polarization slowly increases after the onset of a constant field. One method to avoid creep is to operate fast enough so that the creep effect becomes negligible [12]; however, such effort prevents the use of piezo positioners in slow and static applications. For example, because of drift, it is difficult to precisely fabricate nanofeatures using AFMs when the process time-scale is on the order of minutes, *e.g.*, see [123]. Methods to compensate for creep have been well studied in the past and some examples include the use of feedback control, *e.g.*, [120, 127–129], and model-based feedforward control, *e.g.*, [12, 125, 130–133].

Vibration (or actuator) dynamics, such as structural resonances, limits the operat-

ing bandwidth of piezo-based positioning systems. The effect is caused by command signals exciting the flexible modes of the structure [134, 135]. For example, the frequency response of a piezo-based positioner typically reveals sharp resonant peaks. These peaks can easily be excited by certain command signals like triangular inputs applied to control the positioner. Figure 2.21 clearly illustrate the effect of vibration, where oscillations cause significant tracking error in the displacement versus time response. Such effects cause distortion in the SPM-based imaging, for example the rippling effect in the AFM images. Typically, scan rates (*i.e.*, scan frequencies) are restricted to less than $1/10^{th}$ to $1/100^{th}$ of the first resonant frequency, thus limiting the bandwidth of piezo-based systems because the achievable scan rate is lower for increased resolution in positioning. However, higher operating speed can be achieved by using *stiffer* piezoactuators with higher resonant frequencies [29, 30, 136], for example, Ando *et al.* [28] used a *stiff* piezo with a resonant frequency of 260 kHz in an AFM to image biological macromolecules in action. In general, these stiff piezos have shorter effective displacement ranges. Therefore, the use of stiffer piezos to increase bandwidth also leads to reduction of positioning range.

In summary, hysteresis and dynamics (creep and vibration) effects significantly limit the performance and application of piezo-based nanopositioners. Therefore, this research addresses these effects to enhance the performance of piezo-based systems for tracking periodic trajectories.

2.6 Summary

This chapter introduced hysteresis and hysteretic systems such as the piezoelectric actuator and applications in scanning probe microscopy. A discussion of various applications of piezo-based AFM in the area of nanofabrication was presented and the adverse effects of hysteresis and dynamics (creep and vibration) were discussed in

detail. It is noted that the effects lead to significant loss in positioning precision. Furthermore, it is noted that the focus of this dissertation is to address the effect of hysteresis on the stability of closed-loop systems for designing repetitive controllers (RCs) to achieve high-precision positioning for hysteretic systems. In the next chapter, the concept and design of RC for linear dynamics is discussed. Afterwards, the analysis of the effect of hysteresis on closed-loop system stability is discussed in detail.

Chapter 3

Repetitive Control for Tracking Periodic Trajectories

This chapter describes the repetitive control (RC) approach design for reducing the repeating tracking error for precise positioning in piezo-based nanopositioners. The objective is to achieve high-precision positioning by adding an RC to an existing closed-loop feedback system (such as a PID feedback controller) to improve performance. In this chapter, an enhanced RC is designed. The enhanced repetitive controller is formed by incorporating a low-pass filter and two phase lead compensators to improve robustness and stability.

3.1 Challenges and Motivation

Mechanical systems that exhibit hysteresis and dynamic effects are challenging to control [137]. Particularly, hysteresis is range-dependent and the effect alone can lead to significant tracking error, approximately 20% in piezo-based positioners [138] and SMA actuators [139]. Without compensation, hysteresis can affect the stability and tracking performance of a closed-loop controller, especially when the controller is designed around a linear dynamic model [140]. While hysteresis is typically regarded as a range-dependent effect, dynamics, on the other hand, increases with input frequency. For example the structural vibrations in piezoactuators become significant

when the input frequency approaches the dominant resonant frequency, where high frequency inputs excite lightly-damped structural modes causing severe oscillations in the output response. The total tracking error can exceed 30% [138], and therefore hysteresis and dynamic effects limit both the range as well as the bandwidth of operation. This is especially true in a piezo-based atomic force microscopy (AFM), a type of scanning probe microscope (SPM), where hysteresis and dynamics dominate the response of the piezo positioner, preventing the tool from precisely tracking a desired motion trajectory, such as the scanning trajectory for AFM imaging or probe-based nanofabrication [1, 141]. Moreover, the large tracking error causes the SPM probe tip to experience large tip-to-sample forces that can damage, for example, the SPM probe or soft specimens such as live cells. Precision positioning of the SPM tool tip relative to a sample surface is needed to obtain high-resolution topographical images, measure various properties of a specimen, and investigate nano-scale dynamic interactions in real time [37, 142]. Therefore, control of hysteresis and dynamic effects is critical in nanopositioning systems.

Often, piezoactuators are required to track a desired motion trajectory that is periodic in time, for example, the raster pattern used in the piezo-based SPMs [11]. During the scanning operation, hysteresis and dynamic effects in the actuator cause significant positioning error, and the error repeats itself with the operating cycle, thus limiting the performance of the tool [1]. In the past, other feedback-based controllers and feedforward controllers have been developed to handle the hysteresis and dynamic effects [1, 141]. For instance, PID, H_∞, and adaptive control, are robust and used extensively, but often bandwidth limited [127, 129, 143]. Charge control is a viable approach to minimize hysteresis [122], but it requires a complex charge control circuit. Model-based feedforward control provides excellent tracking performance when accurate models are used, but in general the open-loop nature of the control

scheme lacks robustness [1, 12]. Hysteresis models such as the Preisach model have been used extensively for feedforward control [144, 145]. However, for applications such as AFM imaging or nanowire array fabrication where the reference trajectory is periodic in time, the residual tracking error of these methods repeats from one operating period to the next. To address this issue and exploit the process of repetition for precision control, repetitive control (RC) has recently been considered for nanopositioning systems [7]. The RC approach is based on the Internal Model Principle [146] and is specifically tailored to track periodic reference trajectories. A RC consists of a signal generator that provides high gain at the harmonics of the reference trajectory. The controller can easily be implemented digitally using a pure delay inside of a positive feedback loop [9]. Compared to traditional feedback and feedforward controllers, the tracking error of RC diminishes as the number of operating periods increases. The controller generally requires only the period of the reference trajectory to be known [9]. In many motion control applications, such as SPM-based imaging and patterning, the reference signal's period is known in advance which makes RC attractive. Compared to iterative learning control (ILC) [147–149], a repetitive feedforward control approach effective at reducing the repeating tracking error, RC does not require resetting the initial conditions at the start of each iteration step. It is pointed out that ILC for hysteretic systems requires a cycling process to reset the initial conditions at the beginning of each iteration [149]. For convenience, RC can be plugged into an existing feedback loop to enhance the system performance.

3.2 Enhanced Repetitive Control for Linear Dynamics

Repetitive control is a direct application of the internal model principle, where high-accuracy tracking of a desired periodic trajectory, with period T_p, is achieved if the

controller consists of the transfer function of the reference trajectory. One such controller is a signal generator with period T_p.

In this study, an enhanced discrete-time RC is designed for a linear dynamic model of the piezoactuator to serve as a starting point for designing RC for hysteretic systems. This linear RC system is shown in Fig. 3.1, where $R(z)$ is a given periodic reference trajectory with period T_p, and $Y(z)$ is the output. The piezoactuator dynamics, assumed to be linear, are represented by $G(z)$, where $z = e^{j\omega T_s}$, $\omega \in (0, \pi/T_s)$. The RC is created by wrapping a pure delay, z^{-N}, inside of a positive-feedback loop to create a signal generator with period T_p, where T_s is the sampling period and $N = T_p/T_s \in \mathbb{N}$ is the number of points per period of the reference trajectory. A low pass filter $Q(z)$ is added to lower the high gain of the RC at high frequencies to ensure stability and robustness [150, 151]. However, a tradeoff is made between robustness and high-frequency tracking when such filters are used. To compensate the tradeoff, a RC gain, k_{rc}, and two positive phase-lead compensators, $P_{1,2}(z) = z^{m_{1,2}}$, where m_1, m_2 are non-negative integers, are added to improve tracking performance [7]. Notably, $P_1(z)$ compensates for the phase lag of the low-pass filter $Q(z)$ while $P_2(z)$ compensates for the phase lag of the closed-loop system. It is emphasized that both phase-lead compensators contribute a linear phase lead angle of

$$\theta_i(\omega) \;=\; m_i T_s \omega, \;\; i = 1, 2 \tag{3.1}$$

and in units of radians. A typical feedback controller, such as a PID, is represented by $G_c(z)$ and it is assumed that the feedback controller is part of the forward path. The performance of the RC closed-loop system on tracking periodic reference trajectories is analyzed and presented below.

By inspection, the transfer function of the signal generator that relates $E(z)$ to

$A(z)$ in Fig. 3.1(a) is given by

$$\frac{A(z)}{E(z)} = \frac{Q(z)P_1(z)z^{-N}}{1-Q(z)P_1(z)z^{-N}} = \frac{Q(z)z^{(-N+m_1)}}{1-Q(z)z^{(-N+m_1)}}. \tag{3.2}$$

In the absence of the low-pass filter $Q(z)$ and positive phase lead $P_1(z) = z^{m_1}$, the poles of the signal generator are $1 - z^{-N} = 0$, which implies infinite gain at the harmonics of the periodic reference trajectory ($\omega = 2n\pi/T_p$, where $n = 1, 2, 3, ...$) as shown in Fig. 3.2. Such large gain is what gives the RC its ability to track periodic trajectories. As a result, RC is a useful control method for SPM in which the scanning motion is repetitive, such as the lateral probe motion during AFM imaging and fabricating the patterns for nanowire array growth.

Practical RC design incorporates a low-pass filter $Q(z)$ because the large gain at high frequencies can lead to instability of the closed-loop system. For simplicity,

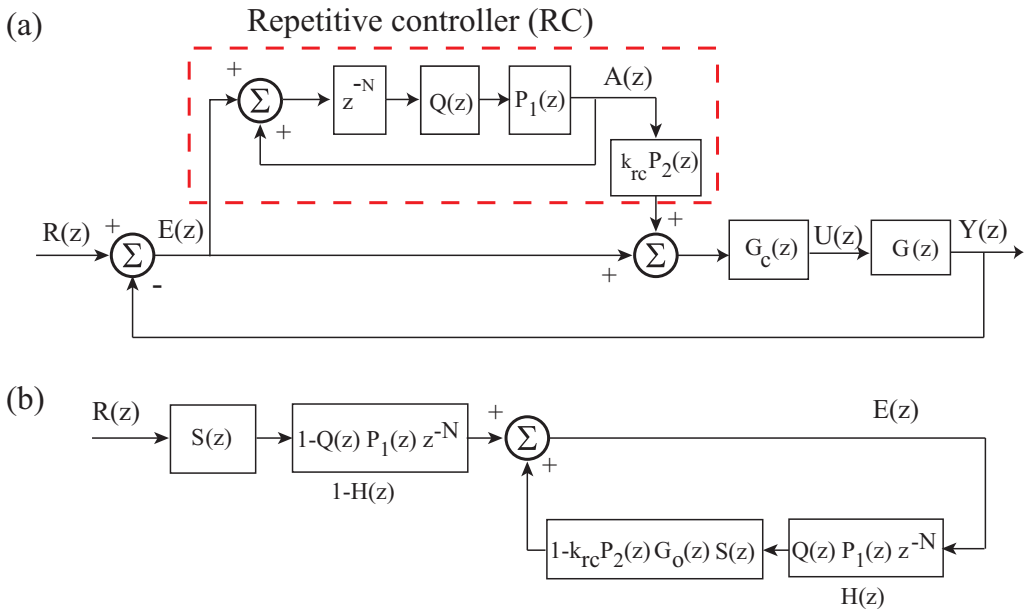

Figure 3.1: (a) The block diagram of repetitive control system consisting of two linear phase-lead compensators, $P_1(z)$ and $P_2(z)$, to enhance performance. (b) An equivalent block diagram of (a) for stability analysis, where $E(z)$ is the error.

a standard low-pass filter of the form $Q(z) = \frac{a}{z+b}$, where $|a| + |b| = 1$, is chosen. Alternatively, a zero-phase filter can also be used [152].

3.2.1 Stability Analysis

For the RC implementation, the main issue will be the balance between the tracking performance and the stability of the RC closed-loop system. The issue will be addressed through choosing the RC gain k_{rc}, along with the values of $m_{1,2}$ for the phase lead compensators $P_1(z)$ and $P_2(z)$ by analyzing the stability of the closed-loop RC system shown in Fig. 3.1(a). The stability analysis of the RC system is presented as follows. Let $H(z) = Q(z)z^{(-N+m_1)}$ and $G_0(z) = G_c(z)G(z)$. Consider the following assumptions:

Assumption 1 *The reference trajectory $R(z)$ is periodic.*

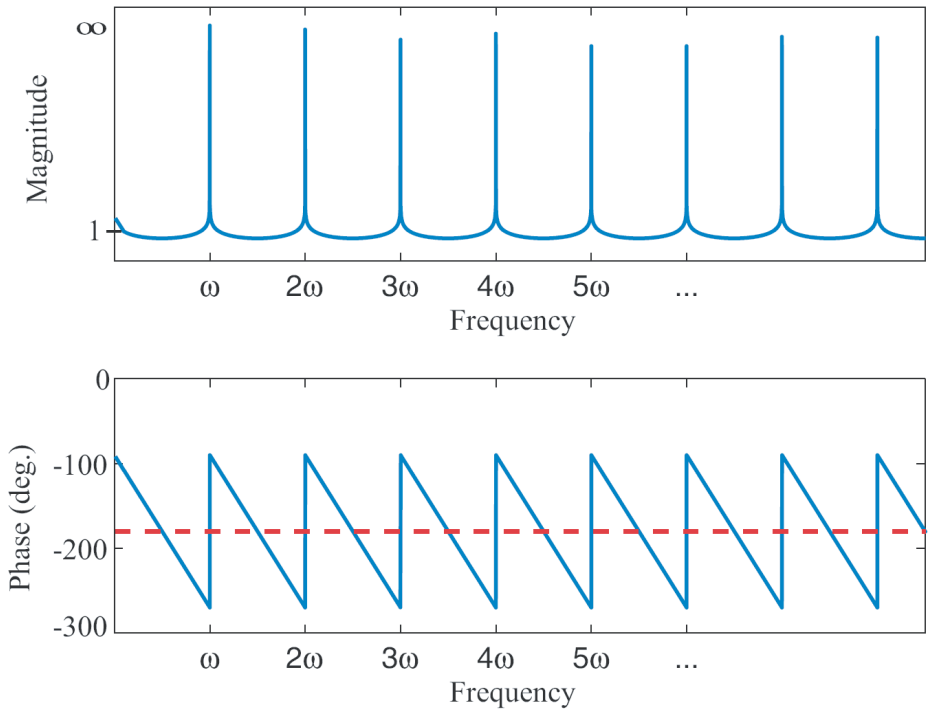

Figure 3.2: Magnitude and phase versus frequency for signal generator $\frac{z^{-N}}{1-z^{-N}}$, where $z = e^{j\omega T_s}$.

Assumption 2 *The closed-loop system without the RC loop is asymptotically stable,* i.e., $1 + G_c(z)G(z) = 0$ *has no roots outside of the unit circle in the z-plane, and* $G_c(z)G(z)$ *has no pole-zero cancelation.*

Theorem 1 (Stability of RC) *Let Assumption 1 and 2 hold. If* $|Q(e^{j\omega T_s})| \leq 1$ *for* $\omega \in (0, \pi/T_s)$, $1 - H(z)$ *is bounded input, bounded output stable, and*

$$0 < k_{rc} < \frac{2\cos[\theta_T(\omega) + \theta_2(\omega)]}{|T(\omega)|}, \tag{3.3}$$

$$-\pi/2 < [\theta_T(\omega) + \theta_2(\omega)] < \pi/2, \tag{3.4}$$

then the RC feedback system shown in Fig. 3.1(a) is asymptotically stable.

Proof: The stability is shown by applying the Small Gain Theorem [153]. First, the transfer function relating the reference trajectory $R(z)$ and the tracking error $E(z)$ is

$$\frac{E(z)}{R(z)} = \frac{[1 - H(z)]}{1 - H(z) + [(k_{rc}P_2(z) - 1)H(z) + 1]G_0(z)}, \tag{3.5}$$

where $H(z) = Q(z)z^{(-N+m_1)}$ and $G_0(z) = G_c(z)G(z)$. Multiplying the numerator and denominator of Eq. 3.5 by the sensitivity function $S(z) = 1/(1 + G_0(z))$ of the feedback system without the repetitive controller, the following expression is obtained,

$$S_{rc}(z) = \frac{E(z)}{R(z)} = \frac{[1 - H(z)]S(z)}{1 - H(z)[1 - k_{rc}P_2(z)G_0(z)S(z)]}, \tag{3.6}$$

where $S_{rc}(z)$ shown above is referred to as the sensitivity function of the closed-loop RC system. Using Eq. (3.6), the RC block diagram in Fig. 3.1(a) is simplified to the equivalent interconnected system shown in Fig. 3.1(b). Referring to Fig. 3.1(b), by Assumption 2, $S(z)$ has no poles outside the unit circle in the z-plane, so it is stable. Replacing $z = e^{j\omega T_s}$, and since $1 - H(z)$ stable, the positive feedback closed-loop

system in Fig. 3.1(b) is asymptotically stable when

$$\begin{aligned} &|H(z)[1 - k_{rc}P_2(z)G_0(z)S(z)]| \\ &\qquad = \ |H(e^{j\omega T_s})[1 - k_{rc}e^{j\theta_2(\omega)}G_0(e^{j\omega T_s})S(e^{j\omega T_s})]| \ < \ 1, \end{aligned} \tag{3.7}$$

for all $\omega \ \epsilon \ (0, \pi/T_s)$, where the phase lead $\theta_2(\omega) = m_2 T_s$. From this equation, it can be observed that both the RC gain k_{rc} and the phase lead $\theta_2(\omega)$ affect the stability and robustness of RC as well as the rate of convergence of the tracking error. In the following, condition in Eq. (3.7) is used to determine explicitly the range of acceptable k_{rc} for a given $Q(z)$ and $G_0(z)$. The effects of the phase lead $\theta_2(\omega)$ on robustness and the phase lead $\theta_1(\omega)$ on the tracking performance are discussed.

Let $T(z)$ represent the complimentary sensitive function of the closed-loop feedback system without RC, that is, $T(z) = G_0(z)S(z)$. Noting that $|Q(e^{j\omega T_s})| \leq 1$ and replacing the complimentary sensitive function of the closed-loop system without RC with

$$T(e^{j\omega T_s}) = G_0(e^{j\omega T_s})S(e^{j\omega T_s}) = \frac{G_0(e^{j\omega T_s})}{1 + G_0(e^{j\omega T_s})} = |T(\omega)|e^{j\theta_T(\omega)}, \tag{3.8}$$

where $|T(\omega)| > 0$ and $\theta_T(\omega)$ are the magnitude and phase of $T(e^{j\omega T_s})$, respectively, Eq. (3.7) can be simplified to

$$|1 - k_{rc}|T(\omega)|e^{j[\theta_T(\omega)+\theta_2(\omega)]}| \ < \ 1. \tag{3.9}$$

Observing that $e^{j\theta} = \cos(\theta) + j\sin(\theta)$ and $k_{rc} > 0$, Eq. (3.9) gives

$$-2k_{rc}|T(\omega)|\cos[\theta_T(\omega) + \theta_2(\omega)] + k_{rc}^2|T(\omega)|^2 \ < \ 0, \tag{3.10}$$

hence the Eq. (3.10) is satisfied if

$$0 \;<\; k_{rc} \;<\; \frac{2\cos[\theta_T(\omega)+\theta_2(\omega)]}{|T(\omega)|} \quad \text{and}$$
$$-\pi/2 \;<\; [\theta_T(\omega)+\theta_2(\omega)] \;<\; \pi/2.$$

This completes the proof. ■

Remark 1 *Based on the Eq. (3.9), if the pre-exist feedback control system without RC is stable, it can guarantee the stability of the RC system for any plug-in repetitive controller with the RC gain k_{rc} and the phase lead $\theta_2(\omega)$ satisfying Eq. (3.10), because the repetitive controller $H(z)$ does not appear in the stability conditions. More generally, if the k_{rc} and $p_2(z)$ are treated as a part of the pre-exist feedback system, then the repetitive controller is no need to be designed to ensure the robust stability of the RC system, as long as the pre-exist feedback system is robust stable.*

Remark 2 *In general, both the RC gain k_{rc} and the phase lead $\theta_1(\omega)$ can enhance the robust stability of feedback control system as well as affect the rate of convergence of the tracking error RC system. In particular, $P(z)$ enhances the robustness of the closed-loop RC system by increasing the frequency at which the phase angle crosses $\pm 90^\circ$.*

Remark 3 *With a stable RC system, its tracking performance is determined by the sensitivity function Eq. (3.6) at multiples of the fundamental frequency within the bandpass of the low-pass filter $Q(z)$. The filter $Q(z)$ reduces the effects of high-frequency dynamics; however, it also shifts the point of maximum gain of the signal generator created by the pure delay z^{-N} [154]. Such a shift inadvertently lowers the RC gain at the harmonics and thus negatively effects the tracking performance of the RC system. But much of the phase lag can be compensated using the linear phase lead*

$\theta_1(\omega)$ in the RC loop to improve the tracking performance [155]. Because $N >> m_1$, the modified delay $z^{(-N+m_1)}$ is causal and can be easily implemented digitally.

3.3 Summary

A discrete time enhanced RC is designed to plug into an existing feedback loop to track periodic reference trajectories. The RC is designed around a linear dynamics to serve as a starting point for designing RC for a hysteretic system. The major challenges with designing RC are ensuring stability and good tracking performance.

Chapter 4

Dual-Stage RC Design

The positioning performance of piezo-based nanopositioning systems is limited by dynamic and hysteresis effects in the piezoactuator. The RC system described in the previous chapter has been applied to track periodic trajectories in piezo-based SPMs. However, the tracking performance is limited by the low-pass filter $Q(z)$ [8]. Herein, to further improve the performance of the enhanced RC, a high-performance, dual-stage repetitive controller (dual-RC) is proposed for tracking periodic trajectories, such as the scanning-type motion SPM applications. Specifically, a discrete-time dual-RC is created by cascading a conventional RC with an odd-harmonic RC. The favorable gain characteristics of the dual-RC coincide with the odd harmonics of the scanning-type periodic reference trajectory. The result is better robustness and lower tracking error compared to the enhanced RC proposed in the previous chapter.

4.1 The Dual-RC Concept

The tracking performance of the conventional RC system shown in Fig. 3.1 is governed by the sensitivity function

$$S_{rc}(z) \triangleq \frac{E(z)}{R(z)} = \frac{[1 - H_1(z)]S(z)}{1 - H_1(z)[1 - k_{rc}G_0(z)S(z)]}, \tag{4.1}$$

where $H_1(z) = Q(z)z^{-N+m_1}$ and $S(z) = 1/[1 + G_0(z)]$ is the sensitivity function of the feedback system without the repetitive controller. One approach to improve the tracking performance of the conventional RC is to reduce the magnitude of S_{rc} by cascading two signal generators together, effectively producing a squaring effect [156]. However, noting that the reference trajectories used in the scanning operation in SPMs are generally odd-harmonic signals (*e.g.*, triangular trajectories), it is preferred that an odd-harmonic RC as depicted in Fig. 4.1(a) be cascaded with a conventional RC as shown in Fig. 4.2(a) instead of cascading two conventional RCs. The resultant sensitivity function is

$$\widetilde{S}_{rc}(z) = \frac{[1 - H_1(z)][1 - H_2(z)]}{W(z) + [1 - H_1(z)(1 - k_1)][1 - H_2(z)(1 - k_2)]G_0(z)}, \tag{4.2}$$

where $W(z) = [1 - H_1(z)][1 - H_2(z)]$ and $H_2(z) = -z^{-\frac{N}{2}+m_2}Q(z)$. The advantage of the enhanced dual-RC design over cascading two conventional RCs together is a more robust system. Cascading two conventional RCs together result in excessive gain at the even harmonics which can degrade the system's performance for tracking odd-harmonic reference trajectories [157]. The performance of the enhanced dual-RC is illustrated by comparing the magnitude response of the sensitivity function $\widetilde{S}_{rc}(z)$ of the enhanced dual-RC in Eq. (4.2) to the magnitude response of the sensitivity function $S_{rc}(z)$ of the conventional RC in Eq. (4.1) and the sensitivity function $\overline{S}_{rc}(z)$

of the odd-harmonic RC in Fig. 4.1(a), given by

$$\overline{S}_{rc}(z) = \frac{[1 - H_2(z)]S(z)}{1 - H_2(z)[1 - k_{rc}G_0(z)S(z)]}. \tag{4.3}$$

The comparison of the three RC configurations is shown in Fig. 4.3, where the frequency response functions are generated in Matlab using the '`margin`' command with $N = 100$, $m_1 = m_2 = 0$, $Q(z) = 1$, and $T_s = 10\ \mu s$ as an illustrative example. The results reveal that the odd-harmonic RC has less affect on the even-harmonics than the conventional RC (gain at first even harmonic: -13.7 dB for conventional RC, 4.49 dB for odd-harmonic RC, and -8.69 dB for dual-RC). However, the magnitude of the sensitivity function for the dual-RC is significantly lower than the conventional RC at the odd-harmonics (-24.4 dB for conventional RC vs. -47.1 dB for dual-RC at the first odd harmonic). This implies that (1) the odd-harmonic RC has the same tracking performance as the conventional RC for tracking odd-harmonic trajectories but it provides the system with more robustness by reducing the gain at the even harmonics, which effectively minimizes the amplification of signals, such as noise and disturbances, outside of the desired frequency range; and (2) the dual-RC provides higher gain than the conventional RC at the odd-harmonics; therefore, the dual-RC will improve the tracking performance of trajectories with odd-harmonics. The stability analysis of the odd-harmonic RC and enhanced dual-RC is discussed in the following.

4.2 Stability Analysis

The stability of the RC system is analyzed using the Small Gain Theorem [153].

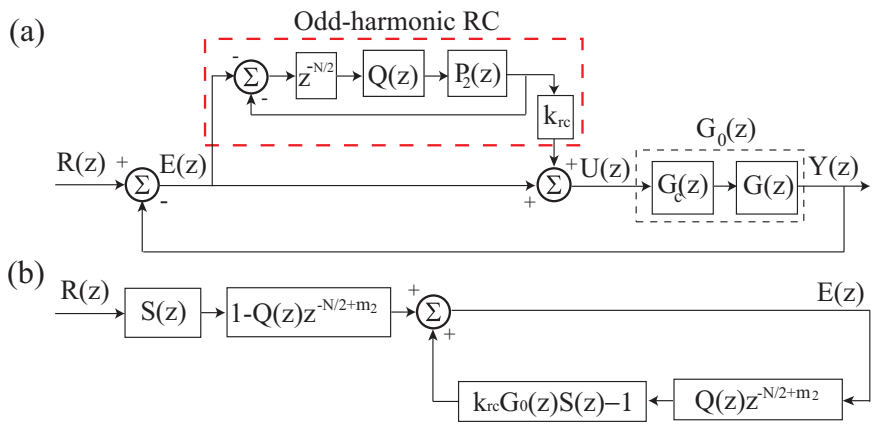

Figure 4.1: (a) An odd-harmonic RC with a linear phase-lead compensator $P_2(z) = z^{m_2}$ and a RC gain k_{rc} to enhance performance. (b) An equivalent block diagram of (a) for stability analysis.

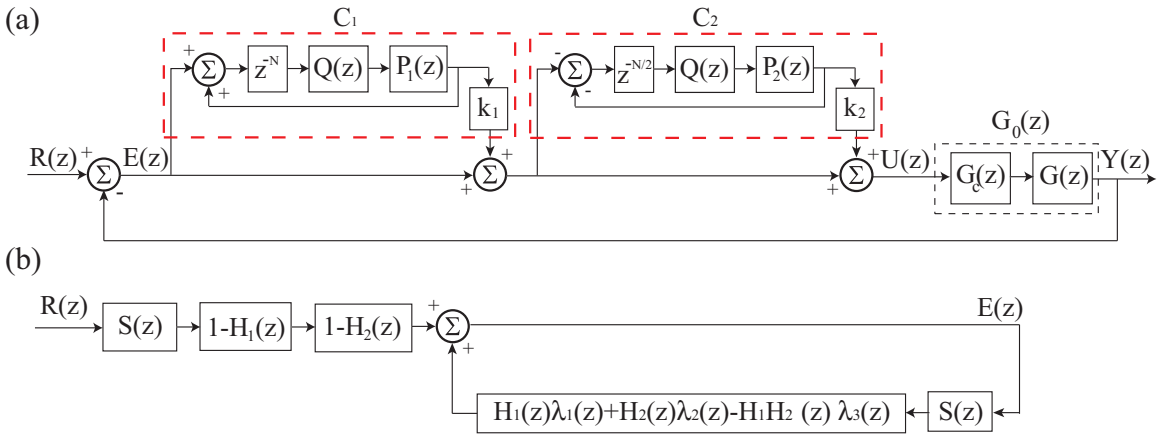

Figure 4.2: (a) A dual-stage RC design consisting of a conventional RC (C_1) cascaded with an odd-harmonic RC (C_2) and (b) the equivalent block diagram of (a) for stability analysis.

4.2.1 Stability Analysis of the Odd-Harmonic RC

Let T_s be the sampling time. Consider the odd-harmonic RC shown in Fig. 4.1(a) and the following assumptions:

Assumption 3 *The reference trajectory $R(z)$ is periodic in time with period T_p.*

Assumption 4 *The closed-loop system without the RC is asymptotically stable, i.e.,*

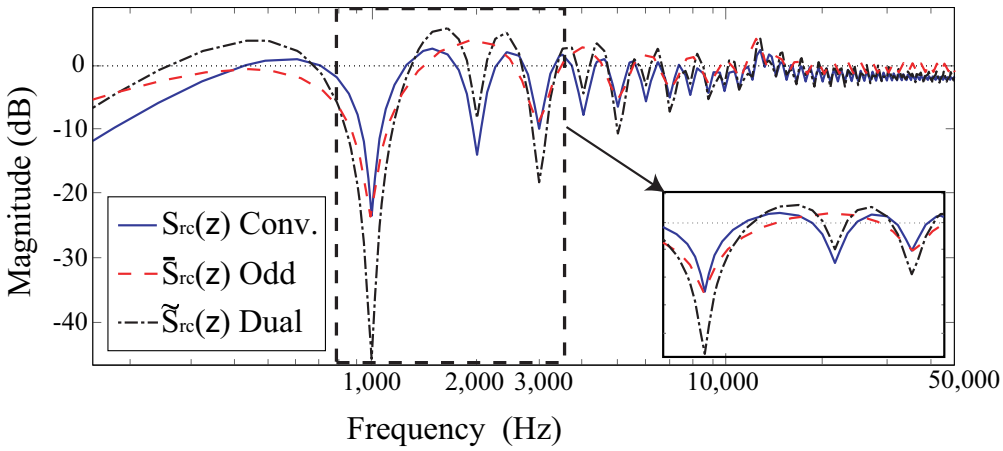

Figure 4.3: Comparison of magnitude versus frequency plots for the sensitivity functions for different RC configurations, where $S_{rc}(z)$ denotes the conventional RC (solid line), $\bar{S}_{rc}(z)$ is for the odd-harmonic RC (dash line), and $\tilde{S}_{rc}(z)$ represents the dual RC (dash-dot line).

$1 + G_0(z) = 0$ *has no roots outside of the unit circle in the z-plane and no pole-zero cancelation.*

The main result for the stability conditions for the odd-harmonic RC is provided in the following theorem.

Theorem 2 (Stability of odd-harmonic RC) *Let Assumptions 3 and 4 hold. If* $|Q(e^{j\omega T_s})| \leq 1$ *and*

$$0 < k_{rc} < \frac{2\cos[\theta_T(\omega)]}{|T(\omega)|} \quad and \quad -\pi/2 < \theta_T(\omega) < \pi/2 \tag{4.4}$$

for $\omega \in (0, \pi/T_s)$*, then the RC feedback system shown in Fig. 4.1(a) is asymptotically stable.*

Proof: First, the RC block diagram in Fig. 4.1(a) is simplified to the equivalent interconnected system shown in Fig. 4.1(b). Since $1 - H_2(z)$ and $S(z)$ are stable, then

the RC system in Fig. 4.1(a) is asymptotically stable when

$$|z^{-\frac{N}{2}+m_2}Q(z)[k_{rc}G_0(z)S(z)-1]|<1. \tag{4.5}$$

Noting that $z=e^{j\omega T_s}$, $|Q(e^{j\omega T_s})|\leq 1$, and the complimentary sensitivity function of the closed-loop system without the RC is given by Eq. (3.8), Eq. (4.5) is satisfied if

$$|k_{rc}|T(\omega)|e^{j\theta_T(\omega)}-1|<1. \tag{4.6}$$

With $e^{j\theta}=\cos(\theta)+j\sin(\theta)$ and $k_{rc}>0$, Eq. (4.6) gives

$$-2k_{rc}|T(\omega)|\cos[\theta_T(\omega)]+k_{rc}^2|T(\omega)|^2<0, \tag{4.7}$$

hence

$$0<k_{rc}<\frac{2\cos[\theta_T(\omega)]}{|T(\omega)|} \quad \text{and} -\pi/2<\theta_{\mathrm{T}}(\omega)<\pi/2.$$

This completes the proof. ■

Theorem 2 states that within an acceptable operating frequency range, there exists a sufficiently small RC gain k_{rc} such that the closed-loop RC system is stable. Next, the stability conditions for the dual-RC, created by cascading an odd-harmonic RC with the conventional RC, is presented.

4.2.2 Stability Analysis of the Enhanced Dual-RC

Consider the enhanced dual-RC system shown in Fig. 4.2(a) and Assumptions 3 and 4 from Section 4.2.1. The stability conditions are summarized in the following theorem.

Theorem 3 (Stability of enhanced dual-RC) *Let Assumptions 3 and 4 hold. If*

$|Q(e^{j\omega T_s})| \leq 1$ *and*

$$\begin{aligned} \frac{3\cos[\theta_T(\omega)] - \Delta}{3|T(\omega)|} &< k_1, k_2 < 1 + \sqrt{1 + \frac{3\cos[\theta_T(\omega)] + \Delta}{3|T(\omega)|}}, \\ -\pi/9 &\leq \theta_T(\omega) \leq \pi/9, \end{aligned} \tag{4.8}$$

with $\Delta = \sqrt{9\cos^2[\theta_T(\omega)] - 8}$ *for* $\omega \in (0, \pi/T_s)$*, then the closed-loop system in Fig. 4.2(a) is asymptotically stable.*

Proof: First, recall that if $a, b, c, d \in \mathbb{C}$, where $\mathbb{C}$ is the set of all complex numbers, and $|a| \leq 1$, $|c| \leq 1$ and $|b| + |d| \leq 1$, then $|a||b| + |c||d| \leq 1$. Now the sensitivity function in Eq. (4.2) is modified to

$$\widetilde{S}_{rc}(z) = \frac{[1 - H_1(z)][1 - H_2(z)]S(z)}{1 - [H_1(z)\lambda_1(z) + H_2(z)\lambda_2(z) - H_1(z)H_2(z)\lambda_3(z)]S(z)}, \tag{4.9}$$

where $\lambda_1(z) = 1 + (1 - k_1)G_0(z)$, $\lambda_2(z) = 1 + (1 - k_2)G_0(z)$, and $\lambda_3(z) = 1 + (1 - k_1)(1 - k_2)G_0(z)$. The RC system in Fig. 4.2(a) is converted to the equivalent interconnected system in Fig. 4.2(b).

Then, according to Fig. 4.2(b) and the Small Gain Theorem, the dual-RC system is internally stable when

$$\left|[H_1(z)\lambda_1(z) + H_2(z)\lambda_2(z) - H_1(z)H_2(z)\lambda_3(z)]S(z)\right| < 1 \tag{4.10}$$

with $1 - H_1(z)$ and $1 - H_2(z)$ designed stable. Applying the triangular inequality and noting that $|H_1(z)| \leq 1$ and $|H_2(z)| \leq 1$ give

$$\begin{aligned} &|[H_1(z)\lambda_1(z) + H_2(z)\lambda_2(z) - H_1(z)H_2(z)\lambda_3(z)]S(z)| \leq \\ &\qquad |\lambda_1(z)S(z)| + |\lambda_2(z)S(z)| + |\lambda_3(z)S(z)|. \end{aligned} \tag{4.11}$$

Then Eq. (4.10) is satisfied if

$$|\lambda_1(z)S(z)| + |\lambda_2(z)S(z)| + |\lambda_3(z)S(z)| < 1. \tag{4.12}$$

Noting $T(z) = G_0(z)S(z)$ and replacing $z = e^{j\omega T_s}$, the gains k_i with $i = 1, 2$ can be determined from Eq. (4.12) as follows:

Case 1: If $|\lambda_3(z)| \leq |\lambda_i(z)|$, Eq. (4.12) can be simplified to

$$|\lambda_1(z)S(z)| + |\lambda_2(z)S(z)| + |\lambda_i(z)S(z)| < \begin{cases} 3|\lambda_1(z)S(z)| < 1, \ \forall \ k_1 \leq k_2 \\ 3|\lambda_2(z)S(z)| < 1, \ \forall \ k_2 \leq k_1 \end{cases},$$

thus

$$3|1 - k_i T(e^{j\omega T_s})| < 1, \ k_i = \max(k_1, k_2). \tag{4.13}$$

Case 2: If $|\lambda_3(z)| \geq |\lambda_i(z)|$, then

$$3|1 - (2k_i - k_i^2)T(e^{j\omega T_s})| < 1. \tag{4.14}$$

Case 3: If $|\lambda_j(z)| \leq |\lambda_3(z)| \leq |\lambda_i(z)|$, $j \neq i$, $j \in \{1, 2\}$, $i \in \{1, 2\}$, Eq. (4.12) can also be simplified to

$$|\lambda_1(z)S(z)| + |\lambda_2(z)S(z)| + |\lambda_i(z)S(z)| < \begin{cases} 3|\lambda_1(z)S(z)| < 1, \ \forall \ k_1 \leq k_2 \\ 3|\lambda_2(z)S(z)| < 1, \ \forall \ k_2 \leq k_1 \end{cases},$$

thus

$$3|1 - k_i T(e^{j\omega T_s})| < 1, \;\; k_i = \max(k_1, k_2). \tag{4.15}$$

Therefore, the gains are found by solving Eq. (4.13), (4.14) and (4.15), *i.e.*,

$$\frac{3\cos[\theta_T(\omega)] - \Delta}{3|T(\omega)|} < k_1, k_2 < 1 + \sqrt{1 + \frac{3\cos[\theta_T(\omega)] + \Delta}{3|T(\omega)|}},$$

$$-\pi/9 \leq \theta_T(\omega) \leq \pi/9$$

with $\Delta = \sqrt{9\cos^2[\theta_T(\omega)] - 8}$. This completes the proof. ■

By satisfying the conditions in Theorem 3, that is, by picking appropriate values for the RC gains, k_1 and k_2, within a particular operating frequency range, the stability of the dual-RC is guaranteed.

4.3 Challenges with RC for Hysteretic Systems

The RC system described above assumes the system is linear, that is, no hysteresis behavior. So when the RC is applied to a hysteretic system, there is no guarantee that the closed-loop RC system is stable. In fact, hysteresis can drastically affect the stability of a closed-loop system if not accounted for. An example to indicate the effect of hysteresis is shown in Fig. 4.4. Plot (a) of Fig. 4.4 is the tracking performance of a stable RC system designed for linear dynamics $G(z)$ in simulation. The result shows tracking error is reduced by RC with the operating cycle increasing. However, direct implementation of this RC to the experimental piezoactuator system causes high frequency oscillations in the output of the closed-loop system, as the black line shown in plot (b) of Fig. 4.4. The amplitude of the oscillations enlarges while the operating cycle increases. By adding an inverse hysteresis compensator to the RC system, the

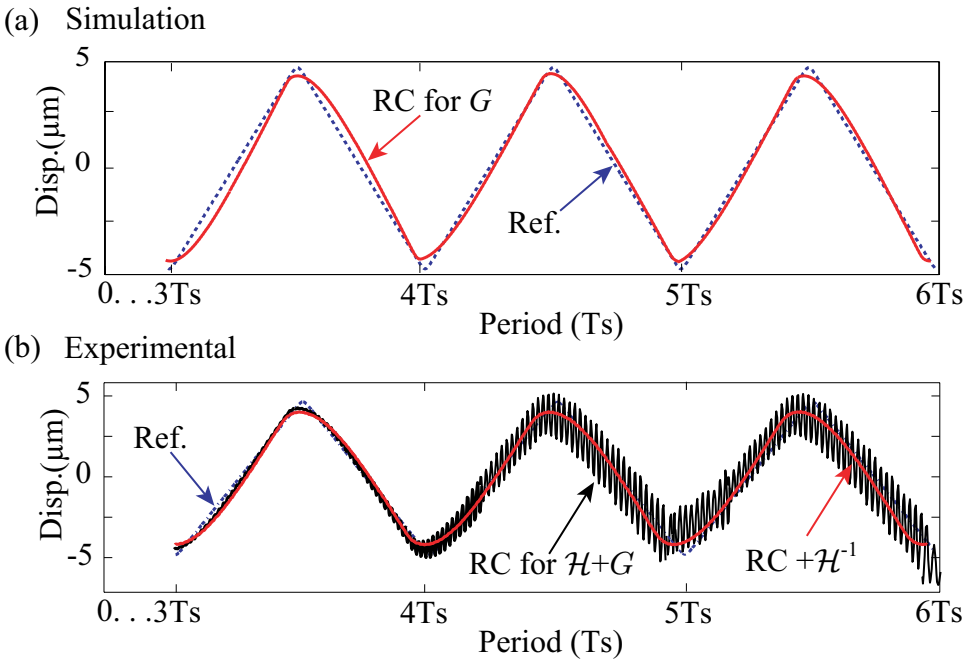

Figure 4.4: Example simulation and experimental results show the effect of hysteresis on closed-loop system stability and tracking performances.

oscillations in the output disappear [the red line in Fig. 4.4 (b)]. Therefore, it is important to quantify the effect of hysteresis on the performance of an RC system because of the wide range of applications for RC in many emerging active-material based motion control systems. These systems commonly exhibit hysteresis.

Although the design of RC for nonlinear systems has been studied in the past [158–161], there are no results on quantifying the effect of hysteresis on the stability of an RC system. Instead, the nonlinearity is commonly handled through an internal feedback loop, such as PID [143], to linearize the system dynamics. Additionally, feedforward control using an inverse hysteresis model has been considered [145, 162]. This research addresses RC design for hysteretic systems by quantifying the effect of hysteresis on RC stability. The approach considers the stability of the system in the $\mathcal{L}_2$ sense, followed by a stability analysis using the Small-Gain Theorem. In the analysis, the hysteresis effect is modeled by the Prandtl-Ishlinskii (P-I) approach [163–165].

The P-I model is a rate-independent phenomenological model and is chosen over other models such as the polynomial model, the BoucWen model, the Duhem model, the Maxwell slip model, and the Preisach model [121,166–171] because it has a smaller parameter space and is suitable for online implementation. Using the P-I model, the effect of hysteresis on the RC closed-loop system stability is analyzed to determine the tolerable *size* of the hysteresis nonlinearity for a stable RC system. If the hysteresis behavior in a system is unacceptably large, a new feedforward controller based on the structure of the P-I model is proposed to compensate for the hysteresis behavior. The Prandtl-Ishlinskii and its inverse are introduced next.

4.4 Summary

A dual-stage repetitive controller was described to help improve tracking performance. The dual-stage RC consists of a signal generator designed to provide high gains at the fundamental and the harmonics of the reference trajectory and another that offers high gain at the odd harmonics of the desired reference trajectory. The dual-RC offers is better robustness and lower tracking error compared to the enhanced RC proposed in the previous chapter.

Chapter 5

The Prandtl-Ishlinskii Hysteresis Model

This chapter focuses on modeling the hysteresis behavior of piezoactuators for RC design and analysis. Specifically, the Prandtl-Ishlinskii hysteresis model is studied in detail. The developed model will be used in the following chapters to analyze the stability of the RC system. The model is also exploited to develop a new model-based feedforward controller to compensate for the hysteresis effect.

5.1 The Prandtl-Ishlinskii Model

There are many models that exist for hysteresis. Models include approximated polynomial model, the BoucWen model, the Duhem model, the Maxwell slip model and the Preisach model [121, 166–171]. For example, the approximated polynomial model represents the hysteresis behavior using two 5^{th}-order polynomial functions with 24 parameters to describe the hysteresis behavior [166]. The BoucWen model is a nonlinear differential model that can be exploited for inverse feedforward control [167, 168]. The Preisach model is one of the most popular models, where the output is a superposition of the elementary hysteresis operators [171]. In comparison, the proposed P-I model involves a smaller number of parameters for identification and can be inverted

analytically for real-time implementation [165].

The Prandtl-Ishlinskii model is an operator-type model which has recently been investigated to model hysteresis in piezoactuators [163–165]. In this model, the output is characterized by the play operator shown in Fig. 5.1 [163]. Let the input u be continuous and monotone over the interval $t_i \in T_i \triangleq [t_i, t_{i+n}]$, for $n = 1, 2, \cdots, N$. Herein, the play operator $\mathcal{P}_r$ is defined by an analytic mathematic function as

$$\mathcal{P}_r[u](0) = p_r(f(0), 0) = 0, \tag{5.1}$$

$$\mathcal{P}_r[u](t) = p_r(f(t), p_r[f](t)), \tag{5.2}$$

with

$$p_r(f(t), p_r[f](t_i)) = \max(f - \gamma, \min(f + \gamma, p_r[f](t_{i-1}))), \tag{5.3}$$

where $f(t) = g_0 u(t) + g_1$ is a linear function of the input $u(t)$, and g_0 and g_1 are constants. In the play operator functions, g_0 represents the DC gain between the input $u(t)$ and the output of the hysteresis behavior. The g_1 determines the offset of the output of the hysteresis behavior relative to the input $u(t)$. The square bracket of the operator ($\mathcal{P}_r[\cdot]$) means that the operator is dependent on the input function. The γ in Eq. 5.3 is called threshold of the play operator, which is defined as $\gamma = \rho j$ with ρ being a constant and $j = 1, 2, 3, ...$ being the number of the operators. The threshold γ determines the width of the play operator curves though deciding where the operator should be turned on, which means the play operator curve is wider when the value of the γ is larger. Therefore, when ρ is a constant and $j = 1, 2, ..., n$ and $n > 1$, with different γ the operator maps the input to output in different curves as shown in Fig. 5.1(a), and the number of γ will affect the smoothness and the shape of the hysteresis curve created by this P-I model. The effect of the number of the γ

on the smoothness and shape of the hysteresis curve is shown in Fig. 5.2.

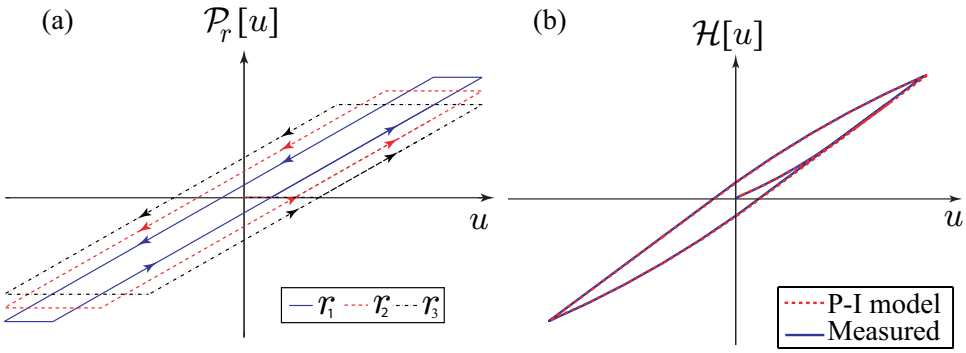

Figure 5.1: (a) The play operator with threshold γ. (b) The output of the Prandtl-Ishlinskii hysteresis model for a piezoactuator *v.s.* the measured hysteresis.

From Fig. 5.1(a), it can be seen the play operator generates the main blocks of the hysteresis curve. In order to form the hysteresis curve shown in Fig. 5.1(b), these operators are firstly superposed through the weighted integral of the play operators:

$$\int_0^R d(\gamma)\mathcal{P}_r[u](t)d\gamma,$$

where the weight $d(\gamma)$ is called the density function, which is added to affect the shape and the size of the curve of the superposition of the operators. This weighted integral transfers the main blocks formed by play operators to the curve feature of hysteresis as shown in Fig. 5.2. The Figure shows that when integrating one P-I operator, one of the main block of the hysteresis curve is formed. However, when more operators are integrated, the curve feature of hysteresis can be formed. Then by adding the weighted integral of the play operator to the linear function of input $f(t)$ as shown in the following equation:

$$v(t) \quad = \quad \mathcal{H}[u](t) \triangleq f(t) + \int_0^R d(\gamma)\mathcal{P}_r[u](t)d\gamma, \tag{5.4}$$

the hysteresis curve of the piezo-based nanopositioner is generated. Compared to the Preisach hysteresis model, the P-I model is less computationally demanding to implement and invert for feedforward control. An example hysteresis curve generated from the P-I model for a piezoactuator is shown in Fig. 5.1(b).

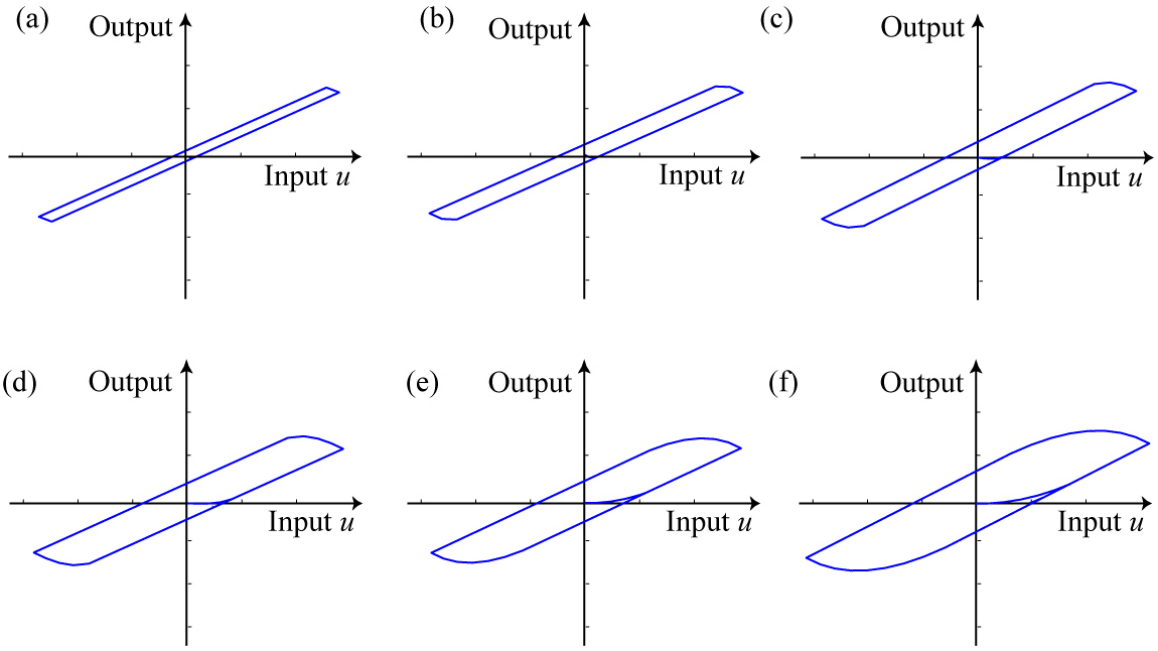

Figure 5.2: The effect of the number of the γ on the smoothness and the shape of the hysteresis curve. Integral result of (a) one play operator, (b) two play operators, (c) three play operators, (d) four play operators, (e) six play operators, and (f) eight play operators.

The discrete-time version of the continuous-time hysteresis model in Eq. (5.4) can be expressed as [172]

$$v(k) \;=\; \mathcal{H}[u](k) \triangleq f(k) + \sum_{j=1}^{n} d(\gamma)\mathcal{P}_r[u](k), \tag{5.5}$$

where $f(k) = g_0 u(k) + g_1$, k is the time step, and n denotes the number of play operators.

5.2 An Inverse Prandtl-Ishlinskii Hysteresis Compensator

A new inverse Prandtl-Ishlinskii model is developed here to handle the hysteresis nonlinearity for RC design. This hysteresis compensator takes the same structure as the forward P-I model. The characteristics of the inverse model is based on the shape of the inverse hysteresis curve, that is, the input versus output curve shown in Fig. 5.3(a) (u versus v plot). Noted that as the output v increases, the input u increases but traverses onto an upper branch of the inverse-hysteresis curve. In contrast, this behavior is opposite to that observed in the hysteresis curve (v versus u plot) where the output climbs up on a lower branch as shown in Fig. 5.1(b). Therefore, a candidate new play-type operator for the inverse-hysteresis model is chosen as shown in Fig. 5.3(b). Figure 5.4 compares the time responses between the desired output (solid line), output from a hysteretic system (dash-dot line), and the output from the proposed inverse-hysteresis model (dash line). Using this new operator offers the advantage that the structure of the forward model can be used directly to map the desired output to the hysteresis-compensating feedforward input. In other words, the P-I output equation (5.4) becomes the inverse map simply by setting the output equal to the input and vice versa.

The inverse hysteresis model takes the following form:

$$\mathcal{H}^{-1}[v](t) \triangleq f(t) + \int_0^R -d(\gamma)\mathcal{P}_r[u](t)d\gamma. \tag{5.6}$$

The input-output response for the inverse model shown in Fig. 5.3(a) is a reflection of Fig. 5.1(b) about the axis $u = v$. Therefore, the inverse operator shown in Fig. 5.3(b)

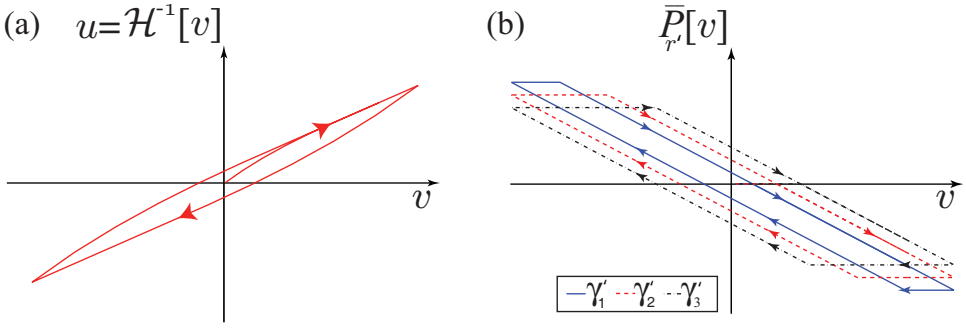

Figure 5.3: (a) Input versus measured output plot. b) A play-type operator for the inverse model with threshold γ_i'.

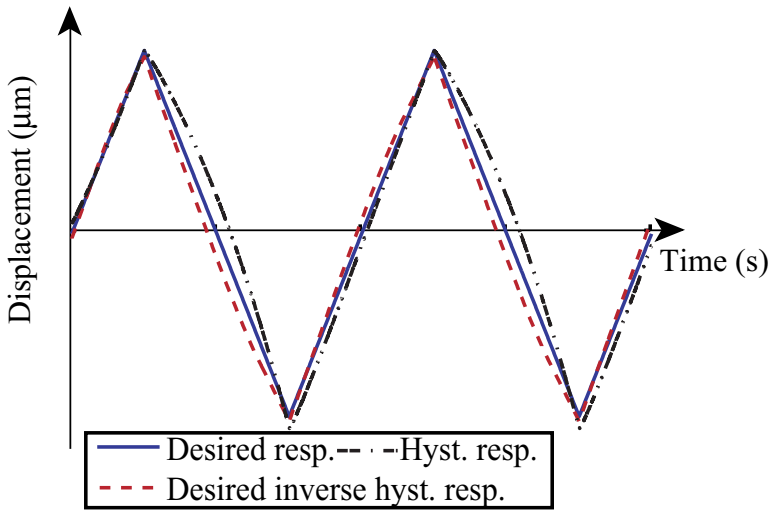

Figure 5.4: Comparison between the hysteresis response (dot-dash line), the desired inverse hysteresis response (dash line) and the desired response.

is defined as

$$\begin{aligned} \overline{P}_{r'}[v](0) &= \overline{p}_{r'}(h(0),0) = 0, \\ \overline{P}_{r'}[v](t) &= \overline{p}_{r'}(h(t), \overline{P}_{r'}[h](t)), \end{aligned} \tag{5.7}$$

with

$$\overline{p}_{r'}(h(t_i), \overline{P}_{r'}[h](t_i)) = \max(-h(t_i) - \gamma', \min(-h(t_i) + \gamma', \overline{P}_{r'}[h](t_{i-1}))), \tag{5.8}$$

where $h(t) = g_0' v(t) + g_1'$ with constants g_0' and g_1', and $v(t)$ is the output of the hysteresis behavior. γ' denotes the threshold of the inverse play operator, which has a representation of $\gamma' = \rho' j$ with ρ' a constant, $j = 1, 2, 3, ...$ Then the output of the inverse hysteresis model is given by

$$\mathcal{H}^{-1}[v](t) \triangleq h(t) + \int_0^R d_{inv}(\gamma') \overline{P}_{r'}[v](t) d\gamma', \tag{5.9}$$

where $d_{inv}(\gamma')$ is the density function of the inverse P-I model. For convenience, the parameters $[g_0',\ g_1',\ \gamma',\ d_{inv}(\gamma')]$ of the inverse P-I model share the same concept as the parameters in the forward P-I model. For the digital implementation of the compensator, the discrete-time version of the continuous-time compensator (5.9) is

$$\mathcal{H}^{-1}[v](k) \triangleq h(k) + \sum_{j=1}^{n} d_{inv}(\gamma') \overline{P}_{r'}[v](k), \tag{5.10}$$

where $h(k) = g_0' u(k) + g_1'$, k is the time step, and n denotes the number of inverse play operators.

5.3 Summary

This chapter introduced the Prandtl-Ishlinskii hysteresis model and an inverse model. In the following chapters, the P-I model will be used as a tool to represent the hysteresis behavior to analyze the effect of hysteresis on closed-loop system stability.

Chapter 6

Repetitive Control for Hysteretic Systems: Theory

In this chapter, an analysis on the effect of hysteresis on closed-loop RC system stability is presented. In this analysis, the Prandtl-Ishlinskii hysteresis model is used to characterize the nonlinear behavior of a piezo positioner. Using this model and the Small Gain Theorem, the effect of the hysteresis on the closed-loop system stability is quantified.

6.1 Stability of RC for Hysteretic Systems

6.1.1 Past Works and Challenges

The major challenges for RC design are the stability and good steady-state tracking performance, especially for a system that exhibits hysteresis behavior. Many efforts have been made to linearize piezoactuator systems for RC implementation rather than quantifying the effect of hysteresis on the RC system. The schemes include using feed-forward hysteresis compensators, for example Prandtl-Ishlinskii model [173] or Dahl model [162] based compensator; and using internal feedback linearization loop, such as an internal PID [143] or a pole-zero cancelation system [174]. However, because the hysteresis phenomenon is so prevalent, it is important to predict its effect on the RC

system. There have been research efforts to formulate the stability of the closed-loop system with hysteresis and the stability of RC system with certain nonlinearities. It has been shown that a stability formulation for a linear control system with Preisach hysteretic nonlinearity was studied in [175], where the passivity theorem was applied to a feedback hysteresis system to analyze the stability. This study provided an approach for analyzing the stability of a closed-loop system where the hysteresis can be defined as a bounded passive operator, but no applicable stability conditions were generated. Likewise, a framework for the $\mathcal{L}_2$ stability of systems, containing a class of passive hysteresis, was given in [176] without quantifying the effect of the *size* of hysteresis on closed-loop system. Other recent works, for example the works in [177], studied the stability of an adaptive control of a class of nonlinear system preceded by Pranditl-Ishlinskii hysteresis nonlinearities. In the study, the Prandtl-Ishlinskii model was fused with an adaptive controller design to mitigate the effects of the hysteresis without an inverse hysteresis compensator, and a control law was achieved to ensure the global stability of the adaptive control system using Lyapunov stability theory and adaptation laws. This stability analysis approach was specified for adaptive controller design. On the topic of RC for nonlinear systems, there has been limited researches [158–161]. Most of the work was on robust analysis and tracking error convergence and is not applicable to systems with hysteresis nonlinearities. In light of the previous work, this dissertation addresses the RC design for hysteretic systems, such as piezoactuators, and quantification of the effect of hysteresis on RC stability. The $\mathcal{L}_2$ stability of the system is certified using the Small-Gain Theorem and the properties of the input-output stability. The main stability theorem leads to an applicable bound on the *size* of the hysteresis to guarantee the stability of the RC system.

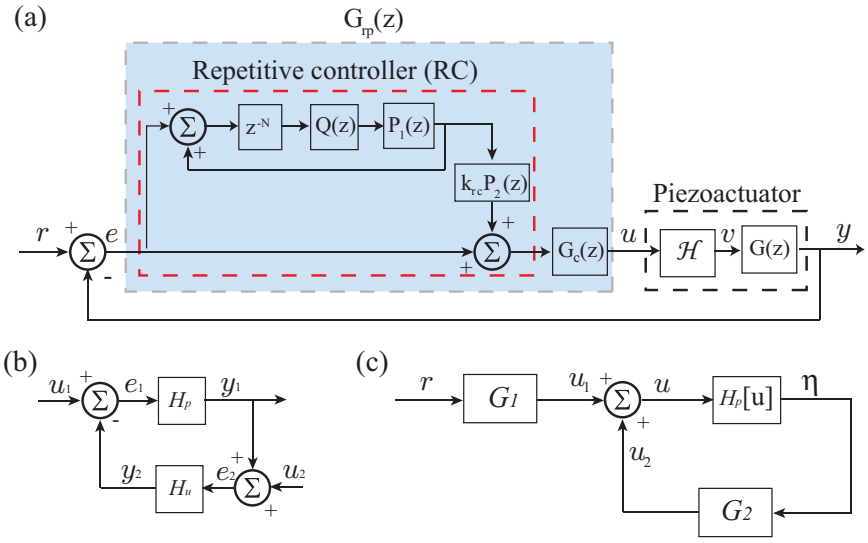

Figure 6.1: (a) The nonlinear RC system, where $G_{rp}(z)$ represents the RC and PID controllers. (b) The feedback connection for stability analysis and application of the Small-Gain Theorem. (c) An equivalent feedback connection of (a) for stability analysis.

6.1.2 Outline of Analysis

The effect of hysteresis on the RC system is analyzed by applying the following steps:

1. The nonlinear control system in Fig. 6.1(a) is converted to the feedback connection shown in Fig. 6.1(b), where H_p and H_u represent the perturbed (hysteretic system) and unperturbed (RC system without hysteresis) dynamics, respectively.

2. The perturbed and unperturbed dynamics are shown to be stable in the finite-gain $\mathcal{L}_2$ sense [178].

3. Based on the finite $\mathcal{L}_2$ gains for the perturbed and unperturbed dynamics, the Small-Gain Theorem is applied to determine stability conditions for the nonlinear RC system. This final step quantifies bounds on the hysteresis nonlinearity in terms of the P-I model parameters for a stable RC.

6.1.3 The Effect of Hysteresis on RC Stability

Step 1: Consider the linear discrete-time SISO dynamic system $G(z)$ with the following controllable canonical form

$$\begin{aligned} \mathbf{x}(k+1) &= \mathbf{A}\mathbf{x}(k) + \mathbf{B}v(k), \\ y(k) &= \mathbf{C}\mathbf{x}(k) + Dv(k), \end{aligned} \tag{6.1}$$

where $\mathbf{x} = [x_1, x_2, .., x_n]^T \in \mathbb{R}^n$ is the state vector, $v, y \in \mathbb{R}$ are the input and output, respectively, and $\mathbf{A}$, $\mathbf{B}$, $\mathbf{C}$, D are of compatible dimensions. The RC controller and the controller $G_c(z)$ shown in Fig. 6.1(a) are lumped into $G_{rp}(z)$, and it is assumed to have the following discrete-time state-space representation:

$$\begin{aligned} \mathbf{z}(k+1) &= \mathbf{A}_{rp}\mathbf{z}(k) + \mathbf{B}_{rp}e(k), \\ u(k) &= \mathbf{C}_{rp}\mathbf{z}(k) + D_{rp}e(k), \end{aligned} \tag{6.2}$$

where $\mathbf{z} = [z_1, z_2, .., z_p]^T \in \mathbb{R}^p$ is the controller state vector, $e = r - y \in \mathbb{R}$ is the tracking error, $u \in \mathbb{R}$ is the controller output, and $\mathbf{A}_{rp}$, $\mathbf{B}_{rp}$, $\mathbf{C}_{rp}$, and D_{rp} are of compatible dimensions.

Next, the system in Fig. 6.1(a) is converted to an equivalent feedback connection depicted in Fig. 6.1(b) for stability analysis. To do this, the perturbed system H_p is defined as

$$\eta(k) = H_p[u](k) \triangleq v(k) - g_0 u(k), \tag{6.3}$$

where $v(k)$ is the output of the discrete-time P-I model defined by Eq. (5.5), $u(k)$ is the output of the controller (6.2), and g_0 is a constants as used in Eq. (5.5).

The unperturbed system H_u is defined as follows. First, solving for $v(k)$ in

Eq. (6.3) and substituting it into Eq. (6.1), the following system is obtained

$$\begin{aligned} \mathbf{x}(k+1) &= \mathbf{A}\mathbf{x}(k) + \mathbf{B}[\eta(k) + g_0 u(k)], \\ y(k) &= \mathbf{C}\mathbf{x}(k) + D[\eta(k) + g_0 u(k)]. \end{aligned} \tag{6.4}$$

Recalling the expression for $u(k)$, Eq. (6.2), $e(k) = r(k) - y(k)$, and D, D_{rp} are finite scalars, the output $y(k)$ can be written as

$$\begin{aligned} y(k) &= \mathbf{C}\mathbf{x}(k) + D[\eta(k) + g_0 u(k)], \\ &= \frac{1}{1 + g_0 D D_{rp}} \begin{bmatrix} g_0 D\mathbf{C}_{rp} & \mathbf{C} \end{bmatrix} \begin{bmatrix} \mathbf{z}(k) \\ \mathbf{x}(k) \end{bmatrix} \\ &\quad + \frac{D}{1 + g_0 D D_{rp}} [\eta(k) + g_0 D_{rp} r(k)]. \end{aligned} \tag{6.5}$$

Then, using Eq. (6.2) and (6.5), the system's closed-loop dynamics excluding hysteresis can be represented as an unperturbed system H_u, *i.e.*,

$$\begin{aligned} \begin{bmatrix} \mathbf{z}(k+1) \\ \mathbf{x}(k+1) \end{bmatrix} &= \mathbf{A}_L \begin{bmatrix} \mathbf{z}(k) \\ \mathbf{x}(k) \end{bmatrix} + \mathbf{B}_1 r(k) + \mathbf{B}_2 \eta(k), \\ u(k) &= \mathbf{C}_L \begin{bmatrix} \mathbf{z}(k) \\ \mathbf{x}(k) \end{bmatrix} + D_1 r(k) + D_2 \eta(k), \end{aligned} \tag{6.6}$$

where $\mathbf{A}_L = \begin{bmatrix} \mathbf{A}_{rp} - \frac{g_0 \mathbf{B}_{rp} D \mathbf{C}_{rp}}{1 + g_0 D D_{rp}} & -\frac{\mathbf{B}_{rp}\mathbf{C}}{1 + g_0 D D_{rp}} \\ \frac{g_0 \mathbf{B}\mathbf{C}_{rp}}{1 + g_0 D D_{rp}} & \mathbf{A} - \frac{g_0 \mathbf{B} D_{rp} \mathbf{C}}{1 + g_0 D D_{rp}} \end{bmatrix}$;

$\mathbf{B}_1 = \begin{bmatrix} \frac{\mathbf{B}_{rp}}{1 + g_0 D D_{rp}} \\ \frac{g_0 \mathbf{B} D_{rp}}{1 + g_0 D D_{rp}} \end{bmatrix}$; $\mathbf{B}_2 = \begin{bmatrix} \frac{-\mathbf{B}_{rp} D}{1 + g_0 D D_{rp}} \\ \frac{\mathbf{B}}{1 + g_0 D D_{rp}} \end{bmatrix}$;

$$\mathbf{C}_L = \left[\frac{\mathbf{C}_{rp}}{1+g_0 DD_{rp}} \qquad -\frac{D_{rp}\mathbf{C}}{1+g_0 DD_{rp}} \right];$$

$$D_1 = \frac{D_{rp}}{1+g_0 DD_{rp}}; \qquad D_2 = \frac{-DD_{rp}}{1+g_0 DD_{rp}}.$$

The transfer relation for the unperturbed dynamics H_u from inputs $r(k)$ and $\eta(k)$ to output $u(k)$ can be represented in the following input/output form:

$$\begin{aligned} U(z) &= [\mathbf{C}_L(zI - \mathbf{A}_L)^{-1}\mathbf{B}_1 + D_1]R(z) + [\mathbf{C}_L(zI - \mathbf{A}_L)^{-1}\mathbf{B}_2 + D_2]\eta(z), \\ &= G_1(z)R(z) + G_2(z)\eta(z). \end{aligned} \tag{6.7}$$

Therefore, the nonlinear RC system in Fig. 6.1(a) is converted to the equivalent structure shown in Fig. 6.1(c), which is associated with Eq. (6.3) (perturbed system H_p) and Eq. (6.7) (unperturbed system H_u).

Step 2: In the following, the finite-gain $\mathcal{L}_2$ stability of the unperturbed (H_u) and perturbed (H_p) dynamics is shown. To do so, it is required to show that (a) $G_1(z)$ is BIBO stable; (b) $G_2(z)$ is finite-gain $\mathcal{L}_2$ stable; and (c) H_p is finite-gain $\mathcal{L}_2$ stable.

(a) First, the RC closed-loop linear system in Fig. 3.1(a) is assumed to be designed internally stable where the closed-loop poles are located in the open unit disc. By inspection when $g_0 = 1$, $G_1(z) = G_L(z)$, where

$$G_L(z) \;=\; \frac{U(z)}{R(z)} \;=\; \mathbf{C}_L(zI - \mathbf{A}_L)^{-1}\mathbf{B}_1 + D_1,$$

and $G_L(z)$ is the transfer relation between the reference $R(z)$ and the controller output $U(z)$ of the RC closed-loop linear system in Fig. 3.1(a). Therefore with the closed-loop linear system in Fig. 3.1(a) designed stable, $G_1(z)$ is BIBO stable, that

is $g_0 \leq M_{G_L}$, where M_{G_L} represents the gain margin of the RC system in Fig. 3.1(a). Then what is left to show is the nonlinear system in Fig. 6.1(a) is stable if the finite gains of $G_2(z)$ and $H_p[u](k)$ satisfy the Small-Gain Theorem [178].

(b) Let $||h||_2$ represent the $\mathcal{L}_2$-norm of a discrete-time function $h(k)$, *i.e.*,

$$||h||_2 \;=\; \left(\sum_{k=0}^{\infty} |h(k)|^2\right)^{1/2}.$$

The finite $\mathcal{L}_2$ gain of $G_2(z)$ in Fig. 6.1(c) is determined using Parseval's theorem [178, 179]. Specifically,

$$\begin{aligned}
\|u_2\|_2^2 &= \sum_{k=0}^{\infty} u_2^T(k)u_2(k), \\
&= \frac{1}{2\pi j}\oint_C z^{-1}U_2(-z)U_2(z)dz, \\
&= \frac{1}{2\pi j}\oint_C z^{-1}\eta(-z)G_2^T(-z)G_2(z)\eta(z)dz, \\
&\leq \left(\sup_{\omega\in\mathbb{S}}\|G_2(z)\|_2\right)^2 \frac{1}{2\pi j}\oint_C z^{-1}\eta(-z)\eta(z)dz, \\
&\leq \left(\sup_{\omega\in\mathbb{S}}\|G_2(z)\|_2\right)^2 \|\eta\|_2^2, \qquad (6.8)
\end{aligned}$$

where $z = e^{j\omega T_s}$, $\mathbb{S} \subset (0, \pi/T_s)$ and C is a contour. Thus, the $\mathcal{L}_2$-gain of $G_2(z)$ is

$$\lambda_1 \;\leq\; \sup_{\omega\in\mathbb{S}}\|G_2(z)\|_2. \qquad (6.9)$$

In other words, the unperturbed system H_u [Eq. (6.7)] is finite-gain $\mathcal{L}_2$ stable provided that

$$\sup_{\omega\in\mathbb{S}}\|G_2(z)\|_2 \;<\; \infty$$

and

$$g_0 \;\leq\; M_{G_L}. \tag{6.10}$$

(c) The finite $\mathcal{L}_2$ gain for the perturbed system H_p is determined as follows. First, Eq. (6.3) is rewritten as

$$\begin{aligned} \eta(k) &= \mathcal{H}[u](k) - g_0 u(k), \\ &= f(k) + \sum_{j=1}^{n} d(\gamma)\mathcal{P}_r[u](k) - g_0 u(k), \end{aligned} \tag{6.11}$$

where $u(k)$ is piecewise continuous function in k. It is pointed out that the P-I hysteresis model $\mathcal{H}[u]$ is continuous in u [163, 172]; therefore, the perturbed system $H_p[u](k)$ is piecewise continuous in k and continuous in $u(k)$. Next, the output of the perturbed system $\eta(k)$ is shown to be bounded in the following form:

$$||\eta_\tau||_2 \;\leq\; \lambda_2 ||u_\tau||_2 + \alpha, \qquad \forall\; \tau \in [0, \infty),$$

where α is a nonnegative constant [178].

Recall that the play operator has the following form:

$$\mathcal{P}_r[u](k) \;=\; \max(f(k_i) - \gamma, \min(f(k_i) + \gamma, \mathcal{P}_r[f](k_{i-1}))), \qquad \forall\; i \geq 1. \tag{6.12}$$

and the range property of the play operator [163, 172], the play operator of Eq. (6.12) is bounded above and below as

$$f(k) - \gamma \;\leq\; \mathcal{P}_r[u](k) \;\leq\; f(k) + \gamma,$$

hence

$$|\mathcal{P}_r[u](k)| \;\leq\; |f(k)| + |\gamma|$$

and

$$\begin{aligned}\left|\sum_{j=1}^{n} d(\gamma)\mathcal{P}_r[u](k)\right| &\leq \sum_{j=1}^{n} |d(\gamma)||\mathcal{P}_r[u](k)| \\ &\leq \sum_{j=1}^{n} |d(\gamma)||f(k)| + \sum_{j=1}^{n} |d(\gamma)\gamma|. \end{aligned} \tag{6.13}$$

With $f(k) = g_0 u(k) + g_1$,

$$\begin{aligned}\left|\sum_{j=1}^{n} d(\gamma)\mathcal{P}_r[u](k)\right| &\leq \sum_{j=1}^{n} |d(\gamma)||f(k)| + \sum_{j=1}^{n} |d(\gamma)\gamma| \\ &\leq \sum_{j=1}^{n} |d(\gamma)||g_0 u(k)| + \sum_{j=1}^{n} |d(\gamma)|(|g_1| + |\gamma|).\end{aligned}$$

By the Minkowski inequality [180], Eq. (6.11) is bounded as follows

$$\begin{aligned}\|\eta(k)\|_2 &\leq \|\sum_{j=1}^{n} d(\gamma) g_0 u(k)\|_2 + \|\sum_{j=1}^{n} |d(\gamma)|(|g_1| + |r|) + g_1\|_2 \\ &\leq \left(|g_0| \sup_{1\leq j\leq n} \|d(\gamma)\|_1\right) \|u(k)\|_2 + \alpha, \end{aligned} \tag{6.14}$$

where $\alpha = \left\|\sum_{j=1}^{n} |d(\gamma)|(|g_1| + |r|) + g_1\right\|_2$ is a nonnegative constant. Therefore, the finite gain for the perturbed system H_p such that it is $\mathcal{L}_2$ stable is

$$\lambda_2 \;\leq\; |g_0| \sup_{1\leq j\leq n} \|d(\gamma)\|_1, \tag{6.15}$$

where $\|\cdot\|_1$ is the $\mathcal{L}_1$ norm. The finite gain λ_2 is proportional to the size of the P-I model's density function.

Step 3: Finally, according to the Small-Gain Theorem, the nonlinear RC system is finite-gain $\mathcal{L}_2$ stable if $\lambda_1\lambda_2 < 1$, hence the nonlinear closed-loop RC system is input-output stable provided that $g_0 \leq M_{G_L}$ [Eq. (6.10)] and

$$\sup_{1\leq j\leq n} \|d(\gamma)\|_1 \quad < \quad \frac{1}{|g_0| \sup_{\omega\in\mathbb{S}} \|G_2(z)\|_2}. \tag{6.16}$$

As long as the conditions given by Eq. (6.16) and (6.10) are satisfied, the RC system is stable. In addition, Eq. (6.16) also bounds the size of the hysteresis nonlinearity for a stable RC.

6.2 Summary

In summary, this chapter discussed the stability analysis for the closed-loop RC system containing hysteresis. The analysis exploited the properties of the Prandtl-Ishlinskii hysteresis model and the Small Gain Theorem. A bound on the hysteresis behavior for RC stability was quantified. Next, the developed stability conditions are experimentally validated.

Chapter 7

Experimental Tracking Results and Discussion

This chapter discusses the evaluation of the repetitive control method and the stability conditions developed in the previous chapters. Experiments were performed on a custom designed high-speed piezo-based nanopositioner. The first section describes the experimental nanopositioning system, followed by a discussion on the modeling of the dynamics and the hysteresis behavior. This modeling process also includes the parameter optimization for an inverse hysteresis compensator. Afterwards, the repetitive control is designed based on the linear dynamics. Then, the developed stability conditions are validated. Finally, simulation and experimental results are presented.

7.1 Experimental Nanopositioning Systems

The control approach was evaluated on a custom-made nanopositioning system. The experimental setup is shown in Fig. 7.3, which includes a piezo amplifier, an analog PID control circuit, an FPGA system for implementing the controllers (on the fast-scanning direction, x-axis, of the nanopositioner), and a desktop computer with a data acquisition hardware (NI-PCI-6221, 16-bit resolution, maximum sampling frequency of 250 kHz) for sending and collecting data. The nanopositioning system is a custom-

design two-axes serial-kinematic nanopositioner [see Fig. 7.2(a)].

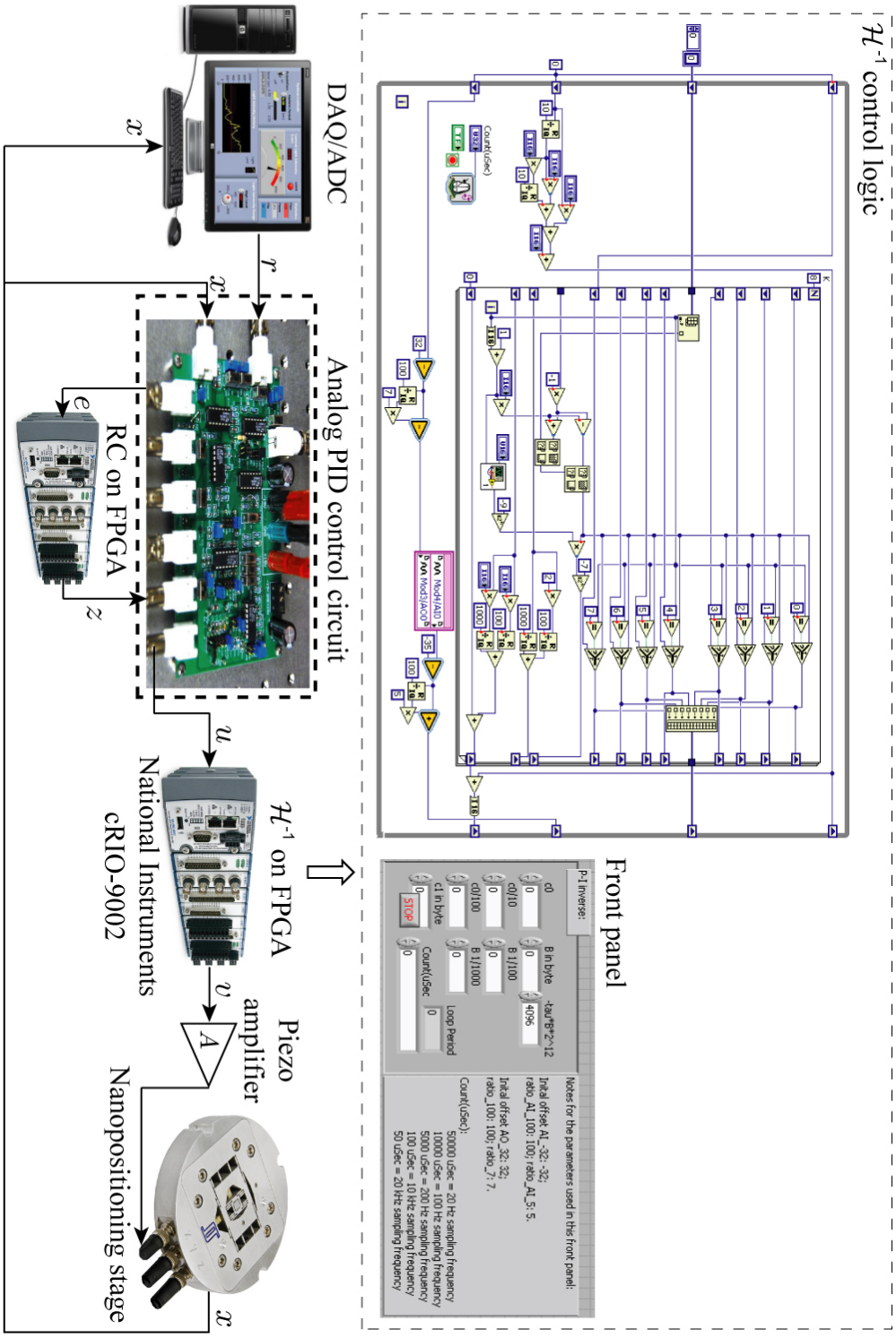

Figure 7.1: The experimental system configuration.

The experimental nanopositioning stage is created specifically for scanning-type applications [181]. For scanning-type applications, such as the rastering movements in AFM imaging, one lateral axis moves much faster (>100-times) than the other axis. Because of this, one axis is designed to have a significantly higher mechanical resonance [142,182]. The lateral range of the positioner is approximately 10×10 μm. Figure 7.2(a) is a photograph of the nanopositioner, where plate-stack piezoactuators ($5 \times 5 \times 10$ mm Noliac SCMAP07) are used to drive the sample platform in x and y directions with a nearly unlimited resolution, and the lateral displacement of the platform is measured by inductive sensors (Kaman SMU9000-15N) with a resolution smaller than 0.5 nm and a bandwidth of 10 kHz. The resonance frequency in the x-axis is about 18 kHz since its small size and low mass, and it is just 4.7 kHz for y-axis because of the larger size and mass. The x-axis is the fast scanning axis because the probe tip moves back and forth at least 100 times faster than the up and down motion in the y-direction during imaging. The PI, RC and $\mathcal{H}^{-1}$ controllers are applied to the fast scanning axis.

The analog PID circuit is custom-designed for PI control in this experiment. The main functions of the circuit include: (1) the sensor output process, (2) tracking error generation and (3) PID control. The sensor output process function is used to filter the noise, amplify and bias the sensor output. The tracking error generator takes the reference signal $r(t)$ to subtract the sensor output $y(t)$ to generate tracking error $e(t)$. The PID control function allows P, I, PI, or PID control.

The FPGA system is from National Instruments for RC and $\mathcal{H}^{-1}$ implementation. This FPGA system is combined by a real-time controller (cRIO-9002 controller) and plug-in AI (Analog Input) and AO (Analog Output) modules. The cRIO-9002 controller contains a FPGA module and is used to store and implement controller VHDL codes. The AI/AO modules are used for data acquisition with a maximum sampling

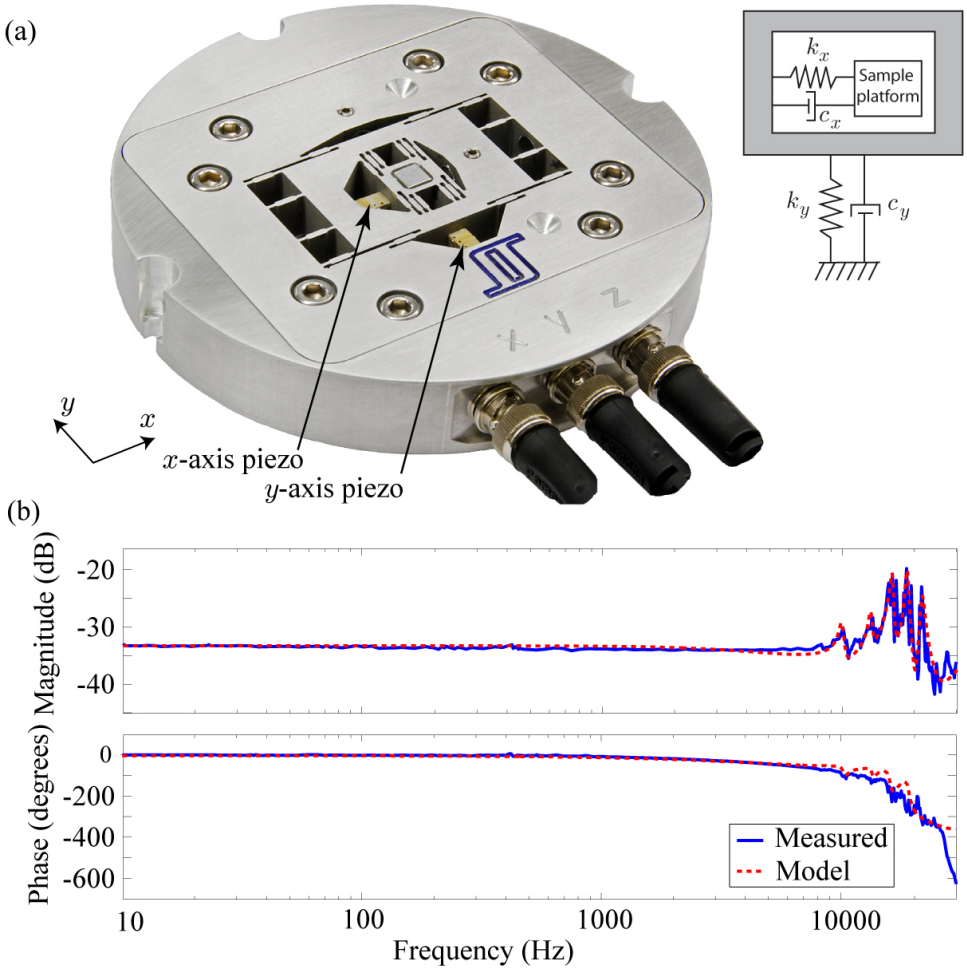

Figure 7.2: (a) Custom-made experimental serial-kinematic piezo-based nanopositioner. (b) The frequency response along the x-direction, where the solid-line is the measured frequency response of the x-direction piezoactuator, and the dash-line is the model for the x-direction piezoactuator.

(a)

Example PID circuit diagram:

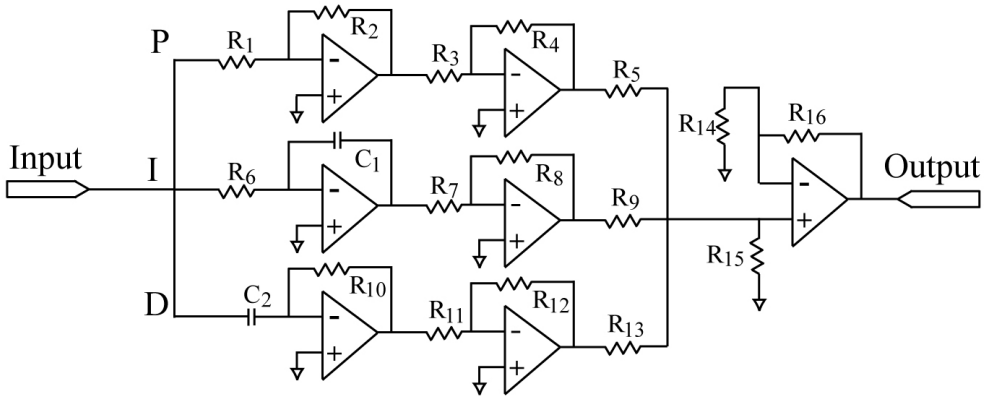

(b)

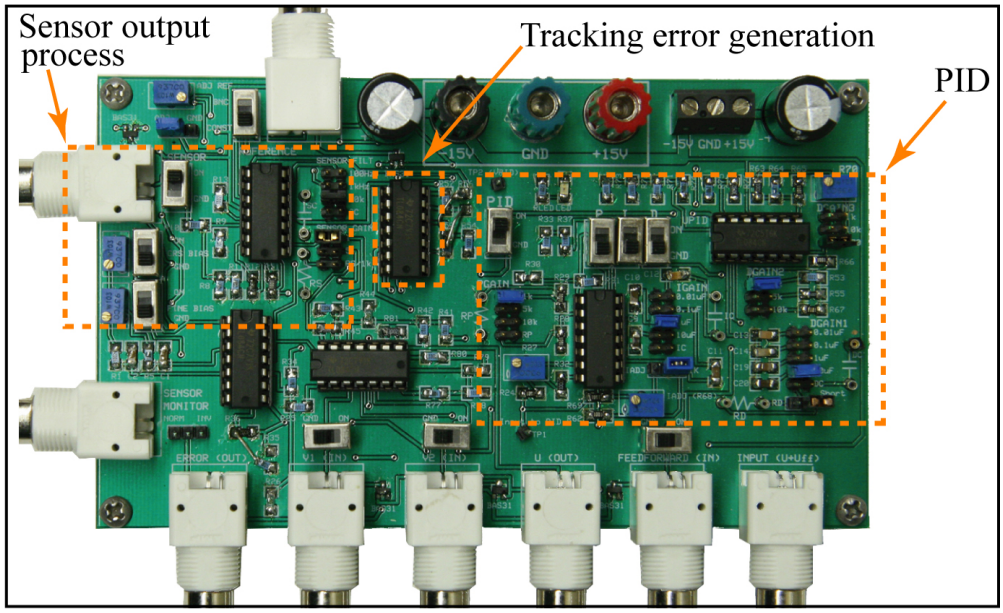

Figure 7.3: (a) An example PID circuit block diagram. (b) A custom designed PID circuit for 1) sensor output process; 2) Tracking error generation [reference *minus* sensor output]; 3) PID control.

frequency of 100 kHz and a resolution of 16-bit. The FPGA system is programmed using NI-LabVIEW FPGA Toolkits. The programming environment is 16 and 32-bit integer mathematics and logics. Toolkits generates VHDL code for controllers, then the code is downloaded to cRIO-9002 through an ethernet cable. The coding and downloading process is presented in Fig. 7.4. In implementation, the controllers are executed independently from computers with a maximum closed-loop sampling

frequency of 100 kHz.

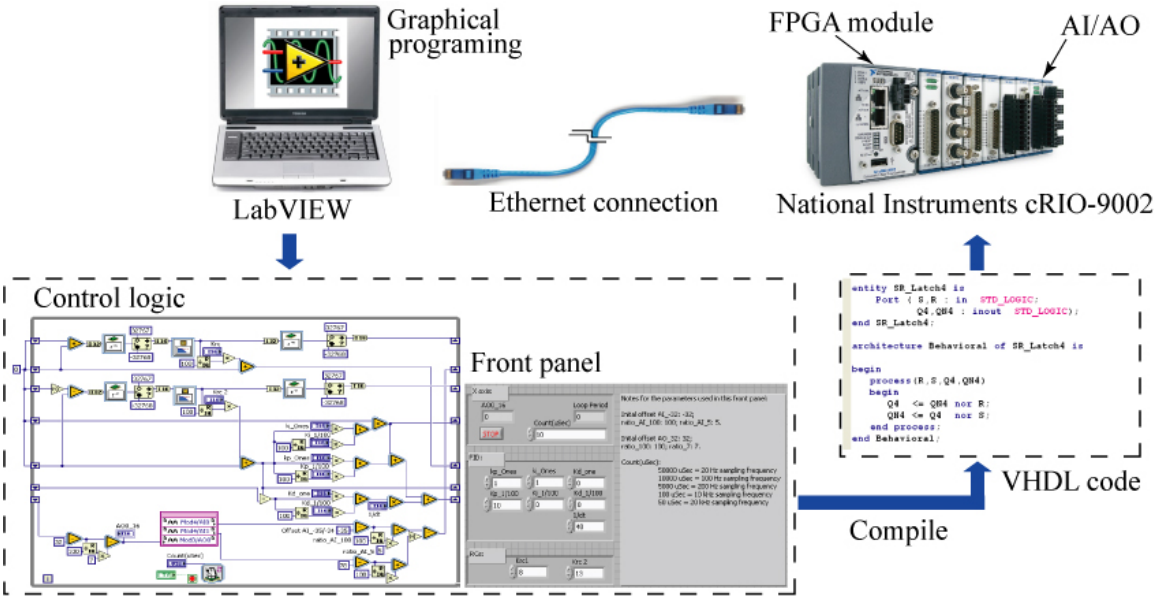

Figure 7.4: The FPGA coding process: the VHDL code is generated using LabVIEW FPGA Toolkit, then downloaded to the real-time controller through an ethernet cable.

7.2 System Modeling

The linear dynamics and hysteresis behavior of the piezoactuator in x-direction of the nanopositioner are modeled respectively for controller design and control system stability analysis.

7.2.1 Linear Dynamics Modeling

A linear dynamic model $G(z)$ is estimated from the measured frequency response, as shown in Fig. 7.2(b). The modeling process is briefly described in Fig. 7.5. The frequency response is measured using a dynamic signal analyzer (DSA) over a small displacement range of the piezoactuator to minimize the hysteresis and above 10 Hz with the creep avoided, since the scanning rate in the experiments is higher than

10 Hz. The measured frequency response is presented in Fig. 7.2(b) as the solid line. A linear 9^{th}-order transfer function model $G(s)$ is developed by curve-fitting method, and then is converted to a discrete-time model $G(z)$ using the $c2d$ command in Matlab with a sampling frequency of 100 kHz. The model is the dashed line shown in Fig. 7.2(b).

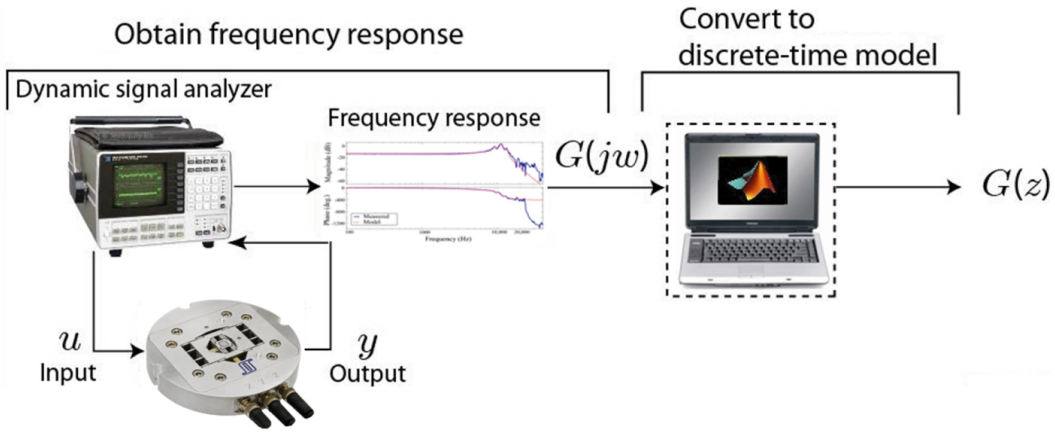

Figure 7.5: Linear dynamics modeling process, which includes (1) obtaining frequency response using dynamic signal analyzer to create the continues-time dynamic model $G(s)$ in Matlab, and (2) converting the continues-time dynamics model to discrete-time model $G(z)$.

7.2.2 Hysteresis Modeling

The hysteresis is modeled using P-I model and curve fitting the measured hysteresis, and the major task is to determine the parameters for the model in Eq. (5.4), such as the real constants g_0 and g_1 for $f(t) = g_0 u(t) + g_1$, and λ, δ, ρ for $d(\gamma) = \lambda e^{-\delta\gamma}$ and $\gamma = \rho j$, $j = 1, 2, \cdots, n$. First, the hysteresis response is measured by driving the piezoactuator to move up to a full range displacement of 10 μm using a triangular trajectory at 1 Hz. The measured response is shown in Fig. 7.6 as the solid line. Then the driving voltage $u(t)$ and the response $y(t)$ are imported to the least-square optimization program for parameters calculation. The process for the parameter

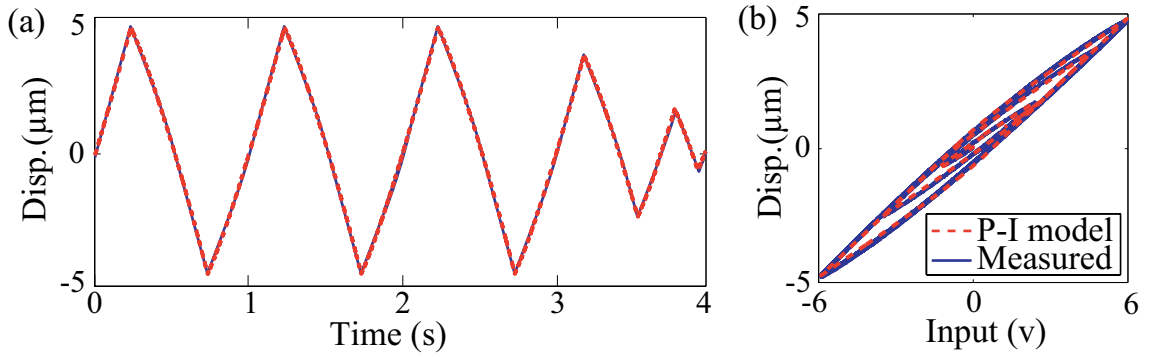

Figure 7.6: Comparison of measured hysteresis behavior and the output of the P-I hysteresis model. (a) The measured and modeled hysteresis behavior in time domain. (b) The hysteresis curves.

calculation is briefly shown in Fig. 7.7. Finally, the parameters of the hysteresis model are optimized to: $g_0 = 0.8331$, $g_1 = 0.0677$, $\lambda = 0.0211$, $\delta = -5.0194$ and $\rho = 0.1079$.

The performance of the P-I model with the optimized parameters is verified by comparing with the measured output in Fig. 7.6. The results show the modeled hysteresis matches the measured output well with maximum error less than 2.1%. The further test on the cascade model (hysteresis + dynamics) of the piezoactuator is done by comparing the open-loop experimental responses with the simulation responses for ± 5 μm rang of motion at 10 Hz, 100 Hz, 1 kHz. The results in Fig. 7.8 show the maximum matching error is less than 2.05% for up to 1 kHz triangular responses [plot (a1) to (c2)]. The accuracy of the cascade model for a 2 kHz sinusoidal scanning motion is shown in Fig. 7.8(d1) and (d2), where the maximum error is less than 2.12%.

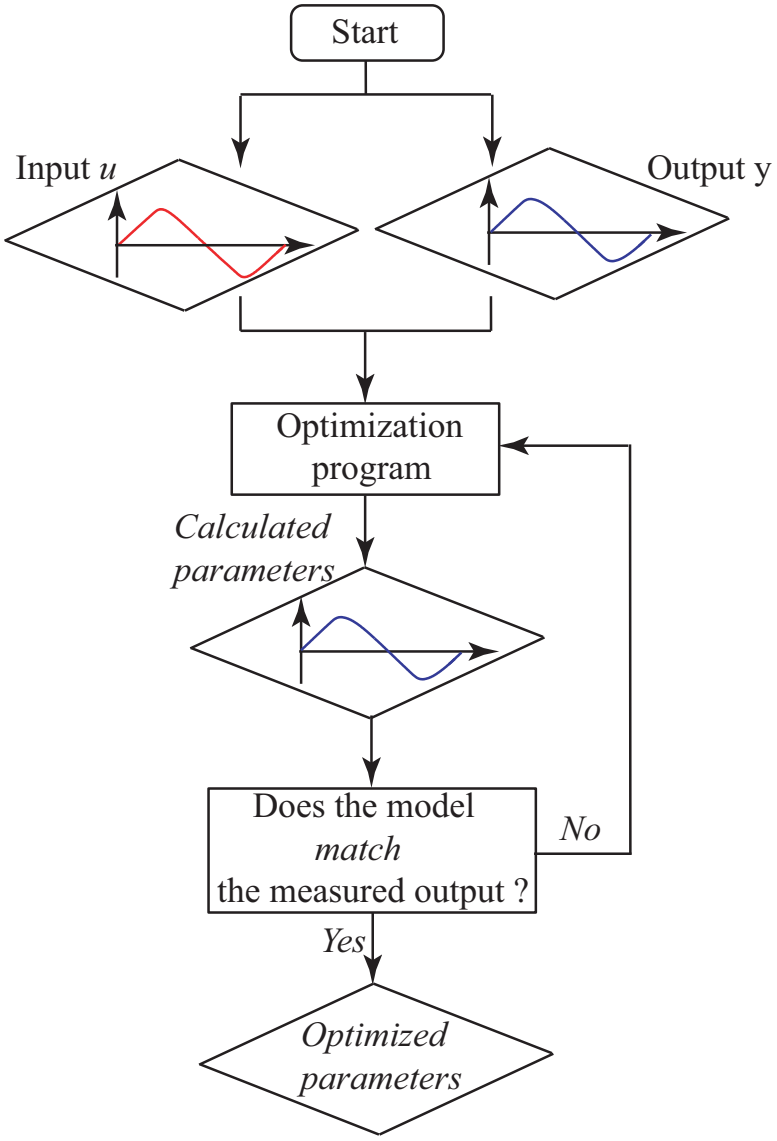

Figure 7.7: The flow diagram for calculating the parameters of the P-I hysteresis model.

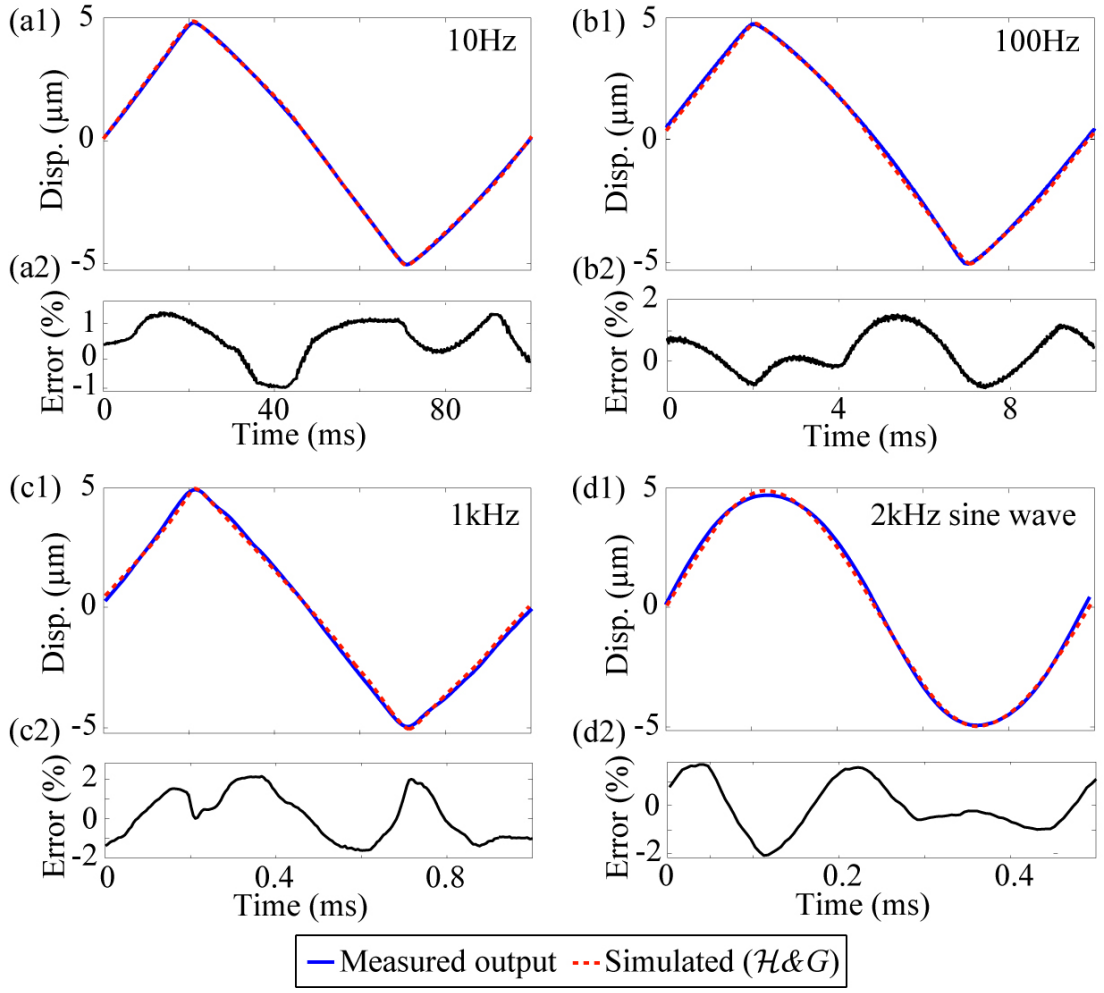

Figure 7.8: Experimental validation of cascade model $[\mathcal{H}[\cdot] + G(z)]$. (a1) and (a2) Displacement and error vs. time between measured (solid line) and model output (dash line) at 10 Hz (triangular trajectory); (b1) and (b2) the comparison for 100 Hz scanning; (c1) and (c2) the comparison for 1 kHz scanning; and (d1) and (d2) the comparison of sinusoidal scanning at 2 kHz.

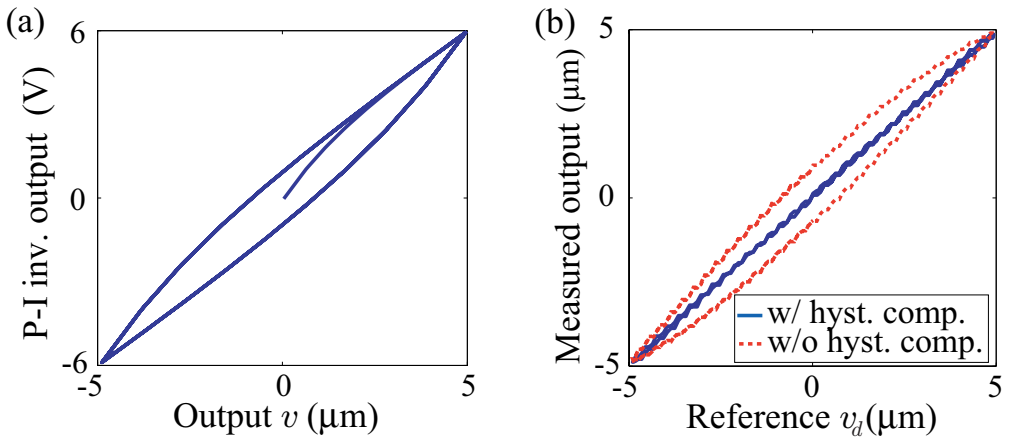

Figure 7.9: (a) Inverse hysteresis model. (b) The hysteresis curves for the piezoactuator with (solid line) and without (dash line) feedforward compensation.

7.3 Inverse Hysteresis Modeling

The parameters of the inverse hysteresis model of Eq. (5.9) is obtained using the measured input-output data from the forward model. For convenience, the density function is chosen as $d_{inv}(\gamma') = \lambda' e^{-\delta'\gamma'}$, where $\gamma' = \rho' j$ is the threshold of the inverse hysteresis operator with $j = 1, 2, \cdots, 8$, and the parameters λ', δ', ρ' are real constants. To determine the value of the parameters for the inverse model, we use measured input-output data as for the hysteresis modeling and a custom modified nonlinear least-square optimization toolbox with the analytic inverse P-I function. Finally the parameters are computed as $g_0' = 1.1354$, $g_1' = -0.3109$, $\lambda' = 0.0211$, $\delta' = -1.813$ and $\rho' = 0.527$.

The performance of $\mathcal{H}^{-1}$ to minimize hysteresis and subsequently linearize the piezoactuator's response is shown in Fig. 7.9(b), where $\mathcal{H}^{-1}$ minimizes the hysteresis curve as shown as the solid line. The compensated response shows that the hysteresis nonlinearity is significantly reduced. To further validate the inverse compensator, the $\mathcal{H}^{-1}$ is applied to the piezoactuator in experiments to compensate the hysteresis behavior over different frequency ranges. By compensating for hysteresis, the output

response is dominated by the dynamic effects $G(z)$ [see Fig. 7.10]. Figure 7.10 shows the measured and simulated outputs versus input plots for a triangular scanning motion at 10 Hz, 100 Hz, 1 kHz and a 2 kHz sinusoidal trajectory. It is pointed out that as the frequency increases, the resulting loop-like appearance is due to the phase shift between the input and output, and not the hysteresis effect. Comparison is made between the measured response and the simulated response from just the dynamics model shows that the maximum error is less than 1.17% and 1.3% for 1 kHz and 2 kHz, respectively. The results show that the hysteresis effect can be compensated for using the proposed inverse model, leaving behind only the dynamics.

7.4 Controller Design and Implementation

In the controller block diagram shown in Fig. 6.1(a), $G_c(s)$ is chosen as a proportional-integral (PI) controller, with transfer function

$$G_c(s) = K_p + \frac{K_i}{s}. \tag{7.1}$$

The gains are tuned using the linear dynamics model to $K_p = 1.3$ and $K_i = 40000$, where Ziegler-Nichols method is used to provide the starting points for tuning the gains. The proportional-integral controller is implemented in both continuous-time domain using the custom-design analog PID circuit (see Fig. 7.3) for experimental implementation, and digitally with a sampling frequency of 100 kHz for RC controller design. The digital controller $G_c(z)$ has a transfer function of

$$G_c(z) = K_p + K_i \frac{T_s z}{z-1}, \tag{7.2}$$

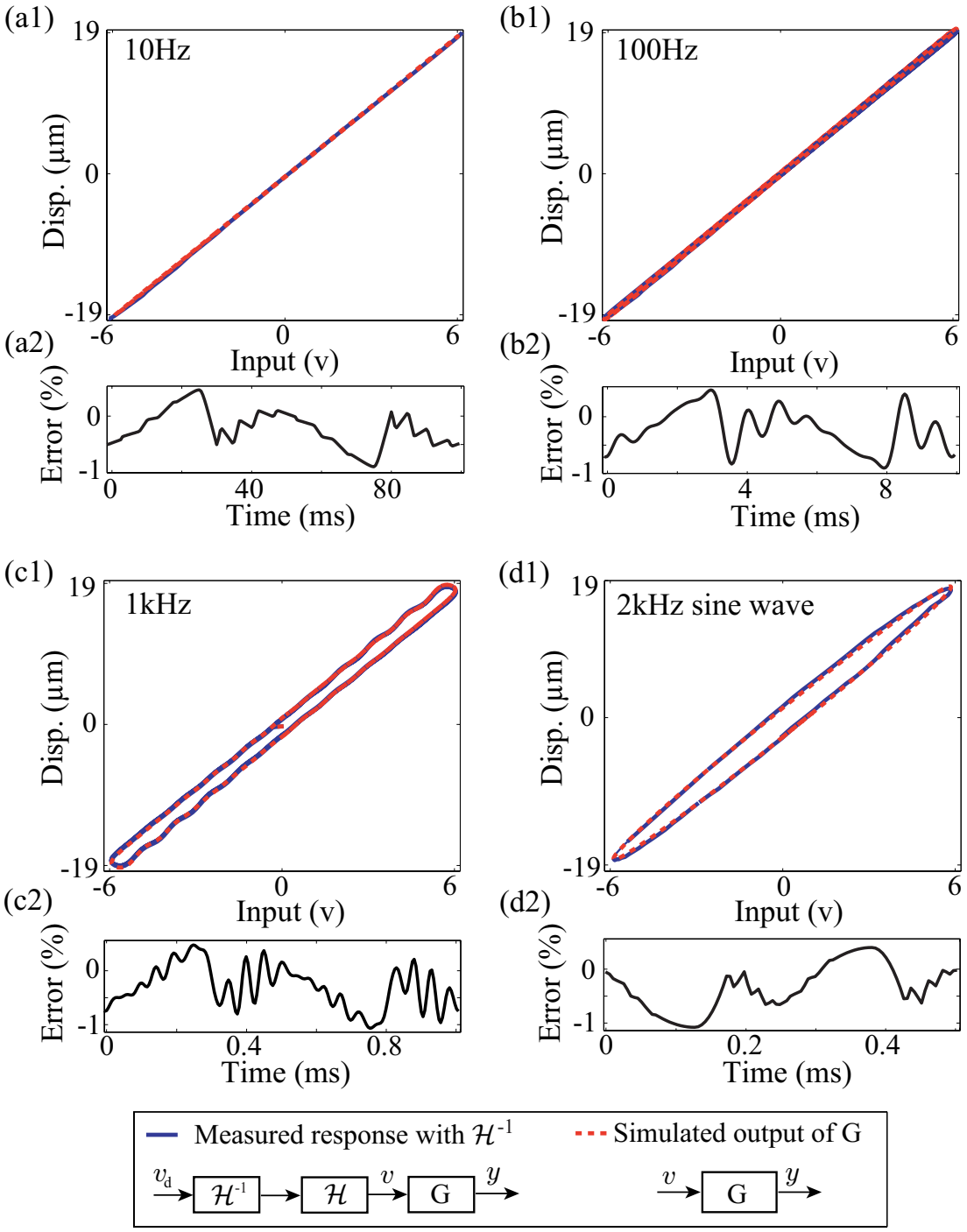

Figure 7.10: Validating cascade model by compensating for hysteresis. Comparison of output vs. input plots and error for: (a1) and (a2) 10 Hz triangular trajectory; (b1) and (b2) 100 Hz triangular trajectory; (c1) and (c2) 1 kHz triangular trajectory; and (d1) and (d2) 2 kHz sinusoidal trajectory.

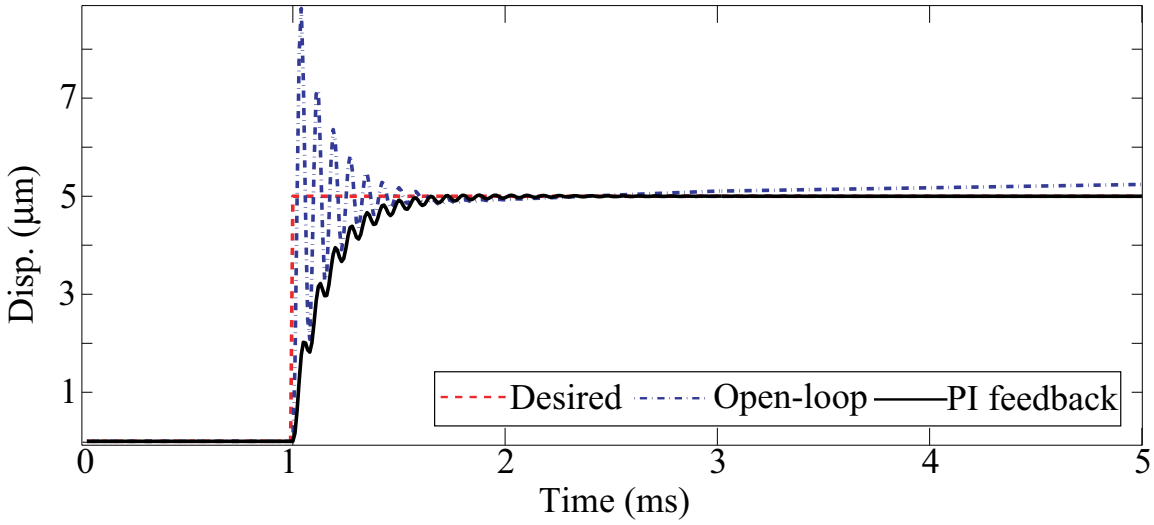

Figure 7.11: Performance of the proportional-integral controller for tracking step response.

and is created by converting the continuous-time controller $G_c(s)$ to the discrete-time domain using Matlab's `c2d` command for RC design with $T_s = 100$ kHz. The performance of the proportional-integral controller to a step reference is shown in Fig. 7.11. It can be observed that without proportional-integral control, the open-loop response shows significant overshoot. Also, after 3 ms creep effect becomes noticeable. Creep is a slow behavior and after several minutes the tracking error can be in excess of 20% [149]. On the other hand, the proportional-integral controller minimized the overshoot and creep effect. The performance of the controller for tracking a triangular trajectory at 10 Hz, 100 Hz, and 1 kHz is validated and presented in Section 7.6.2.

Then RC is designed with $G(z)$ and $G_c(z)$. The block-diagram of the system for RC design is as indicated in Fig. 3.1(a). The process includes designing a low-pass filter $Q(z)$ and phase lead compensator z^{m_2} via m_2 to satisfy the stability conditions in Eqs. (3.3) and (4.4) for stability and robustness; then tuning the RC gain k_{rc} and z^{m_1} for tracking performance and closed-loop stability [Eqs. (3.3)]. The low-pass

filter used in the RC loop is in form of

$$Q(z) = \frac{a}{z+b} \text{ with } |a| + |b| = 1.$$

The selection of the cutoff frequency ω_{ct} is limited by the lowest frequency that makes $\theta_T(\omega) + \theta_2(\omega) = \pm 90^\circ$ [Eq. 4.4] [7]. Also, the cutoff frequency limits the achievable scan rate to about one-tenth of the cutoff frequency, i.e., $\omega_{ct}/10$.

The phase response for $\theta_T(\omega)$ of the closed-loop feedback system without RC and with different phase lead $\theta_2(\omega)$ is in Fig. 7.12. The figure shows, for example, without the phase lead compensator ($m_2 = 0$) the lowest frequency making $\theta_T(\omega) + \theta_2(\omega) = \pm 90^\circ$ is about 7.3 kHz. This value determines the maximum cutoff frequency for the low-pass filter and the maximum scan rate. By considering the maximum scanning rate in this study is 1 kHz and the hardware limitation of the FPGA system, the phase lead compensator is selected as $m_2 = 0$ to have the cutoff frequency to be 7 kHz. It is noted that the scan rate can be improved by increasing the $\pm 90^\circ$ crossover frequency adding phase lead through the parameter m_2. For example, with the addition of phase lead, such as $m_2 = 1$, the $\pm 90^\circ$ crossover frequency is increased to above 30 kHz. Therefore, the cutoff frequency of the low-pass filter can be improved up to above 30 kHz to raise the RC's bandwidth permitting for a scanning rate at 3 kHz or even higher. Subsequently, the RC gain [Eq. (3.3)] can be increased.

Simulations are done to demonstrate the stability condition in Eq. (4.4) and to validate the stability of the closed-loop system with RC for different low-pass filter cutoff frequencies and values of m_2. The validation is achieved through observing: 1) whether the chosen cutoff frequency $\omega_{ct} = 7$ kHz and the phase lead parameter $m_2 = 0$ following the stability condition in Eq. (4.4) can ensure the stability of the closed-loop system; and 2) whether the RC closed-loop system with $m_2 = 0$ and ω_{ct} above the crossover frequency 7.3 kHz becomes unstable. The results regarding to the

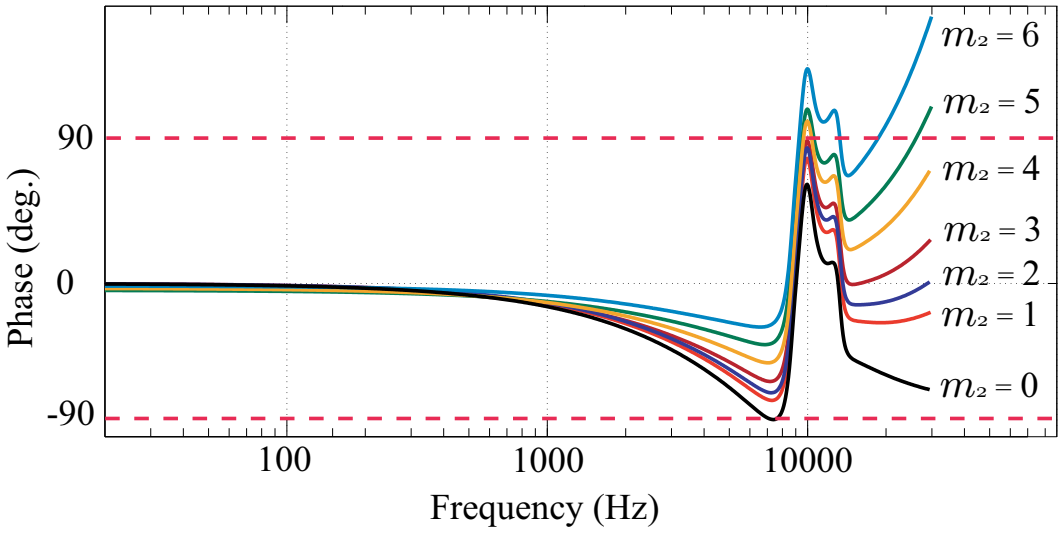

Figure 7.12: Phase response $[\theta_T(\omega)+\theta_2(\omega)]$ of the feedback closed-loop system without RC, with phase lead compensator z^{m_2}

above 2 tasks are summarized in Table 7.1. According to the summary in Table 7.1, when the cutoff frequency is below the crossover frequency of 7.3 kHz with $m_2 = 0$, the closed-loop RC system is stable. As the cutoff frequency increases, for example 8 kHz and above, the RC system is unstable. But the stability can be achieved by adding phase lead through m_2 as shown by the results in Table 7.1.

Table 7.1: Stability of RC system for different low-pass filter cutoff frequencies and phase lead z^{m_2}.

	Low-pass filter $Q(z)$'s cutoff frequency (Hz)				
Phase lead m_2	5 k	7 k	9 k	10 k	30 k
0	Stable	Stable	Unstable	Unstable	Unstable
1	Stable	Stable	Stable	Stable	Stable
3	Stable	Stable	Stable	Stable	Unstable
5	Stable	Stable	Stable	Unstable	Unstable

Next, the RC gain k_{rc} and z^{m_1} are determined in simulation. The chosen cutoff

frequency $\omega_{ct} = 7$ kHz for the low-pass filter $Q(z)$ and zero phase lead ($m_2 = 0$) are used in the RC loop in the simulation. The reference trajectory used is the triangular trajectory at 1 kHz for ± 5 μm range scanning. The RC gain $k_{rc} = 0.8$ is tuned in the rang of Eq. (3.3) by assuming the $m_1 = 0$ for system stability and tracking performance. Example simulated tracking results of RC system with different k_{rc} and with $m_1 = 0$ are shown in Fig. 7.13. The results indicate that increasing the value of k_{rc} can cause instability, as shown in plots (c1) and (c2). Reducing the RC gain, however, slows the convergence rate of the tracking error, which can be observed by comparing the plot (b2) to plot (a2). The steady-state tracking error is minimally affected by the RC gain and the phase lead through m_2.

Finally, the $m_1 = 6$ is tuned with $k_{rc} = 0.8$, $m_2 = 0$, and $\omega_{ct} = 7$ kHz by looking at the maximum tracking error versus different m_1 values for tracking 1 kHz triangular trajectory for 10 μm displacement. The maximum tracking error is defined as:

$$e_{max}(\%) = \frac{\max(|y - r|)}{\max(r) - \min(r)} \times 100\% \tag{7.3}$$

where r and y are the reference and measured outputs, respectively. The e_{max} *v.s.* m_1 plot is shown in Fig. 7.14, where the simulation results are plotted along with experimental results. It can be seen from the results the smallest maximum tracking error is achieved at $m_1 = 6$. Therefore, the parameters for the RC controller are chosen as $m_1 = 6$, $m_2 = 0$, $k_{rc} = 0.8$ and the cutoff frequency of $Q(z)$ as 7 kHz. In experiments, the RC and $\mathcal{H}^{-1}$ are implemented on FPGA with a closed-loop sampling frequency of 100 kHz.

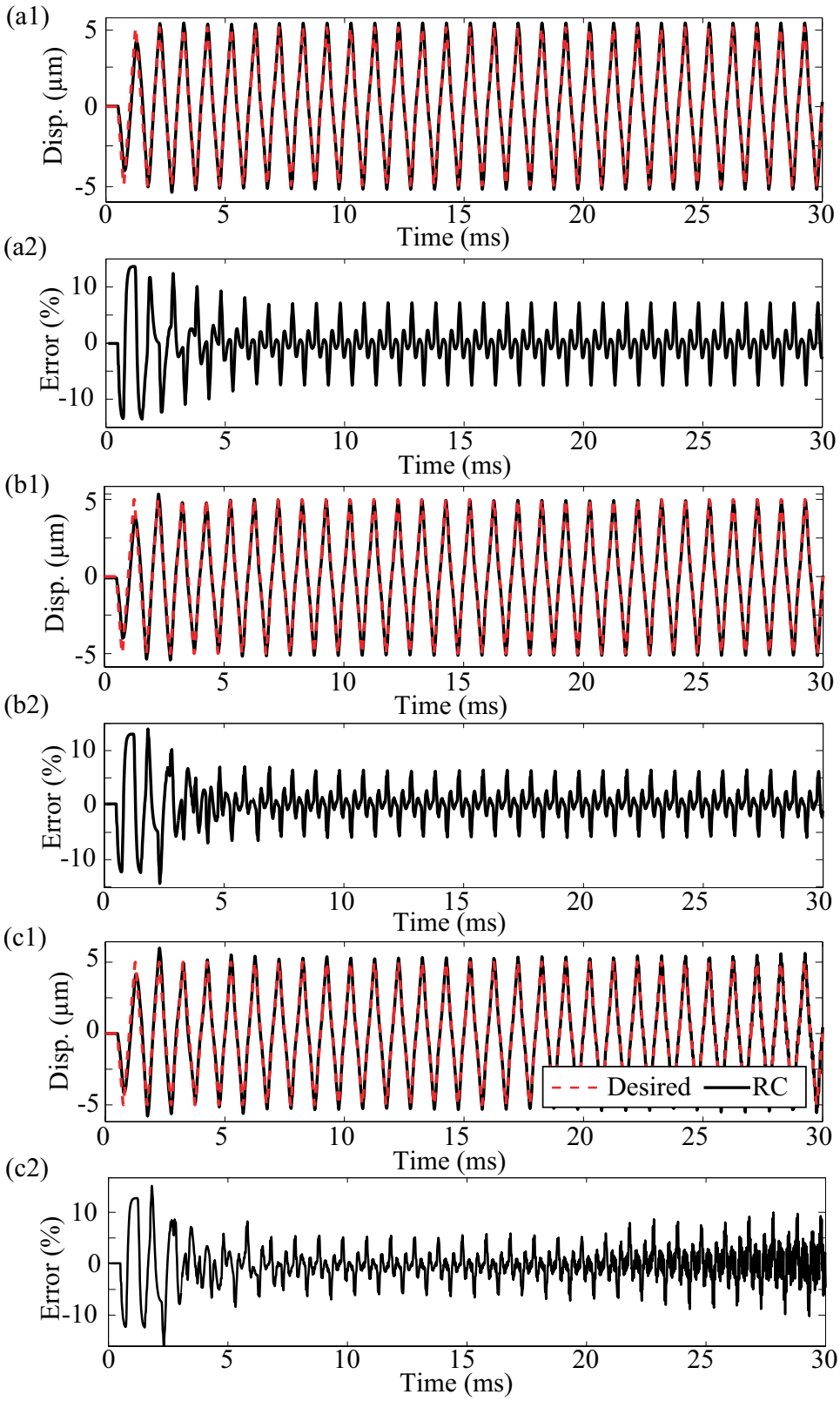

Figure 7.13: Simulation results at 1 kHz triangular trajectory tracking to show the effect of k_{rc} on system stability and tracking performance. (a1) and (a2) belong to RC with k_{rc}=0.6; (b1) and (b2) belong to RC with k_{rc}=0.8; (c1) and (c2) belong to RC with k_{rc}=1.1.

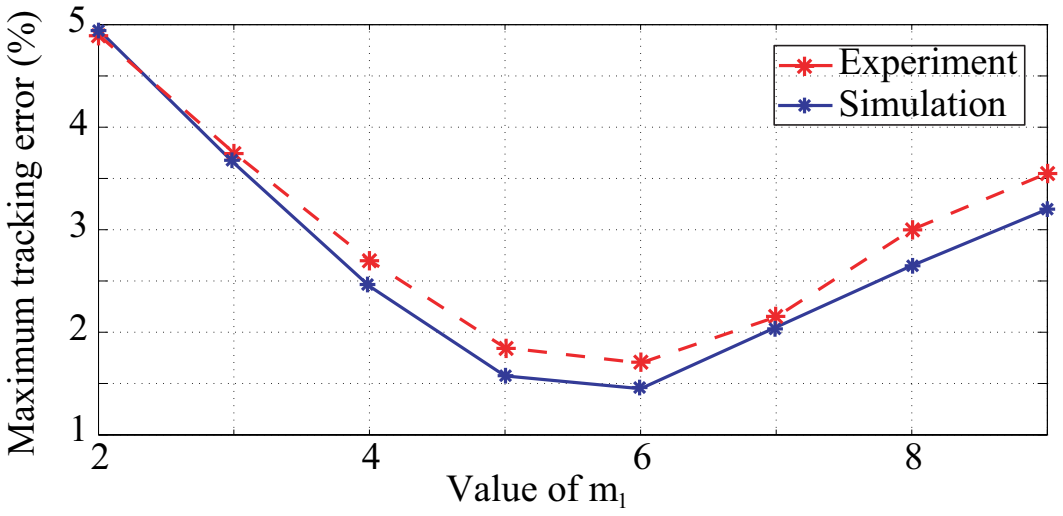

Figure 7.14: The maximum tracking error versus phase lead compensator parameter m_1.

7.5 Quantifying the Effect of Hysteresis

The effect of hysteresis on RC stability is quantified using the stability conditions given in Eq. (6.10) and (6.16). First, the gain margin of the linear RC system is found from the frequency response of the RC system shown in Fig. 7.15, where the sampling frequency is 100 kHz. From the frequency response, the gain margin is $M_{G_L} = 20.1$ dB (magnitude of 10.12), and compared to the constant g_0 from the forward P-I model, $g_0 = 0.8331 < M_{G_L} = 10.12$. Therefore the first part of the stability conditions, Eq. (6.10), is satisfied.

Now for the second part of the stability conditions, Eq. (6.16). To determine $G_2(z)$, first $G_{rp}(z)$ is written as

$$\begin{aligned} G_{rp}(z) &= \left[\frac{k_{rc} z^{-N+m_1} Q(z)}{1 - z^{-N+m_1} Q(z)} + 1\right] G_c(z), \\ &= \frac{G_c(z)}{1 - z^{-N+m_1} Q(z)}, \end{aligned} \tag{7.4}$$

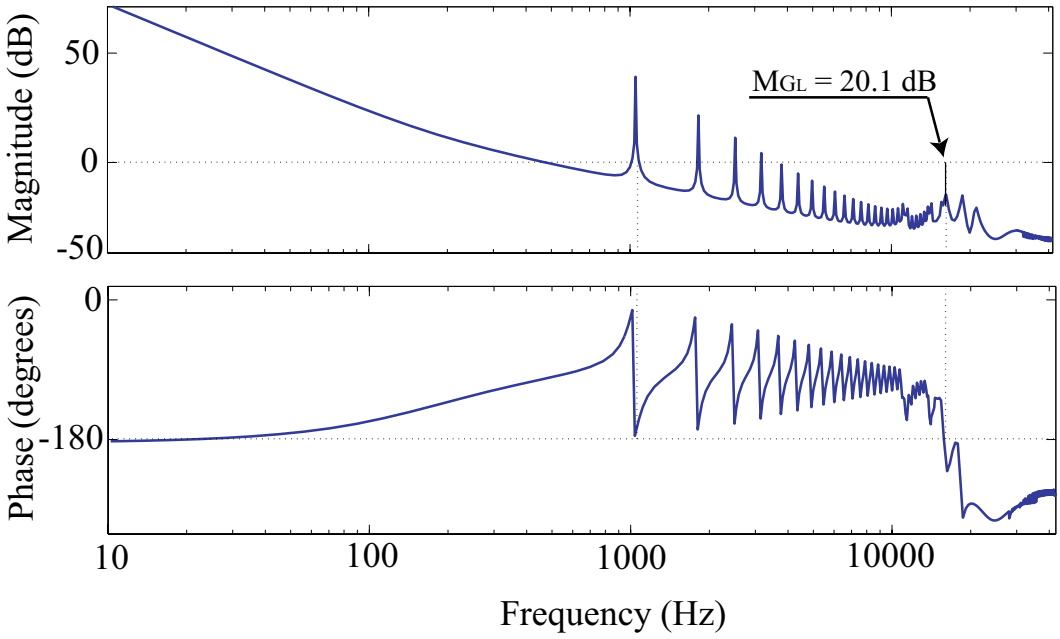

Figure 7.15: Frequency response of the open-loop linear RC system showing the gain margin M_{G_L}.

where

$$Q(z) = \frac{0.3558}{z - 0.6442},$$

$$G_c = 1.3 + \frac{0.4z}{z - 1},$$

$k_{rc} = 0.8$, and $z^{-N+m_1} = z^{-94}$ with sampling frequency $F_s = 100$ kHz. Then $G_2(z)$ is developed from the state space representations of $G(z)$ and $G_{rp}(z)$, where it is determined that $\sup_{\omega \in \mathbb{S}} \|G_2(z)\|_2 = 5.31$, which implies that

$$\frac{1}{|g_0| \sup_{\omega \in \mathbb{S}} \|G_2(z)\|_2} = 0.222.$$

Compared to the $\sup_{1 \le j \le n} \|d(\gamma)\|_1 = 0.409$, there is:

$$\sup_{1 \le j \le n} \|d(\gamma)\|_1 \not< \frac{1}{|g_0| \sup_{\omega \in \mathbb{S}} \|G_2(z)\|_2}$$

which means the second part of the stability condition, Eq. (6.16), is not satisfied. Therefore, direct implementation of the RC system designed around the linear dynamics model will cause the closed-loop system to be unstable, and thus hysteresis compensation is required. This conclusion is further verified in simulation and experiments, and the results are shown next.

7.6 Simulation and Experimental Tracking Results

7.6.1 The Effects of Hysteresis

The simulations and experiments are implemented to show the effect of hysteresis on RC stability. The simulative evaluation is achieved in Matlab using the RC, $G_c(z)$, $G(z)$ and the P-I hysteresis model. The experimental evaluation is using the same controllers but implemented in analog (proportional-integral controller) and on FPGA (RC). Finally, the $\mathcal{H}^{-1}$ is implemented in simulation and experiment to further validate the effect of hysteresis on system stability. The verification is applied for tracking a 1 kHz triangular trajectory for approximately 10 μm displacement.

First, the hysteresis of piezoactuator in the x-axis of the nanopositioner modeled by the P-I model is shown in Fig. 7.16 (a1), where it's size is 0.409 [Eq. (6.16)]. Using this model, the simulated response of the RC control system is shown in Fig. 7.16(b1) and an expanded view of one period of the scanning response is shown in (b2). It can be readily seen that the size of the nonlinearity causes the simulated response to exhibit excessive oscillation, indicating impending instability. The experimental results of the same controller confirms that the controller becomes unstable as illustrated in Fig. 7.16(c1) and the expanded view in (c2). The RC system becomes unstable at approximately 4.5 ms, indicating that the hysteresis effect if significant reduces the stability margin of the closed-loop system. However, the simulated response of the

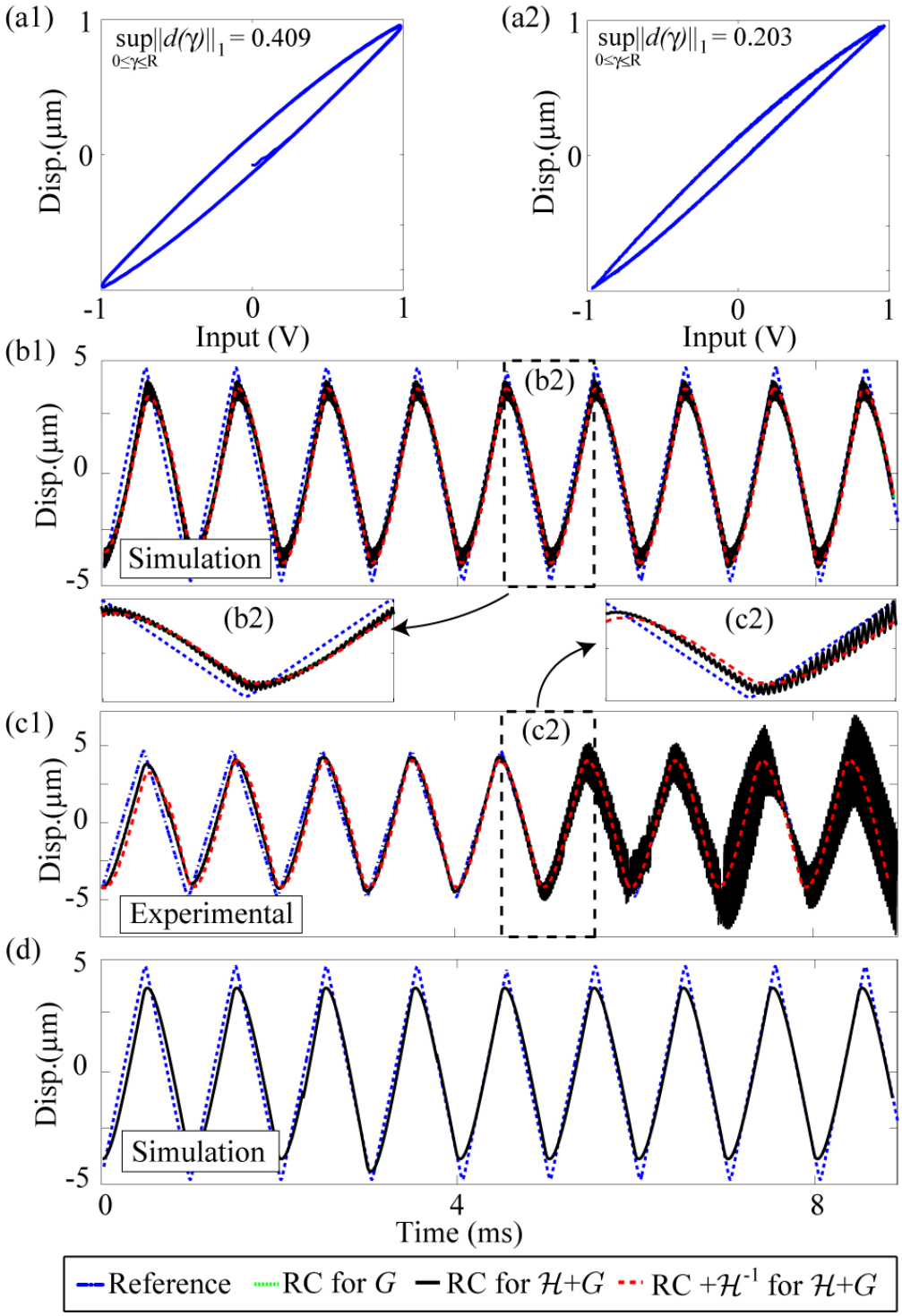

Figure 7.16: The effect of hysteresis on RC stability for tracking 1 kHz triangular trajectory: (a1) The hysteresis of piezoactuator in the x-axis of the nanopositioner, size of 0.409. (a2) The P-I model hysteresis with size of 0.203. (b1) and (b2) Simulation results using hysteresis in (a1). (c1) and (c2) Experimental results for hysteresis in (a1). (d) Simulation result using hysteresis in (a2).

RC controller where the hysteresis nonlinearity is smaller (0.203), such as that shown in Fig. 7.16 (a2), is stable [see Fig. 7.16(d)]. Therefore, the size of the nonlinearity can drastically affect the stability of the RC.

7.6.2 The Performance of RC with/without the Inverse Hysteresis Compensator

Besides using the inverse hysteresis compensator to stabilize the closed-loop system, another option is to reduce the size of the controller to satisfy the stability conditions in Eq. (6.10) and Eq. (6.16). The size of the controller is reduced by re-designing the proportional-integral controller gains from $k_p = 1.3$ and $k_i = 40000$ to $k_p = 1.1$ and $k_i = 40000$ to satisfy the stability conditions and for good tracking performances. Experiments are done to validate this by evaluating the tracking performance for standard proportional-integral control and RC with and without hysteresis compensation $\mathcal{H}^{-1}$. Experiments are run to track triangular trajectories at 10 Hz, 100 Hz and 1 kHz for full range (10 μm) displacement of the piezoactuator and comparing with the performances of the regular proportional-integral and RC without $\mathcal{H}^{-1}$.

One example of the tracking results, 1 kHz tracking, is shown in Fig. 7.17. The plots (a), (b) and (c) are the tracking error results of the controllers. The plot (d) shows the measured tracking results of the overall closed-loop systems at steady-state stage. The detail of the controller performances for tracking reference trajectories at 10 Hz, 100 Hz and 1 kHz is in Table 7.2. The table compares the maximum tracking error [$e_{max}(\%)$] and root-mean-square error [$e_{rms}(\%)$]. The root-mean-square error is given by:

$$e_{rms}(\%) = \frac{\sqrt{\frac{1}{T_s}\int_0^T [|y(t)| - |r(t)|]^2 dt}}{\max(r) - \min(r)} \times 100\% \tag{7.5}$$

where T_s is the signal period time. The tracking results show that, with the size of the

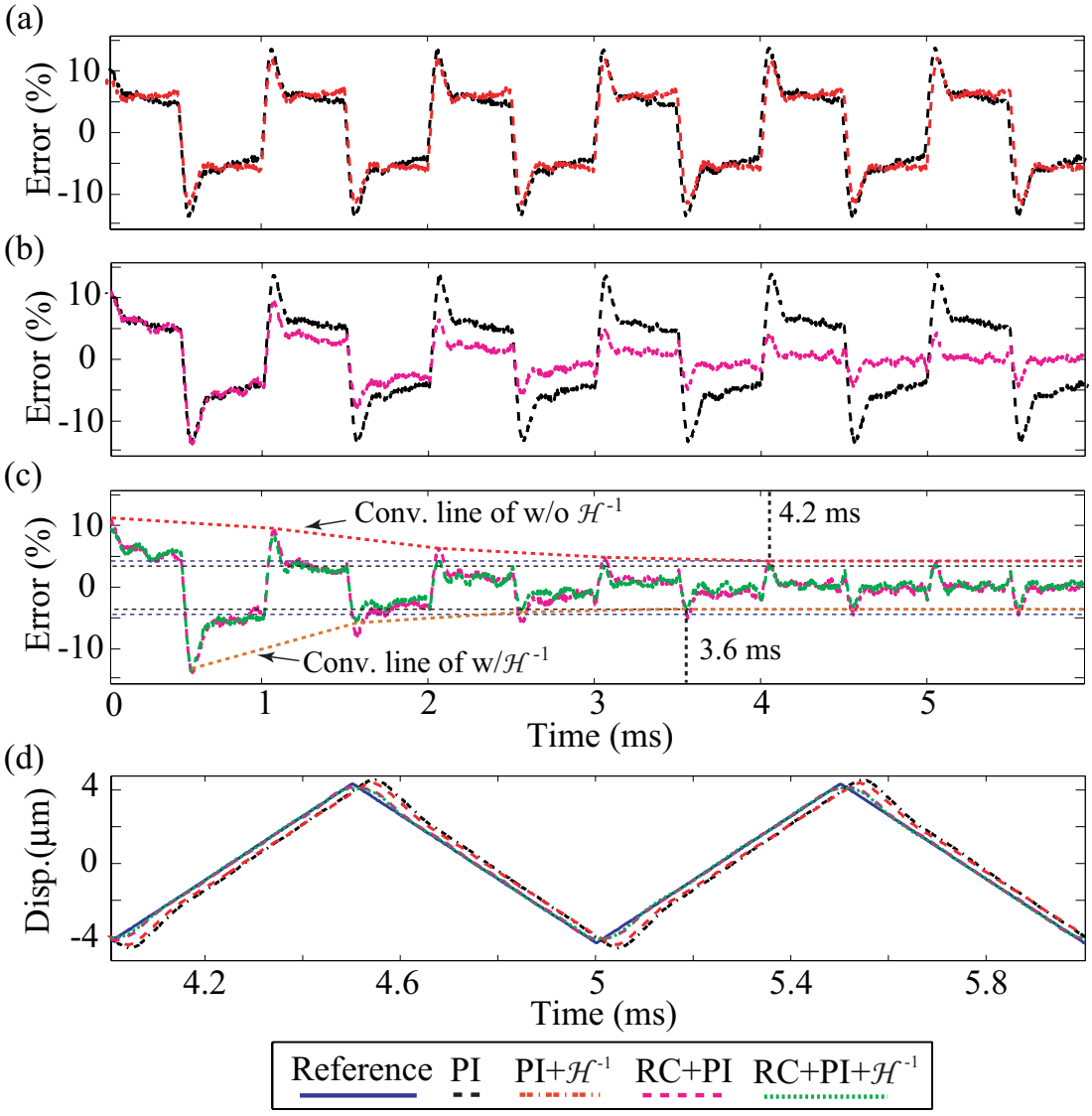

Figure 7.17: Experimentally measured tracking error comparing (a) PI with and without $\mathcal{H}^{-1}$; (b) PI and RC (without $\mathcal{H}^{-1}$); (c) PI+RC and PI+RC+$\mathcal{H}^{-1}$; and (d) steady-state displacement vs. time

control system reduced ($k_p = 1.3$ reduce to $k_p = 1.1$) and the stability condition satisfied, the closed-loop system with hysteresis is stabilized, which results in the remove of the distortion shown in Fig. 7.16(c2). It can also be seen the maximum tracking error of the proportional-integral controller is reduced from 13.7% to 12.0% at 1 kHz by combining the $\mathcal{H}^{-1}$ to the proportional-integral controller. By adding just the RC to PI controller, the repeating tracking error of the PI control system is reduced with the operating cycle increase as shown in Fig. 7.17. Also, the tracking error is reduced to 4.5% at 1 kHz. Finally, the addition of $\mathcal{H}^{-1}$ lowers the maximum tracking error to 3.9%. Beside reducing the tracking errors of PI and RC, the hysteresis compensator also increases the converge rate of the tracking error of the RC system by about 14% from 4.2 ms to 3.6 ms as shown in Fig. 7.17(c), where the converge rate is defined as the rate of the tracking error arrives the steady-sate value.

Table 7.2: Tracking error at last two periods of the tracking results.

Controller	**10 Hz**		**100 Hz**		**1 kHz**	
	e_{max}	e_{rms}	e_{max}	e_{rms}	e_{max}	e_{rms}
PI	2.37	1.36	5.52	4.04	13.7	11.42
PI+$\mathcal{H}^{-1}$	1.73	1.1	3.99	2.46	12.0	9.46
PI+RC	0.99	0.42	1.77	0.69	4.5	1.6
PI+RC+$\mathcal{H}^{-1}$	0.72	0.28	1.26	0.46	3.9	1.38

Therefore, the stability of the closed-loop system for hysteresis can be certified by following the stability conditions defined in Eq. (6.10) and Eq. (6.16). According to the stability conditions, there are two approaches to stabilize the system when the size of the hysteresis is over the tolerance of the closed-loop system robustness: Approach one is to reduce the size of the controller to make the stability conditions satisfied; approach two is to use the hysteresis compensator $\mathcal{H}^{-1}$ to stabilize the sys-

tem. Comparing these two approaches, the advantages of the hysteresis compensator are it can enhance the tracking performances of the control system, and increase the converge rate of the tracking error.

7.7 Summary

This chapter discussed the implementation of the RC control system, as well as validating the stability conditions developed in previous chapter. The hysteresis behavior is modeled to quantify the system stability and an inverse hysteresis compensator was determined for hysteresis compensation. Based on the simulation and experimental results, the conclusion is made that the stability theory developed can quantify the effect of hysteresis on the closed-loop system stability effectively; and the proposed RC approach can achieve high-precision positioning in tracking periodic reference motion. Additionally, when compared to existing feedback control approaches, such as proportion-integral controller, the approach reduces the repeating tracking error with the operating cycle increases. Furthermore, the performance of the RC is validated in the nano-hole arrays pattern fabrication for ZnO nanowire growth to test its potential application in AFM-based nanofabrication.

Chapter 8

Nanofabrication Results and Quantification

To illustrate the application of the research, the RC is applied to AFM-based fabrication of a nano-sized holes array pattern. Such holes array can be used to create ZnO nanowire arrays. The experiments will investigate the potential for using a piezo-based AFM as a tool to fabricate platforms/templates for controlled growth of ZnO nanowire arrays. The advantage of AFM compared to traditional fabrication methods are, for example, nanoscale precision, lower power consumption, potentially higher throughput and lower costs. The performance of the RC can also be compared to other control methods for nanofabrication, such as traditional PID control.

Nanofabrication involves making structures with dimension at nanometer level (100 nm or less). To do this, there are photolithography, nanoimprint, self-assembly, scanning probe microscopy (STM, AFM, near-field scanning optical microscopy)-based nanothecnologies, etc. Recently, the AFM tool has attracted great attention as a viable option for fabricating a wide range of nanostructures. The benefits include: (1) the ability to simultaneously fabricate and visualize the nanostructures with the same equipment, (2) operation in a standard room environment, (3) capable of nano-precision operation, and (4) applicable to different materials (*e.g.*, metal, semiconductor, polymer, bio-molecules, organic materials and inorganic salts). AFM-based

nanofabrication technologies such as nanomanipulation, force-lithography, nanografting, nanoaxidation and dip-pen nanolithgraphy, were developed to physically or chemically modify surfaces and perform manipulation at nanometer scale, which have the potential applications in nanoelectronics, bioanalysis, biosensors, actuators, and high-density data storage devices. In this study, the force-lithography is chosen over other AFM-based nanofabrication approaches due to its simplicity.

Zinc oxide (ZnO) nanostructures, particularly nanoscale ZnO nanowires, are promising oxide semiconductors and have attracted much attention due to their versatile properties and potential applications in optoelectronic, sensing, energy, and piezoelectronic devices. However, to create such devices, precise control of the morphology, alignment, and position of the nanoscale structures is need to fabricate the ZnO nanowires [183–186]. For example, in the design of the ZnO nanowire based nanogenerator, ZnO nanowire array needs to be well-aligned in spacing and shaping, since the density of the ZnO nanowire array, the spaces between the ZnO nanowires, and the size and the shape of the ZnO nanowires affect the efficiency of the voltage generation [187]. In this study, the pattern fabrication for selectively controlled growth of ZnO nanorod arrays on the desired areas of substrates is investigated to validate the performance of the designed RC system. At current stage, the nanogenerator is designed in a square shape with equal spaced ZnO nanowires as shown in Fig. 8.1(a). To achieve the structure, the required tracking signal in x-axis of the AFM-based nanofabrication system is periodic as shown in Fig. 8.1(c). The performance of the RC for tracking this type of periodic signal is validated experimentally. Further more, the performance of the controllers is tested in nanofabricating the patterns in Fig. 8.1(a) for ZnO nanowire array growth by using the periodic signal in Fig. 8.1(c) as a reference trajectory in x-axis. It is noted, in the nanofabrication, the repetitive control system is applied to the x-axis of the AFM-based nanofabrication system; and

a regular PID controller is applied to the y-axis.

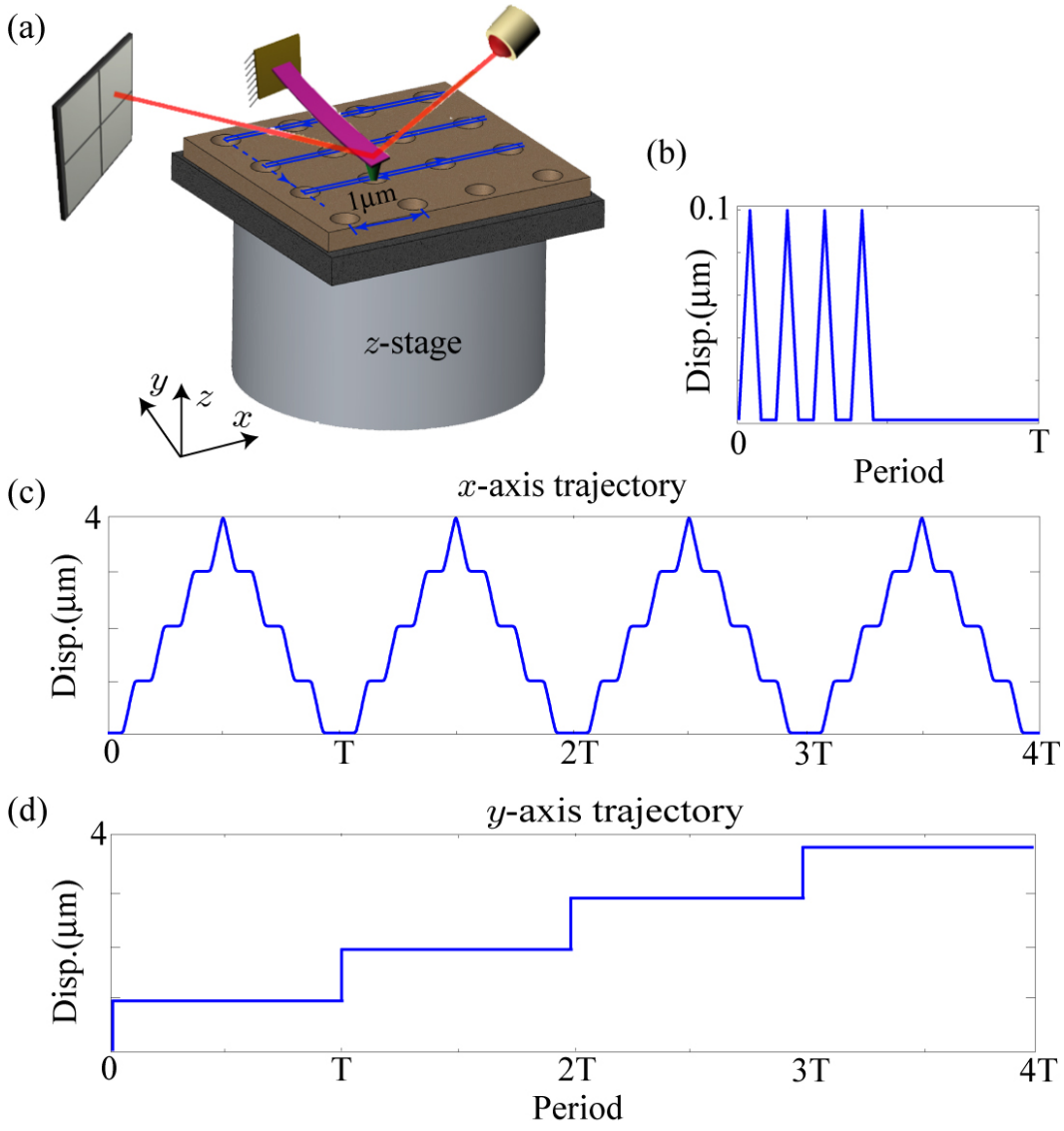

Figure 8.1: (a) An example nano-hole arrays pattern for ZnO nanowire array growth. The signals for fabricating nano-hole arrays for ZnO nanowire array in (b) z-axis; (c) x-axis (periodic trajectory); (d) y-axis.

The process to create the ZnO array includes three main steps as shown in Fig. 8.2, where Step 1 and 2 are performed to demonstrate feasibility of the control approach. More specifically, the process includes:

1. Coating the ZnO buffer layer onto the substrates, such as Si, as the seed for

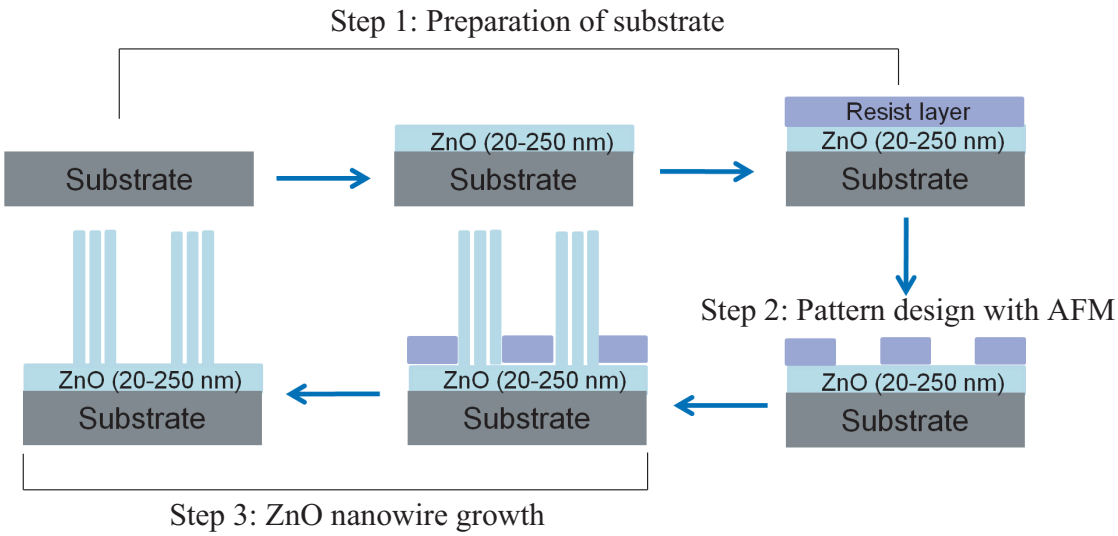

Figure 8.2: The steps for fabricating ZnO nanowire array. The steps 1 and 2 are processed in this study, and the step 3 is left as a future work due to the laboratory condition we have.

nanowire growth;

2. Spin coating the resist layer, such as polymethylmethacrylate (PMMA), onto the ZnO layer for patterning;

3. Patterning the resist layer using the AFM (scratching);

4. Growing the ZnO nanowires through chemical reaction in solution; and

5. Removing the resist layer away through chemical etching.

The following three steps are typically carried out for ZnO nanowire growth:

Step 1: Preparation of Substrates for Nanofabrication The preparation step involves two different sub-tasks, which are coating ZnO layer onto substrates and spin coating the resist layers. The ZnO layer serves as the seeds for nanowire growth. The PMMA layer is used as a sacrificial layer for AFM to create pattern for further nano feature growth.

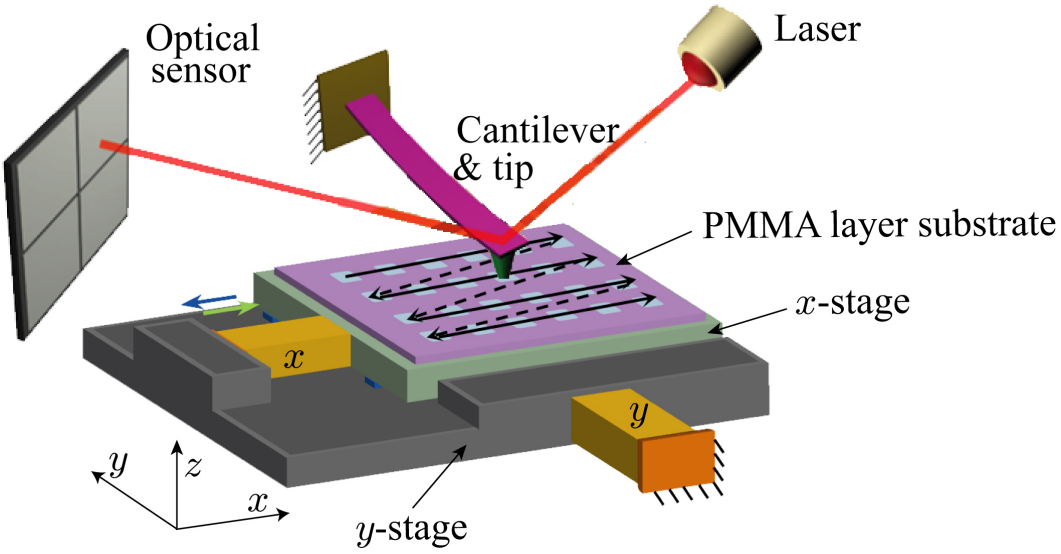

Figure 8.3: The patterns to be created on PMMA using an AFM, where the piezo-based nanopositioning stage positions the substrate in x, y, and z directions, the nano-hole arrays are created by a AFM tip.

Step 2: Mechanical Scratching with AFM for Pattern Design on PMMA Layer In this step, the AFM is used as a tool to create desired patterns on the PMMA layer, such as the hole array with equal space and size for the controlled growth of ZnO nanowire arrays. These holes are created though a mechanical method, which means to use the tip at the end of the cantilever of the AFM to directly scratch nano-scale holes on the PMMA layer, as shown in Fig. 8.3. The spacing and sizing of the holes are controlled trough the designed RC system. For effective fabrication of the nanowire array, preliminary tests are carried out first, for example, the force test to determine the force required to remove the selected PMMA layer with certain thickness and the thickness test to determine the thickness of the PMMA thin film. Finally, nano-hole arrays are fabricated with RC and inverse hysteresis compensator at different speeds to validate the performance of RC at high-speed nanofabrications, and the results are compared with the results from PID with hysteresis compensator control and open-loop fabrication.

Step 3: ZnO Nanowire Growth This step involves the ZnO nanowire growth and the resistant layer remove. The ZnO nanowire is grown using a chemical methods. After that, the PMMA layer is removed from the substrate through chemical etching as the steps 4 and 5 shown in Fig. 8.2 to complete the nanofabrication process.

It is noted that the first two steps of the nanofabrication process have been completed and the last step is left for future work whichs need to be processed in a clean room.

8.1 Experimental System for Nanofabrication

The experimental nanofabrication system is built around a custom-designed piezo-based long-range 3-axis nanopositioner and a commercial AFM scanner. The system configuration is shown in Fig. 8.4. In the configuration, there are also a Matlab xPC Target system formed by a host computer with a target computer for controller implementation and data communication with a maximum closed-loop sampling frequency of 25 kHz; as well as a custom-designed high-bandwidth piezo amplifier to drive the high-speed x and z axes piezoactuator systems of the nanopositioner, and a commercial piezo amplifier (TRek PZD350A) to drive the y axis piezo system. The commercial AFM system is Nanosurf easyScan 2 from NanoSurf. It is combined by a scanning head and a controller, and is operated using a desktop computer with a operating software (Nanosurf easyScan 2 Control Software).

The nanopositioner positions the PMMA coated ZnO/Si substrate in x, y, and z directions for nano-hole arrays pattern fabrication. The long-range stage, shown in Fig. 8.6(a), couples $5 \times 5 \times 12$ mm Naliac SCMAP07 plate stack actuators (total 6 stacks) with free stroke of 14.7 μm with a mechanical displacement amplifier to provide a final stage displacement of approximately 40 μm in x and y directions, and couples 1 plate stack actuator in z direction to provide approximately 2.5 μm

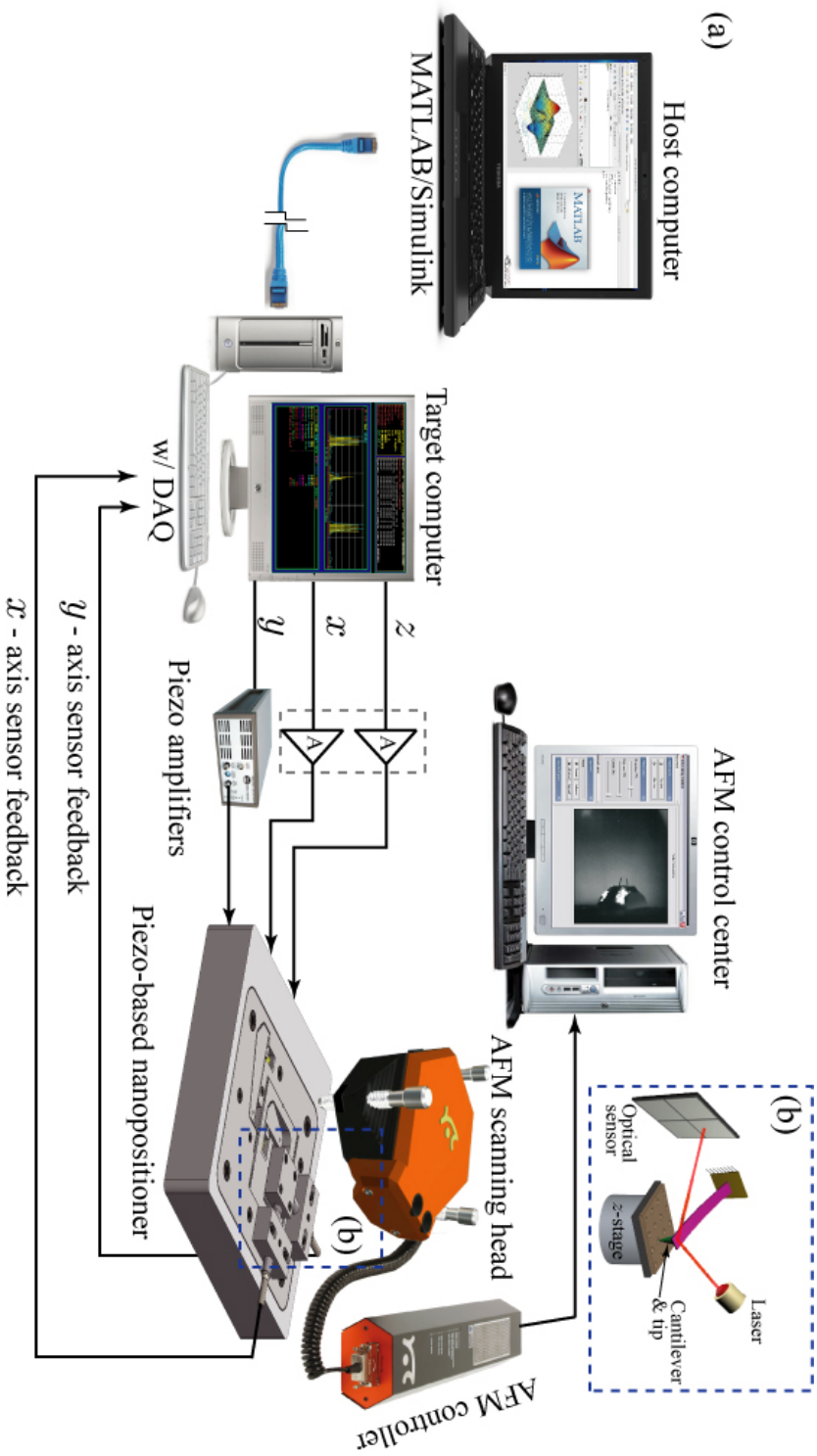

Figure 8.4: (a) Experimental nanofabrication system. (b) A closed-view of the interaction section of the nanofabrication system: AFM cantilever, tip, and the substrate for fabrication.

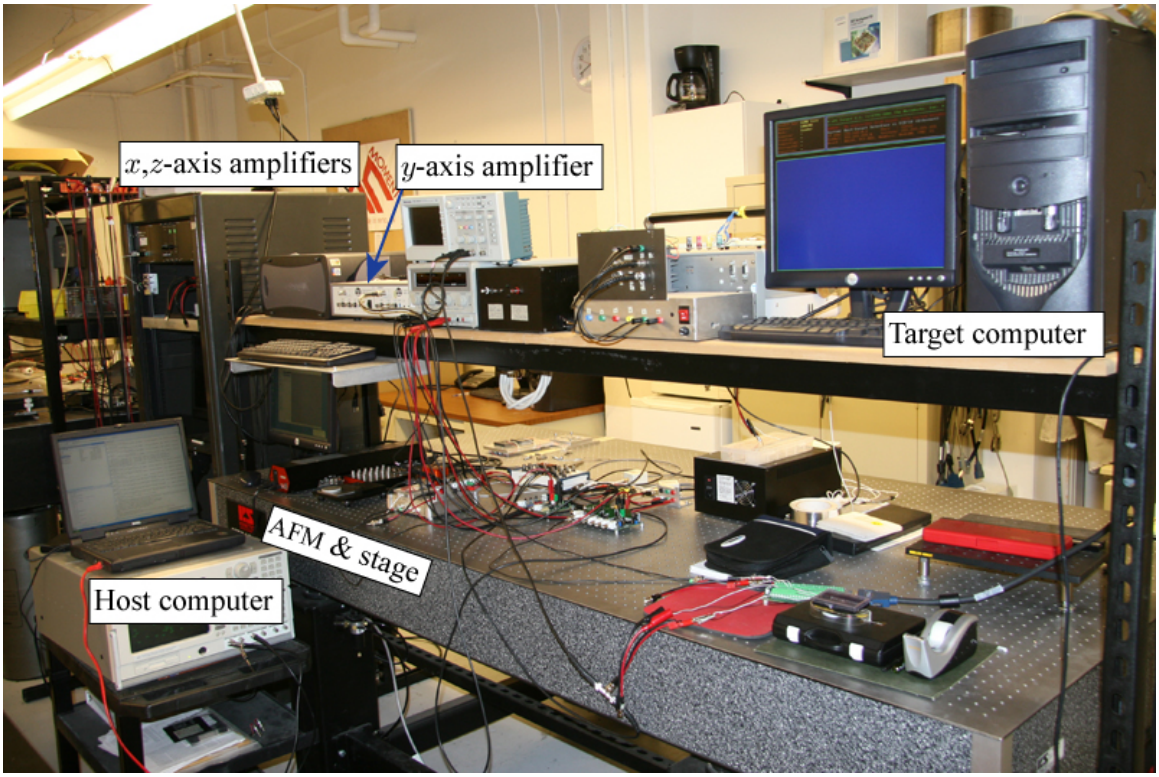

Figure 8.5: A photograph of experimental nanofabrication system setup.

displacement. The stock ceramic end caps of the actuators are replaced with alumina plates to increase the actuator stiffness as described in [188]. In the x and y directions, the lever arm of the mechanical amplifier has an ideal mechanical displacement amplification of 5.82 ($K_{mech} = u_{out}/u_{in}$) and a practical amplification under 4 times. This is due to compliance in the lever and associated flexures. The stage bodies are guided linearly with compliant flexures. Compound flexures are attached to the corners to keep the stage compact while maintaining low actuation stiffness. Beam flexures are added to the fore and aft ends of the stage bodies to increase rotational stiffness, thus reducing the effects of parasitic motion and dynamic cross coupling. Parabolic fillets are used instead of constant radius corner fillets in areas subject to high-strain, to decrees stress concentration values. The stage is outfitted with inductive sensors (Kaman SMU9000-15N) to measure displacement in the lateral x and y directions.

The final stage displacement is determined to be 41.76 μm and 43.25 μm for the x- and y-axis. The first mechanical resonance modes for the x- and y-stages are shown in Figs. 8.6(b) and (c) to occur at 718.5 Hz and 532.2 Hz respectively; both in their corresponding actuation directions.

The xPC Target is a real-time system that enables to execute the digital controller on a target computer for hardware-in-the-loop (HIL) simulation and real-time control applications. A standard xPC Target control system normally contains two computers. One is called the *host* computer, and the other is called the *Target* computer. The *host* computer is a standard personal computer with Matlab, Simulink, and xPC Target Toolbox installed. This computer is used to create Simulink model of the control system, to compile the Simulink model to C-code for *Target* computer implementation, and to store and process input and output data. The *Target* computer is used to execute the Simulink model created on the *host* computer, and to send and collect experimental data. This computer has a real-time operator system and a data-acquisition hardware (DAQ). In the implementation, the real-time operator system on the *Target* computer is driven by a *Bootdisk* created by *xPC Target Explorer* on the host computer to run the complied C-code of the Simulink model. The DAQ (NI PCI-6040E, 12-bit resolution, maximum sampling rate of 500 kS/s) is used to interface with physical components in the experiment system for data communication. The host computer communicates with target computer through a crossover cable. It is noted that the Simulink model for xPC Target implementation is different from the Simulink model for Matlab simulation. For example, in Matlab simulation, the Simulink model for a PID feedback closed-loop system is formed by a PID controller with a system model of the experimental plant, such as a linear dynamics $G(z)$ of a piezoactuator. However, in the Simulink model for xPC Target, $G(z)$ is replaced by the input/output modules of DAQ to communicate with the real experimental plant,

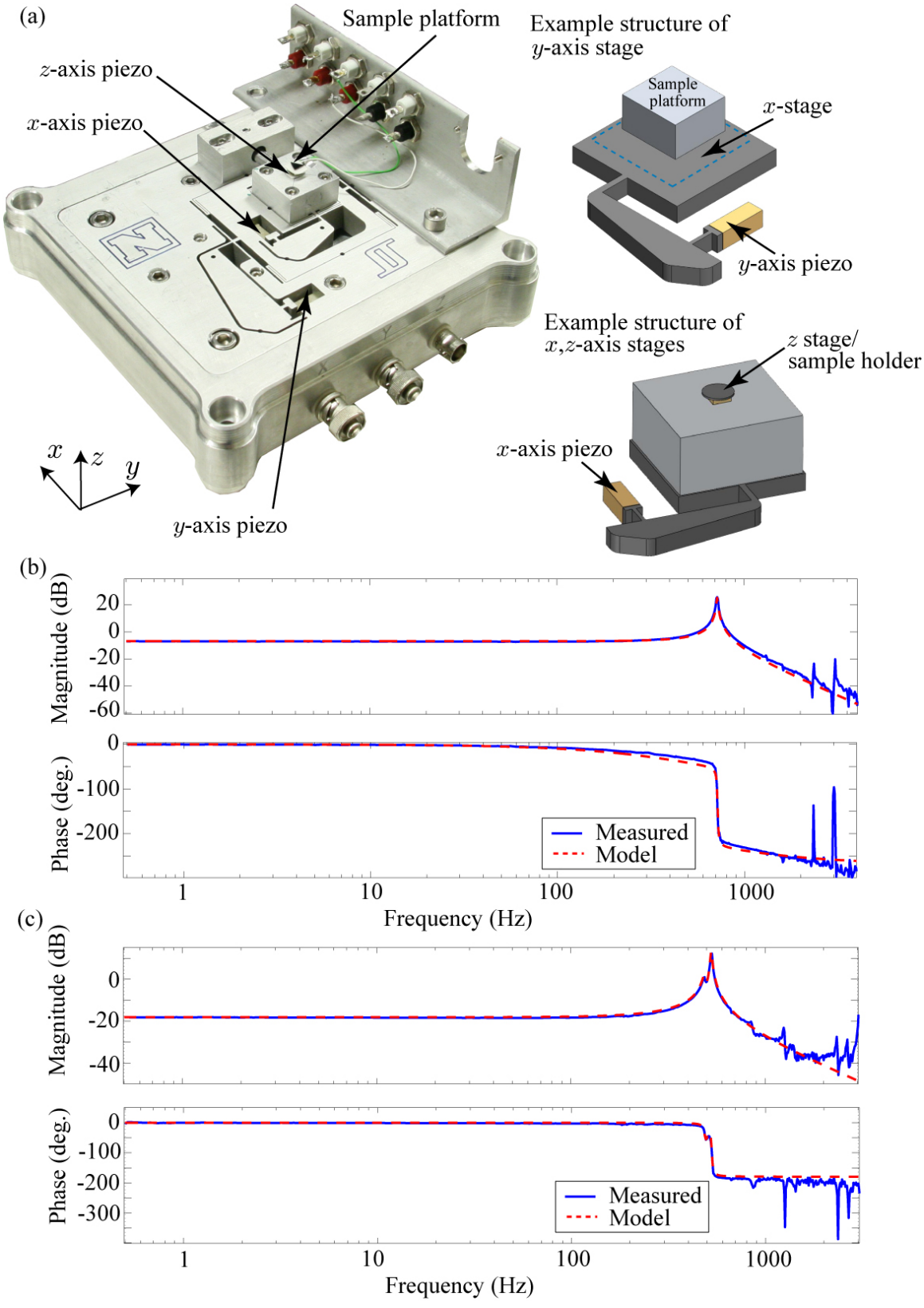

Figure 8.6: (a) The piezo-based long-range stage for nanofabrication, which includes a photo of the stage and solid model images of x, z-axes stages and y-axis stage. (b) The frequency response of the x-axis of the nanopositioning system. (c) The frequency response of the y-axis of the nanopositioning system.

as shown in Fig. 8.16.

The Nanosurf easyScan 2 AFM system is used for nano-hole arrays fabrication and imaging of the fabricated results. The hardware for the AFM system involved in the experiments includes a scan head and a controller operated by a desktop computer with the easyScan 2 software. In the scanning head, there are scanning cantilever holder and positioner to position the cantilever in x, y, and z directions for nanometer scale resolution measurements of topography or nanofabrication of a sample surface. The highest drive resolution in x and y-axis is approximately 0.15 nm and is about 0.027 nm in z-axis. The maximum scanning range is 110 μm in x, y-axis and 22 μm in z-axis. A video module allows the user to monitor the approach of the AFM tip to the sample surface and observe the sample surface in 4×4 μm (top view)/ 5×3 μm (side view) range, and a signal module sends and receives signals form the controller. The controller controls the scan head, for example to apply PID control to the cantilever in the z-axis and to approach the AFM tip to a sample surface, through a DAQ (16 bit, $\pm$10 V). It also processes the video/control and operating signal communicating between the scan head and the computer, and shows the status of the scan head. The easyScan 2 software provides a friendly interface for users to operate the scan head and to process the data.

This AFM scan head can be operated in, for example, static force and dynamic modes, and allows the scan speed up to 60 ms/line at 128 data points/line. The maximum achievable data point is 2048×2048 points. In experiments, the AFM scan head is operated in static force mode with a constant force loaded on the cantilever for nanofabrication and imaging; and only the z-axis of the AFM scanner is used to hold the cantilever to have a static load using the z-axis PID controller while the x and y-axes of the AFM scan head are disabled. The static load is chosen as 10 nN for imaging, and the load for nanofabrication is determined in Section 8.3.2. The

z-axis maximum measurement noise level is approximately 0.8 nm. Compared to the maximum scanning range of 22 μm, the noise is less than 0.01% of the scanning range.

8.1.1 System Modeling

x-axis System Modeling

The x-axis piezo-actuator system of the long range nanopositioner is modeled for controller design and implementation.

First, the linear dynamic model of the x-axis piezo-actuator system is estimated using the same method as discussed in Section 7.2.1. The frequency response is measured from 0.5 Hz to 3 kHz to cover the main resonances of the system. The measured frequency response is shown by the solid line in Fig. 8.6(b). A linear 3^{rd}-order dynamic model $G(s)$ generated by curve fitting the measured frequency response has the following representation:

$$G(s) = \frac{3.391 \times 10^{10}}{s^3 + 3759s^2 + 2.063 \times 10^7 s + 7.514 \times 10^{10}}. \tag{8.1}$$

The discrete-time version of the dynamics model is converted in Matlab using the $c2d$ command and zoh method with a sampling frequency of 10 kHz to:

$$G(z) = \frac{0.001304z^3 + 0.01319z^2 + 0.01224z + 0.001041}{z^3 - 2.485z^2 + 2.233z - 0.6867}. \tag{8.2}$$

The frequency response of the dynamics model is compared to the measured frequency response in Fig. 8.6(b).

The hysteresis of the x-axis piezo-actuator system is modeled using the P-I hysteresis modeling approach. The parameters for the P-I model are optimized to: $g_0 = 0.658$, $g_1 = 0.0606$, $\lambda = 0.6684$, $\delta = 0.6859$ and $\rho = 0.3569$. The performance of the P-I model with these optimized parameters is validated by comparing

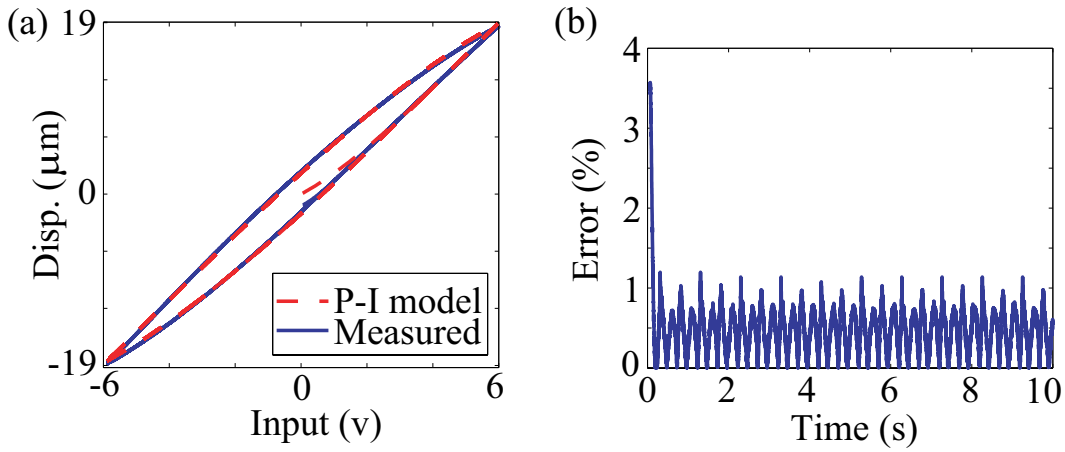

Figure 8.7: The P-I hysteresis model *v.s.* the measured hysteresis. (a) The hysteresis curve. (b) The matching error between the model and the measured hysteresis.

with the measured hysteresis behavior for tracking triangular trajectory at 1 Hz as shown in Fig. 8.7. From Fig. 8.7(b), the maximum matching error at steady state is no more than 1.15%, which reveals the accuracy of the optimized P-I hysteresis approach on modeling hysteresis behavior of the x-axis piezo system.

With the modeled dynamics and hysteresis, the cascade model of the x-axis piezo system is also validated. The validation is achieved through comparing the simulation output of the cascade model with the open-loop output of the experimental system. The driving signals for the open-loop response are two types: triangular trajectories and signals for nano-hole arrays fabrication for 38 μm rang of motion at 1 Hz, 10 Hz, and 50 Hz. The results are shown in Fig. 8.8 and Fig. 8.9. It can be seen that the maximum matching error is less than 1.9% for up to 50 Hz triangular response [plot (a1) to (c2) in Fig. 8.8]. The maximum matching error for nanofabrication signal response up to 50 Hz [plot (a1) to (c2) in Fig. 8.9] is less than 1.7%. Therefore, the dynamics and hysteresis models can represent the experimental system well for controller design.

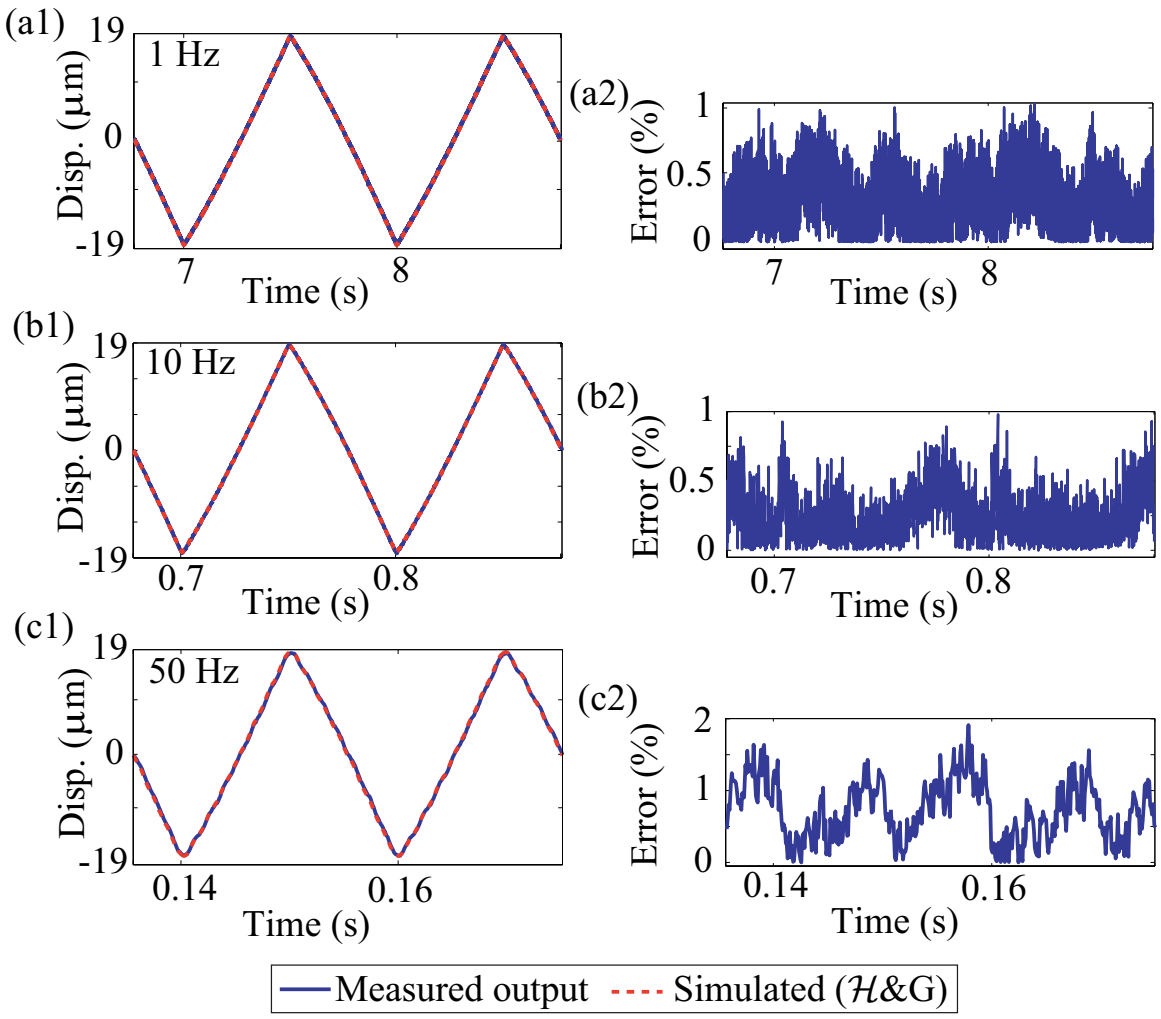

Figure 8.8: Experimental validation of cascade model with triangular trajectory inputs. (a1) and (a2) Displacement and error vs. time between measured (solid line) and model output (dash line) at 1 Hz; (b1) and (b2) the comparison for 10 Hz scanning; (c1) and (c2) the comparison for 50 Hz scanning.

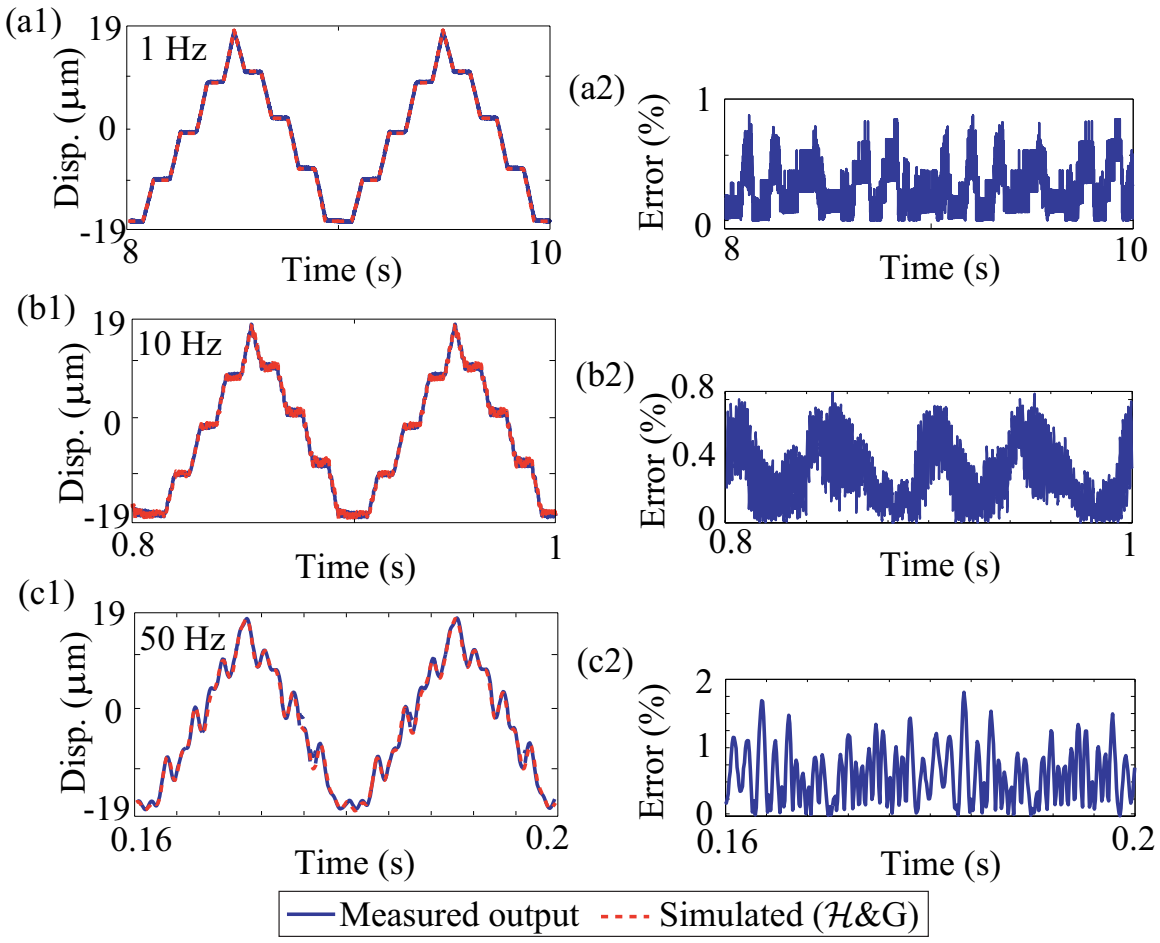

Figure 8.9: Experimental validation of cascade model with the input signals for hole array fabrication. (a1) and (a2) Displacement and error vs. time between measured (solid line) and model output (dash line) at 1 Hz; (b1) and (b2) the comparison for 10 Hz scanning; (c1) and (c2) the comparison for 50 Hz scanning.

y-axis System Modeling

A 4^{th}-order linear dynamic model is developed for y-axis of the nanopositioning system for PI controller design. The transfer function of the model is:

$$G(s) = \frac{1.313 \times 10^6 s^2 + 1.899 \times 10^8 s + 1.282 \times 10^{13}}{s^4 + 196 s^3 + 2.042 \times 10^7 s^2 + 2.049 \times 10^9 s + 1.035 \times 10^{14}}, \quad (8.3)$$

and its discrete-time version is developed in Matlab using the $c2d$ command with zoh method and a sampling frequency of 10 kHz:

$$G(s) = \frac{0.002174 z^4 + 0.004532 z^3 - 0.01201 z^2 + 0.004418 z + 0.002138}{z^4 - 3.779 z^3 + 5.551 z^2 - 3.742 z + 0.9806}. \quad (8.4)$$

The frequency response of the dynamics model is compared to the measured frequency response in Fig. 8.6(c). The PI controller design according to this model is discussed in Section 8.1.4.

8.1.2 Inverse Hysteresis Compensator

An inverse hysteresis compensator is designed for the high-speed x-axis of the nanopositioner. The parameters of the inverse hysteresis compensator are calculated using the method of Section 7.3, and the parameters are determined as follows: $g_0' = 1.4188$, $g_1' = -0.1582$, $\lambda' = 0.2873$, $\delta' = 0.5769$ and $\rho' = 0.7521$. The behavior of the hysteresis compensator with the optimized parameters is presented in Fig. 8.10(a) and (b). Figure 8.10(a) shows the inverse hysteresis curve between the output of the compensator (u_{PI}) and the desired output response (v_d) imported to the compensator. Figure 8.10(b) compares the responses of experimental hysteresis output, inverse hysteresis compensator output and the desired output, and shows that the designed P-I inverse hysteresis compensator achieves the desired behavior of the expected inverse hysteresis compensator in Fig. 5.4. The performance of the inverse P-I hysteresis

compensator on minimizing the hysteresis for system linearization is highlighted in Fig. 8.10(c) and (d). Plot (c) compares the output curve of the linearized system (linearized system output $[v]$ versus reference $[v_d]$) with the hysteresis curve of the system without hysteresis compensation (hysteresis output $v.s.$ reference $[v_d]$). The maximum tracking error of the inverse hysteresis compensator is shown in plot (d). The tracking error at steady-state stage is less than 1.3%, which reveals the performance of the inverse hysteresis compensator on minimizing the hysteresis for system linearization.

Next, the inverse compensator is validated in experiments to the x-axis piezo system to compensate hysteresis behavior over different frequency ranges. The reference trajectories for the validation are triangular trajectories and nanofabrication trajectories at 1 Hz, 10 Hz, and 50 Hz. The tracking results are compared with the simulation output of the linear dynamics $G(z)$ in Fig. 8.11 [triangular trajectories tracking results] and Fig. 8.12 [nanofabrication trajectories tracking results]. The maximum tracking error for tracking triangular trajectories is less than 2.0% for frequencies up to 50 Hz. The maximum error for tracking nanofabrication trajectories is less than 2.2%. The results show the hysteresis compensator can compensate for the hysteresis well and leave behind only the dynamics.

8.1.3 Controller Implementation for x-axis of the Nanopositioner

A PID controller is designed for the linear dynamics $G(z)$ to represent the $G_c(z)$ in the block-diagram of the linear control system in Fig. 3.1(a). The transfer function of the PID controller is:

$$G_c(z) = k_p + k_i \frac{T_s z}{z-1} + k_d \frac{z-1}{T_s z}, \tag{8.5}$$

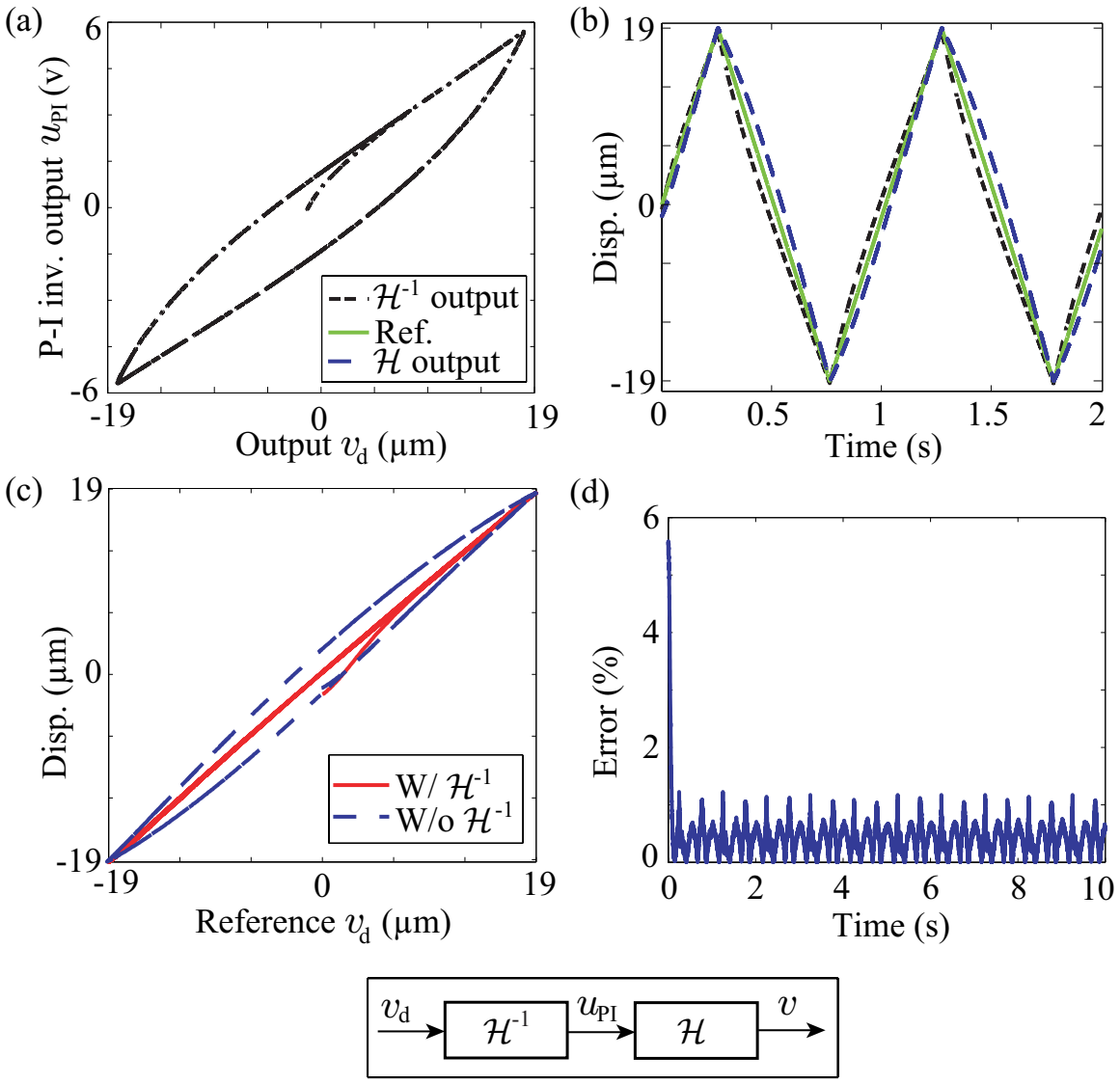

Figure 8.10: (a) The inverse hysteresis compensator response. (b) The comparison between the hysteresis response (blue line), the inverse hysteresis response and the desired reference. (c) The hysteresis curves for the piezoactuator with (solid line) and without (dash line) feedforward compensation. (d) The tracking error between the compensation system output and the reference.

where $T_s = 10$ kHz is the sampling frequency, the controller parameters are tuned following the process discussed in Section 7.4 to $k_p = 0.02$, $k_i = 1000$, $k_d = 0.0001$. The performance of the PID controller to a step reference is shown in Fig. 8.13. The result shows the open-loop response without controller has significant overshoot

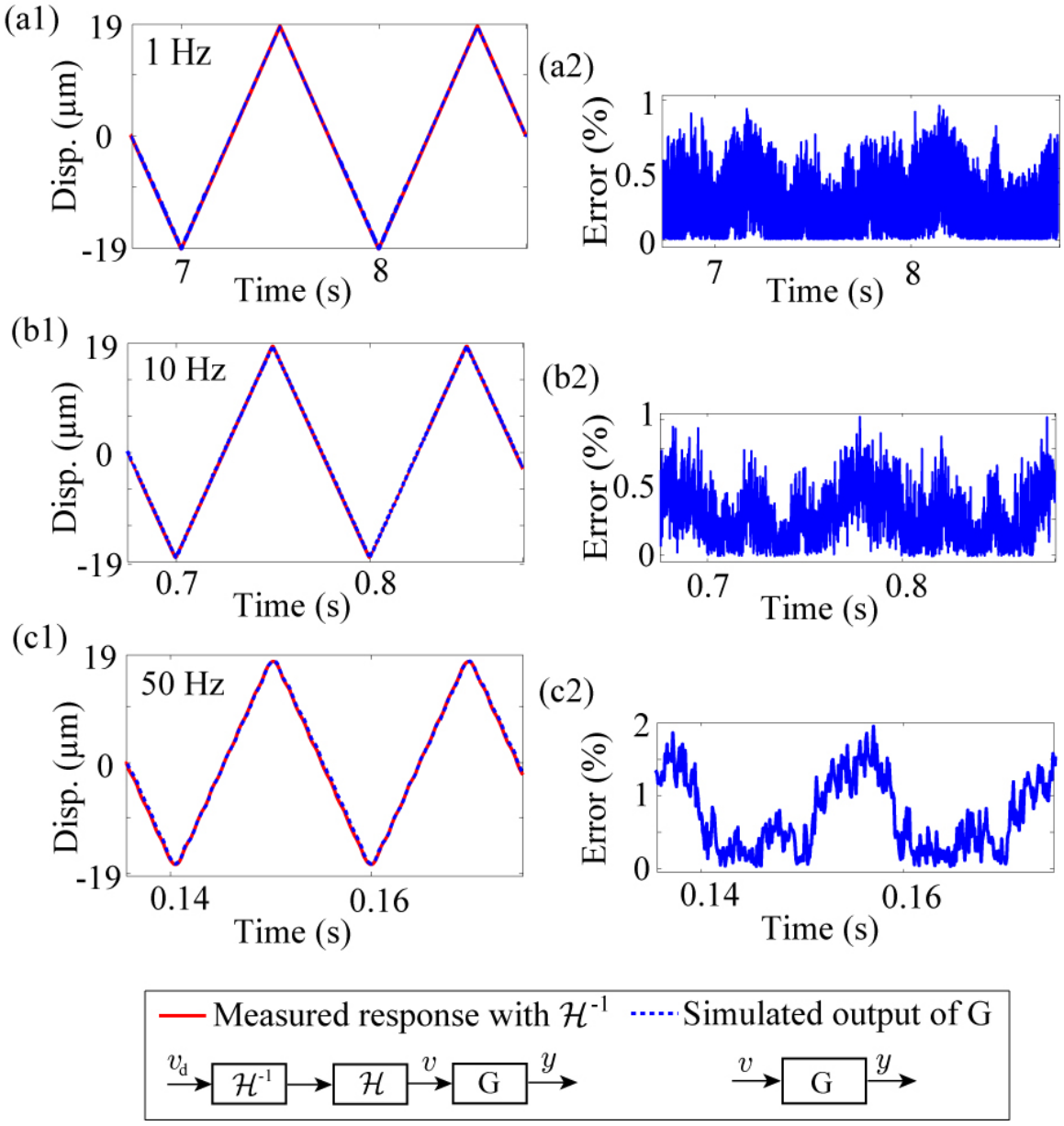

Figure 8.11: Validating cascade model by compensating for hysteresis with triangular trajectories as inputs. Comparison of output and error vs. time plots for: (a1) and (a2) 1 Hz; (b1) and (b2) 10 Hz; (c1) and (c2) 50 Hz.

and noticeable creep. By applying the PID control, the overshoot and creep effect are minimized. The performance of the PID controller for tracking a triangular trajectory and a nanofabrication trajectory is discussed in Section 8.2.

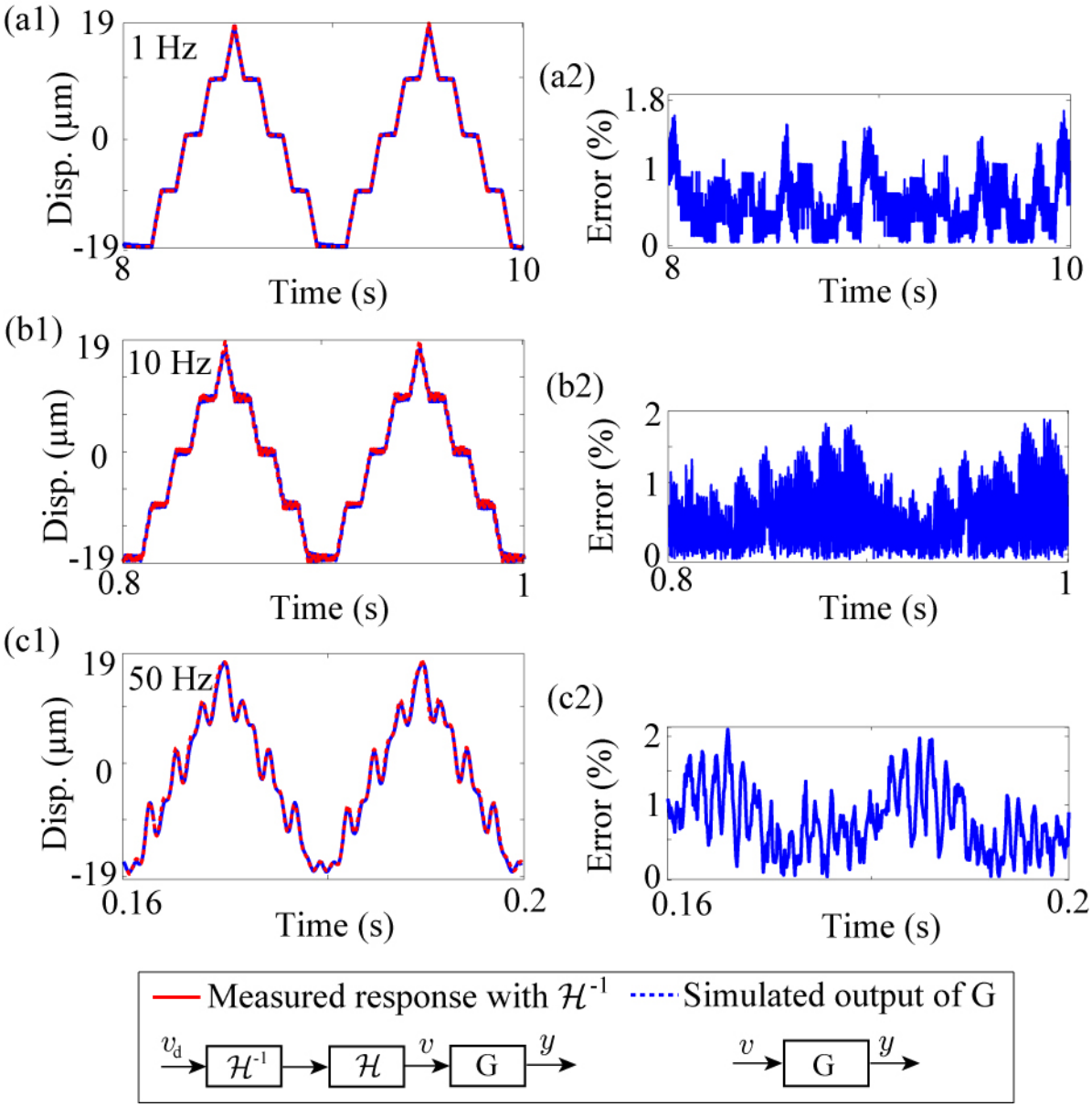

Figure 8.12: Validating cascade model by compensating for hysteresis with input signals used for nanofabrication. Comparison of output and error vs. time plots for: (a1) and (a2) 1 Hz; (b1) and (b2) 10 Hz; (c1) and (c2) 50 Hz.

The RC is designed with $G_c(z)$ for the linear dynamics $G(z)$. The design process follows the procedure in Section 7.4 and the stability conditions provided in

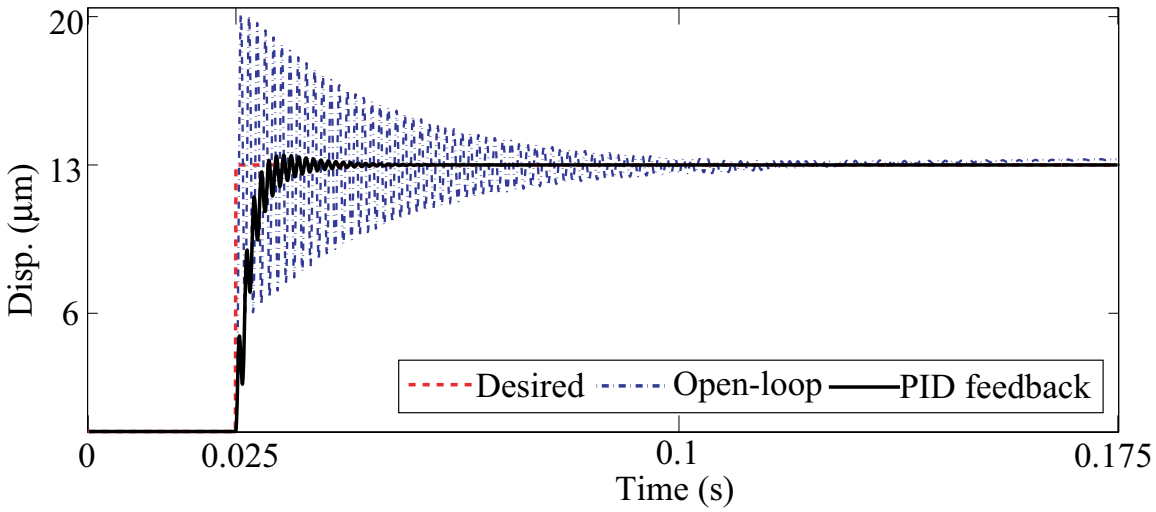

Figure 8.13: Performance of the PID controller for tracking step response.

Section 3.2. The low-pass filter is chosen as

$$Q(z) = \frac{a}{z+b}, \quad \text{with } a = 0.2696 \text{ and } b = -0.7304$$

for cutoff frequency of 500 Hz with sampling frequency of $T_s = 10$ kHz. The selection of the cutoff frequency ω_Q uses the phase response of the $\theta_T(\omega)$ with different $\theta_2(\omega)$ as shown in Fig. 8.14. The inset in Fig. 8.14 shows the $\pm 90^\circ$ crossover frequency versus the phase lead parameter m_2. From the phase response and the inset plot, when there is no phase lead $\theta_2(\omega)$ contributed by the phase lead compensator $P_2(z) = z^{m_2}$ ($m_2 = 0$), the $\pm 90^\circ$ crossover frequency for $\theta_T(\omega) + \theta_2(\omega)$ is approximately 380 Hz. This value sets the maximum cutoff frequency for the low-pass filter to be no higher than 380 Hz and the relative maximum scan rate. However, when $m_2 = 1$, the maximum cutoff frequency of $Q(z)$ can be about 800 Hz. Also the inset plot indicates that, when the $m_2 > 1$, the higher values of m_2 show no improvement in the crossover frequency. In the nanofabrication implementations, the chosen cutoff frequency for $Q(z)$ is 500 Hz and phase lead of $m_2 = 1$ is used. Therefore, the maximum fabrication

rate in the x-axis is chosen as 50 Hz. It is noted that for higher rate fabrication, the cutoff frequency can be increased, but only up to 800 Hz when $m_2 = 1$ (see Fig. 8.14). The 500 Hz cutoff frequency was chosen because it provided a safety margin.

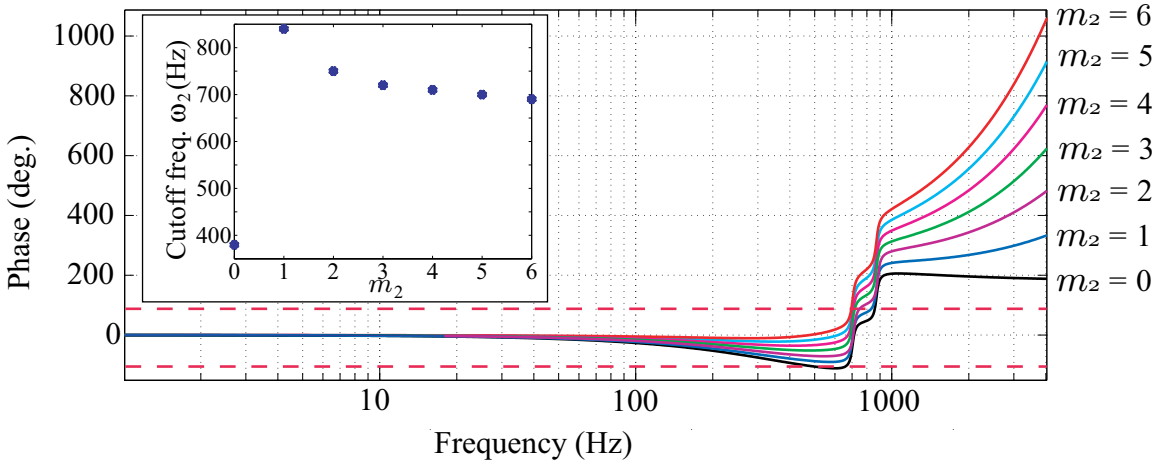

Figure 8.14: Phase response of $\theta_T(\omega) + \theta_2(\omega)$, where the $\theta_2(\omega)$ is contributed by the parameter m_2 of phase lead compensator z^{m_2}. The inset plot shows the cutoff frequency versus the phase lead parameter m_2. As m_2 changes, the frequency range for stability changes.

The RC gain k_{rc} and the m_1 for z^{m_1} are determined to be $k_{rc} = 0.4$ and $m_1 = 4$ respectively for the system stability and tracking performances with the designed $Q(z)$ and $m_2 = 1$. The values of k_{rc} and m_1 are determined in the simulation to track the nanofabrication signal [see Fig. 8.15] for ± 19 μm scan range at 50 Hz for the best tracking performance. The k_{rc} and m_1 share the same tuning process. An example result for optimizing the value of m_1 is shown in Fig. 8.15(b). As shown in the figure, the optimum value is $m_1 = 4$ and this value is also used in the experiments discussed below.

In experiments, the RC, PID controllers and the $\mathcal{H}^{-1}$ are implemented digitally using the Matlab Simulink and xPC Target. To use xPC Target to implement controllers, the control system is built in Matlab Simulink in discrete-time first on a host computer, then the control system is compiled through *xPC-Target Toolbox* in Matlab

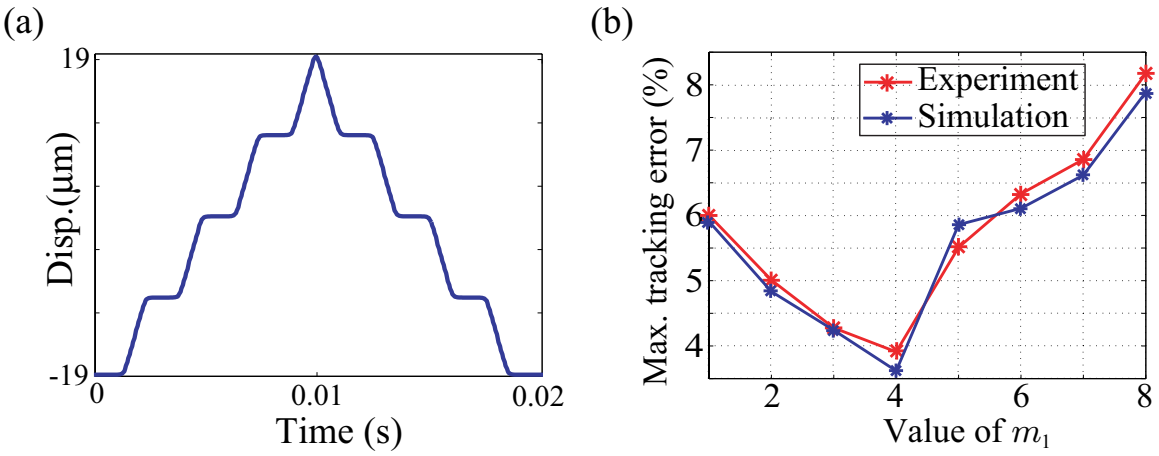

Figure 8.15: (a) The reference trajectory of 50 Hz used in the experiments and simulations for m_1 value determination. (b) The maximum tracking error versus the parameter m_1 of phase lead compensator $P_1(z) = z^{m_1}$.

to executable C-codes. Next, the C-codes is download through a crossover cable to a *Target* computer booted by a *Bootdisk* created on the host computer. Finally, the compiled digital control system is executed on the *Target* computer through a data acquisition system with a closed loop sampling frequency of 10 kHz. This process is briefly presented in Fig. 8.16.

8.1.4 Controller Implementation for y-axis of the Nanopositioner

For the nanofabrication experiments, the y-axis piezoactuator system is controlled by a PID controller to compensate the dynamics and hysteresis effects. The transfer function of the PID controller is:

$$G_c(z) = 4 + 12000\frac{T_s z}{z-1} + 0.08\frac{z-1}{T_s z}, \tag{8.6}$$

where $T_s = 10$ kHz is the sampling frequency, and the controller gains are tuned experimentally. In implementation, the PID controller for y-axis is applied along

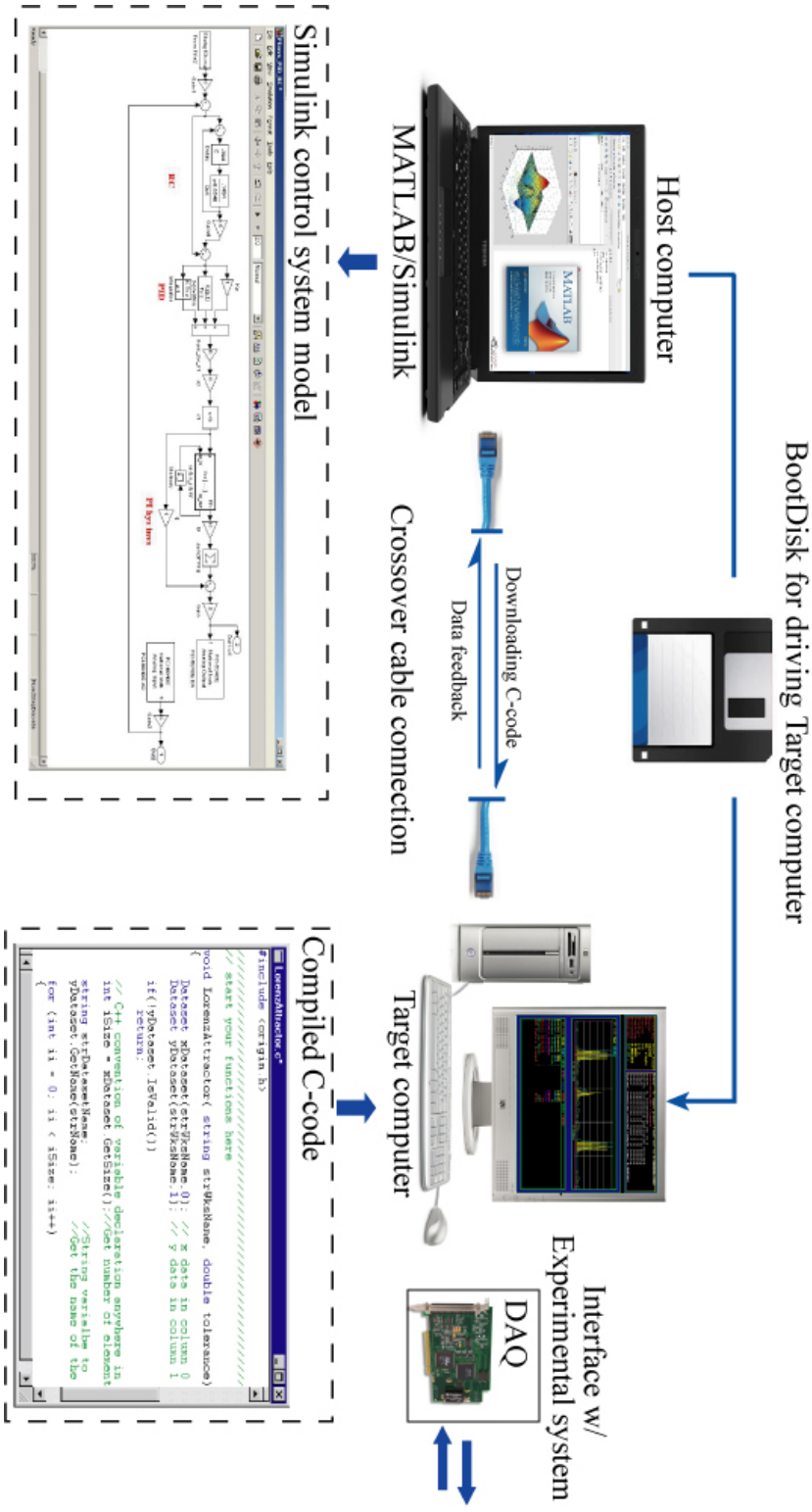

Figure 8.16: An example xPC Target coding process: the C-code of the controllers is generated in Matlab Simulink on a host computer, then is downloaded to the Target computer for execution through a crossover cable.

Table 8.1: Tracking error at last two periods of the triangular trajectory tracking results.

Controller	**1 Hz**		**10 Hz**		**50 Hz**	
	e_{max}	e_{rms}	e_{max}	e_{rms}	e_{max}	e_{rms}
PID	1.8	1.49	4.3	3.12	10.6	7.59
PID+$\mathcal{H}^{-1}$	1.5	1.19	3.6	2.36	9.3	6.80
PID+RC	0.5	0.21	1.3	0.51	2.5	0.89
PID+RC+$\mathcal{H}^{-1}$	0.4	0.16	1.2	0.44	2.2	0.78

with the control system for x-axis using Matlab Simulink and xPC Target.

8.2 Experimental Tracking Results of the Nanofabrication Signals

To implement the repetitive control system for AFM-based nano-hole arrays fabrication, the performance of the control system for tracking triangular trajectories and hole array fabrication trajectories is first validated. In experiments, the reference signals are at 1 Hz, 10 Hz, and 50 Hz for ± 19 μm range displacement [a full range displacement]. The reference trajectories are passed through a two-pole zero-phase-shift filter with a cutoff frequency of 500 Hz to remove high-frequency components before applying it to the closed-loop system. The cutoff frequency for the low-pass filter $Q(z)$ in the RC loop is set at 500 Hz. The $m_2 = 1$ was chosen to give a maximum fabrication frequency of 50 Hz. The RC gain is chosen as $k_{rc} = 0.4$ and $m_1 = 4$ for the best performance and the stability conditions given by Eqs. (3.3) and (4.4).

The tracking results for the PID, PID with $\mathcal{H}^{-1}$, RC, and RC with $\mathcal{H}^{-1}$ for 38 μm scanning at 50 Hz is presented in Fig. 8.17 and Fig. 8.18. The steady-state tracking errors for the controllers scanning and fabricating at 1 Hz, 10 Hz, and 50 Hz are

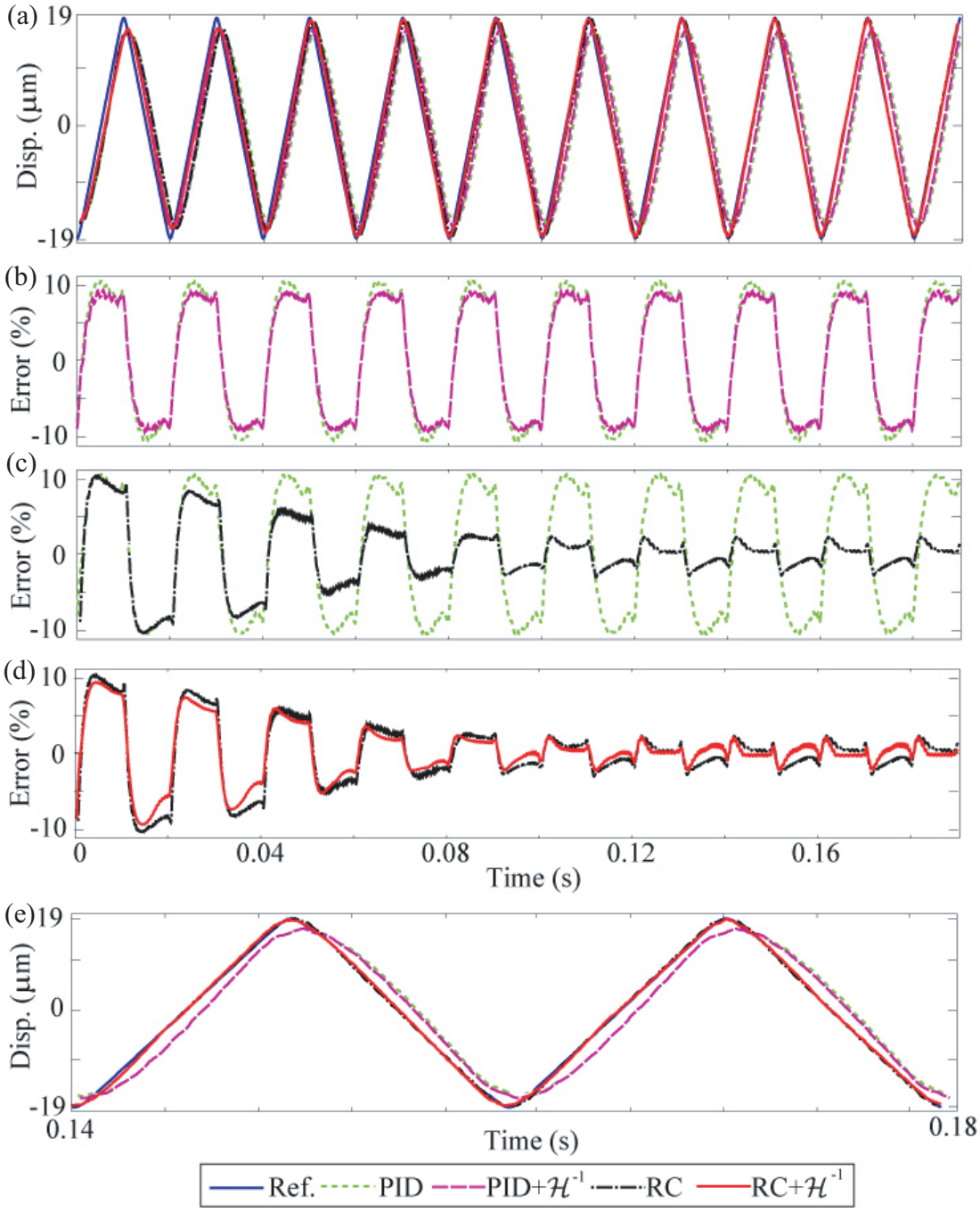

Figure 8.17: (a) Experimentally measured tracking results of triangular trajectory at 50 Hz for PID, PID with $\mathcal{H}^{-1}$, RC, and RC with $\mathcal{H}^{-1}$. Experimentally measured tracking error at 50 Hz comparing (b) PID with and without $\mathcal{H}^{-1}$; (c) PID and RC (without $\mathcal{H}^{-1}$); (d) PID+RC and PID+RC+$\mathcal{H}^{-1}$; and (e) steady-state displacement vs. time

described in Table 8.1 and Table 8.2. In particular, the maximum error $[e_{max}(\%)]$ [Eq. (7.3)] and root-mean-squared error $[e_{rms}(\%)]$ [Eq. (7.5)] are reported. Figure 8.17 and Table 8.1 show the triangular trajectory tracking results, as well as the tracking results for nanofabrication trajectory are in Fig. 8.18 and Table 8.2. Because the action of the repetitive controller is delayed by one scan period, the tracking response for the first period are similar for the PID and RC as shown in Fig. 8.17 and Fig. 8.18. However, after the first period the RC begins to take action as illustrated by the reduction in the tracking error from one cycle to the next. On the other hand, the tracking error of the PID controller persists from one cycle to the next.

The 50 Hz scanning results shown in Figs. 8.17 and 8.18, and Tables 8.1 and 8.2 demonstrate that the RC controller reduces the maximum tracking error from 10.6% to 2.5% compared to the PID for tracking triangular trajectory, and reduces the maximum tracking error from 10.8% to 3.9% for tracking nanofabrication trajectory. The reductions are 76.4% and 63.9% respectively. By adding the $\mathcal{H}^{-1}$ to the PID and RC controllers, an additional reduction on the tracking error is achieved. For example, by adding the $\mathcal{H}^{-1}$ to RC controller, the tracking error of PID controller decreases from 10.6% to 2.2%, a total 79.3% reduction, for triangular trajectory tracking. For the nanofabrication trajectory tracking, the total decrease is 65.4%, and the maximum tracking error is only 3.74%. Therefore, the RC with $\mathcal{H}^{-1}$ enables precision tracking and nanofabrication at higher scan rates, which reveals the implementation of RC and $\mathcal{H}^{-1}$ to AFM-based nano-hole array fabrication can enhance the accuracy and speed of the nanofabrication.

8.3 Nanofabrication Results

The remaining section of this chapter discusses nano-hole arrays pattern fabrication on a PMMA film coated ZnO/Si substrate to validate the performance of the RC sys-

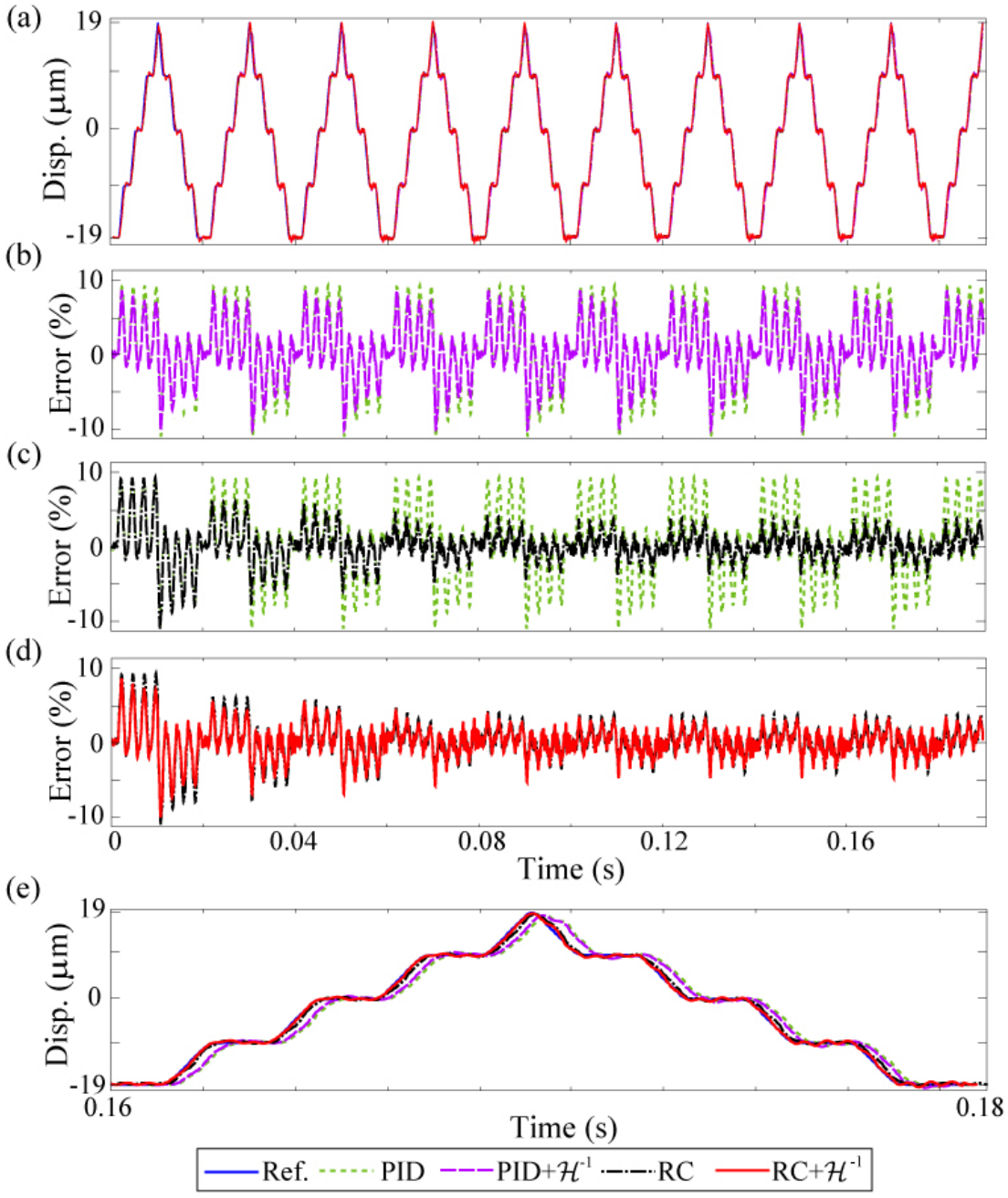

Figure 8.18: (a) Experimentally measured tracking results of nanofabrication trajectory at 50 Hz for PID, PID with $\mathcal{H}^{-1}$, RC, and RC with $\mathcal{H}^{-1}$. Experimentally measured tracking error at 50 Hz comparing (b) PID with and without $\mathcal{H}^{-1}$; (c) PID and RC (without $\mathcal{H}^{-1}$); (d) PID+RC and PID+RC+$\mathcal{H}^{-1}$; and (e) steady-state displacement vs. time

Table 8.2: Tracking error at last two periods of the nanofabrication signal tracking results.

Controller	**1 Hz**		**10 Hz**		**50 Hz**	
	e_{max}	e_{rms}	e_{max}	e_{rms}	e_{max}	e_{rms}
PID	3.90	3.16	5.81	4.38	10.8	8.48
PID+$\mathcal{H}^{-1}$	3.62	2.64	4.96	3.68	10.1	7.80
PID+RC	0.91	0.40	1.93	0.75	3.90	1.52
PID+RC+$\mathcal{H}^{-1}$	0.87	0.34	1.85	0.69	3.74	1.46

tem on enhancing fabrication precision. By using these nano-hole arrays as templets, ZnO nanowires can be controlled grown within these nano-holes on Si substrate by a hybrid approach. The fabrication of the patterns requires the following process: (1) coating zinc-oxide (ZnO) buffer layer onto the substrate, which is silicon (Si) wafer in this study, as the seed for nanowire growth; (2) spin-coating the resist layer, polymethylmethacrylate (PMMA), onto the ZnO layer for patterning; and (3) patterning the resist layer by force lithography using the nanofabrication system in Fig. 8.4. This section is presented according to above process. Afterwards, the fabrication results are quantified and discussed.

8.3.1 Step 1: Substrates Preparation for Nanofabrication

The aim of this step is to prepare PMMA coated ZnO/Si substrates for fabricating nanno-hole arrays on the PMMA thin film. There are mainly two tasks, which are to deposit ZnO layer to Si wafer, then to spin coat a PMMA resist layer on the surface of ZnO/Si substrates.

The Si wafers are commercially available from UniversityWafer. The ZnO seed layer with a thickness of around 40 nm is coated on the Si wafers for experiments. The Si wafers [P/B (100) 1-10 ohm-cm SSP 380 μm PRIME] are type P with a diameter

of $3''$ and a thickness of 380 μm. The ordination of the Si wafer is $\langle 100 \rangle$ and the resistance is $1 - 10$ ohm-cm. The ZnO seed layer is deposited on the Si wafer by the facility of UniversityWafer, and the ZnO/Si wafers are used as they are purchased.

Several sheets of ZnO/Si wafer are spin coated with PMMA film. The spin coat is produced in a class 10 clean room of the Nanofabrication Laboratory at Pennsylvania State University (Penn State). First of all, these ZnO/Si wafers are washed in acetone with the aid of ultrasonic agitation for 10 minutes, then in isopropanol and distilled water for another 10 minutes respectively. After the preliminary cleaning, the substrates are placed in a steam of high purity nitrogen (N_2) to dry. Next, the ZnO/Si substrates are spin coated with PMMA. PMMA with a molecular weight of 15kg/mol is used as received. A 1wt.% solution of PMMA in anisole is prepared, which is generated using, for example, approximately 1 g of PMMA in 99 g of anisole. The PMMA solution is then spin coated onto the ZnO/Si wafers in two-step spin, which are 500 rpm for 40 s in the first step and 5000 rpm for another 40 s in the second step. Afterwards, these PMMA coated wafers are split into 3 groups to soft bake at $75°C$, $100°C$, and $150°C$ respectively for 30 minutes for different hardness of PMMA films. The film thickness of PMMA coated on the ZnO/Si wafers are around 25 nm. In the study, the PMMA coated ZnO/Si wafer baked at $75°C$ are used, because of the softness. The thickness of the PMMA film is measured by FESEM in the clean room at Penn State and is verified by AFM in EASYLab at UNR as shown in the coming section.

8.3.2 Step 2: Mechanical Scratching with AFM for Pattern Design on PMMA Layer

All the nano-hole arrays are fabricated and imaged using the nanofabrication system in Fig. 8.4 in a regular lab environment at room temperature. In fabrication and imaging, the AFM scan head is operated in a static force mode with a constant force

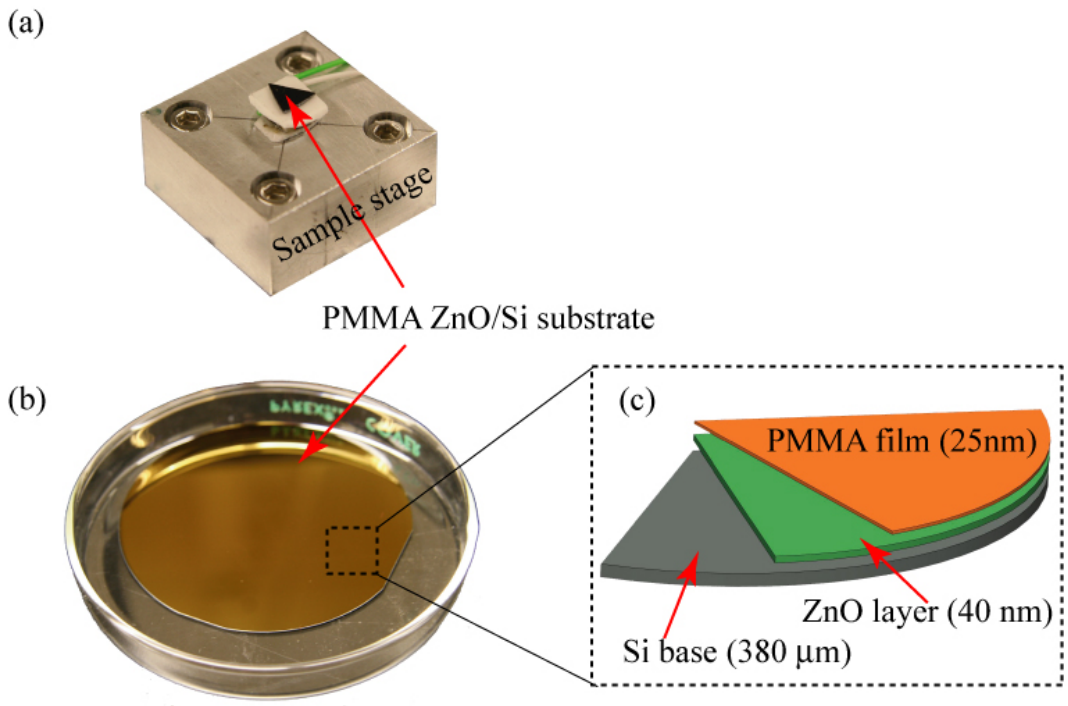

Figure 8.19: photographes of the ZnO/Si substrate coated with PMMA film with a schematic diagram of each layer. (a) The PMMA coated ZnO/Si substrate on the sample stage of the nanopositioner. (b) A photograph of the PMMA coated ZnO/Si wafer. (c) A schematic diagram of the layers of the substrate.

loaded on the AFM tip. Vistaprobes^{TM} silicon tips (T190R-10, nanoScience) with a radius of approximately 10 nm for the curvature of the tip and a spring constant of approximately 48 N/m are employed for AFM mechanical lithography and imaging in static force mode. The AFM scanner positions the cantilever/tip in vertical direction (z-axis) to hold a certain force (load), and the nanopositioner drives the substrate in lateral x and y directions to determine the location of the holes and in z-axis for the AFM tip to punch holes.

Before the imaging and nanofabrication, a PMMA film coated ZnO/Si wafer is cut into custom size to fit the sample platform of the nanopositioner. The wafer is cut using a diamond scribe, and washed in 1% acetone with the aid of ultrasonic agitation for 5 minutes, then in distilled water for another 5 minutes to remove the

dust generated during the wafer cleaving. Then the substrate is adhered to the sample holder of the nanopositioner by a double-side tape as shown in Fig. 8.6(a). The sample holder is made from alumina ceramic sheet because the sheet has high mechanical strength, density and flat surface to minimize the tilt of the substrate on it for high-quality fabrication and imaging. The double-side tape is selected over other glues, since using tapes makes the exchange of the substrate much easier. In this study, the fabrication is operated in normal lab environment instead of clean room, and the particles in air may deposit on the substrate surface, therefore a substrate is not used in fabrication for a long time, and the exchange of the substrate is required.

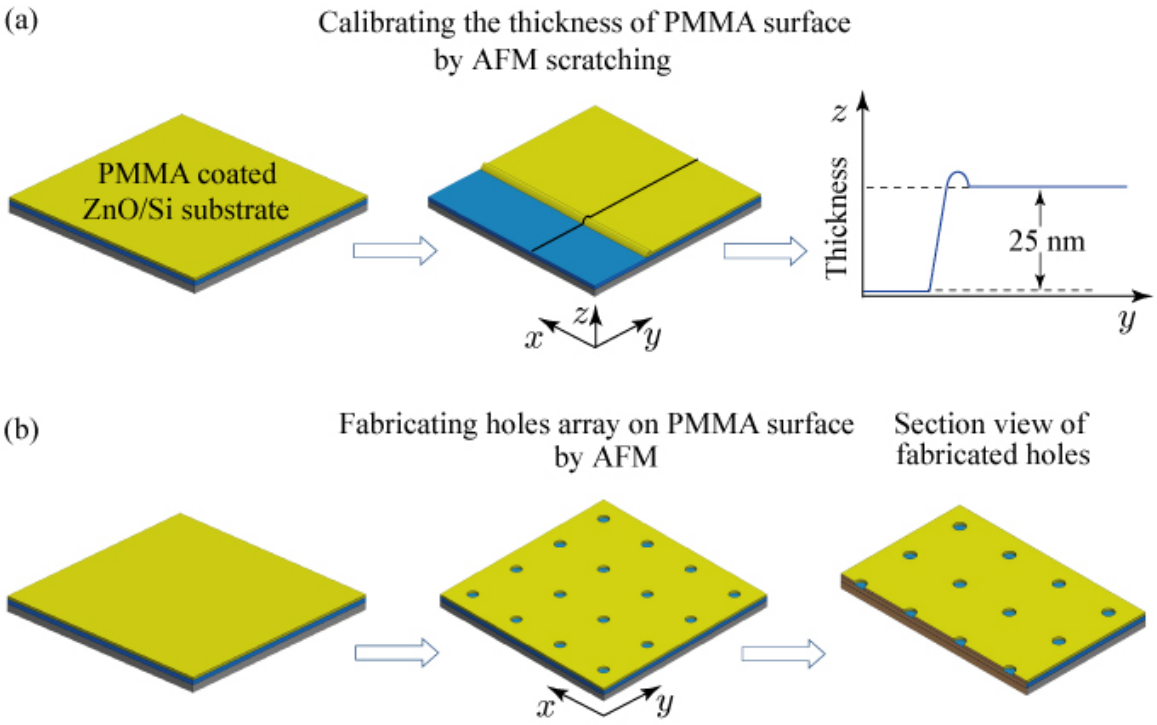

Figure 8.20: Schematic plots of concept tasks for experimental nanofabrication. (a) Calibration of the thickness of the PMMA film on the ZnO/Si substrate. (b) The fabrication of nano-hole array on the PMMA film for ZnO nanowire growth. These results are compared with the standard calibration sample for validation.

A schematic diagram of two main tasks in the nanofabrication experiments is shown in Fig. 8.20. The PMMA thickness verification is a key factor for AFM-based

force lithography to create through holes on PMMA film successfully. After the thickness calibration, nano-hole arrays fabrication is performed at several writing speeds. Before the thickness verification and nanofabrication, the topographical information of the PMMA film is characterized by AFM to give an observation on the PMMA film surface conditions. The results are show in Fig. 8.21. The plot (a) shows a typical AFM topography image, from which it can be seen the color of the PMMA surface is evenly distributed. It reflects the flatness of the surface. Also, a 3-D image of the PMMA film in plot (b) shows the surface condition in another view. The root-mean-square roughness for the PMMA film surface is approximately 0.84 nm.

To validate the thickness of the PMMA film spun on the ZnO/Si substrate using AFM, an engraving force is estimated from the Sneddon formulism of indentation based on the thickness of PMMA film first [189]. By calculation, the force is estimated as 3 μN based the thickness of PMMA determined from FESEM (25 nm). In the AFM system, this engraving force is caused by the bend of the cantilever. Therefore, the force can be determined and monitored through the bend of the cantilever in z-axis. The relation of the engraving force and the bend of the cantilever is described in Fig. 8.22, and is estimated using the mathematical equations in Eq. (8.7) [190].

$$\sigma_{max} = \frac{P}{k} \text{ and } \sigma_{max} = \frac{Pl^3}{3EI}, \tag{8.7}$$

where σ_{max} is the maximum bend of the cantilever under the engraving force P, k is the spring constant of the cantilever, l is the length of the cantilever as shown in Fig. 8.22(a), E is the young's modulus, and I is the moment of inertia. $I = bh^3/12$, where b and h is the width and thickness of the cantilever shown in Fig. 8.22(a). According to the equation, the deflection at the tip end of the cantilever should be around 71 nm for the cantilever to generate an engraving force of 3 μN. Figure 8.22(b) shows the experimental deflection result of 71 nm for the cantilever in z-axis, which

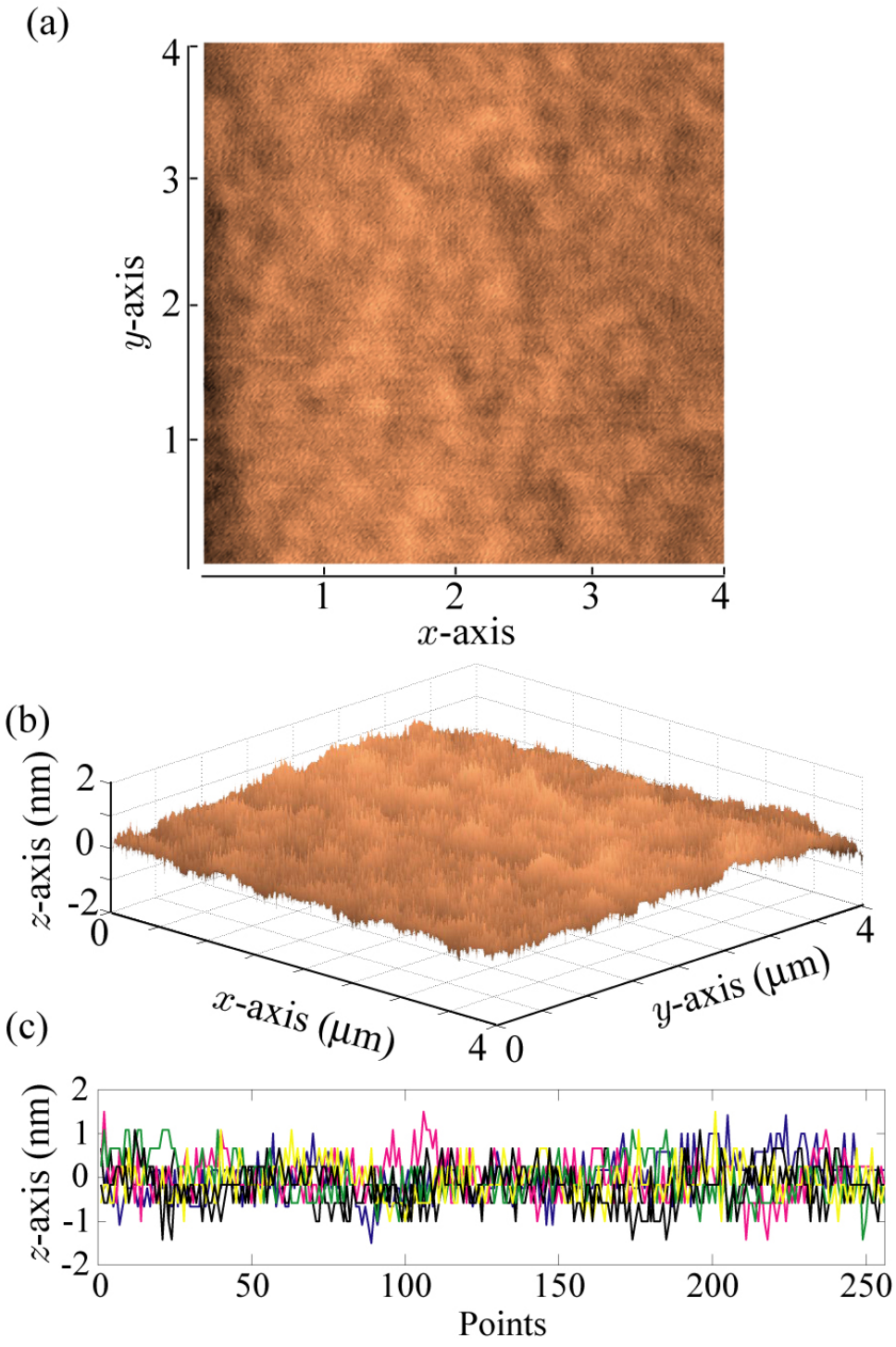

Figure 8.21: (a) Topography image of the PMMA film spun on the ZnO/Si substrate. (b) A 3-D image of the PMMA surface. (c) The topological information of z-axis.

is measured by operating the AFM cantilever in static force mode with a high PID gain for z-axis controller, and is determined by comparing with the cantilever deflection output for measuring a calibrations sample with a feature height of 19 nm [see Eq. (8.8)] with a small PID gain.

$$\frac{\sigma_{z1}}{19\ nm} = \frac{\text{Signal output of } z\text{-axis for } \sigma_{z1}}{\text{Signal output of } z\text{-axis for } 19\ nm}, \tag{8.8}$$

where σ_{z1} represents the bend of the cantilever for an engraving force of 3 μN. In fabrication experiments, the output of the cantilever in z-axis for a bend of 71 nm is used as a feedback signal for the PID controller in z-axis to maintain an engraving force of 3 μN.

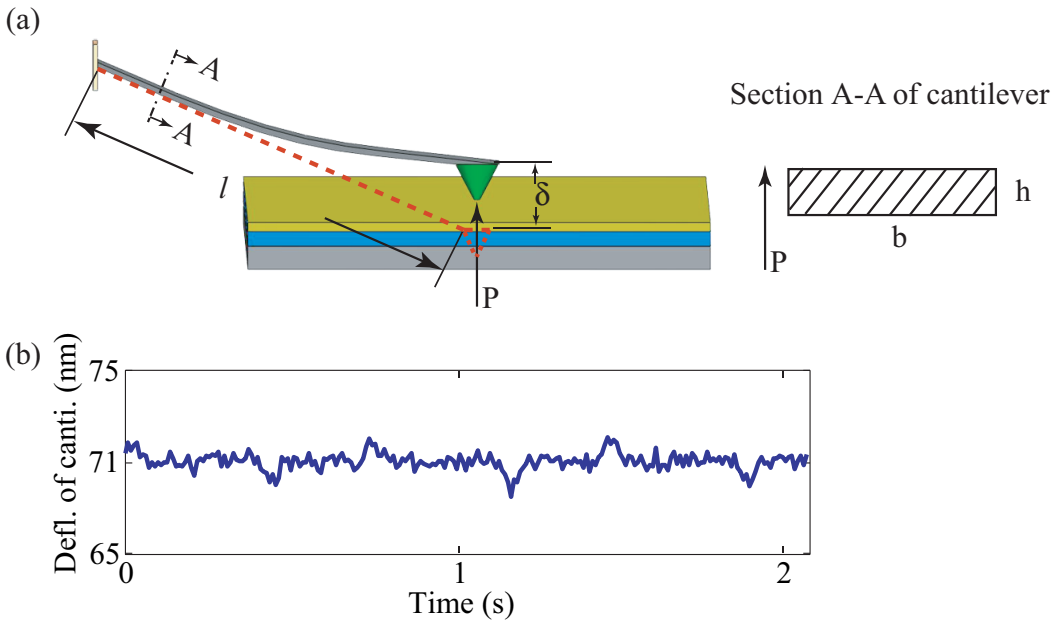

Figure 8.22: (a) The conceptual diagram of the force relative to the bend of the cantilever, where P is the load, l is the length of the cantilever, h is the thickness of the cantilever in the direction of load P, b is the width of the cantilever, and δ is the deflection of the cantilever under the load P. (b) The experimental deflection result of cantilever for a static force of 3 μN for nanofabrication.

Now, the thickness of the PMMA film is characterized through scratching the

film. The film is scratched using a Vistaprobes^{TM} Silicon cantilever/tip (a radius of approximately 10 nm for the tip curvature), and the tip is positioned by the AFM scan head in x, y, and z-axes. These scratches are produced with a engraving load of 3 μN at the tip end of the cantilever and with the z-axis controller disabled. The images of the scratched surface are presented in Fig. 8.23(a1), (b1) and (c1), and the depth of the scratch [plots (a2), (b2), and (c2)] is determined by comparing the z-axis difference of the scratched feature images with the z-axis difference of the calibration sample images as shown in Fig. 8.23(e1) and (e2). From these image results, it can be seen that the vertical distance between the scratched surface and the unscratched surface is about 19 nm, when it is scratched once, as shown in plots (a1) and (a2). By scratching two more times, the vertical distance is increased to 25 nm [see plots (b1) and (b2)]. Then another two more trials is added, and the distance becomes 28 nm as shown in plots (c1) and (c2). However, by increasing the trails from 5 to 8 does not enlarge the vertical distance between the scratched and unscratched surface, therefore the PMMA film is scratched through, and the AFM tip touches the ZnO surface. Finally, the thickness of the PMMA film is around 28 nm in the lab environment.

8.3.3 Experimental Nanofabrication Results

With the use of the calibrated engraving force 3 μN, the PMMA film coated ZnO/Si substrate is fabricated by a Vistaprobes^{TM} AFM tip to form a nano-hole arrays pattern. In fabrication experiments, the nanofabrication signals in Fig. 8.1(b) to (d) are applied to the z, x, and y-axes of the nanopositioner respectively to position the PMMA film coated ZnO/Si substrate relative to the AFM tip. The designed RC and P-I inverse hysteresis compensator are implemented to the x-axis of the piezo-based long-range nanopositioner to demonstrate its ability on ensuring the even spacing and size of nano holes. The performance of RC with inverse hysteresis compensator

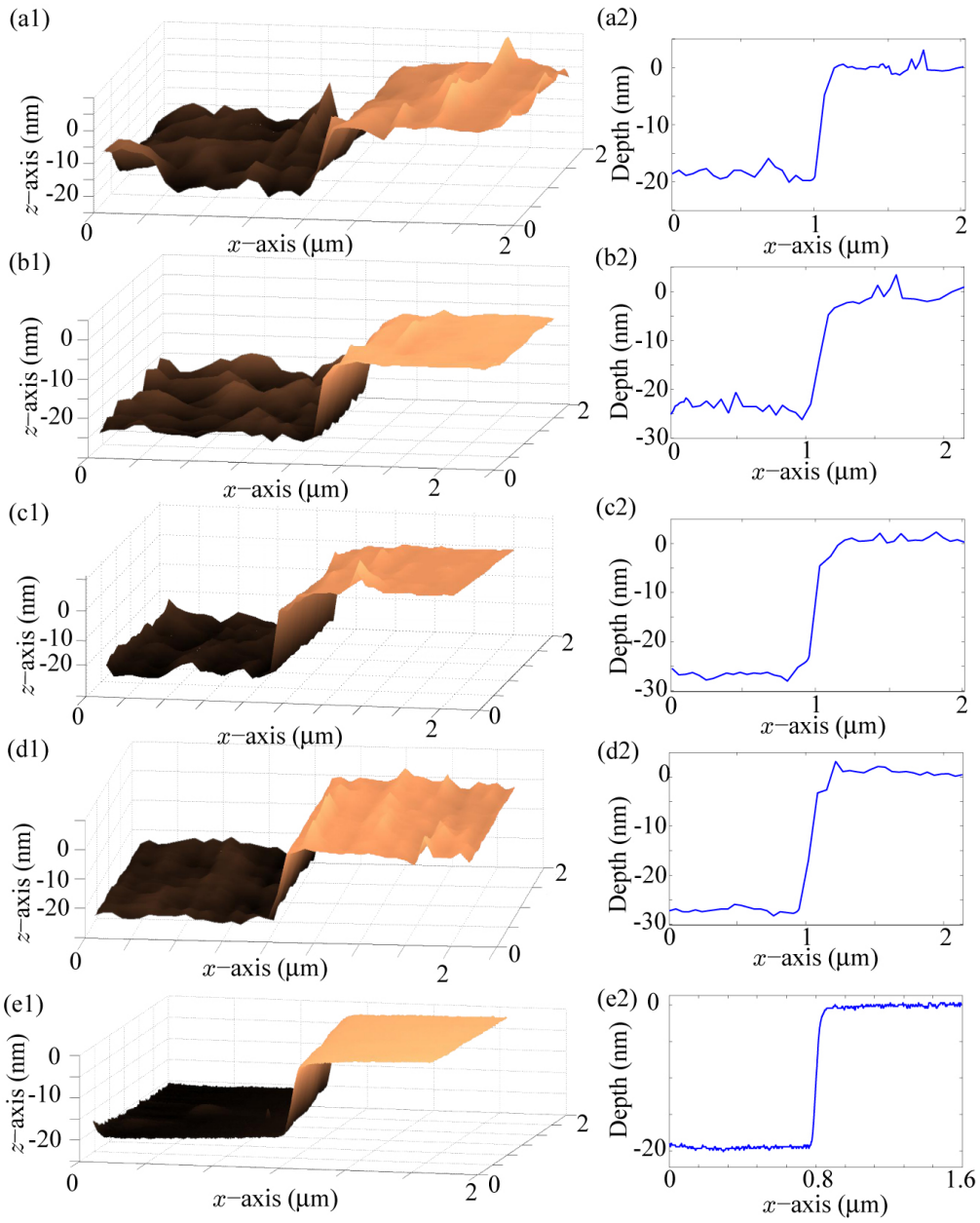

Figure 8.23: The thickness measurement of a PMMA film by AFM scratching. (a1) and (a2) The image and line map of a PMMA surface scratched for 1 trial. (b1) and (b2) The image and line map of a PMMA surface scratched for 3 trial. (c1) and (c2) The image and line map of a PMMA surface scratched for 5 trial. (d1) and (d2) The image and line map of a PMMA surface scratched for 8 trial. (e1) and (e2) The image and line map of a standard calibration sample with a feature hight of 19 nm.

is compared with PID + $\mathcal{H}^{-1}$ and open-loop results to reveal the benefit of RC and inverse hysteresis compensator in precise positioning in AFM based nanofabrication. On the slow scanning y-axis, a PID controller is applied to ensure the fabrication accuracy of the hole array in y-axis. However, the positioning accuracy in the fast scanning x-axis of the piezo-based nanopositioner is the focus of this study.

The AFM images of the PMMA film surface after patterning are shown in Fig. 8.24. These images are scanned using the NanoSurf AFM scan head and nanopositioner. The AFM scan head is operated in static force mode with a constant load of 10 nN on the AFM tip and with the z-axis PID controller on. The z-axis controller output to the cantilever is collected as the topological information of the PMMA film surface to create images. The nanopositioner drives the substrate in x, y-axis for scanning. The scanning ranges in x and y-axes is 4×4 μm. The scanning rate in x-axis is 0.1 Hz for imaging.

The images in Fig. 8.24 show nano-hole arrays fabricated without controller (open-loop) and with PID + $\mathcal{H}^{-1}$ and RC + $\mathcal{H}^{-1}$ at scanning rates of 1, 10, and 50 Hz. The scanning rate represents the frequency of the nanofabrication signal applied to the x-axis, the fast scanning axis. According to these scanning rates, the fabrication speeds in x-axis are 8 μm/s, 80 μm/s, and 400 μm/s at 1, 10, and 50 Hz respectively, which results in the fabrication speeds for z-axis of the nanopositioner are 2.66 μm/s, 26.6 μm/s, and 133 μm/s. From the image results, it can be observed the effect of the fabrication rate on the quality of the fabricated holes. For example, the fasciated holes of the open-loop at 1 Hz are nearly equally arranged, and the size of the holes are closely even. However, with the fabrication rate increased, for example at 50 Hz, the AFM tip begins to cause damage round the desired nano-holes on the PMMA surface, and holes are not evenly spaced any more. The damage is caused by the vibration of the piezoactuator in x-axis of the nanopositioner during the fabrication.

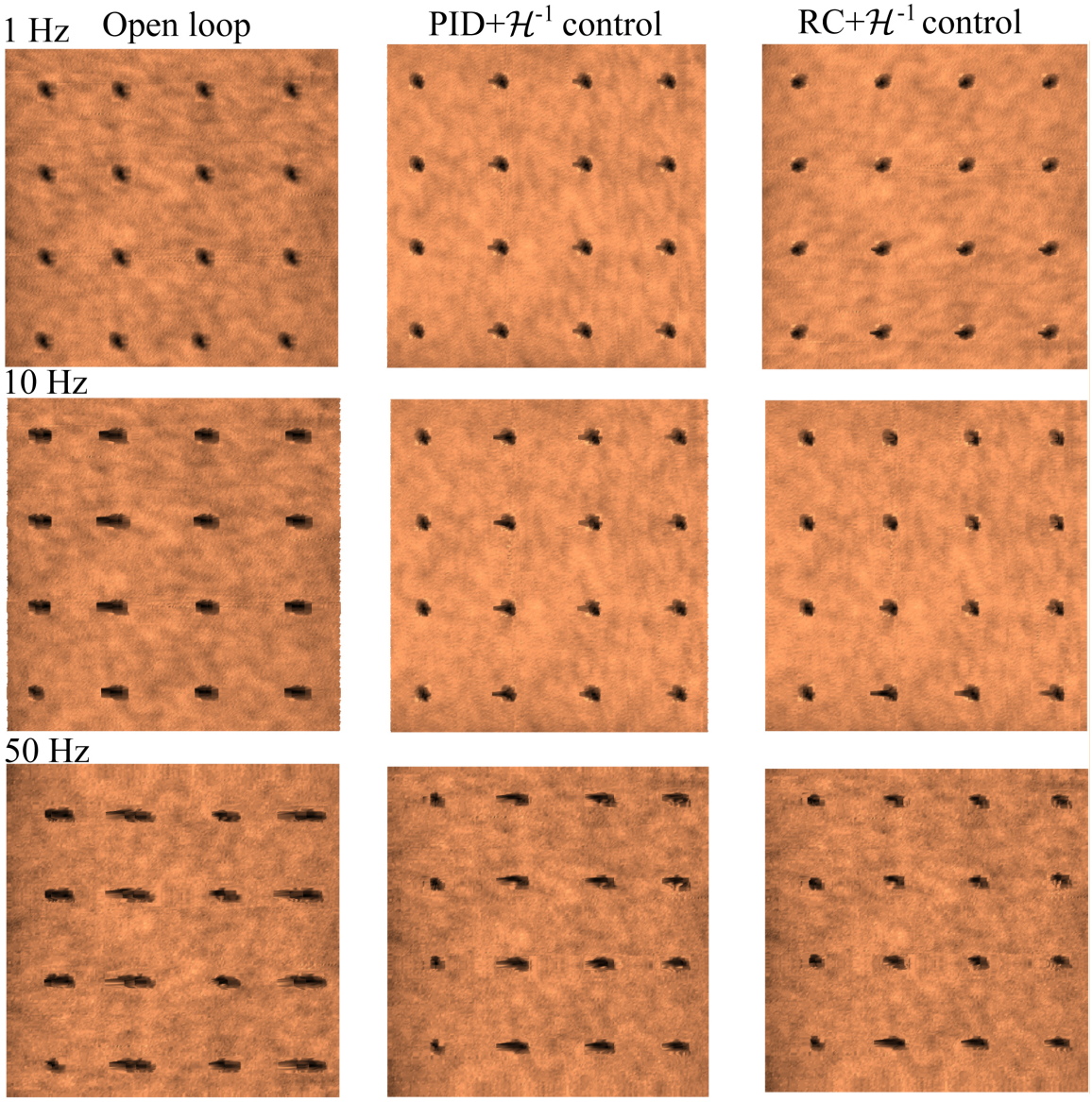

Figure 8.24: Images of nanofabrication results, which compare the fabricated results from open-loop, PID with hysteresis compensator, and RC with hysteresis compensator. The images are measured using the Nanosurf AFM scan head and the long-range nanopositioner at 0.1 Hz.

By implementing the PID with inverse hysteresis compensator, the quality of the fabricated nano-hole arrays is increased. However, the enhancement on the quality is limited, for example at 50 Hz, the damage caused by the AFM tip is still significate. By adding RC to the PID+$\mathcal{H}^{-1}$ control system, an additional reduction on the damage

to the PMMA surface and the positioning error of the hole location is achieved, when the operating cycle increased. The performances of the controllers on reducing the positioning error of nano-holes and the damages to the PMMA surface are further quantified in the next section. As well as the depth of the fabricated holes.

8.3.4 Quantifications of the Fabricated Results

As mentioned before, to develop the ZnO naowaire generator, a precision control of the morphology (shape and size) of the ZnO nanowire, and the alignment and position of the ZnO nanowire arrays are required [191]. The well alignment and morphology of the ZnO nanowire arrays are determined by the nano-holes array patterns. Therefore, the fabricated nano-hole arrays patterns are quantified in this section in term of alignment, morphology (size), and depth.

The quantification results on alignment and morphology (size) are presented in Fig. 8.25 [1 Hz], Fig. 8.26 [10 Hz] and Fig. 8.27 [50 Hz]. These figures show the fabricated nano-hole arrays results from open-loop [plots (a1) to (a3)], PID+$\mathcal{H}^{-1}$ [plots (b1) to (b3)] and RC+$\mathcal{H}^{-1}$ [plots (c1) to (d3)]. Specifically, the plots (a1), (b1), and (c1) show the AFM images of the fabricated 4×4 (columns $\times$ lines) nano-hole arrays, as well as compare the center of the fabricated hole [green dot] with the desired location of the center [brown dot] to show the performance of RC+$\mathcal{H}^{-1}$ on enhancing the alignment accuracy. In these images, the labels No.1.1 and No.4.4 represent the starting and ending points of the fabrication respectively, which tells the AFM tip pouched the first hole at No.1.1 and the last one at No.4.4 in the nanofabrication following the sequence:

$$\text{No.1.1} \longrightarrow \text{No.1.2} \longrightarrow \text{..No.1.4} \longrightarrow \text{No.2.1..} \longrightarrow \text{No.2.4..} \longrightarrow \text{No.3.4..} \longrightarrow \text{No.4.4}$$

The ID for each hole is defined as No.$m.n$, where $m, n = 1, 2, 3, 4$ represent the location

of a hole in line (x-axis direction) and column (y-axis direction). The center of each fabricated nano-hole is defined in Matlab by the deepest location of the fabricated hole. The desired locations of the centers of the holes are plotted on the top of the AFM image of the fabricated nano-hole arrays in Matlab.

The matching errors between the real hole center and the desired hole center are presented in plots (a2), (b2), and (c2) for open-loop, PID+$\mathcal{H}^{-1}$, and RC+$\mathcal{H}^{-1}$ control respectively. The matching error is defined by:

$$e_{center} = \frac{D_1}{D_2} \ ,$$

where D_1 is the distance between the real center and idea center of a hole in x-axis, and D_2 is the idea space between neighbor holes in x-axis. From the plots, it can be seen the RC+$\mathcal{H}^{-1}$ enhances the alignment accuracy by reducing the centering error between the fabricated hole center and the desired hole center. For example, at 50 Hz fabrication [see Fig. 8.27], by applying PID+$\mathcal{H}^{-1}$ control, the maximum centering error of open-loop is reduced from 19.7% to 2.45%, an approximately 87.5% reduction. Then adding RC to the PID+$\mathcal{H}^{-1}$ control system contributes an additional 81.6% reduction on the centering error to the PID+$\mathcal{H}^{-1}$ control system. By RC+$\mathcal{H}^{-1}$ control, the centering difference between the real and idea locations at steady-stage is only about 4.5 nm comparing to the idea spacing of 1 μm, a centering error of approximately 0.45%.

The quantification on the morphology of the fabricated holes is achieved through determining the size and shape of the fabricated holes in x-y surface. The shape of the nano-hole can be determined through the shape of the AFM tip used in the fabrication. For example, rectangular shape holes can be fabricated using an AFM tip with a rectangular shape. The quantification results on the size of the nano-hole are shown in plots (a3), (b3) and (c3) of Figs. 8.25, 8.26 and 8.27 for open-loop,

PID+$\mathcal{H}^{-1}$ and RC+$\mathcal{H}^{-1}$ respectively. From the Fig. 8.24, it can be visually seen the effects of fabrication speed and the dynamics and hysteresis of the piezo-based nanopositioner on the size of the fabricated holes; as well as the performance of the PID+$\mathcal{H}^{-1}$ and RC+$\mathcal{H}^{-1}$ on reducing the surface damage caused by the AFM tip through compensating the dynamics and hysteresis effects.

The quantification results in plots (a3), (b3), and (c3) are calculated by comparing the size of the fabricated holes with the size of hole No.1.1 using the following equation:

$$\text{Hole size ratio} = \frac{S_{m.n}}{S_{1.1}},$$

where $S_{m.n}$ represents the size of any hole in the fabricated 4×4 nano-hole arrays with $m, n = 1, 2, 3, 4$, and $S_{1.1}$ is the size of the hole No.1.1. The size of the hole is calculated following the logic described in Fig. 8.28. The hole No.1.1 is selected as a reference hole for size quantification, because the hole No.1.1 as the starting point of the fabrication is not affected by the dynamics and hysteresis of the piezoactuator. Therefore, ideally, all holes in the 4×4 nano-hole arrays should have the same size and shape as the hole No.1.1. The quantification results show that the RC+$\mathcal{H}^{-1}$ reduces the surface damage around the fabricated hole. For example, at 50 Hz, the maximum hole size ratio of open-loop fabrication is about 3.5. By adding PID+$\mathcal{H}^{-1}$, the maximum hole size ratio is reduce to 2.5. Then adding the RC to PID+$\mathcal{H}^{-1}$ reduces the hole size ratio to 1.28 at the steady stage (the line 3 and line 4), which means, by using RC + $\mathcal{H}^{-1}$, the surface damage caused by the AFM tip around the fabricated hole is about 28% of the desired hole size. However, with no compensation of the hysteresis and dynamics, the surface damage is about 250% of the desired hole size.

The quantification on the depth of the fabricated nano-holes is shown in Fig. 8.29 for fabrication at 1 Hz, Fig. 8.30 for 10 Hz fabrication, and Fig. 8.31 for 50 Hz

fabrication. The plots (a1), (b1) and (c1) are 3-D images of the fabricated hole arrays of open-loop, PID+$\mathcal{H}^{-1}$, and RC+$\mathcal{H}^{-1}$ respectively. The plots (a2), (b2) and (c2) are the depth of holes in an example line, which are results of open-loop, PID+$\mathcal{H}^{-1}$, and RC+$\mathcal{H}^{-1}$ control system respectively. The results show that, by driving the z-axis stage of the piezo-based nanopositioner to move in a range of 100 nm, the hole depth of 28 nm is achieved at different fabrication rate with or without controller. However, the shape of the cross-section of the fabricated hole bottom is changing while the fabrication speed is increasing. For example, the bottom of the open-loop fabricated hole changes from a desired dot shape [see plots (a2) in Fig. 8.29] into a line shape [see plots (a2) in Fig. 8.31] when the fabrication rate increases from 1 Hz to 50 Hz. The changing in the shape is caused by the dynamics and hysteresis in the piezoactuator. The shape of the bottom of the hole will affect the shape and consequently the property of the grown ZnO nanowire. By applying PID+$\mathcal{H}^{-1}$, the shape of the cross-section of the hole at high fabrication rate begins to recover. However, there are still line shapes in some of the fabricated holes [see plots (b2) in Fig. 8.31]. Adding RC to the PID+$\mathcal{H}^{-1}$, the desired dot shape for the bottom of the fabricated hole is achieved at steady-stage [see plots (c2) in Fig. 8.31].

8.4 Summary

In summary, this chapter discussed the implementation of the RC and the inverse P-I hysteresis compensator for AFM-based fabrication of nano-hole arrays. The process involves modeling the hysteresis and dynamics of the piezo-based long-range nanopositioner, design of the inverse hysteresis compensator, PID, and RC controllers, and preparation of PMMA coated ZnO/Si substrate. The experimental results show that the proposed RC and inverse P-I hysteresis compensator can achieve high-precision positioning for fabricating nano-hole arrays patterns. The results show good align-

ment, positioning, and morphology of the nano-holes for ZnO nanowire growth. Additionally, when compared to conventional PID feedback approach, the RC approach provides additional error reduction with respect to feature alignment and morphology. It is demonstrated that the RC approach can be used in AFM-based nanofabrication, where tracking of periodic trajectories is required.

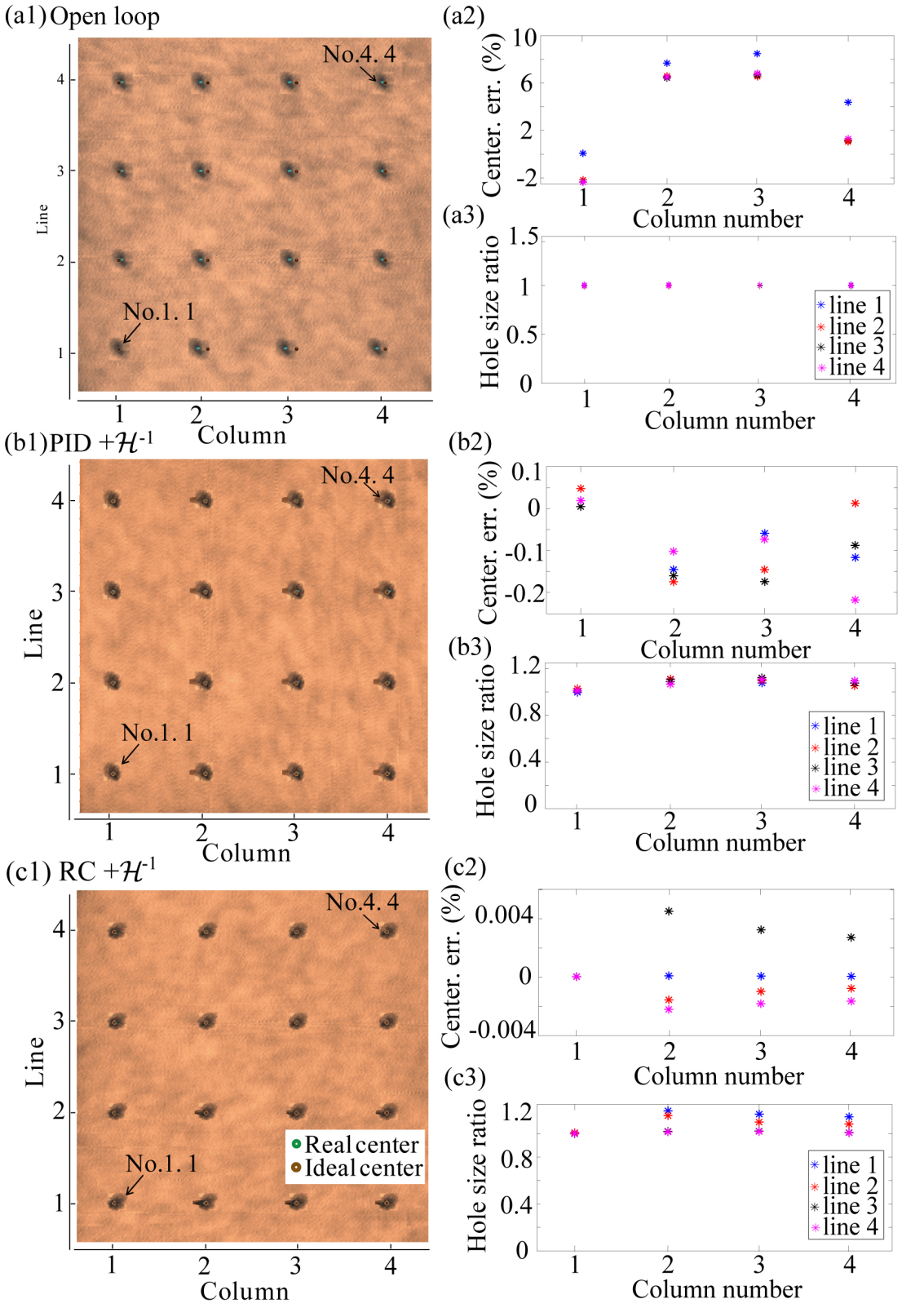

Figure 8.25: Fabrication results at 1 Hz: (a1) Image of the fabricated results of open-loop; (a2) the matching error between the real center of the fabricated holes and the desired hole center; (a3) the ratio of the size of the fabricated holes compared with the hole No.1.1. (b1) and (c1) Images of the fabricated results of PID + $\mathcal{H}^{-1}$ and RC + $\mathcal{H}^{-1}$ respectively; (b2) and (c2) the matching error between the real center of the fabricated holes and the desired hole center for PID and RC respectively; (b3) and (c3) the ratio of the size of the fabricated holes compared with the hole No.1.1 for PID + $\mathcal{H}^{-1}$ and RC + $\mathcal{H}^{-1}$ respectively.

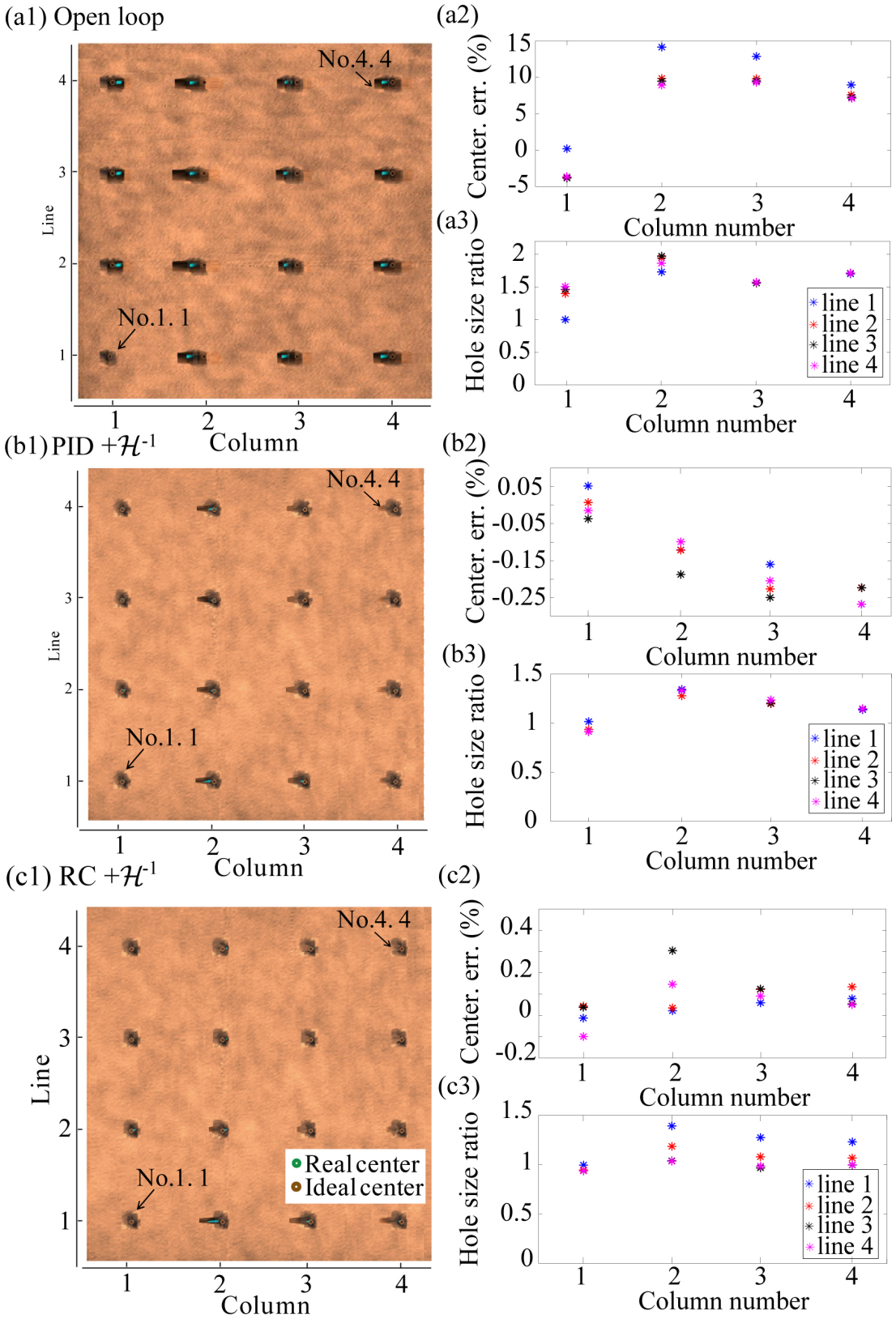

Figure 8.26: Fabrication results at 10 Hz: (a1) Image of the fabricated results of open-loop; (a2) the matching error between the real center of the fabricated holes and the desired hole center; (a3) the ratio of the size of the fabricated holes compared with the hole No.1.1. (b1), (b2), and (b3) are the image, matching error of centering, and hole size results from PID + $\mathcal{H}^{-1}$. (c1), (c2), and (c3) are from RC + $\mathcal{H}^{-1}$.

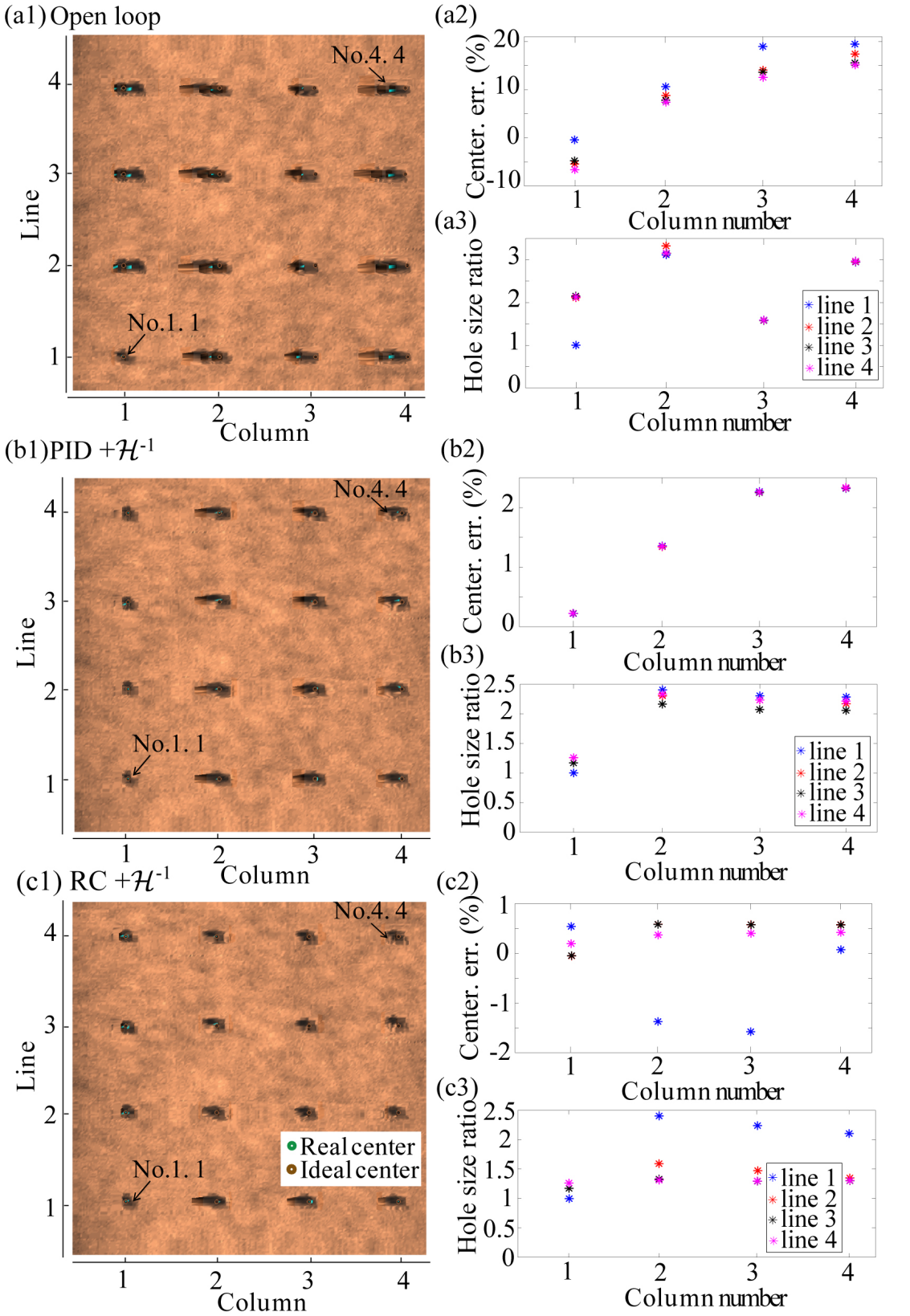

Figure 8.27: Fabrication results at 50 Hz: (a1), (a2), and (a3) are the image, matching error of centering, and hole size results from open-loop. (b1), (b2), and (b3) are from PID + $\mathcal{H}^{-1}$. (c1), (c2), and (c3) are from RC + $\mathcal{H}^{-1}$.

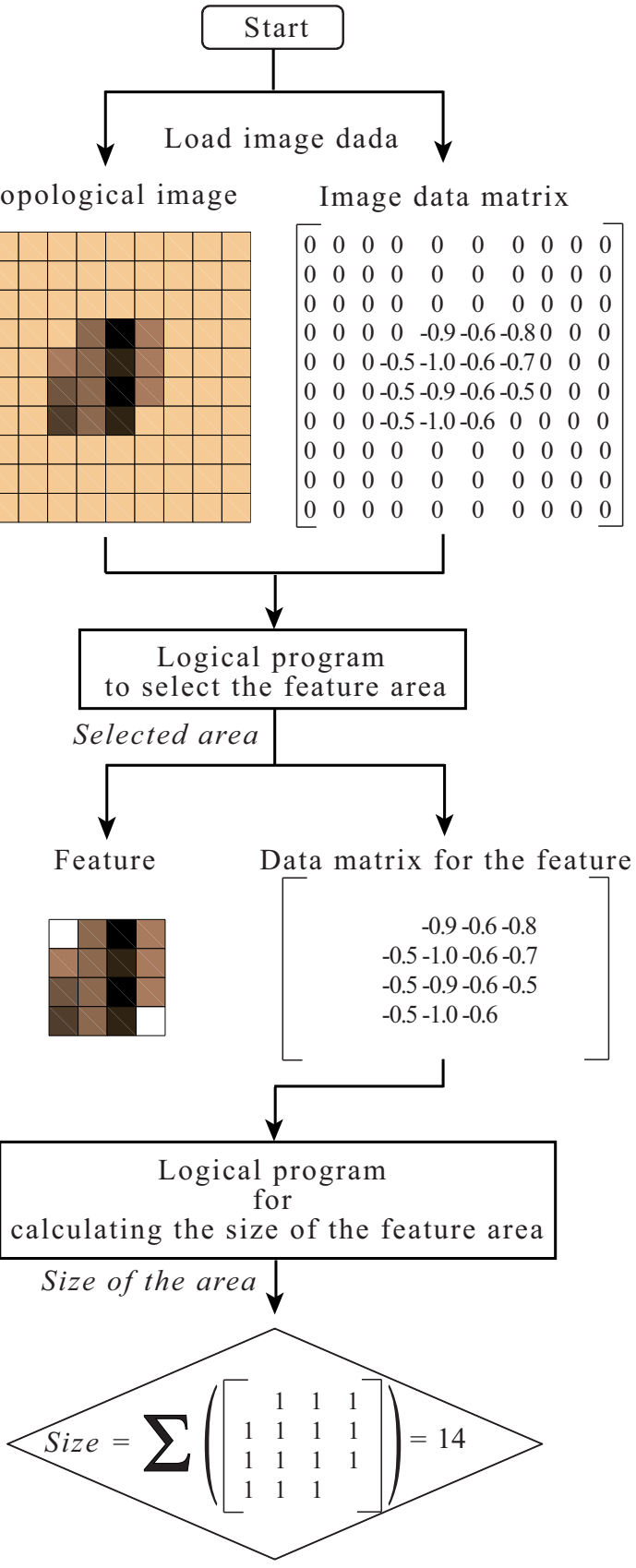

Figure 8.28: Schematic diagram of the logic for calculating the size of the fabricated holes.

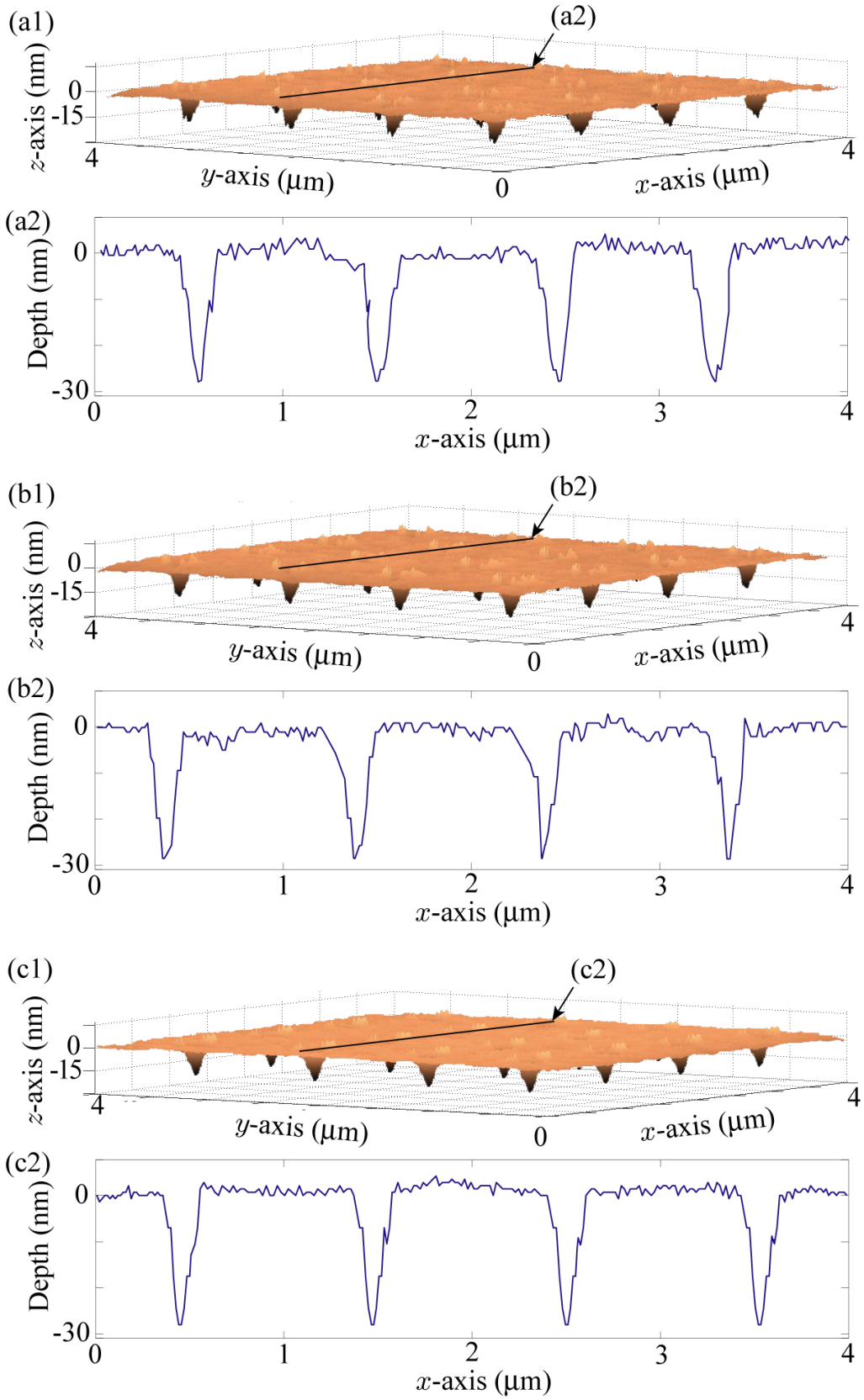

Figure 8.29: Depth calibration for fabricated holes at 1 Hz. (a1) and (a2) The 3-D image of the fabricated holes of open-loop and the depth of an example hole line. (b1) and (b2) The 3-D image of the fabricated holes of PID+$\mathcal{H}^{-1}$ and the depth of an example hole line. (c1) and (c2) The 3-D image of the fabricated holes of RC+$\mathcal{H}^{-1}$ and the depth of an example hole line.

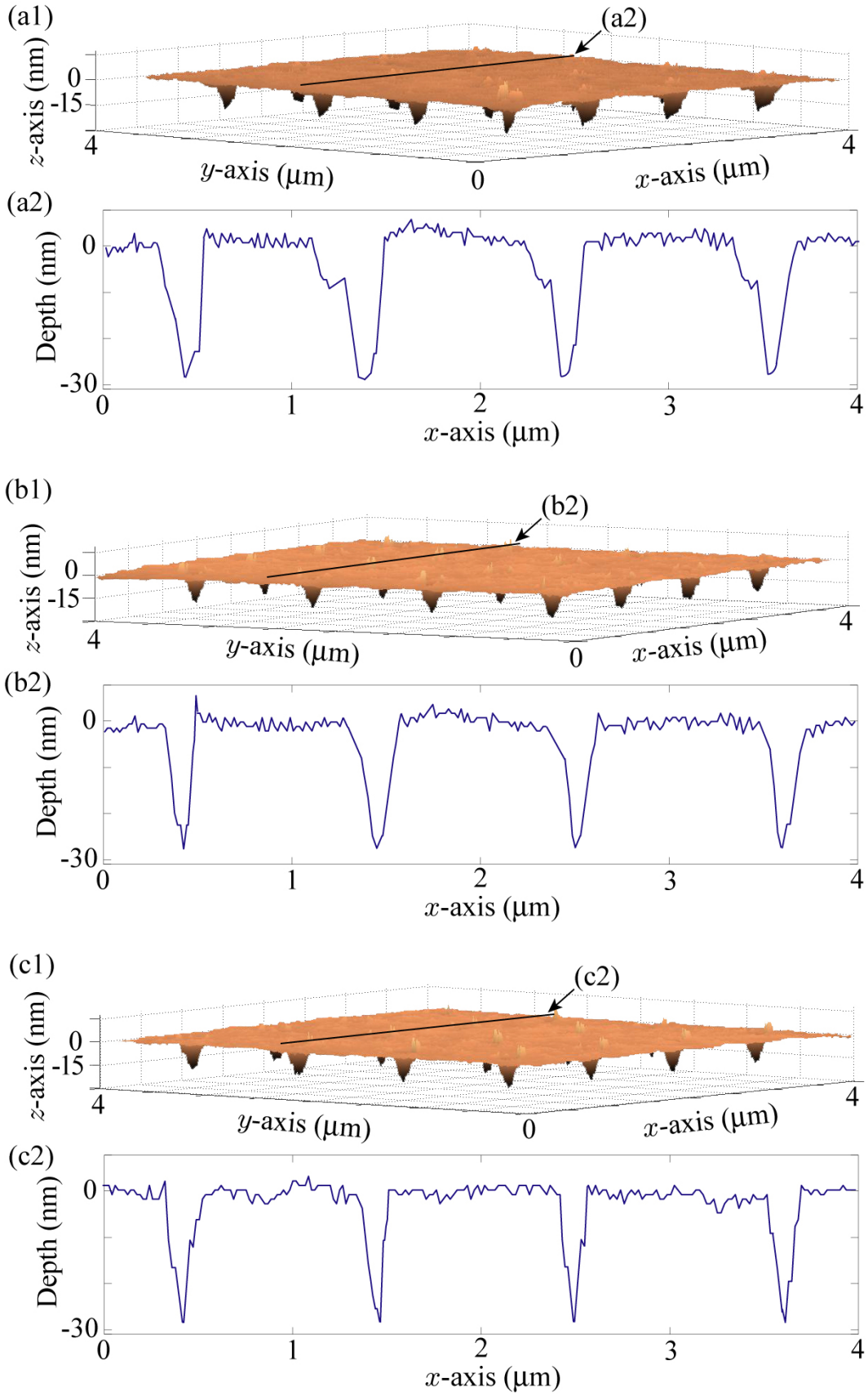

Figure 8.30: Depth calibration for fabricated holes at 10 Hz. (a1), (b1), and (c1) The 3-D image of the fabricated holes of open-loop, PID+$\mathcal{H}^{-1}$, and RC+$\mathcal{H}^{-1}$ respectively. (a2), (b2), and (c2) The depth of example holes line of open-loop, PID+$\mathcal{H}^{-1}$, and RC+$\mathcal{H}^{-1}$ respectively.

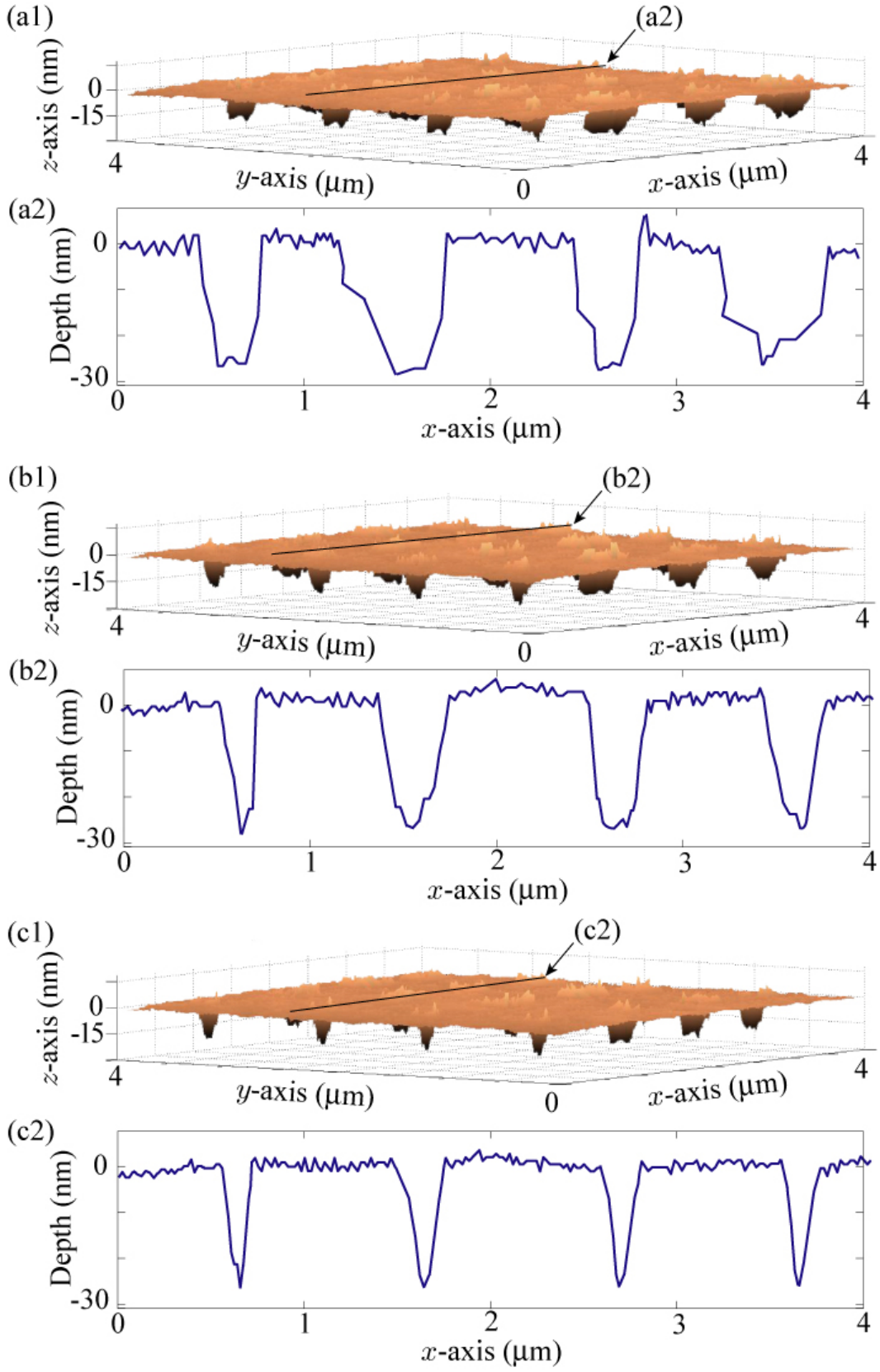

Figure 8.31: Depth calibration for fabricated holes at 50 Hz. (a1), (b1), and (c1) The 3-D image of the fabricated holes. (a2), (b2), and (c2) The depth of example holes line.

Chapter 9

Conclusions and Suggested Future Work

This dissertation studied high-precision tracking of periodic motion trajectories in hysteretic systems, in particular, piezo-based nanopositioners. To precisely track periodic motion trajectories, repetitive control (RC), which exploits the process of repetition, is designed. First, an enhanced RC and an odd-harmonic RC were designed for linear dynamics to serve as a starting point for designing RC for hysteretic systems. In this process, the stability and performances of the RCs for linear dynamics were analyzed, and stability conditions were developed to ensure the linear RC system is stable, as well as the tracking performance is enhanced by the addition of phased-lead compensators and RC gains. Second, the effect of hysteresis on RC closed-loop system stability was analyzed. The hysteresis of the piezoactuator was modeled using a Prandtl-Ishlinskii hysteresis model. Then the effect of hysteresis on the RC closed-loop stability was analyzed and the allowable size of the hysteresis nonlinearity for a stable RC was quantified. In the stability analysis, conditions were developed for the bounded-input bounded-output (BIBO) stability of the repetitive controlled hysteretic system in the $\mathcal{L}_2$-norm sense. Combining this result with the

Small-Gain Theorem, bounds on the hysteresis nonlinearity were determined to guarantee closed-loop stability. When the hysteresis effect exceeds the maximum bound, a new inverse-hysteresis feedforward controller based on the Prandtl-Ishlinskii hysteresis model was developed to compensate hysteresis for closed-loop stability and tracking performances. Finally, the control approach and the developed stability theorem were validated experimentally on a custom-designed piezoactuator driven nanopositioning stage. Experimental results showed that the enhanced RC design ensured that the closed-loop RC system was stable. The experimental tracking and nanofabrication results also showed that the repetitive control system can reduce the repeating tracking error and enhance the positioning accuracy in AFM-based nanohole array fabrication. For example, the tracking results at 1 kHz show that by adding hysteresis compensation, a 14% improvement in the stability margin and rate of convergence of the RC was achieved. Likewise, the enhanced RC reduced the repeating tracking error of PI control from 13.7% to 3.9% (using RC with hysteresis compensation), a 71% reduction. The nanofabrication results at 50 Hz showed that adding enhanced RC to PID+$\mathcal{H}^{-1}$ control system reduced the location error of the fabricated holes by 81.6%. The surface damage was decreased from 150% (PID+$\mathcal{H}^{-1}$) to about 28%. Both the tracking and nanofabrication results underscore the benefits of RC with hysteresis compensation on reducing repeating tracking error and minimizing the effect of hysteresis.

Suggested future work includes growing and quantifying the structural and optical properties of the ZnO nanowire arrays to further determinate the quality of the nanohole arrays pattern fabricated using AFM. The growth of the ZnO nanowire arrays includes the nanowires growth using a chemical methods and the remove of the PMMA layer from the substrate through chemical etching. Specifically, the growth of ZnO nanowires need to be produced in solution with zinc hexahydrate ($Zn(NO_3)\cdot 6H_2O$)

and water-soluble hexamethylene tetraammine ($C_6H_{12}N_4$) as reagents [184]. This chemical reaction process is less complex, but the growth results can be affected by serval parameters, such as pH of the solution, the temperature of the flask and the reaction time. After the growth of the ZnO nanowire arrays, the PMMA layer can be removed using isopropyl alcohol. The quantification on the structure of the grown ZnO nanowire will be to determine the length, diameter and the morphology of the fabricated ZnO nanowire using a field emission scanning electron microscopy (FE-SEM). The optical property quantification is to test the photoluminescence spectra of the grown nanowires through the UV emission the fabricated nanowires.

Additional work can also include implementing the repetitive control system on other types of AFM based nanofabrication, such as AFM-based ferroelectric materials polarizing and AFM-based nanooxidation, while requires using periodic motion trajectories.

Bibliography

[1] G. M. Clayton, S. Tien, K. K. Leang, Q. Zou, and S. Devasia, "A review of feedforward control approaches in nanopositioning for high speed SPM," *ASME J. Dyn. Syst. Meas. and Cont., Special issue on Dynamic Modeling, Control, and Manipulation at the Nanoscale*, vol. 131, no. 6, p. 061101 (19 pages), 2009.

[2] S. O. R. Moheimani and A. J. Fleming, *Piezoelectric transducers for vibration control and damping (advances in industrial control)*. Springer, 2006.

[3] D. Lagoudas, *Shape Memory Alloys: Modeling and Engineering Applications*. New York: Springer, 2008.

[4] G. Song, B. Kelley, and B. N. Agrawal, "Active position control of a shape memory alloy wire actuated composite beam," *Smart Materials and Structures*, vol. 9, pp. 711–716, 2000.

[5] X. Tan and J. S. Baras, "Modeling and control of hysteresis in magnetostrictive actuators," *Automatica*, vol. 40, pp. 1469 – 1480, 2004.

[6] R. Wiesendanger, *Scanning probe microscopy and spectroscopy*. Cambridge: Cambridge University Press, 1994.

[7] U. Aridogan, Y. Shan, and K. K. Leang, "Design and analysis of discrete-time repetitive control for scanning probe microscopes," *ASME J. Dyn. Syst. Meas.*

and Cont., Special issue on Dynamic Modeling, Control, and Manipulation at the Nanoscale, vol. 131, p. 061103 (12 pages), 2009.

[8] Y. Shan and K. K. Leang, "Dual-stage repetitive control for high-speed nanopositioning," in *IFAC Symposium on Mechatronic Systems and ASME Dynamic Systems and Control Conference (DSCC), Invited session on Micro- and Nanoscale Dynamics and Control*, Cambridge, Massachusetts, USA, 2010.

[9] T. Inoue, M. Nakano, and S. Iwai, "High accuracy control of a proton synchrotron magnet power supply," in *Proc. 8th World Congr. IFAC*, vol. 20, 1981, pp. 216 – 221.

[10] S. Hara, Y. Yamamoto, T. Omata, and M. Nakano, "Repetitive control system: a new type servo system for periodic exogenous signals," *IEEE Trans. Autom. Cont.*, vol. 33, no. 7, pp. 659 – 668, 1988.

[11] K. K. Leang, Q. Zou, and S. Devasia, "Feedforward control of piezoactuators in atomic force microscope systems: inversion-based compensation for dynamics and hysteresis," *IEEE Cont. Syst. Mag., Special Issue on Hysteresis*, vol. 29, no. 1, pp. 70 – 82, 2009.

[12] D. Croft, G. Shed, and S. Devasia, "Creep, hysteresis, and vibration compensation for piezoactuators: atomic force microscopy application," *ASME J. Dyn. Syst., Meas., and Control*, vol. 123, no. 1, pp. 35–43, 2001.

[13] M.-S. Tsai and J.-S. Chen, "Robust tracking control of a piezoactuator using a new approximate hysteresis model," *ASME J. Dyn. Syst., Meas., Control*, vol. 125, no. 1, pp. 96–102, 2003.

[14] R. Cross, *Unemployment, hysteresis, and the natural rate hypothesis.* New York: Basil Blackwell Ltd., 1988.

[15] D. C. Jiles and D. L. Atherton, "Theory of ferromagnetic hysteresis," *J. Magnetism and Magnetic Materials*, vol. 61, pp. 48–60, 1986.

[16] P. J. Chen and S. T. Montgomery, "A macroscopic theory for the existence of the hysteresis and butterfly loops in ferroelectricity," *Ferroelectrics*, vol. 23, pp. 199–207, 1980.

[17] H. Cao and A. G. Evans, "Nonlinear deformation of ferroelectric ceramics," *J. Amer. Ceram. Soc.*, vol. 76, pp. 890–896, 1993.

[18] I. D. Mayergoyz, *Mathematical models of hysteresis.* New York: Springer-Verlag, 1991.

[19] W. P. Mason, "Quartz crystal applications," in *Quartz crystals for electrical circuits*, R. A. Heising, Ed. New York: D. Van Nostrand Co., Inc., 1946, pp. 11 – 56.

[20] A. Ballato, "Piezoelectricity: history and new thrusts," in *IEEE Ultrasonics Symposium*, 1996, pp. 575–583.

[21] W. G. Cady, *Piezoelectricity.* New York: McGraw-Hill, 1946.

[22] D. Berlincourt, "Piezoelectric ceramics: characteristics and applications," *J. Acoust. Soc. Am.*, vol. 70, no. 6, pp. 1586–1595, 1981.

[23] T. G. King, M. E. Preston, B. J. M. Murphy, and D. S. Cannell, "Piezoelectric ceramic actuators: a review of machinery applications," *Precision Engineering*, vol. 12, no. 3, pp. 131–136, 1990.

[24] C. B. Sawyer, "The use of rochelle salt crystals for electrical reproducers and microphones," *Proceedings of the Institute of Radio Engineers*, vol. 19, no. 11, pp. 2020 – 2029, 1931.

[25] L. APC International, *Piezoelectric ceramics: principles and applications*. Mackeyville, PA: APC International, Ltd., 2002.

[26] C. J. Chen, "Electromechanical deflections of piezoelectric tubes with quartered electrodes," *Appl. Phys. Lett.*, vol. 60, no. 1, pp. 132–134, 1992.

[27] J. V. Ramsay and E. G. V. Mugridge, "Barium titanate ceramics for fine-movement control," *J. Sci. Instrum.*, vol. 39, pp. 636 – 637, 1962.

[28] T. Ando, N. Kodera, D. Maruyama, E. Takai, K. Saito, and A. Toda, "A high-speed atomic force microscope for studying biological macromolecules in action," *Jpn. J. Appl. Phys. Part 1*, vol. 41, no. 7B, pp. 4851 – 4856, 2002.

[29] G. Schitter, K. J. Astrom, B. E. DeMartini, P. J. Thurner, K. L. Turner, and P. K. Hansma, "Design and modeling of a high-speed afm-scanner," *IEEE Trans. Cont. Sys. Tech.*, vol. 15, no. 5, pp. 906 – 915, 2007.

[30] K. K. Leang and A. J. Fleming, "High-speed serial-kinematic AFM scanner: design and drive considerations," in *American Control Conference, Invited Session on Modeling and Control of SPM*, Seattle, WA, USA, 2008, pp. 3188 – 3193.

[31] M. J. Rost, L. Crama, P. Schakel, E. van Tol, G. B. E. M. van Velzen-Williams, C. F. Overgauw, H. ter Horst, H. Dekker, B. Okhuijsen, M. Seynen, A. Vijftigschild, P. Han, A. J. Katan, K. Schoots, R. Schumm, W. van Loo, T. H. Oosterkamp, and J. W. M. Frenken, "Scanning probe microscopes go video rate and beyond," *Rev. Sci. Instr.*, vol. 76, pp. 053 710–1 – 053 710–9, 2005.

[32] A. V. Srinivasan and D. M. McFarland, *Smart structures: analysis and design*. New York: Cambridge University Press, 2001.

[33] S. Stilson, A. McClellan, and S. Devasia, "High-speed solution switching using piezo-based micro-positioning stages," in *Proc. American Control Conference*, Arlington, VA, 2001, pp. 2238–2243.

[34] R. B. Evans, J. S. Griesbach, and W. C. Messner, "Piezoelectric microactuator for dual stage control," *IEEE Trans. Magnetics*, vol. 35, no. 2, pp. 977–982, 1999.

[35] J.-H. Park, K. Yoshida, and S. Yokota, "A piezoelectric micropump using resonance drive: proposal of resonance drive and basic experiments on pump characteristics," in *Proc. of the 1997 ASME Inter. Mech. Eng. Congress and Exposition: The Fluid Power and Systems Technology Division*, vol. 4, Dallas, TX, 1997, pp. 77–82.

[36] C. F. Quate, "Scanning probes as a lithography tool for nanostructures," *Surface Science*, vol. 386, pp. 259–264, 1997.

[37] S. M. Salapaka and M. V. Salapaka, "Scanning probe microscopy," *IEEE Control Systems Magazine*, vol. 28, no. 2, pp. 65 – 83, 2008.

[38] G. Binnig and C. F. Quate, "Atomic force microscope," *Phys. Rev. Lett.*, vol. 56, no. 9, pp. 930–933, 1986.

[39] S. Kasas, N. H. Thomson, B. L. Smith, P. K. Hansma, J. Miklossy, and H. G. Hansma, "Biological applications of the afm: from single molecules to organs," *Int. J. of Imaging Syst. and Technol.*, vol. 8, no. 2, pp. 151–161, 1997.

[40] N. Jalili and K. Laxminarayana, "A review of atomic force microscopy imaging systems: application to molecular metrology and biological sciences," *Mechatronics*, vol. 14, no. 8, pp. 907 – 945, 2004.

[41] Q. Tang, S. Shi, and L. Zhou, "Nanofabrication with atomic force microscopy," *J. Nanosci. Nanotech.*, vol. 4, pp. 946 – 963, 2004.

[42] Y. Chen and A. Pepin, "Nanofabrication: Conventional and nonconventional methods," *Electrophoresis*, vol. 22, pp. 187 –207, 2001.

[43] G. M. Whitesides, J. Mathias, and C. Seto, "Molecular self-assembly and nanochemistry: a chemical strategy for the synthesis of nanostructures," *Science*, vol. 254, no. 5036, pp. 1312 – 1319, 1991.

[44] D. Pisignano, L. Persano, M. Raganato, P. Visconti, R. Cingolani, G. Barbarella, L. Favaretto, and G. Gigli, "Room-temperature nanoimprint lithography of non-thermoplastic organic films," *Adv. Mater.*, vol. 16, no. 6, pp. 525 – 529, 2004.

[45] F. Giessibl, "Advances in atomic force microscopy," *Rev. Mod. Phys.*, vol. 75, no. 3, pp. 949 – 983, 2003.

[46] F. J. Rubio-Sierra, W. M. Heckl, and R. W. Stark, "Nanomanipulation by atomic force microscopy," *Adv. Engr. Mater.*, vol. 7, no. 4, pp. 193 – 196, 2005.

[47] R. Magno and B. R. Bennelt, "Nanostructure patterns written in III-V semiconductors by an atomic force microscope," *Appl. Phys. Lett.*, vol. 70, no. 14, pp. 1855 – 1857, 1997.

[48] L. G. Rosa and J. Liang, "Atomic force microscope nanolithography: dip-pen, nanoshaving, nanografting, tapping mode, electrochemical and thermal nanolithography," *J. Phys.*, vol. 21, no. 48, pp. 483 001 – 483 015, 2009.

[49] L. B. and S. D., "Nanooxidation of silicon with an atomic force microscope: A pulsed voltage technique," *Appl. Phys. Lett.*, vol. 74, no. 26, pp. 123 257 – 123 260, 1999.

[50] R. D. Piner, J. Zhu, F. Xu, S. Hong, and C. A. Mirkin, "Dip-pen nanolithography," *Science*, vol. 283, pp. 661 – 663, 1999.

[51] Y. Kim and C. M. Lieber, "Machining oxide thin films with an atomic force microscope: pattern and object formation on the nanometer scale," *Science*, vol. 257, pp. 375 – 377, 1992.

[52] P. E. Sheehan and C. M. Lieber, "Nanotribology and nanofabrication of MoO_3 structures by atomic force microscopy," *Science*, vol. 272, no. 5265, pp. 1158 – 1161, 1996.

[53] R. Luthi, E. Meyer, H. Haefke, L. Howald, W. Gutmannsbauer, and H.-J. Guntherodt, "Sled-type motion on the nanometer scale: Determination of dissipation and cohesive energies of C_{60}," *Science*, vol. 266, no. 5193, pp. 1979 – 1981, 1994.

[54] T. Junno, K. Deppert, L. Montelius, and L. Samuelson, "Controlled manipulation of nanoparticles with an atomic force microscope," *Applied Physics Letters*, vol. 66, no. 26, pp. 3627 – 3629, 1995.

[55] C. Baur, B. C. Gazen, B. Koel, T. R. Ramachandran, A. A. G. Requicha, and L. Zini, "Robotic nanomanipulation with a scanning probe microscope in a networked computing environment," *J. Vac. Sci. Technol. B*, vol. 15, no. 4, pp. 1577–1580, 1997.

[56] T. R. Ramachandran, C. Baur, A. Bugacov, A. Madhukar, B. E. Koel, A. Requicha, and C. Gazen, "Direct and controlled manipulation of nanometer-sized particles using the non-contact atomic force microscope," *Nanotechnology*, vol. 9, no. 3, pp. 237 – 245, 1998.

[57] S. L. Brandow, W. J. Dressick, C. S. Dulcey, T. S. Koloski, L. M. Shirey, J. Schmidt, and J. M. Calvert, "Nanolithography by displacement of catalytic metal clusters using an atomic force microscope tip," *J. Vac. Sci. Technol. B*, vol. 15, no. 5, pp. 1818 – 1825, 1997.

[58] D. Q. Yang and E. Sacher, "Local surface cleaning and cluster assembly using contact mode atomic force microscopy," *App. Surf. Sci.*, vol. 210, no. 3-4, pp. 158 – 164, 2003.

[59] D. M. Schaefer, R. Reifenberger, A. Patil, and R. P. Andres, "Fabrication of two-dimensional arrays of nanometer-size clusters with the atomic force microscope," *Appl. Phys. Lett.*, vol. 66, no. 8, pp. 1012 – 1015, 1995.

[60] R. Resch, C. Baur, A. Bugacov, B. E. Koel, A. Madhukar, A. A. G. Requicha, and P. Will, "Building and manipulating three-dimensional and linked two-dimensional structures of nanoparticles using scanning force microscopy," *Langmuir*, vol. 14, no. 23, pp. 6613 – 6616, 1998.

[61] P. Guthner and K. Dransfeld, "Local poling of ferroelectric polymers by scanning force microscopy," *Appl. Phys. Lett.*, vol. 61, no. 9, pp. 1137 – 1139, 1992.

[62] O. Kolosov, A. Gruverman, J. Hatano, K. Takahashi, and K. Tokumoto, "Nanoscale visualization and control of ferroelectric domains by atomic force microscopy," *J Mater Process Technol*, vol. 74, no. 21, pp. 4309 – 4312, 1995.

[63] C. H. Ahn, T. Tybell, L. Antognazza, K. Char, R. H. Hammond, M. R. Beasley, O. Fischer, and J.-M. Triscone, "Local, nonvolatile electronic writing of epitaxial $Pb(Zr_{0.52}Ti_{0.48})O_3/SrRuO_3$ heterostructures," *Science*, vol. 16, pp. 1100 – 1103, 1997.

[64] T. Hidaka, T. Maruyama, M. Saitoh1, N. Mikoshiba, M. Shimizu, T. Shiosaki, L. A. Wills, R. Hiskes, S. A. Dicarolis, and J. Amano, "Formation and observation of 50 nm polarized domains in $PbZr_{1-x}Ti_xO_3$ thin film using scanning probe microscope," *Appl. Phys. Lett.*, vol. 68, no. 17, pp. 2358 – 2359, 1996.

[65] T. Tybell, C. H. Ahn, and J.-M. Triscone, "Ferroelectricity in thin perovskite films," *Appl. Phys. Lett.*, vol. 75, no. 6, pp. 856 – 858, 1999.

[66] X. Q. Chen, H. Yamada, T. Horiuchi, K. Matsushige, S. Watanabe, M. Kawai, and P. S. Weiss, "Surface potential of ferroelectric thin films investigated by scanning probe microscopy," *J. Vac. Sci. Technol. B*, vol. 17, no. 5, pp. 1930 –1934, 1999.

[67] C. Durkan, M. E. Welland, D. P. Chu, and P. Migliorato, "Scaling of piezoelectric properties in nanometre to micrometre scale," *Electronics Letters*, vol. 36, no. 18, pp. 1538 – 1539, 2000.

[68] S. F. Lyuksyutov, R. A. Vaia, P. B. Paramonov, S. Juhl, L. Waterhouse, R. M. Ralich, G. Sigalov, and E. Sancaktar, "Electrostatic nanolithography in polymers using atomic force microscopy," *Nature Materials*, vol. 2, pp. 468 – 472, 2003.

[69] Y. Yan, T. Sun, Y. Liang, and S. Dong, "Investigation on afm-based micro/nano-cnc machining system," *International Journal of Machine Tools and Manufacture*, vol. 47, pp. 1651 –1659, 2007.

[70] L. A. Porter, Jr., A. E. Ribbe, and J. M. Buriak, "Metallic nanostructures via static plowing lithography," *Nano Letters*, vol. 3, no. 8, pp. 1043 – 1047, 2003.

[71] J. Chen, S. Liao, and Y. Tsai, "Electrocheical synthesis of polypyrrole within pmma nanochannels produced by afm mechanical lithography," *Synthetic Matals*, vol. 155, pp. 11 –17, 2005.

[72] A. A. Tseng, "A comparison study of scratch and wear properties using atomic force microscopy," *Appl. Surf. Sci.*, vol. 256, pp. 4246 – 4252, 2010.

[73] E. Dubois and J. Bubbendorff, "Nanometer scale lithography on silicon, titanium and pmma resist using scanning probe microscopy," *Solid-State Electronics*, vol. 43, pp. 1085 – 1089, 1999.

[74] S. Hu, A. Hamidi, S. Altmeyer, T. Koster, B. Spangenberg, and H. Kurz, "Fabrication of silicon and metal nanowires and dots using mechanical atomic force lithography," *J. Vac. Sci. Tech. B*, vol. 16, no. 5, pp. 2822 – 2824, 1998.

[75] T. Fang and W. Chang, "Effect of AFM-based nanomachining process on aluminum surface," *J. Phy. Chem. Solids*, vol. 64, pp. 913 – 918, 2003.

[76] B. Yu, H. Dong, L. Qian, Y. Chen, J. Yu, and Z. Zhou, "Friction-induced nanofabrication on monocrystalline sillicon," *Nanotechnology*, vol. 20, pp. 465 303 – 465 310, 2009.

[77] K. Umemura, T. Wang, M. Hara, R. Kuroda, O. Uchida, and M. Nagai, "Nanocharaterization and nanofabrication of a Nafion thin film in liquids by atomic force microscopy," *Langmuir*, vol. 22, pp. 3306 – 3312, 2006.

[78] C. Martin, G. Rius, X. Borrise, and F. Perez-Murano, "Nanolithography on thin layers of pmma using atomic force microscopy," *Nanotechnology*, vol. 16, pp. 1016 – 1022, 2005.

[79] S. Skabernaa, M. Versena, B. Klehna, U. Kunzea, D. Reuterb, and A. D. Wieckb, "Fabrication of a quantum point contact by the dynamic plowing tech-

nique and wet-chemical etching," *Ultramicroscopy*, vol. 82, no. 1-4, pp. 153 – 157, 2000.

[80] M. Versena, B. Klehna, U. Kunzea, D. Reuterb, and A. D. Wieckb, "Nanoscale devices fabricated by direct machining of GaAs with an atomic force microscope," *Ultramicroscopy*, vol. 82, no. 1-4, pp. 159 – 163, 2000.

[81] V. Bouchiat and D. Esteve, "Lift-off lithography using an atomic force microscope," *Applied Physics Letters*, vol. 69, no. 20, pp. 3098 – 3100, 1996.

[82] S. Xu, C. Lao, B. Weintraub, and Z. Wang, "Nanometer-scale fabrication by simultaneous nanoshaving and molecular self-assembly," *Langmuir*, vol. 13, no. 2, pp. 127 – 129, 1997.

[83] R. G. Nuzzo and D. L. Allara, "Adsorption of bifunctional organic disulfides on gold surfaces," *J. Am. Chem. Soc.*, vol. 105, no. 13, pp. 4481 – 4483, 1983.

[84] N. A. Amro, S. Xu, and G. Liu, "Patterning surfaces using tip-directed displacement and self-assembly," *Langmuir*, vol. 16, no. 7, pp. 3006 – 3009, 2000.

[85] D. Zhou, X. Wang, L. Birch, L. Rayment, and C. Abell, "Afm study on protein immobilization on charged surfaces at the nanoscale: Toward the fabrication of three-dimensional protein nanostructures," *Langmuir*, vol. 19, no. 25, pp. 10 557 – 10 562, 2003.

[86] S. Xu, P. E. Laibinis, and G. Liu, "Accelerating the kinetics of thiol self-assembly on gold-A spatial confinement effect," *J. Am. Chem. Soc.*, vol. 120, no. 36, pp. 9356 – 9361, 1998.

[87] J. Liu, J. R. Von Ehr, C. Baur, R. Stallcup, J. Randall, and K. Bray, "Fabrication of high-density nanostructures with an atomic force microscope," *Appl. Phys. Lett.*, vol. 84, no. 8, pp. 1359 – 1361, 1994.

[88] M. B. Ali, T. Ondarcuhu, M. Brust, and C. Joachim, "Atomic force microscope tip-induced local oxidation of silicon: kinetics, mechanism, and nanofabrication," *Appl. Phys. Lett.*, vol. 71, no. 2, pp. 285 – 287, 1997.

[89] J. A. Dagata, T. Inoue, J. Itoh, K. Matsumoto, and H. Yokoyama, "Role of space charge in scanned probe oxidation," *J. Appl. Phys.*, vol. 84, no. 12, pp. 6891 –6900, 1998.

[90] P. Avouris, R. Martel, T. Hertel, and R. Sandstrom, "Afm-tip-induced and current-induced local oxidation of silicon and metals," *Appl. Phys. A*, vol. 66, pp. 5659 – 5667, 1998.

[91] R. Garcia, M. Calleja, and H. Rohrer, "Patterning of silicon surfaces with non-contact atomic force microscopy: Field-induced formation of nanometer-size water bridges," *J. Appl. Phys.*, vol. 86, no. 4, pp. 1898 – 1903, 1999.

[92] F. Perez-Murano, C. Martin, N. Barniol, H. Kuramochi, H. Yokoyama, and J. A. Dagata, "Measuring electrical current during scanning probe oxidation," *Appl. Phys. Lett.*, vol. 82, no. 18, pp. 3086 – 3088, 2003.

[93] A. Majumdar, P. I. Oden, J. P. Carrejo, L. A. Nagahara, J. J. Graham, and J. Alexander, "Nanometer-scale lithography using the atomic force microscope," *Appl. Phys. Lett.*, vol. 61, no. 19, pp. 2293 – 2295, 2002.

[94] E. S. Snow and P. M. Campbell, "Fabrication of Si nanostructures with an atomic force microscope," *Appl. Phys. Lett.*, vol. 64, no. 15, pp. 1932 – 1935, 1994.

[95] S. Gwo, C.-L. Yeh, P.-F. Chen, Y.-C. Chou, T. T. Chen, T.-S. Chao, S.-F. Hu, and T.-Y. Huang, "Local electric-field-induced oxidation of titanium nitride films," *Appl. Phys. Lett.*, vol. 74, no. 8, pp. 1090 – 1092, 1999.

[96] F. S.-S. Chien, Y. C. Chou, T. T. Chen, W.-F. Hsieh, T.-S. Chao, and S. Gwo, "Nano-oxidation of silicon nitride films with an atomic force microscope: Chemical mapping, kinetics, and applications," *J. Appl. Phys.*, vol. 89, no. 4, pp. 2465 –2472, 2001.

[97] E. S. Snow and P. M. Campbell, "Afm fabrication of sub-10-nanometer metal-oxide devices with in situ control of electrical properties," *Science*, vol. 270, no. 5242, pp. 1639 – 1641, 1995.

[98] F. S.-S. Chien, W.-F. Hsieh, S. Gwo, A. E. Vladar, and J. A. Dagata, "Silicon nanostructures fabricated by scanning probe oxidation and tetra-methyl ammonium hydroxide etching," *J. Appl. Phys.*, vol. 91, no. 12, pp. 10 044 –10 051, 2002.

[99] D. S. Ginger, H. Zhang, and C. A. Mirkin, "The evolution of dip-pen nanolithography," *Angew. Chem.*, vol. 43, no. 1, pp. 30 – 45, 2003.

[100] G. Agarwal, L. A. Sowards, R. R. Naik, and M. O. Stone, "Dip-Pen nanolithography in tapping mode," *J. Am. Chem. Soc.*, vol. 125, no. 2, pp. 580 – 583, 2003.

[101] S. Hong, J. Zhu, and C. A. Mirkin, "Multiple ink nanolithography: Toward a multiple-pen nano-plotter," *Science*, vol. 286, no. 5439, pp. 523 – 525, 1999.

[102] C. A. Mirkin, S. Hong, and L. Demers, "Dip-Pen nanolithography: Controlling surface architecture on the sub-100 nanometer length scale," *Phys. Chem.*, vol. 2, no. 1, pp. 37 – 39, 2001.

[103] A. Ivanisevic and C. A. Mirkin, ""Dip-Pen" nanolithography on semiconductor surfaces," *J. Am. Chem. Soc.*, vol. 123, no. 32, pp. 7887 – 7889, 2001.

[104] B. W. Maynor, Y. Li, and J. Li, "Fabrication of luminescent nanostructures and polymer nanowires using Dip-Pen nanolithography," *Nano Letters*, vol. 2, no. 2, pp. 109 – 112, 2002.

[105] J. C. Smith, K.-B. Lee, Q. Wang, M. G. Finn, J. E. Johnson, M. Mrksich, and C. A. Mirkin, "Nanopatterning the chemospecific immobilization of cowpea mosaic virus capsid," *Nano Letters*, vol. 3, no. 7, pp. 883 – 886, 2003.

[106] H. Zhang, S.-W. Chung, and C. A. Mirkin, "Fabrication of sub-50-nm solid-state nanostructures on the basis of Dip-Pen nanolithography," *Nano Letters*, vol. 3, no. 1, pp. 43 – 45, 2003.

[107] L. M. Demers, D. S. Ginger, S.-J. Park, Z. Li, S.-W. Chung, and C. A. Mirkin, "Direct patterning of modified oligonucleotides on metals and insulators by Dip-Pen nanolithography," *Science*, vol. 296, no. 5574, pp. 1836 –1838, 2002.

[108] H. Zhang, Z. Li, and C. Mirkin, "Dip-Pen nanolithography-based methodology for preparing arrays of nanostructures functionalized with oligonucleotides," *Adv. Mater.*, vol. 14, no. 20, pp. 1472 – 1474, 2002.

[109] J. Hyun, S. J. Ahn, W. K. Lee, A. Chilkoti, and S. Zauscher, "Molecular recognition-mediated fabrication of protein nanostructures by Dip-Pen lithography," *Nano Letters*, vol. 2, no. 11, pp. 1203 – 1207, 2002.

[110] M. Su and V. P. Dravid, "Colored ink Dip-Pen nanolithography," *Appl. Phys. Lett.*, vol. 80, no. 23, pp. 4434 – 4437, 2002.

[111] A. Ivanisevic, J.-H. Im, K.-B. Lee, S.-J. Park, L. M. Demers, K. J. Watson, and C. A. Mirkin, "Redox-controlled orthogonal assembly of charged nanostructures," *J. Am. Chem. Soc.*, vol. 123, no. 49, pp. 12 424 – 12 425, 2001.

[112] P. Manandhar, J. Jang, G. C. Schatz, M. A. Ratner, and S. Hong, "Anomalous surface diffusion in nanoscale direct deposition processes," *Phys. Rev. Lett.*, vol. 90, no. 11, pp. 115 505 – 115 509, 2003.

[113] R. McKendry, W. T. S. Huck, B. Weeks, M. Fiorini, C. Abell, and T. Rayment, "Creating nanoscale patterns of dendrimers on silicon surfaces with Dip-Pen nanolithography," *Nano Letters*, vol. 2, no. 7, pp. 713 – 716, 2002.

[114] L. Fu, X. Liu, Y. Zhang, V. P. Dravid, and C. A. Mirkin, "Nanopatterning of "Hard" magnetic nanostructures via Dip-Pen nanolithography and a sol-based ink," *Nano Letters*, vol. 3, no. 6, pp. 757 – 760, 2003.

[115] M. B. Ali, T. Ondarcuhu, M. Brust, and C. Joachim, "Atomic force microscope tip nanoprinting of gold nanoclusters," *Langmuir*, vol. 18, no. 3, pp. 872 – 876, 2002.

[116] Y. Benjamin, W. Maynor, and J. Liu, "Electrochemical afm Dip-Pen nanolithography," *J. Am. Chem. Soc.*, vol. 123, no. 9, pp. 2105 – 2106, 2001.

[117] L. A. Porter, Jr., H. C. Choi, J. M. Schmeltzer, A. E. Ribbe, L. C. C. Elliott, and J. M. Buriak, "Electroless nanoparticle film deposition compatible with photolithography, microcontact printing, and Dip-Pen nanolithography patterning technologies," *Nano Letters*, vol. 2, no. 12, pp. 1369 – 1372, 2003.

[118] B. W. Maynor, Y. Li, and J. Li, "Au "Ink" for afm "Dip-Pen" nanolithography," *Langmuir*, vol. 19, no. 9, pp. 2575 – 2578, 2001.

[119] D. Leonard, M. Krishnamurthy, C. M. Reaves, S. P. Denbaars, and P. M. Petroff, "Direct formation of quantum-sized dots from uniform coherent islands of ingaas on gaas surfaces," *Applied Physics Letters*, vol. 63, no. 23, pp. 3203 – 3205, 1993.

[120] R. C. Barrett and C. F. Quate, "Optical scan-correction system applied to atomic force microscopy," *Rev. Sci. Instr.*, vol. 62, no. 6, pp. 1393–1399, 1991.

[121] H. J. M. T. A. Adriaens, W. L. d. Koning, and R. Banning, "Modeling piezoelectric actuators," *IEEE/ASME Trans. Mechatronics*, vol. 5, no. 4, pp. 331–341, 2000.

[122] A. J. Fleming and S. O. R. Moheimani, "A grounded-load charge amplifier for reducing hysteresis in piezoelectric tube scanners," *Rev. Sci. Instr.*, vol. 76, pp. 073 707–1, 2005.

[123] S. M. Hues, C. F. Draper, K. P. Lee, and R. J. Colton, "Effect of pzt and pmn actuator hysteresis and creep on nanoindentation measurements using force microscopy," *Rev. Sci. Instr.*, vol. 65, no. 5, pp. 1561–1565, 1994.

[124] K. R. Koops, P. M. L. O. Scholte, and W. L. d. Koning, "Observation of zero creep in piezoelectric actuators," *Applied Physics A*, vol. 68, pp. 691–697, 1999.

[125] H. Jung and D.-G. Gweon, "Creep characteristics of piezoelectric actuators," *Rev. Sci. Instr.*, vol. 71, no. 4, pp. 1896–1900, 2000.

[126] W. D. Callister, *Materials science and engineering: an introduction.* New York: John Wiley and Sons, Inc., 1994.

[127] G. Schitter, P. Menold, H. F. Knapp, F. Allgöwer, and A. Stemmer, "High performance feedback for fast scanning atomic force microscopes," *Rev. Sci. Instr.*, vol. 72, no. 8, pp. 3320–3327, 2001.

[128] G. Schitter and A. Stemmer, "Fast closed loop control of piezoelectric transducers," *J. Vac. Sci. Technol. B*, vol. 20, no. 1, pp. 350–352, 2002.

[129] S. Salapaka, A. Sebastin, J. P. Cleveland, and M. V. Salapaka, "High bandwidth nano-positioner: a robust control approach," *Rev. Sci. Instr.*, vol. 73, no. 9, pp. 3232–3241, 2002.

[130] H. Janocha and K. Kuhnen, "Real-time compensation of hysteresis and creep in piezoelectric actuators," *Sensors and actuators A*, vol. 79, pp. 83–89, 2000.

[131] H. Jung, J. Y. Shim, and D. Gweon, "New open-loop actuating method of piezoelectric actuators for removing hysteresis and creep," *Rev. Sci. Instr.*, vol. 71, no. 9, pp. 3436–3440, 2000.

[132] P. Krejci and K. Kuhnen, "Inverse control of systems with hysteresi and creep," *IEE Proc.-Control Theory Appl.*, vol. 148, no. 3, pp. 185–192, 2001.

[133] O. M. E. Rifai and K. Youcef-Toumi, "Creep in piezoelectric scanners of atomic force microscopes," in *Proc. of American Control Conference*, Anchorage, AK, 2002, pp. 3777–3782.

[134] A. E. Holman, P. M. L. O. Scholte, W. C. Heerens, and F. Tuinstra, "Analysis of piezo actuators in translation construction," *Rev. Sci. Instr.*, vol. 66, no. 5, pp. 3208–3215, 1995.

[135] D. Croft and S. Devasia, "Vibration compensation for high speed scanning tunneling microscopy," *Rev. Sci. Instr.*, vol. 70, no. 12, pp. 4600–4605, 1999.

[136] T. Sulchek, R. Hsieh, J. D. Adams, S. C. Minne, and C. F. Quate, "High-speed atomic force microscopy in liquid," *Rev. Sci. Instr.*, vol. 71, no. 5, pp. 2097–2099, 2000.

[137] X. Tan and R. V. Iyer, "Modeling and control of hysteresis," *IEEE Cont. Syst. Mag.*, vol. 29, no. 1, pp. 26 – 29, 2009.

[138] K. K. Leang and S. Devasia, "Feedback-linearized inverse feedforward for creep, hysteresis, and vibration compensation in AFM piezoactuators," *IEEE Trans. Cont. Syst. Tech.*, vol. 15, no. 5, pp. 927 – 935, 2007.

[139] K. K. Leang, S. C. Ashley, and G. Tchoupo, "Iterative and feedback control for hysteresis compensation in sma," *ASME J. Dyn. Syst. Meas. and Cont.*, vol. 131, p. 014502 (6 pages), 2009.

[140] J. A. Main and E. Garcia, "Piezoelectric stack actuators and control system design: strategies and pitfalls," *AIAA J. Guidance, Control, and Dynamics*, vol. 20, no. 3, pp. 479–485, 1997.

[141] S. Devasia, E. Eleftheriou, and S. O. R. Moheimani, "A survey of control issues in nanopositioning," *IEEE Trans. Cont. Syst. Tech.*, vol. 15, no. 5, pp. 802 – 823, 2007.

[142] T. Ando, T. Uchihashi, and T. Fukuma, "High-speed atomic force microscopy for nano-visualization of dynamic biomolecular processes," *Progress in Surface Science*, vol. 83, no. 7–9, pp. 337–437, 2008.

[143] G. S. Choi, Y. A. Lim, and G. H. Choi, "Tracking position control of piezoelectric actuators for periodic reference inputs," *Mechatronics*, vol. 12, no. 5, pp. 669–684, 2002.

[144] P. Ge and M. Jouaneh, "Tracking control of a piezoceramic actuator," *IEEE Trans. Cont. Syst. Tech.*, vol. 4, no. 3, pp. 209–216, 1996.

[145] H.-S. Ahn, "Design of a repetitive control system for a piezoelectric actuator based on the inverse hysteresis model," in *The Fourth International Conference on Control and Automation*, Montreal, Canada, 2003, pp. 128 – 132.

[146] B. A. Francis and W. M. Wonham, "The internal model principle of control theory," *Automatica*, vol. 12, no. 5, pp. 457 – 465, 1976.

[147] K. L. Moore, M. Dahleh, and S. P. Bhattacharyya, "Iterative learning control: a survey and new results," *Journal of Robotic Systems*, vol. 9, no. 5, pp. 563–594, 1992.

[148] Y. Wu and Q. Zou, "Iterative control approach to compensate for both the hysteresis and the dynamics effects of piezo actuators," *IEEE Control Systems Technology*, vol. 15, no. 5, pp. 936 – 944, 2007.

[149] K. K. Leang and S. Devasia, "Design of hysteresis-compensating iterative learning control for piezo positioners: application to atomic force microscopes," *Mechatronics*, vol. 16, no. 3–4, pp. 141 – 158, 2006.

[150] H. L. Broberg and R. G. Molyet, "Reduction of repetitive errors in tracking of periodic signals: theory and application of repetitive control," in *First IEEE Conference on Control Applications*, vol. 2, 1992, pp. 1116 – 1121.

[151] K. K. Chew and M. Tomizuka, "Digital control of repetitive errors in disk drive systems," *IEEE Cont. Syst. Mag.*, vol. 10, no. 1, pp. 16 – 20, 1990.

[152] M. Tomizuka, "Zero-phase tracking algorithm for digital control," *ASME J. Dyn. Syst. Meas. and Cont.*, vol. 109, pp. 65 – 68, 1987.

[153] K. Zhou and J. C. Doyle, *Essentials of robust control.* Prentice-Hall, Inc., 1998.

[154] H. L. Broberg and R. G. Molyet, "A new approach to phase cancellation in repetitive control," in *IEEE Industry Applications Society Annual Meeting*, vol. 3, 1994, pp. 1766 – 1770.

[155] Y. Wang, D. Wang, B. Zhang, K. Zhou, and Y. Ye, "Robust repetitive control with linear phase lead," in *American Control Conference*, vol. 2006, Minneapolis, MN, USA, 2006, pp. 232 – 237.

[156] B.-S. Kim and T.-C. Tsao, "A performance enhancement scheme for robust repetitive control system," *ASME J. Dyn. Syst. Meas. and Cont.*, vol. 126, no. 1, pp. 224 – 229, 2004.

[157] R. Costa-Castello, R. Grino, and E. Fossas, "Odd-harmonic digital repetitive control of a single-phase current active filter," *IEEE Trans. Power Electronics*, vol. 19, no. 4, pp. 1060 – 1068, 2004.

[158] T. Omata, S. Hara, and M. Nakano, "Nonlinear repetitive control with application to trajectory control of manipulators," *J. Robot. Syst.*, vol. 4, no. 5, pp. 631 – 652, 1987.

[159] H. Hikita, M. Yamashita, and Y. Kubota, "Repetitive control for a class of nonlinear systems," *JSME Int. J.*, vol. 36, no. 4, pp. 430 – 434, 1993.

[160] J. Ghosh and B. Paden, "Nonlinear repetitive control," *IEEE Trans. Autom. Cont.*, vol. 45, no. 5, pp. 949–953, 2000.

[161] X. Li, T. W. S. Chow, and J. K. L. Ho, "Quasi-sliding mode based repetitive control for nonlinear continuous-time systems with rejection of periodic disturbances," *Automatica*, vol. 45, no. 1, pp. 103 – 108, 2009.

[162] Q. Xu and Y. Li, "Dahl model-based hysteresis compensation and precise positioning control of an XY parallel micromanipulator with piezoelectric actuation," *ASME J. Dyn. Syst., Meas., Control*, vol. 132, pp. 1–12, 2010.

[163] M. Brokate and J. Sprekels, *Hysteresis and phase transitions*. New York: Springer, 1996.

[164] K. Kuhnen, "Modeling, identification and compensation of complex hysteretic nonlinearities: a modified prandtl-ishlinskii approach," *European Journal of Control*, vol. 9, no. 4, pp. 407 – 418, 2003.

[165] M. A. Janaideh, C.-Y. Su, and S. Rakheja, "Development of the rate-dependent Prandtl-Ishlinskii model for smart actuators," *Smart Mater. Struct.*, vol. 17, p. 035026 (11pp), 2008.

[166] J. D. Kim and S. R. Nam, "A piezoelectrically driven micro-positioning system for the ductile-mode grinding of brittle materials," *J Mater Process Technol*, vol. 61, no. 3, pp. 309 – 319, 1999.

[167] B. M. Chen, T. H. Lee, C. C. Hang, Y. Guo, and S. Weerasorriva, "An H∞ almost disturbance decoupling robust controller design for a piezoceramic bimorph actuator with hysteresis," *IEEE Trans Control Syst Techno*, vol. 7, no. 2, pp. 160 –174, 1999.

[168] J. Song and D. K. Armen, "Generalized Bouc-Wen model for highly asymmetric hysteresis," *J. Eng. Mech.*, vol. 132, no. 6, pp. 610 – 618, 2006.

[169] R. Banning, W. L. de Koning, H. J. M. T. A. Adriaens, and R. K. Koops, "State-space analysis and identification for a class of hysteretic systems," *Automatica*, vol. 37, pp. 1883–1892, 2001.

[170] G. Michael and C. Nikola, "Modeling piezoelectric stack actuators for control of micromanipulation," *IEEE Cont. Syst Mag*, vol. 17, no. 3, pp. 69 – 79, 1997.

[171] Y. Yu, Z. Xiao, N. G. Naganathan, and R. V. Dukkipati, "Dynamic preisach modelling of hysteresis for the piezoceramic actuator system," *Mechanism and Machine Theory*, vol. 37, pp. 75 – 89, 2002.

[172] M. A. Janaideh, S. Rakheja, and C. Su, "A generalized Prandtl-Ishlinskii model for characterizing the hysteresis and saturation nonlinearities of smart actuators," *Smart Mater. Struct.*, vol. 18, no. 4, pp. 045 001 – 045 009, 2009.

[173] Y. Shan and K. K. Leang, "Repetitive control with Prandtl-Ishlinskii hysteresis inverse for piezo-based nanopositioning," in *American Control Conference, Invited Session on Advances in Control of Nanopositioning and SPM Systems*, St. Louis, MO, 2009, pp. 301 – 306.

[174] Y. Okazaki, "A micro-positioning tool post using a piezoelectric actuator for diamond turning machines," *Precision Engineering*, vol. 12, no. 3, pp. 151–156, 1990.

[175] R. B. Gorbet, K. A. Morris, and D. W. L. Wang, "Passivity-based stability and control of hysteresis in smart actuators," *IEEE Trans. Cont. Syst. Tech.*, vol. 9, no. 1, pp. 5–16, 2001.

[176] T. E. Pare and J. P. How, "Robust stability and performance analysis of systems with hysteresis nonlinearities," in *Proc. Amer. Control Conf.*, Montreal, Canada, 1998, pp. 1904 – 1908.

[177] Q. Wang and C.-Y. Su, "Robust adaptive control of a class of nonlinear systems with Prandtl-Ishlinskii presentations," *Automatica*, vol. 42, pp. 859 – 867, 2006.

[178] H. K. Khalil, *Nonlinear Systems*, 3rd ed. Prentice-Hall, 2002.

[179] K. Ogata, *Discrete-time control systems*. Englewood Cliffs: Prentice Hall, 1995.

[180] G. A. Korn and K. T. M., *Mathematical Handbook for Scientists and Engineers: Definitions, Theorems, and Formulas for Reference and Review*. New York: Dover Publications, 2000.

[181] B. J. Kenton and K. K. Leang, "Design and control of a three-axis serial-kinematic high-bandwidth nanopositioner," *IEEE/ASME Trans. Mechatronics (in press)*, 2011.

[182] K. K. Leang and A. J. Fleming, "High-speed serial-kinematic AFM scanner: design and drive considerations," *Asian Journal of Control, Special issue on Advanced Control Methods for Scanning Probe Microscopy Research and Techniques*, vol. 11, no. 2, pp. 144 – 153, 2009.

[183] Y. Tak and K. Yong, "Controlled growth of well-aligned ZnO nanorod array using a novel solution method," *J. Phys. Chem. B*, vol. 109, pp. 19 263 – 19 269, 2005.

[184] Q. Ahsanulhaq, J.-H. Kim, and H. Y.-B., "Controlled selective growth of ZnO nanorod arrays and their field emission properties," *Nanotechnlogy*, vol. 18, pp. 485 307 – 485 313, 2007.

[185] B. Weintraub, Y. Deng, and Z. Wang, "Density-controlled growth of aligned zno nanowire arrays by seedless chemical approach on smooth surfaces," *J. Phys. Chem. C*, vol. 111, no. 28, pp. 10 162 – 10 165, 2007.

[186] S. Xu, C. Lao, B. Weintraub, and Z. Wang, "Density-controlled growth of aligned zno nanowire arrays by seedless chemical approach on smooth surfaces," *J. Meter. Res.*, vol. 23, no. 8, pp. 2072 – 2077, 2008.

[187] Z. L. Wang and J. Song, "Piezoelectric nanogenerators based on zinc oxide nanowire arrays," *Science*, vol. 312, pp. 242 – 246, 2006.

[188] A. J. Fleming and K. K. Leang, "High performance nanopositioning with integrated strain and force feedback," in *IFAC Symposium on Mechatronic Systems and ASME Dynamic Systems and Control Conference (DSCC), Invited Session*

on Micro- and Nanoscale Dynamics and Control, Cambridge, Massachusetts, USA, 2010.

[189] J.-H. Hsu, C.-Y. Lin, and H.-N. Lin, "Fabrication of metallic nanostructures by atomic force microscopy nanomachining and lift-off process," *J. Vac. Sci. Technol. B*, vol. 22, no. 6, pp. 2768 – 2772, 2004.

[190] R. C. Hibbeler, *Mechanics of materials*, 6th ed. Pearson/Prentice Hall, 2005.

[191] D. F. Liu, Y. J. Xiang, X. C. Wu, Z. X. Zhang, L. F. Liu, L. Song, X. W. Zhao, S. D. Luo, W. J. Ma, J. Shen, W. Y. Zhou, G. Wang, C. Y. Wang, and S. S. Xie, "Periodic ZnO nanorod arrays defined by polystyrene microsphere self-assembled monolayers," *Nano Lett.*, vol. 6, no. 10, pp. 2375 – 2378, 2006.

Appendix A

System Modeling Program

The following programs complements the modeling for the piezo-based nanopositioning system discussed in previously in Section 7.2 and Section 8.1. The Prandtl-Ishlinskii optimization program computes the parameters g_0, g_1, λ, δ and ρ for the Prandtl-Ishlinskii model, as well as the inverse Prandtl-Ishlinskii optimization program.

A.1 Dynamic System Program

A.1.1 Dynamic System Program for High Speed Stage

```
% MATLAB Code
% Linear Dynamic Model for High-Speed Stage
% Yingfeng Shan
% ====================================================


% load x y axis data==================================
    load X0921.mat
```

```
        w = x0921(:,1);
        G = x0921(:,2);
% Magnitude and phase  --------------------------------
    mag=20*log10(abs(G));
    ph = unwrap(angle(G))*180/pi-180;
% complex freq response G (Transfer Function)----------
    i = sqrt(-1);
    for k = 1:length(w)
        a = 10^(mag(k)/20)*cos(ph(k)*pi/180);
        b = 10^(mag(k)/20)*sin(ph(k)*pi/180);
        G(k,1) = a+b*i;
    end
        Wrad_s = w*2*pi;
        [N, D] = invfreqs(G,Wrad_s,7,9);

% Model of the HP x-x----------------------------------
    Z = roots(N);
    Z = 1.0e+005 *[
        0.2421 + 1.5878i; 0.2421 - 1.5878i;
       -0.0341 - 1.2642i; -0.0341 + 1.2642i
       -0.0681 + 1.0382i; -0.0681 - 1.0382i
       -0.0253 + 0.6399i; -0.0253 - 0.8399i
       -0.0253 + 0.8399i; -0.0253 - 0.6399i
        2.1953 + 0.1779i;  2.1953 - 0.1779i
       -1.1481 ];
    P = roots(D);
```

```
    P = 1.0e+005 * [
        0.3431 + 1.9559i;  0.3431 - 1.9559i
        0.0301 + 1.3559i;  0.0301 - 1.3559i
       -0.0185 + 1.1736i; -0.0185 - 1.1736i
       -0.0181 + 0.9784i; -0.0181 - 0.9784i
       -0.0151 + 0.8284i; -0.0151 - 0.8284i
       -0.0151 + 0.6284i; -0.0151 - 0.6284i
       -0.3554 ];

    [N,D] = zp2tf(Z,P,1);
      sys = tf(N,D);
        K = 10^(mag(1)/20)/dcgain(sys);
    [N,D] = zp2tf(Z,P,K);
      Gtf = tf(N,D);

% compare measured with model--------------
    G_model = freqs(N,D,Wrad_s);
    Mag_model = 20*log10(abs(G_model));
    Ph_model = unwrap(angle(G_model))*(180/pi);

    figure(2); clf;
         subplot(211);semilogx(w,mag,w,Mag_model,'r');
                      ylabel('Magnitude (dB)');
                      xlabel('Frequency (Hz)');
         subplot(212);semilogx(w,ph,w,Ph_model,'r');
                      xlabel('Frequency (Hz)');
```

```
                    ylabel('Phase (degrees)');
```

A.1.2 Dynamic System Program for Long Range Stage

```
% MATLAB Code
% Linear Dynamic Model for Long-Range Stage
% Yingfeng Shan
% ============================================================
  close all
  clear all
  clc
% Frequency response data from the DSA ========================
    load LRCF1k1.mat;
         data = lrcf1k1;
         size(data);
% frequency;
    w = data(:,1);
    G = data(:,2);
% Magnitude and Phase;
    mag=20*log10(abs(G));
    ph = unwrap(angle(G))*180/pi;
% Frequency response plot
    subplot(211);semilogx(w,mag,'b'); hold on
                 ylabel('Magnitude (dB)');
                 xlabel('Frequency (Hz)');
                 grid on
                 title('Frequency response of the piezo-stage')
```

```
    subplot(212);semilogx(w,ph,'b'); hold on
                 xlabel('Frequency (Hz)');
                 ylabel('Phase (degrees)');
                 grid on
% Dynamic model ================================================
% complex freq response G
    i = sqrt(-1);
     for k = 1:length(w)
         a = 10^(mag(k)/20)*cos(ph(k)*pi/180);
         b = 10^(mag(k)/20)*sin(ph(k)*pi/180);
         G(k,1) = a+b*i;
     end
         Wrad_s = w*2*pi;
         [N, D] = invfreqs(G,Wrad_s,0,3);

% Model of the Lang Range Stage x-x
    Z = roots(N)
    Z = [];
    P = roots(D)
    P = 1.0e+003*[
        -0.0353 + 4.5132i
        -0.0353 - 4.5132i
        -3.6885
        ];
    [N D] = zp2tf(Z,P,1);
    sys = tf(N,D);
```

```
    k = 10^(mag(1)/20)/dcgain(sys);
    [N D] = zp2tf(Z,P,k);
    Gtf = tf(N,D)
  % Discrete time model
    Fs = 10000;
    Gz = c2d(Gtf,1/Fs,'foh')
% compare measured with model ==================================
  G_model = freqs(N,D,Wrad_s);
  Mag_model = 20*log10(abs(G_model));
  Ph_model = unwrap(angle(G_model))*(180/pi);
        subplot(211);semilogx(w,Mag_model,'r');
                     ylabel('Magnitude (dB)');
                     xlabel('Frequency (Hz)');
                     legend('Measure X-X','Model X-X');
        subplot(212);semilogx(w,Ph_model,'r');
                     xlabel('Frequency (Hz)');
                     ylabel('Phase (degrees)');
```

A.2 The Prandtl-Ishlinskii Hysteresis Program

The following programs implement the modeling of the Prandtl-Ishlinskii hysteresis, which include the parameter calculation and modeling codes.

A.2.1 Optimization Program for Parameters Calculation

The parameters calculation program using a custom modified nonlinear least-squares curve fitting method and the measured hysteresis data. This program outputs the

optimized value for the parameters g_0, g_1, λ, δ and ρ to make the P-I modeled hysteresis to match the measured hysteresis with smallest root-means square error.

```
% ==================================================================
% main program
% ==================================================================
% The parameters calculation program loads the input triangular signal,
% measured hysteresis output, and a custom designed function. Then
% these values and function are input to the lsqcurvefit function to
% output the optimized parameters.
% Yingfeng Shan
% ------------------------------------------------------------------
  clear all
  close all
  clc
% input signal----------------------------
  load prtri1hz10k12vpp.in
       xdata = prtri1hz10k12vpp(1:50000)';
       xdata = xdata;
% ------------------------------------------------------------------
% Loading the experimental hysteresis data for calculating the
% parameters for PI model to fit the measured model
% ------------------------------------------------------------------
 load prtri1hz10k12vpp2.out
      y = prtri1hz10k12vpp2(:,1);
      ydata = y(1:50000)';
      ydata = ydata-ydata(1);
```

```
      ydata = ydata-(min(ydata)-min(xdata)+max(ydata)-max(xdata))/2;
      ydata = ydata/0.681;
      plot(xdata);hold on
      plot(ydata,'r')

% initial point for parameters g0, g1, lambda, delta and rho
% ------------------------------------------------------------------
  x0 =[0; 0.0211; 0; 0; 0];

% lsqcurvefit function for parameter optimization with a custom
% defined function, myfun, and the input and output data
% ------------------------------------------------------------------
  [x,resnorm] = lsqcurvefit(@myfun,x0,xdata,ydata)

% ==================================================================
% Function: myfun
% ==================================================================
% a custom defined function "myfun" to calculate the parameters for
% the P-I hysteresis model, which is developed from the analytic
% equation of the P-I model
% Yingfeng Shan
% ------------------------------------------------------------------

  function F = myfun(x,xdata)
      a = x(4)*xdata+x(5);
  for k = 1:1:8;
      r(k) = x(1)*k;
```

```
    wint(k) = 0;
    for i = 1:1:length(a);
        v_r(k,i) = a(i)-r(k);
        vr(k,i) =a(i)+r(k);
        w(k,i) = max(v_r(k,i),min(vr(k,i),wint(k)));
        wint(k)=w(k,i);
    end
    pr(k) = x(2)*exp(-x(3)*r(k));
    PFr(k,:) = pr(k)*w(k,:);
end
    ItPFr = sum(x(1)*PFr);
    F = a+ItPFr;
```

A.2.2 Example Prandtl-Ishlinskii Modeling Program

```
% This program validate the Prandtl-Ishlinskii model with
% the parameters calculated from the optimization program
% by comparing with the measured hysteresis output
% Yingfeng Shan
% ========================================================
  clear all
  close all
  clc
% Load the input signal to the P-I model ------------------
  load prtri1hz10k12vpp.in
       xdata = prtri1hz10k12vpp(1:50000)';
       u = xdata;
```

```
% Load the measured hysteresis data for the P-I model to fit
% ------------------------------------------------------------
  load prtri1hz10k12vpp2.out
       y = prtri1hz10k12vpp2(:,1);
       ydata = y(1:50000)';
       ydata = ydata-ydata(1);
       ydata = ydata-(min(ydata)-min(xdata)+max(ydata)-max(xdata))/2;
       ydata = ydata/0.681;

% The P-I model ---------------------------------------------
% The optimized Parameters
  B = 0.3569; rho = 0.6684; tau = 0.6859; c0 = 0.6580; c1 = 0.0606;
% The model
    a = c0*u+c1;

  for k = 1:1:8;
      r(k) = B*k;
      wint(k) = 0;
      for i = 1:1:length(a);
          v_r(k,i) = a(i)-r(k);
          vr(k,i) =a(i)+r(k);
          w(k,i) = max(v_r(k,i),min(vr(k,i),wint(k)));
          wint(k)=w(k,i);
      end
      pr(k) = rho*exp(-tau*r(k));
```

```
      PFr(k,:) = pr(k)*w(k,:);
  end
     ItPFr = sum(B*PFr);
     yp = a+ItPFr;

% Plotting the response ------------------------------------
  freq = 10000;
  t = [0:1:length(u)-1]/freq;

  figure(3);
        plot(t,yp,'r');hold on
        plot(t,ydata)
        xlabel('Time (s)'); ylabel('Disp. (v)');
        legend('P-I model','Hysteresis')

  figure(4);
        plot(u,yp,'r'); hold on
        plot(u,ydata); hold on
        xlabel('Input (v)'); ylabel('Disp. (v)');
        title('Hysteresis curve')
        legend('Model','Measured hysteresis')

% The matching error between the model and measured hysteresis
% -------------------------------------------------------------
  emax = abs(yp-ydata)/[max(ydata)-min(ydata)]*100;
       figure(6);clf;
```

```
        plot(t,emax)
        xlabel('Time (s)'); ylabel('Error');
        title('Error plot')
dif = yp-ydata;
dif2 = dif.^2;
itg = sum(dif2)/50000;
erms = sqrt(itg)/[max(y)-min(y)]*100
```

A.2.3 Example Simulink System Model Configuration

An example Simulink model for piezo-based nanopositioning system is presented in this section in Fig. A.1. This Simulink model simulate the piezo-based nanopositioning system with a cascade model of hysteresis and dynamics as shown in Fig. A.1(a). It is noted that the main logic of the Prandtl-Ishlinskii model is defined by a *for loop* is a sub Simulink model as shown in Fig. A.1(b).

A.3 The Inverse Prandtl-Ishlinskii Hysteresis Program

The programs for modeling the inverse hysteresis compensator and calculating the parameters of the inverse hysteresis compensator are presented in this section.

A.3.1 Optimization Program for Parameters Calculation

The optimization program calculates the parameters g_0', g_1', λ', δ' and ρ' for the inverse Prandtl-Ishlinskii hysteresis compensator. The parameters calculation program loads a triangular signal, measured hysteresis output, and a custom designed function to the *lsqcurvefit* function to compute the optimized parameters, where the the measured hysteresis output is used as a input for calculation, and the triangular signal is used for

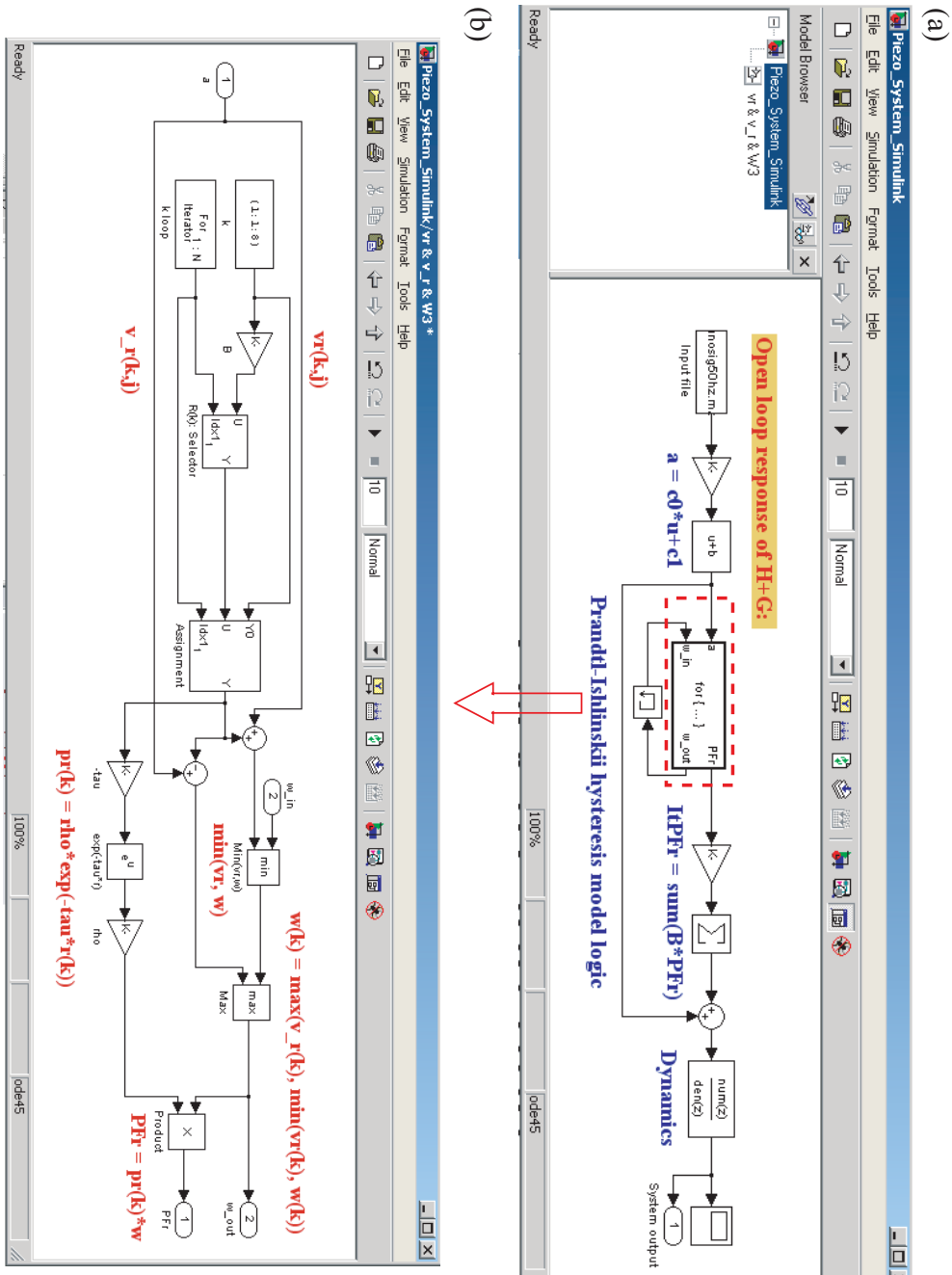

Figure A.1: (a) The main block diagram of Simulink model of the piezo system $[\mathcal{H} + G(z)]$. (b) The logic loop of the Prandtl-Ishlinskii model.

the inverse P-I hysteresis with the computed parameter to compare with to determine the optimized parameters.

```
% ==================================================================
% main program
% ==================================================================
% load measured hysteresis, reference triangular trajectory, initial
% value for the P-I inverse model parameters, and a custom designed
% function "myfun" to lsqcurvefit function to calculate the parameters.
% Yingfeng Shan
% ------------------------------------------------------------------
clear all
close all
clc

% load the measured hysteresis output ------------------------
   load prtri1hz10k12vpp2.out
        x = prtri1hz10k12vpp2(:,1);
        xdata = x';
        xdata = xdata-xdata(1);
        xdata = xdata-(min(xdata)-min(ydata)+max(xdata)-max(ydata))/2;
        xdata = xdata/0.681;

% load the reference triangular trajectory ---------------------------
   load prtri1hz10k12vpp.in
        ydata = prtri1hz10k12vpp';

% initial point for parameters g0', g1', lambda', delta' and rho'
% ------------------------------------------------------------------
```

```
   x0 =[0; 0.0211; 0; 0; 0];

% lsqcurvefit function for parameter optimization with a custom
% defined function, myfun, and the input and output data
% ------------------------------------------------------------------
  [x,resnorm] = lsqcurvefit(@myfunInv,x0,xdata,ydata)

% ==================================================================
% Function: myfunInv
% ==================================================================
% a custom defined function "myfunInv" to calculate the parameters for
% the inverse P-I hysteresis model, which is developed from the analytic
% equation of the inverse P-I model
% Yingfeng Shan
% ------------------------------------------------------------------
  function F = myfunInv(x,xdata)
            a = x(4)*xdata+x(5);
  for k = 1:1:8;
      r(k) = x(1)*k;
      wint(k) = 0;
      for i = 1:1:length(a);
          v_r(k,i) = -a(i)-r(k);
          vr(k,i) =-a(i)+r(k);
          w(k,i) = max(v_r(k,i),min(vr(k,i),wint(k)));
          wint(k)=w(k,i);
      end
      pr(k) = x(2)*exp(-x(3)*r(k));
```

```
      PFr(k,:) = pr(k)*w(k,:);
  end
      ItPFr = sum(x(1)*PFr);
      F = a+ItPFr;
```

A.3.2 Example Inverse Prandtl-Ishlinskii Modeling Program

An example inverse Prandtl-Ishlinskii modeling program is shown here for validation of the performance of the inverse hysteresis compensator on minimizing hysteresis effect.

```
% This program validate the inverse Prandtl-Ishlinskii model
% with the parameters calculated from the optimization program
% by comparing with the desired system response.
% Yingfeng Shan
% ========================================================
  clear all
  close all
  clc
% Load the signal (the measured hysteresis) input to the inverse
% P-I model ------------------------------------------------
   load prtri1hz10k12vpp2.out
        x = prtri1hz10k12vpp2(:,1);
        xdata = x';
        xdata = xdata-xdata(1);
        xdata = xdata-(min(xdata)-min(ydata)+max(xdata)-max(ydata))/2;
        xdata = xdata/0.681;
```

```
% Load the desired system output for the inverse P-I model output
% to fit with ------------------------------------------------
   load prtri1hz10k12vpp.in
        ydata = prtri1hz10k12vpp';
        ydata = ydata;

% The inverse P-I model ---------------------------------------
% The optimized Parameters
   B = 0.7521; rho = 0.2873;   tau = 0.5769; c0 = 1.4188;  c1 = -0.1582;
% The inverse model main logic
  a = c0*xdata+c1;

  for k = 1:1:8;
      r(k) = B*k;
      wint(k) = 0;
      for i = 1:1:length(a);
          v_r(k,i) = -a(i)-r(k);
          vr(k,i) =-a(i)+r(k);
          w(k,i) = max(v_r(k,i),min(vr(k,i),wint(k)));
          wint(k)=w(k,i);
      end
      pr(k) = rho*exp(-tau*r(k));
      PFr(k,:) = pr(k)*w(k,:);
  end
      ItPFr = sum(B*PFr);
      yp = a+ItPFr;
```

```
% Plotting the response ------------------------------------
  freq = 10000;
  t = [0:1:length(xdata)-1]/freq;

  figure(3);
        plot(t,yp,'r');hold on
        plot(t,ydata)
        plot(t,xdata,'k')
        xlabel('Time (s)'); ylabel('Disp. (v)');
        legend('W/ hyst. comp.','Reference','W/o hyst. comp.')

  figure(4);
        plot(ydata,yp,'r'); hold on
        plot(ydata,xdata); hold on
        xlabel('Input (v)'); ylabel('Disp. (v)');
        title('Hysteresis curve')
        legend('W/ hyst. comp.','W/o hyst. comp.')

% The matching error between the desired output and the compensated
% output ----------------------------------------------------------
  emax = abs(yp-ydata)/[max(ydata)-min(ydata)]*100;
       figure(6);clf;
       plot(t,emax)
       xlabel('Time (s)'); ylabel('Error');
       title('Error plot')
```

```
dif = yp-ydata;
dif2 = dif.^2;
itg = sum(dif2)/100000;
erms = sqrt(itg)/[max(ydata)-min(ydata)]*100
```

Example Simulink Inverse hysteresis compensation Configuration

An example Simulink model for validating the performance of the inverse hysteresis compensator in minimizing the hysteresis effect in piezo-based nanopositioning system is presented in this section in Fig. A.2. This Simulink model demonstrates the performance of inverse P-I compensator by adding the inverse P-I model to the feed-forward loop of the cascade model of hysteresis and dynamics as shown in Fig. A.2(a), and comparing with the output of dynamics. It is noted that the main logic of the inverse Prandtl-Ishlinskii model is defined by a *for loop* is a sub-Simulink model as shown in Fig. A.2(b).

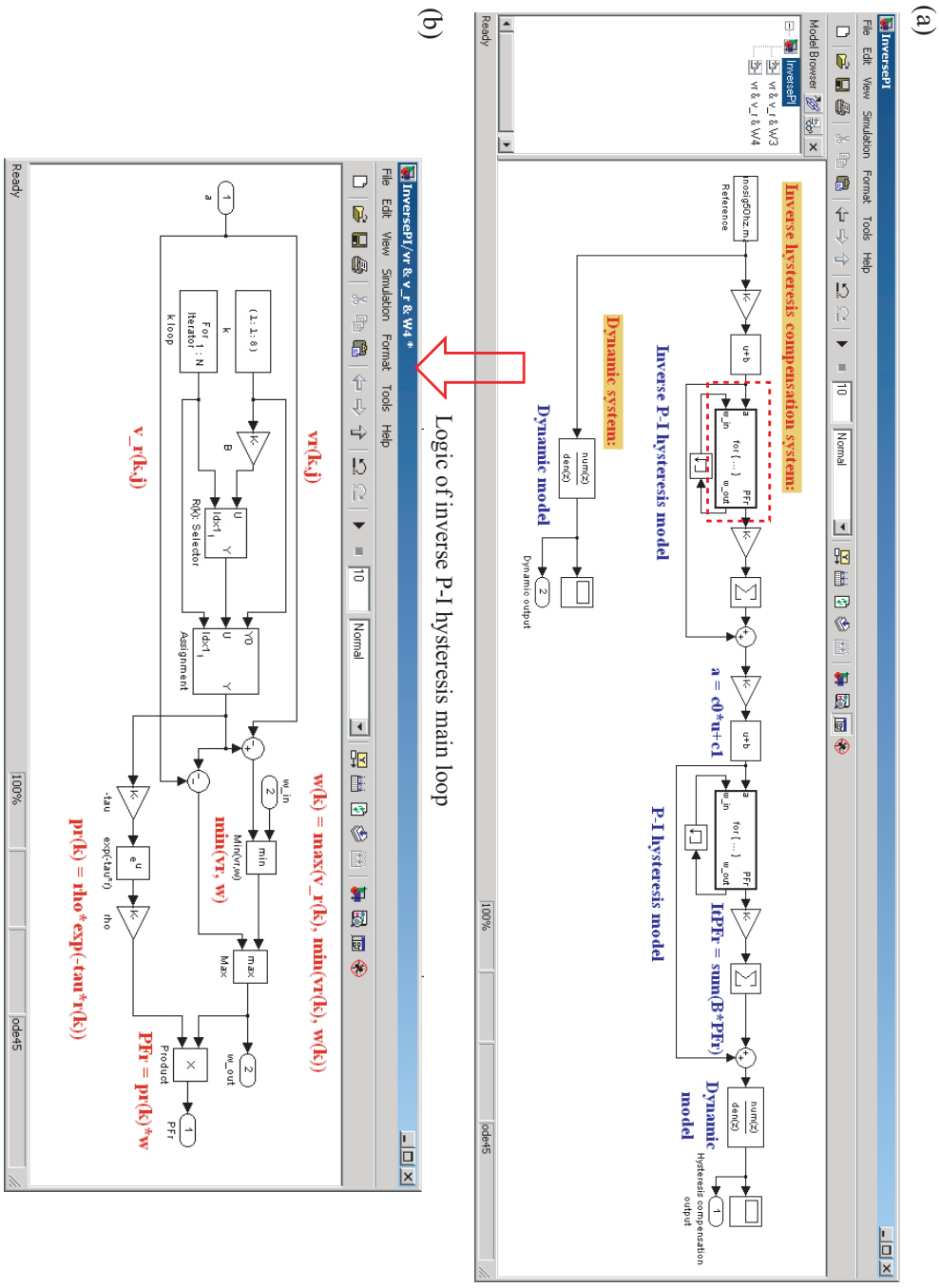

Figure A.2: (a) The main block diagram of Simulink model of the inverse hysteresis compensation system. The output of the inverse hysteresis compensation system is compared to the dynamic system output to validate the performance of the inverse P-I model on minimizing hysteresis. (b) The logic loop of the inverse Prandtl-Ishlinskii model.

Appendix B

Repetitive Controller Design Program

The section presents example Matlab codes used in designing repetitive control system, which are the program for calculating m_2 for phase lead compensator P_2 and cut-off frequency for low pass filter $Q(z)$, and optimizing the values of m_1 and k_{rc} for the enhanced RC design.

B.1 Phase Response of $\theta_T + \theta_2$

The following program is the phase response of $\theta_T + \theta_2$ to determine the m_2 for phase lead compensator P_2 and cut-off frequency for low pass filter $Q(z)$ for the enhanced RC.

```
% to analysis the phase response of the closed-loop feedback with
% phase lead compensator P2
  clear all
  close all
  clc
% Frequency response data from the DSA ==========================
  load LRCF1k1.mat;
     data = lrcf1k1;
```

```
     size(data);
% frequency;
  w = data(:,1);
  G = data(:,2);
% Magnitude and Phase;
  mag=20*log10(abs(G));
  ph = unwrap(angle(G))*180/pi;
% Dynamic model ============================
% complex freq response G
    i = sqrt(-1);
     for k = 1:length(w)
         a = 10^(mag(k)/20)*cos(ph(k)*pi/180);
         b = 10^(mag(k)/20)*sin(ph(k)*pi/180);
         G(k,1) = a+b*i;
     end
         Wrad_s = w*2*pi;
         [N, D] = invfreqs(G,Wrad_s,0,3);
% Model of the Lang Range Stage x-x
    Z = [];
    P = 1.0e+003*[
        -0.0353 + 4.5132i
        -0.0353 - 4.5132i
        -3.6885
        ];
    [N D] = zp2tf(Z,P,1);
    sys = tf(N,D);
```

```
    k = 10^(mag(1)/20)/dcgain(sys);
    [N D] = zp2tf(Z,P,k);
    Gtf = tf(N,D);
% PID controller ================================================
    GPID = tf([.0001 0.02 3000],[1 0]);   % PID
    sys1 = GPID*Gtf;
    Gt = feedback(sys1,1);
    num = [3.391e006  6.781e008  1.017e014];
    den = [1  3759  2.402e007   7.581e010  1.017e014];
    Gt_model = freqs(num,den,Wrad_s);
    Mag_Gt = 20*log10(abs(Gt_model));
    Ph_Gt = unwrap(angle(Gt_model))*(180/pi);
% compare measured with model-------------------------
    G_model = freqs(N,D,Wrad_s);
    Mag_model = 20*log10(abs(G_model));
    Ph_model = unwrap(angle(G_model))*(180/pi);
% plot the phase of the closed-loop system with zm2================
% phase of the zm2--------------------------
    Ts = 1/10000;
    m2 = [0 1 2 3 4 5 6];          % value of the m2 for phase lead
                                   % compensator P2
    for k = 1:1:length(m2);
        zm2(k,:) = cos(m2(k)*Wrad_s*Ts)+sin(m2(k)*Wrad_s*Ts)*j;
        Ph_zm2(k,:) = unwrap(angle(zm2(k,:)))*(180/pi);
        Ph_cl(k,:) = Ph_Gt'+Ph_zm2(k,:);
    end
```

```
    figure(3);
        subplot(211);semilogx(w,Ph_Gt,'k',w,Ph_cl,'r'); hold on
                     xlabel('Frequency (Hz)');
                     ylabel('Phase (degrees)');
                     legend('w_2=0','w_2=6')
                     grid on
% Table of the m_2 vs the cutoff frequency of the low pass filter
    cutoff = [380 840 750 720 710 700 690];
    figure
      plot(m2,cutoff,'*')
```

B.2 Simulink Model for m_1 and k_{rc}

The following Simulink model is used to determine the optimized value of m_1 and k_{rc} for the enhanced RC design. The Simulink model is shown in Fig. B.1.

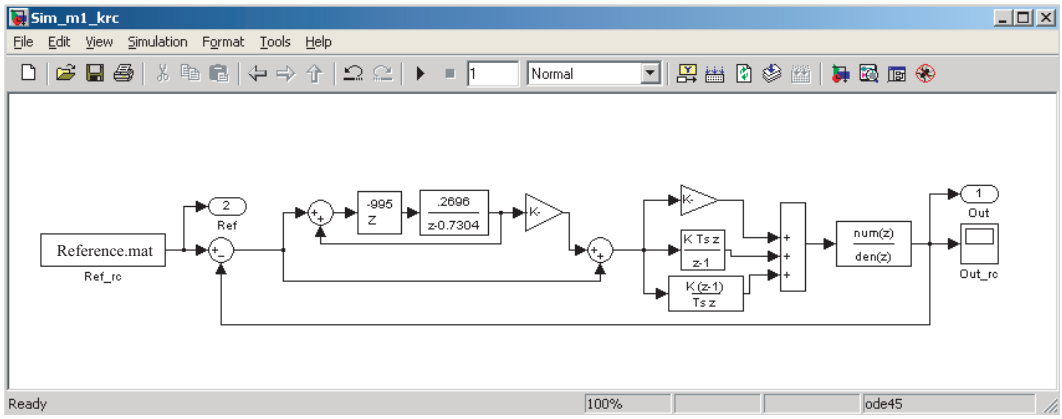

Figure B.1: The Simulink model for m_1 and k_{rc} optimization.

Appendix C

FPGA Codes for Controllers Implementation

This chapter shows example FPGA codes used to implement enhanced repetitive controller, dual-stage repetitive controller for validating the performance of the RC on tracking periodic trajectories in piezo-based high-speed nanopositioner with a closed-loop sampling frequency of 100 kHz.

C.1 FPGA Code for Enhanced RC with PI Controller

Figure C.1 shows the FPGA code of an enhanced RC with PI controller.

C.2 FPGA Code for Dual-Stage RC with PID Controller

This section shows the FPGA code for the dual-stage RC with PID controller in Fig. C.2, where the dual-stage RC is formed by an enhanced RC with an odd-harmonic RC in serial.

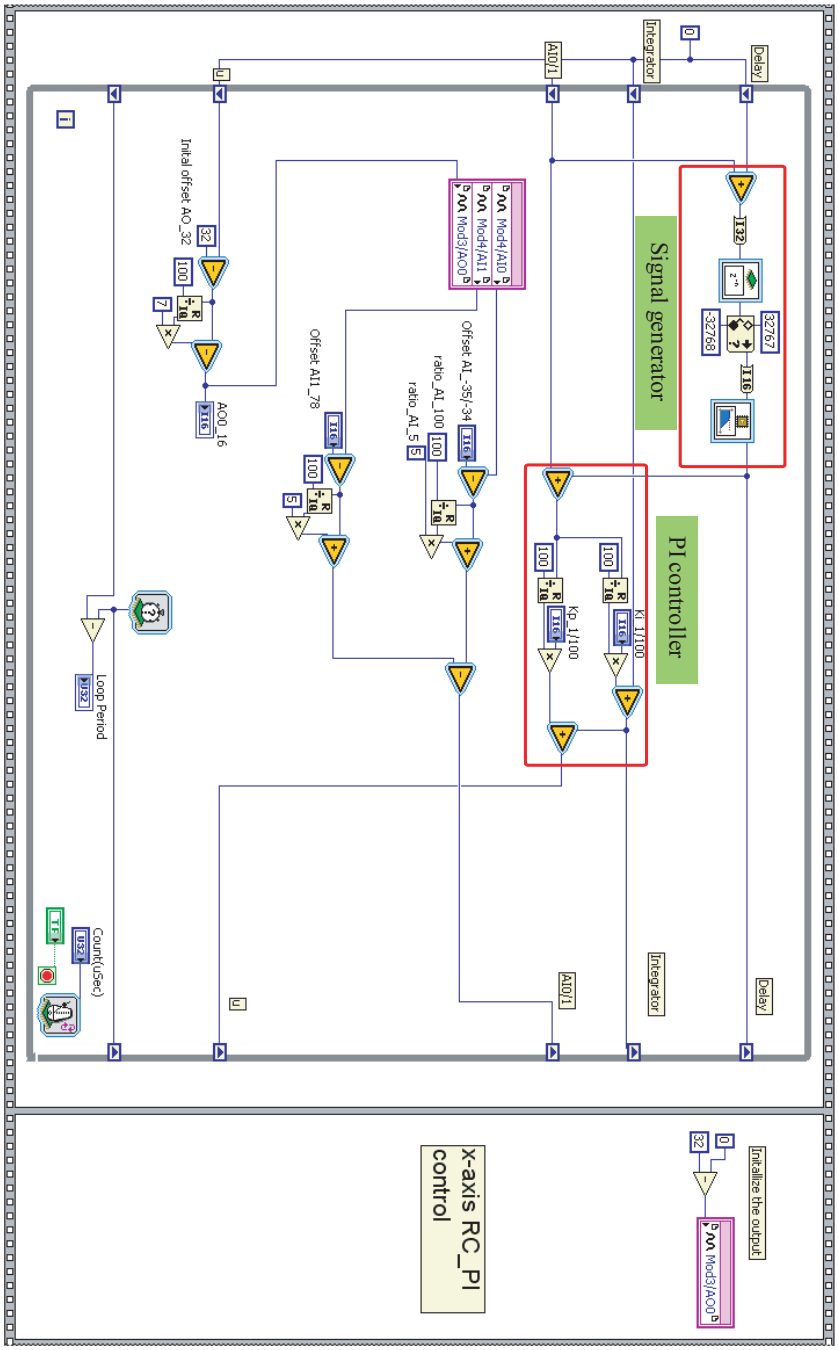

Figure C.1: The FPGA logic of enhanced RC with PI controller.

C.3 FPGA Code for Controlling x and y-axes of the Nanopositioner

Figure C.3 shows the control system for x and y-axes control of the nanopositioner. Specifically, the x-axis is controlled by an enhanced RC with PI control, and y-axis

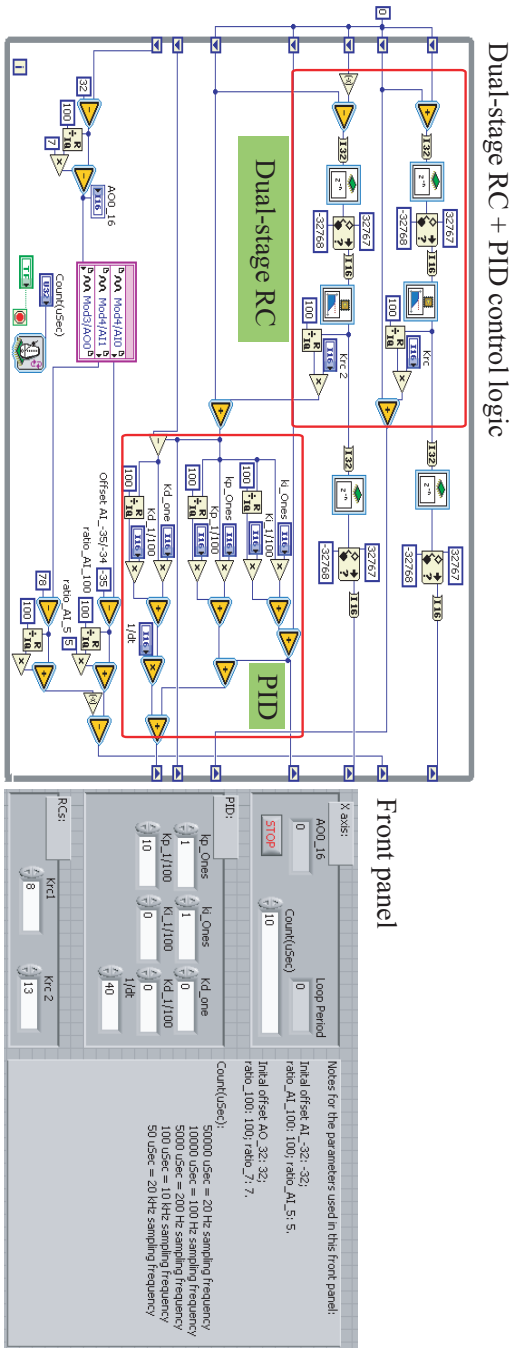

Figure C.2: The FPGA logic of enhanced dual-stage RC with PID controller.

is controlled with a radular PI controller.

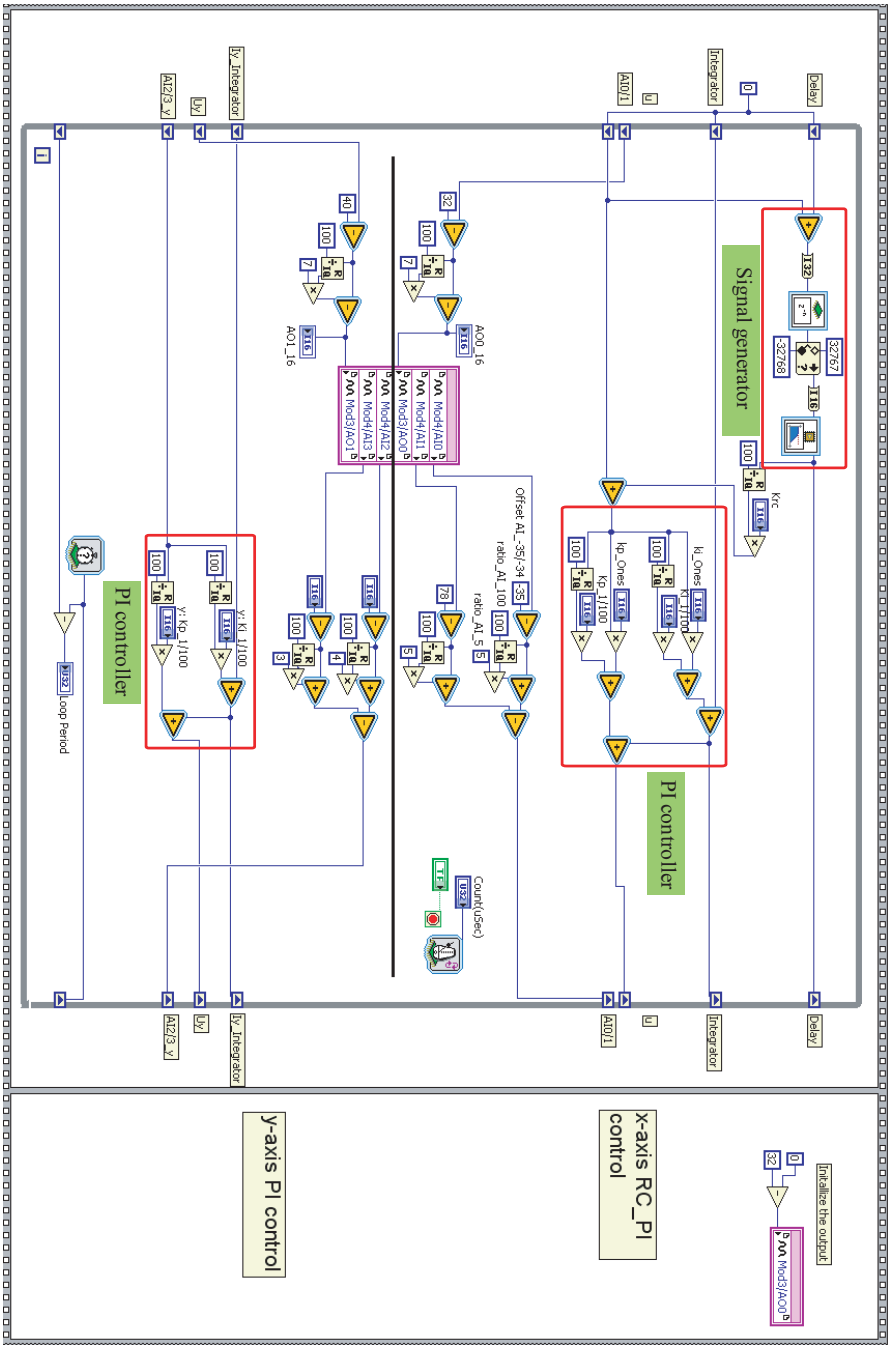

Figure C.3: The FPGA logic of controlling the x and y-axes of the nanopositioner.

C.4 FPGA Code for Enhanced RC with Inverse Hysteresis Compensator

The FPGA code for enhanced RC + $\mathcal{H}^{-1}$ is shown in Fig C.4, where the enhanced RC contains a signal generator with a low pass filter, a phase lead compensator and

a RC gain.

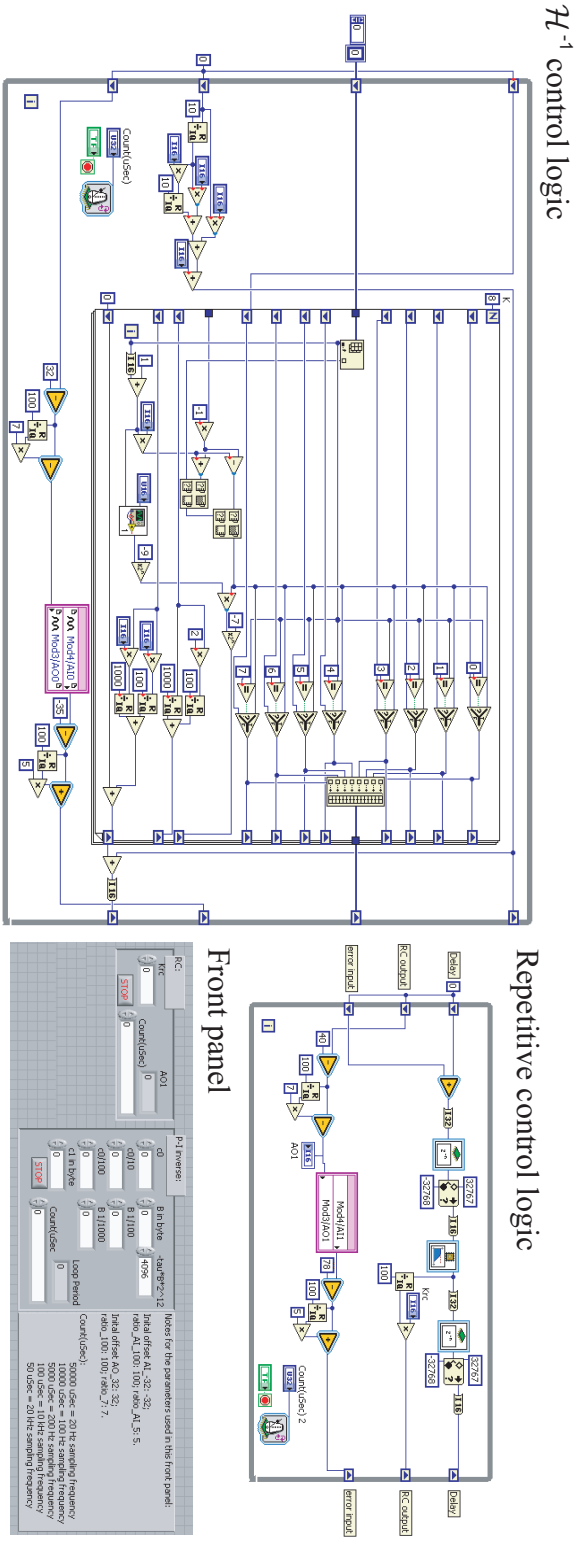

Figure C.4: The FPGA logic of RC with inverse hysteresis compensator.

Appendix D

Matlab Program for Determining Repetitive Control Closed-Loop Stability

Example Matlab codes for determining the closed-loop stability using the stability conditions developed in Eq. (6.10) and (6.16).

D.1 Matlab Program for Gain Margin M_{G_L} Calculation

The following program shows the Matlab program for calculating the gain margin M_{G_L} for the stability condition in Eq. (6.10).

```
% Gain margin of the open loop linear RC system for RC
% closed-loop system stability that contains hysteresis
% Yingfeng Shan
% ================================================
  clear all
  close all
  clc
% ========================Dynamic Model G(z)=======
% load data
```

```
    load X0921.mat
    w = x0921(:,1);
    G = x0921(:,2);
% Magnitude & phase
    mag=20*log10(abs(G));
    ph = unwrap(angle(G))*180/pi-180;
% complex freq response G (Transfer Function)---------
    i = sqrt(-1);
    for k = 1:length(w)
        a = 10^(mag(k)/20)*cos(ph(k)*pi/180);
        b = 10^(mag(k)/20)*sin(ph(k)*pi/180);
        G(k,1) = a+b*i;
    end
        Wrad_s = w*2*pi;
        [N, D] = invfreqs(G,Wrad_s,7,9);
% Pool and Zero
    Z = roots(N);
    Z = 1.0e+005 *[ 0.2421 + 1.5878i;
        0.2421 - 1.5878i;  -0.0341 - 1.2642i
       -0.0341 + 1.2642i;  -0.0681 + 1.0382i
       -0.0681 - 1.0382i;  -0.0253 + 0.6399i
       -0.0253 - 0.8399i;  -0.0253 + 0.8399i
       -0.0253 - 0.6399i;   2.1953 + 0.1779i
        2.1953 - 0.1779i;  -1.1481];
   P = roots(D);
   P = 1.0e+005 * [
```

```
       0.3431 + 1.9559i;    0.3431 - 1.9559i
       0.0301 + 1.3559i;    0.0301 - 1.3559i
      -0.0185 + 1.1736i;   -0.0185 - 1.1736i
      -0.0181 + 0.9784i;   -0.0181 - 0.9784i
      -0.0151 + 0.8284i;   -0.0151 - 0.8284i
      -0.0151 + 0.6284i;   -0.0151 - 0.6284i
      -0.3554];
% Transfer function
    [N,D] = zp2tf(Z,P,1); sys = tf(N,D);
    K = 10^(mag(1)/20)/dcgain(sys);
    [N,D] = zp2tf(Z,P,K);
    Gtf = tf(N,D);
% Complex number model
    G_model = freqs(N,D,Wrad_s);
    Mag_model = 20*log10(abs(G_model));
    Ph_model = unwrap(angle(G_model))*(180/pi);
% ============================closed loop =================
    Freq = 100000;
    s = tf('s');
% --------------------------PI controller----------------
    kp = 1.1; ki = 40000;
    Gc = kp+ki/s;
    Gop = Gc*Gtf;
    GGc = c2d(Gop,1/Freq,'zoh');
% --------------------------RCRCRCRCRCRC-----------------
    krc = 0.5;
```

```
    z =tf('z',1/Freq);
    H = z^(-194)*0.3558/(z-0.6442);
    RC = H/(1-H);
    RCk = krc*RC;
    Grc = (RCk+1)*GGc;
  figure(3);clf
    margin(Grc);
```

D.2 Matlab Program for Quantifying the *Size* of Hysteresis and Linear RC System

This section presents the Matlab program for calculating the size of hysteresis and the *size* of linear RC closed-loop system for the stability condition in Eq. (6.10).

D.2.1 An Example Matlab Program for Quantifying the *Size* of Hysteresis

The following program calculates the size of the hysteresis in the x-axis of the high-speed piezo-based nanopositioner for the stability condition in Eq. (6.10) developed in Section 6.

```
  clear all
  close all
  clc
% triangle 1hz============================
  B =0.1079; rho = 0.0211; tau = -5.0194; c0 = 0.8331; c1 = 0.0677;
  for k = 1:1:8;
      r(k) = B*k;
      wint(k) = 0;
```

```
      pr(k) = rho*exp(-tau*r(k));
  end
  Size of d(r) = sum(B*pr)
```

D.2.2 An Example Matlab Program for Quantifying the *Size* of Linear RC Closed-Loop System

The following program calculates the size of the linear RC closed-loop system for the stability condition in Eq. (6.10).

```
  clear all
  close all
  clc
% ========================Dynamic Model G(z)======================
    load X0921.mat
    w = x0921(:,1);
    G = x0921(:,2);
% Magnitude & phase
    mag=20*log10(abs(G));
    ph = unwrap(angle(G))*180/pi-180;
% complex freq response G (Transfer Function)---------------------
    i = sqrt(-1);
    for k = 1:length(w)
        a = 10^(mag(k)/20)*cos(ph(k)*pi/180);
        b = 10^(mag(k)/20)*sin(ph(k)*pi/180);
        G(k,1) = a+b*i;
    end
      Wrad_s = w*2*pi;
```

```
      [N, D] = invfreqs(G,Wrad_s,7,9);
% Pool and Zero
    Z = roots(N);
    Z = 1.0e+005 *[ 0.2421 + 1.5878i
        0.2421 - 1.5878i;  -0.0341 - 1.2642i
       -0.0341 + 1.2642i;  -0.0681 + 1.0382i
       -0.0681 - 1.0382i;  -0.0253 + 0.6399i
       -0.0253 - 0.8399i;  -0.0253 + 0.8399i
       -0.0253 - 0.6399i;   2.1953 + 0.1779i
        2.1953 - 0.1779i;  -1.1481];
   P = roots(D);
   P = 1.0e+005 * [ 0.3431 + 1.9559i
       0.3431 - 1.9559i;  0.0301 + 1.3559i
       0.0301 - 1.3559i; -0.0185 + 1.1736i
      -0.0185 - 1.1736i; -0.0181 + 0.9784i
      -0.0181 - 0.9784i; -0.0151 + 0.8284i
      -0.0151 - 0.8284i; -0.0151 + 0.6284i
      -0.0151 - 0.6284i; -0.3554];
% Transfer function
    [N,D] = zp2tf(Z,P,1); sys = tf(N,D);
        K = 10^(mag(1)/20)/dcgain(sys);
    [N,D] = zp2tf(Z,P,K); Gtf = tf(N,D);
% Complex number model
    G_model = freqs(N,D,Wrad_s);
    Mag_model = 20*log10(abs(G_model));
    Ph_model = unwrap(angle(G_model))*(180/pi);
```

```
% state-space representation of G(z)--------------
    Freq = 100000;
    Gz = c2d(Gtf,1/Freq,'zoh');
    Pol = pole(Gz); Zer = zero(Gz);
    [A,B,C,D] = zp2ss(Zer,Pol,1);
% ============================RC+PI====================
    s = tf('s');
% PI controller
    kp = 1.1; ki = 40000;
    Gc = kp+ki/s;                        % Transfer function Gc(s)
    Gcz = c2d(Gc,1/Freq,'zoh');          % Transfer function Gc(z)
% state-space representation of Gc(z)------------------
    Polc = pole(Gcz); Zerc = zero(Gcz);
    [Ac,Bc,Cc,Dc] = zp2ss(Zerc,Polc,1.1);
% RC
    krc = 0.5;
    z =tf('z',1/Freq);
    H = z^(-94)*0.3558/(z-0.6442); % z^-100 for 1kHz signal Q = 7kHz
    RC = H/(1-H);                  % Transfer function RC
    RCk = krc*RC;                  % Transfer function RC*krc
% RC+PI
    Grp = (RCk+1)*Gcz;             % Transfer function Grp = RC*Gc
% state-space representation of Grp(z)--------------------
    Pgrp = pole(Grp); Zgrp = zero(Grp);           % pole and zeros
    [Arp,Brp,Crp,Drp] = zp2ss(Zgrp,Pgrp,1.1);
% ======================================================
```

```
% Sup of the G_2
% ====================================================
% R to Y
    Gcl = Grp*Gz/(1+Grp*Gz);
% R to u
    Gru = Gcz/(1+Gcz*Gz);
    Gru = Grp/(1+0.9*Grp*Gz);
% G2(z)-------------------------------------------
    Pol = pole(Gru); Zer = zero(Gru); % pole and zeros
    [NUM,DEN] = ZP2TF(Zer,Pol,1.068);
    NUM = NUM-2*DEN;
    Gru = tf(NUM,DEN);
% get the G(jw) and G(-jw)
    [mag,phase,w]=bode(Gru);
    ma = 20*log10(mag(:));
    ph = phase(:);
% complex number of the transfer function
    gcp1 = mag(:).*[cos(pi*ph/180)+sin(pi*ph/180)*j];
    gcp2 = mag(:).*[cos(pi*ph/180)-sin(pi*ph/180)*j];
    Gsup= gcp2.*gcp1;
% sup||G2||2 ----------------------------
    sup_G = max(sqrt(Gsup(21:end)))
```

Appendix E

Publications

Journal papers on repetitive control design, nanopositioning, mechatronics, and related activities:

1. Repetitive control for hysteretic systems: nanopositioning example, **Y. Shan** and K. K. Leang, Automatica (Accepted).

2. Dual-stage repetitive control with Prandtl-Ishlinskii hysteresis inversion for piezo-based nanopositioning, **Y. Shan**, B. J. Kenton and K. K. Leang, Mechatronics, Special Issue on Mechatronic Systems for Micro- and Nanoscale Applications (In press).

3. Design and analysis of discrete-time repetitive control for scanning probe microscopes, U. Aridogan, **Y. Shan** and K. K. Leang, ASME Journal of Dynamic Systems, Measurement, and Control, Special issue on Dynamic Modeling, Control, and Manipulation at the Nanoscale, Vol. 131, 061103 (12 pages), 2009.

4. Integrated sensing for IPMC actuators using strain gages for underwater applications, K. K. Leang, **Y. Shan**, S. Song and K. J. Kim, IEEE/ASME Transactions on Mechatronics (In press).

5. Frequency-weighted feedforward control for dynamic compensation in ionic

polymer-metal composite actuators, **Y. Shan** and K. K. Leang, Smart Materials and Structures, Vol. 18, pp. 125016 (11 pages), 2009.

6. Low-cost reflective infrared sensors for sub-micro-level position measurement and control, **Y. Shan**, J.E. Speich and K.K. Leang, IEEE/ASME Trans. on Mechatronics, Vol. 13, No. 6, pp. 700-709, 2008.

Conference papers:

1. Repetitive control design for piezoelectric actuators, **Y. Shan** and K. K. Leang, ASME Conference on Smart Materials, Adaptive Structures and Intelligent Systems (SMASIS, 2011), September 18-21, Scottsdale, AZ.

2. Dual-stage repetitive control for high-speed nanopositioning, **Y. Shan** and K. K. Leang, 2010 IFAC Symposium on Mechatronic Systems and 2010 ASME Dynamic Systems and Control Conference (DSCC), Invited session on Micro- and Nanoscale Dynamics and Control, Cambridge, Massachusetts, USA, September 13-15.

3. Tracking control of oscillatory motion in IPMC actuators for underwater applications, S. Song, **Y. Shan**, K. J. Kim and K. K. Leang, 2010 IEEE/ASME International Conference on Advanced Intelligent Mechatronics, Invited session on EAP, July 6-9, Montreal, Canada, 2010.

4. Repetitive control with Prandtl-Ishlinskii hysteresis inverse for piezo-based nanopositioning, **Y. Shan** and K. K. Leang, American Control Conference, Invited Session on Advances in Control of Nanopositioning and SPM Systems, St. Louis, MO, pp. 301-306, 2009.

5. Discrete-time phase compensated repetitive control for piezoactuators in scanning probe microscopes, U. Aridogan, **Y. Shan** and K. K. Leang, ASME Dy-

namic Systems and Control Conference, Invited Session on Modeling, Dynamics and Control of Systems with Smart Materials, Ann Arbor, Michigan, pp. 1325-1332, October 20-22, 2008.

6. Application of feedforward dynamics compensation in ionic-polymer metal composite actuators, **Y. Shan** and K. K. Leang, SPIE Smart Structures and Materials and NDE for Health Monitoring and Diagnostics Conference, San Diego, CA., Vol. 6927, pp. 69270F-1 (12 pages), 2008.

7. A biaxial shape memory alloy actuated cell/tissue stretching system, **Y. Shan**, J. Dodson, S. Abraham, J. E. Speich, R. Rao and K. K. Leang, ASME International Mechanical Engineering Congress and Exposition (IMECE), Seattle, WA, USA, November 11 - 15, 2007.